Dissertation
Submitted to the
Combined Faculties for Natural Sciences and for Mathematics
of the Ruperto-Carola University of Heidelberg, Germany
for the degree of
Doctor of Natural Sciences

Presented by:

Physicist: Klaus-Peter Heue

Born in: Baden-Baden

Oral Examination: 20.12.2005

Airborne Multi AXis DOAS instrument and measurements of two-dimensional tropospheric trace gas distributions

Referees: Prof. Dr. Ulrich Platt

Prof. Dr. Konrad Mauersberger

Abstract

Airborne Multi AXis DOAS instrument and measurements of two-dimensional tropospheric trace gas distributions

The Airborne Multi AXis DOAS instrument was developed and successfully operated during four measurement campaigns. Depending on the purpose the instrument was installed on two different aeroplanes flying either close to the tropopause or in the mixing layer.

In a detailed sensitivity study the possibilities of the measurements were investigated. For a qualitatively good observation of tropospheric trace gases (e.g. NO_2 and HCHO) additional information about the mixing layer height and the aerosol extinction is essential. This information can be gained from either independent measurements or retrieved from the measurements themselves. For example based on the O_4 observation from different lines of sight the aerosol extinction can be estimated.

A very good agreement between tropospheric vertical NO_2 columns for AMAXDOAS and SCIAMACHY measurements will be derived, if the AMF calculation is based on independent observation. The linear correlation between the datasets results in a slope of 1 ± 0.07.

Due to the measurement system the AMAXDOAS instrument is ideal for flux estimations. For one flight just above the mixing layer the total HCHO production of Milano is estimated to $3.5*10^{24}$ molec/s. In total the plume was 20 km wide.

A detailed plume study in lee of a power plant was performed. Here the different NO_2 slant column densities were used for the reconstruction of a 2-dimensional trace gas distribution. The estimated flux originating from the power plant equals $2.5*10^{24}$ molec/s.

Zusammenfassung

Flugzeug gestütztes multi-axiales DOAS Instrument und Messungen zweidimensionaler troposphärischer Spurengasverteilungen

Ein flugzeuggestütztes multi-axiales DOAS (AMAXDOAS) Instrument wurde entwickelt und in vier Messkampagnen eingesetzt. Auf Grund der unterschiedlichen Ziele der Messkampagnen wurde es auf unterschiedlichen Flugzeugen eingebaut. Die Standardflughöhe war entweder nahe der Tropopause oder in der Grenzschicht.

Für eine qualitativ hochwertige Interpretation der Messergebnisse ist eine möglichst genaue Kenntnis des Lichtweges notwendig, dieser wird unter anderem vom Aerosolgehalt beeinflusst. Die Aerosolextinktion kann man entweder unabhängigen Messungen entnehmen oder mittels der eigenen O_4-Messungen abschätzen. Die Sensitivität des Instruments wurde für verschiedene Bedingungen untersucht.

Ein Schwerpunkt der Arbeit war die Validierung der mit SCIAMACHY gemessenen vertikalen troposphärischen NO_2-Säulendichte. Eine sehr gute Übereinstimmung zwischen den Messungen des AMAXDOAS Instruments und denen von SCIAMACHY kann erzielt werden, wenn die lokalen atmosphärischen Bedingungen berücksichtigt werden. Eine lineare Regression der Datensätze ergab eine Steigung von 1 ± 0.07.

Das AMAXDOAS Instrument eignet sich sehr gut zur Bestimmung von Flüssen. Eine Fallstudie für einen Flug in der Grenzschicht ergab für Milano eine HCHO Produktion von $3.5*10^{24}$ Moleküle/s. Die Abluftfahne der Stadt war ungefähr 20 km breit.

Die NO_2-Konzentrationsverteilung in der Abgasfahne eines Kraftwerks konnte mittels der unterschiedlichen Säulendichten entlang unterschiedlicher Lichtwege rekonstruiert werden. Der NO_2-Fluss am Ort der Messung wurde zu $2.5*10^{24}$ Moleküle/s abgeschätzt.

Table of contents

1 Introduction

In this study, a new airborne DOAS instrument and its applications for atmospheric trace gas measurements are presented. The Airborne Multi AXis DOAS (AMAXDOAS) was invented in cooperation with the Institut für Umweltphysik, Universität Bremen.

Airborne DOAS measurements have been performed before in our group in Heidelberg [Pfeilsticker and Platt, 1994] and also in other groups around the globe [e.g., Melamed et al., 2003, Petritoli et al., 2002 and McElroy et al., 1999]. Depending on the different aims, different instrumental approaches were realized. A zenith directed telescope was used for the detection of stratospheric trace gases. [Pfeilsticker and Platt, 1994]. Measurements using lines of sight directed to the horizon were performed to retrieve profile information around the flight altitude [McElroy et al., 1999]. For the quantification of anthropogenic emissions a combination of nadir and zenith observations has been used [Melamed et at., 2003]. Especially for such plume studies the DOAS method is of great advantage. Using an in situ instrument it is absolutely necessary to measure at the plume's altitude. With a DOAS instrument the total column inside the plume is observed, independent of the instruments altitude. However when concentrating on nadir and zenith only [Melamed et al., 2003], the plume's altitude and the vertical extent cannot be determined, here additional information is necessary.

Many trace gases can be detected with the DOAS method, We concentrate on nitrogen dioxide (NO_2) and formaldehyde (HCHO) mainly. Both species play an important role in the atmospheric chemistry. Nitrogen oxides are directly emitted, whereas formaldehyde is additionally built in photochemical processes, hence it can be used to estimate the photochemical activity of the atmosphere. The concentration of these trace gases inside the emission plume are determined, both the plume of big cities (Milano) and single power plants are studied. The observation of tropospheric NO_2 columns form high flight altitudes are compared with the respective SCIAMACHY data product.

With the new AMAXDOAS instrument additional information about the vertical trace gas distribution can be retrieved. When flying with an aeroplane in the boundary layer the information gained from the different lines of sight can be used to reconstruct a 2-dimensional concentration distribution of a local plume. The knowledge about the trace gas concentration distribution offers the possibility to investigate the different chemical processes at the plume's edge and in the plume's centre. In this work first results of a 2-dimensional reconstruction will be presented. These demonstrate the capabilities of the instrument in combination with the reconstruction technique. However, future missions of the instrument will hopefully result in even better reconstruction and improve the knowledge about the chemical processes. The results might be used to validate chemical transport models, where the actual knowledge is implemented.

For emission plumes of large sources like towns additional aspects like a change in the aerosol extinction around the town have to be considered. The simultaneous measurements of O_4 with several different elevation angles allow the approximation of the aerosol extinction profile. When the aerosol extinction is known the sensitivity of the DOAS instruments can be determined more accurate. For the HCHO production of Milano this approach was successfully used and the total flux was estimated.

In our instrument the advantages of airborne measurements were combined with the successful ground based MAX-DOAS instruments [e.g. Hönninger et al., 2004]. While the ground based instruments stay fixed to a certain position the aeroplane performs measurements covering large distances within a short time period. For example a complete north-south cross section over Germany can be performed in less than 2 hours. Due to the long range of the aeroplanes and the high spatial resolution the AMAXDOAS instrument is ideal for the validation of the new satellite instrument SCIAMACHY on ENVISAT. For a new instrument a validation is essential, to demonstrate it measures correctly. The tropospheric NO_2 columns from our instrument can directly be compared to the related product from SCIAMACHY. Both instruments AMAXDOAS and SCIAMACHY observe scattered sunlight and rely on the DOAS method for analysing the observed spectra. The viewing geometry enables us to separate the stratospheric and the tropospheric column densities. The latter can be compared to scientific SCIAMACHY data products developed recently. The validation of SCIAMACHY is performed for both the final product (vertical column) and the intermediate products (slant column densities and air mass factors).

Before the most interesting results of the AMAXDOAS measurements are presented some fundamental aspects concerning tropospheric chemistry, the DOAS method and the radiative transport will be explained. Also some sensitivity studies on the reconstruction of 2-dimensional distributions are given. The sensitivity of the AMAXDOAS instrument for tropospheric absorbers under various conditions like different flight altitudes was studied. The instrument and how it was used are described as well in this work. The focus of this work is on the result of the above mentioned measurements.

2 Tropospheric Chemistry

Validation measurements for SCIAMACHY on ENVISAT and plume studies were mentioned as the main scopes of the AMAXDOAS instrument in the introduction. The main reason for the measurements is to improve our knowledge of atmospheric chemistry. In the following section a short introduction to the atmospheric chemistry is given concentrating on NO_2 and HCHO in the troposphere. Here several trace gases directly influence human health, e.g. ozone or nitrogen oxides. Besides it is harmful to humans in very high concentrations, NO_2 plays an important role in the catalytic production and destruction of ozone. In combination with high concentrations of hydrocarbons the nitrogen oxides cause the summer smog, i.e. enhanced ozone concentration.

2.1 Nitrogen Oxides and Ozone

There is a variety of anthropogenic and natural sources of NO and NO_2. Among the anthropogenic sources there are all kinds of fossil fuel consumption processes, e.g. car traffic, power generation or heating. Other anthropogenic sources are biomass burning but also fertilizing. Natural fires, lightning and soil emission are the most important natural sources. No matter, if the origin is natural or anthropogenic, the largest group of sources are all kind of burning processes. According to the Zel' Dovich mechanism at temperatures $T > 2000$ K the molecules N_2 and O_2 dissociate and NO and NO_2 are formed:

R1)
$$\begin{gathered} O + N_2 \rightarrow NO + N \\ N + O_2 \rightarrow NO + O \\ NO + HO_2 \leftrightarrow NO_2 + OH \end{gathered}$$

The ration of NO_2 to NO depends on a variety of parameters, e.g. for one boiler of a power plant the ratio varies between less than 10 % NO_2 up to 40 % depending on the operation mode, typically it is about 5 % to 10 % [Bland et al., 2000]. Normally the operators avoid emitting NO_2 because it is known to be harmful and because of its brown colour, which causes bad publicity. In the presence of O_3, NO rapidly reacts to NO_2. NO_2 photodissociates for wavelengths below 420 nm to NO and atomic oxygen. The latter reacts with molecular oxygen and forms ozone:

R2) $$NO + O_3 \rightarrow NO_2 + O_2$$

R3) $$NO_2 \xrightarrow{h\nu} NO + O \qquad \text{for } \lambda \leq 420\ nm$$

R4) $$O + O_2 + M \rightarrow O_3 + M$$

These three reactions define a photochemical stationary state, where the ratio between NO and NO_2 is constant. It is given by the Leighton ratio:

$$L := \frac{[NO]}{[NO_2]} = \frac{J(NO_2)}{k_2 \cdot [O_3]}$$

where k_2 is the reaction constant of R2, and $J(NO_2)$ is the photolysis frequency of R3. According to [Atkinson et al, 2004] the reaction constant k_2 equals $1.8*10^{-14}$ $cm^3/(molec*s)$ at 298 K. The photolysis rate can be calculated as:

$$J(NO_2) = \int_0^\infty \Phi(\lambda) \cdot \sigma(\lambda) \cdot F(\lambda) \cdot d\lambda$$

$\Phi(\lambda)$ stands for the quantum yields which is the efficiency for the reaction (close to zero for wavelength longer than 420 nm), $\sigma(\lambda)$ is the absorption cross section of NO_2 and $F(\lambda)$ represents the actinic flux of light, which is the total incident light intensity integrated over all solid angles.

For calculation of the photolysis frequency a theoretical value of the actinic flux depending only on the solar zenith angle is often used [Finlayson-Pitts and Pitts, 1986]. For a solar zenith angle of 55° this theoretical photolysis frequency equals $6.2*10^{-3}$ 1/s.

During the FORMAT campaigns (chapter 6 and 8) the actinic flux was measured by Wolfgang Junkermann. According to his measurements (file date: 1/03/04) $J(NO_2)$ varies between 7 and $10*10^{-3}$ s^{-1} depending on the altitude level between 600 m and 2000 m. In higher altitudes above the mixing layer less light is absorbed compared to ground level and the photolysis frequency increases(Figure 2-1).

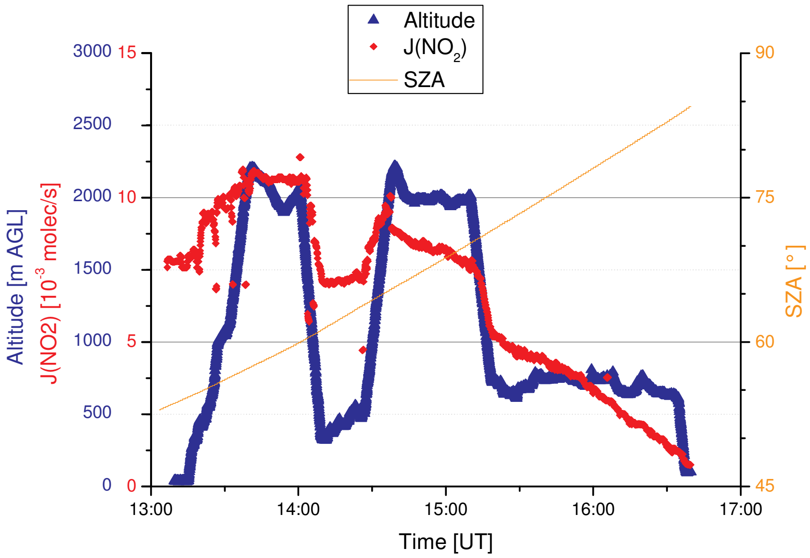

Figure 2-1: Measured photolysis frequency for NO_2 (red). It depends on the flight altitude (blue) and the solar zenith angle (orange). Above the boundary layer the photolysis frequency increases (Wolfgang Junkermann, personal communication 01/03/04).

As the chemical reactions between NO and NO_2 (R2-R4) are very fast, these two species are usually summarised to NO_x, and instead of the NO to NO_2 ratio the NO_2 to NO_x ratio is used:

$$f_{NO_2} = \frac{[NO_2]}{[NO_x]} = \frac{1}{1+L}$$

For a typical O_3 mixing ratio of 55 ppb and a photolysis rate of $7*10^{-3}$ s^{-1}, the NO_2 to NO_x ratio equals 77 % in the boundary layer (600 m).

The reactions R2, R3 and R4 are the main reactions defining the concentrations of O_3, NO and NO_2. However, there are further reactions including hydrocarbons influencing this photochemical state. In the following sections we will discuss some of them; first we concentrate on the sinks of nitrogen oxides.

Although the chemistry during night and day is complete different, in both cases NO_x is removed by reactions forming HNO_3 which is finally removed by precipitation.
During daytime NO_2 reacts with OH (R12) to form HNO_3:

R5) $$NO_2 + OH + M \rightarrow HNO_3 + M$$

During night-time NO_3 is formed by a reaction of NO_2 and O_3, then N_2O_5 is produced, by reaction with a second NO_2 molecule. N_2O_5 reacts heterogeneously on aerosols or surfaces to form HNO_3 in a water droplet. During daytime NO_3 rapidly photodissociates, hence the following reactions are only important in the night:

R6) $$NO_2 + O_3 \rightarrow NO_3 + O_2$$

R7) $$NO_3 + NO_2 + M \rightarrow N_2O_5 + M$$

R8) $$N_2O_5 + H_2O \xrightarrow{het} 2HNO_3$$

2.2 Hydroxyl Radical and Carbon Oxides

The Leighton ratio describes a steady state. This will very easily be perturbed if other oxidising tracers are present. The most relevant oxidising species are the hydroperoxyl radical HO_2 and the hydroxyl radical OH, summarised as HO_x. The importance is shown below:

R9) $$NO + HO_2 \rightarrow NO_2 + OH$$

R10) $$CO + OH \rightarrow CO_2 + H$$

R11) $$H + O_2 \rightarrow HO_2$$

Here one NO molecule is oxidised to NO_2 without the destruction of O_3. Together with the reactions R3 and R4 we get the net reaction:

$$CO + 2O_2 \rightarrow CO_2 + O_3$$

The concentration of OH and HO_2 are not influenced by the total reactions R9 to R11, also the concentration of NO is not reduced by the total process. These reactions result in a catalytic production of ozone. Here carbon oxide is used as an example; similar reactions are possible with hydrocarbons (section 2.3 – R15-R18).
Photodissociation of ozone is an important source of the hydroxyl radical. The exited atomic oxygen reacts with a water molecule and two OH molecules are produced:

R12) $$O_3 \xrightarrow{h\nu} O_2 + O(^1D)$$ for $\lambda < 310\,nm$

R13) $$O(^1D) + H_2O \rightarrow 2OH$$

According to [Finlayson-Pitts and Pitts, 2000] only 10 % of the $O(^1D)$ reacts with water (at 50% relative humidity and 300 K), most of it is deactivated to the ground state and reacts with oxygen to ozone. Photodissociation of HONO is a second source of OH. It photodissociates at wavelength shorter than 400 nm:

R14) $$HONO \xrightarrow{h\nu} OH + NO \qquad \text{for } \lambda < 400\,nm$$

The third and in urban or suburban conditions one of most important sources of HO_2 is given by photodissociation of formaldehyde (R20-R21).

2.3 Formaldehyde and VOCs

Two of the campaigns, the AMAXDOAS measurements concentrated on the distribution of formaldehyde (chapters 6.3, 6.4 and 8). Therefore we will discuss the chemistry of HCHO a bit more in detail. Formaldehyde is directly emitted by fossil fuel combustion and biomass burning or it is produced in chemical reactions, mainly from methane but also from other hydrocarbons (NMHC – non methane hydrocarbons):

R15) $$CH_4 + OH \rightarrow CH_3 + H_2O$$

R16) $$CH_3 + O_2 + M \rightarrow CH_3O_2 + M$$

R17) $$CH_3O_2 + NO \rightarrow CH_3O + NO_2$$

R18) $$CH_3O + O_2 \rightarrow HCHO + HO_2$$

These reactions are summarised as:

$$CH_4 + OH + NO + 2O_2 \rightarrow HCHO + HO_2 + NO_2 + H_2O$$

In those reactions a hydroxyl radical is oxidises to a hydroperoxyl radical, in addition a nitrogen dioxide is formed out of a nitric oxide. In combination with reaction and R9 and R3 – R4, two ozone molecules are formed:

R9) $$NO + HO_2 \rightarrow NO_2 + OH$$

R3) $$2\,(NO_2 \xrightarrow{h\nu} NO + O)$$

R4) $$2(O + O_2 + M \rightarrow O_3 + M)$$

If there are many hydrocarbons present, NO will be oxidised to NO_2 without the depletion of O_3, this leads to a net O_3 production:

$$CH_4 + 4O_2 \xrightarrow{h\nu} HCHO + 2O_3 + H_2O$$

Similar reaction chains as described for methane can be observed for other hydrocarbons as well. The reactions R15 – R18 can be replaced by the respective reactions. Here CH_3 is replaced by a hydrocarbon rest R. In most of the following secondary reactions formaldehyde is produced as a by-product. This is the reason why formaldehyde can be used as a tracer for photo chemical activity, besides it is an important source of OH via the photolysis.
For the removal of formaldehyde three reaction paths are important, in the end two of them lead to CO and HO_2 (R20,R21 and R22,R23) and one produces H_2 and CO (R19):

R19) $$HCHO \xrightarrow{h\nu} H_2 + CO \qquad \lambda < 360\,nm$$

R20) $$HCHO \xrightarrow{h\nu} H + HCO \qquad \lambda < 340\ nm$$

R21) $$\begin{gathered} H + O_2 \rightarrow HO_2 \\ HCO + O_2 \rightarrow CO + HO_2 \end{gathered}$$

For wavelengths between 323 nm and 360 nm R19 is the dominant path, for smaller wavelengths the reactions R20 and R21 are more important. During the FORMAT campaigns (chapters 6.3 and 6.4), at noon, about 37 % of the photodissociated formaldehyde forms HO_2 (Claudia Hak, private communication, 20/09/2005).
The third reaction is not photochemical but oxidises the hydroxyl radical OH to HO_2:

R22) $$HCHO + OH \rightarrow HCO + H_2O$$

R23) $$HCO + O_2 \rightarrow CO + HO_2$$

Photolysis is the dominant sink of formaldehyde. The concentration of HO_x radicals did not change during the production of formaldehyde. During the photolytic destruction process on average 0.37 HO_2 molecules are produced per HCHO molecule. In total a net production of oxidising species is observed.
The net production of ozone per hydrocarbon depends on the individual species. For the typical hydrocarbon found in the atmosphere, containing 2 – 6 carbon atoms, 4 – 14 ozone molecules are produced [Sillmann et al., 1990]. As not all hydrocarbons interact in the tropospheric chemical process, the subgroup of volatile organic compounds (VOCs) is considered only. Depending on the sources different VOCs are emitted of both natural and anthropogenic sources. Terpenes for example are emitted by trees, but also incomplete combustion processes emit VOCs like benzene. An overview over the chemistry of NO_x, O_3, OH and hydrocarbons is given in Figure 2-2:

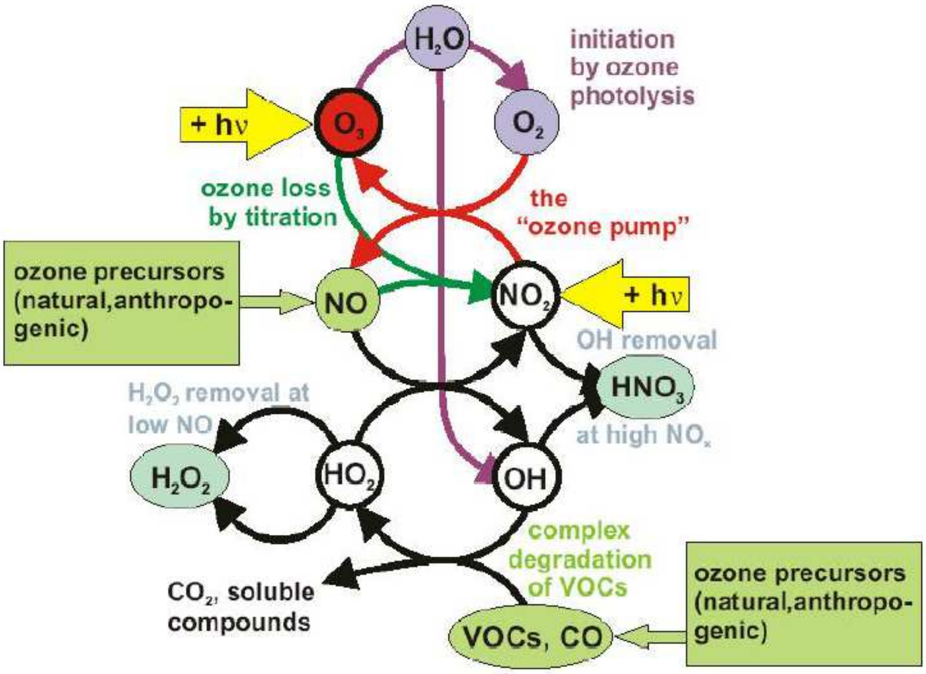

Figure 2-2: Overview of the formation of tropospheric ozone including the most relevant precursors [Beirle, 2004 and reference therein].

The ozone producing reactions were described above. However the ozone production is reduced if there are too many nitrogen oxides or it only few nitrogen oxide molecules are available. In theoretical sensitivity studies [e.g. Sillman et al., 1990] it was observed that the ozone concentration depends on the initial concentration of NO_x and hydrocarbons a shown in Figure 2-3:

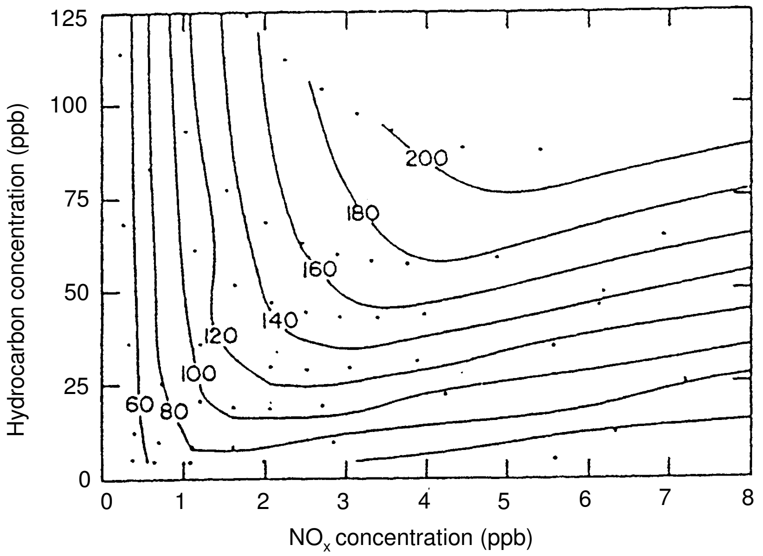

Figure 2-3: Ozone isopleths in ppb as a function of the concentration of NOx and hydrocarbons [Sillman et al., 1990]. The dots are given by individual runs of the computer simulations, where the emission rates where given as input parameters.

For a given initial hydrocarbon concentration (25 ppb) the ozone mixing ratio increases with increasing NO_x concentration until it reaches a maximum at (120 ppb O_3 at 2.5 ppb NO_x), after wards it decreases with increasing NO_x concentration. The later situation is called “VOCs limited case”, as a further increase in VOC would increase the total ozone.

The other case a decreasing O_3 concentration with increasing VOC at constant NO_x concentration is not observed. But here also a maximum is reached, after a certain threshold of VOC the ozone level remains constant independent of the VOC. This situation is referred to as “NO_x-limited”.

The theoretical studies have been proved in various measurements. For an efficient reduction of tropospheric ozone, during summer smog episodes, the knowledge about the actual situation is important. If the local system is VOC-limited a reduction of NO_x will be contra productive and the ozone concentration will further increase. The actual concentration of formaldehyde and nitrogen dioxide can help to interpret the situation correctly.

A recent study [Martin et al., 2004] suggests using the $HCHO/NO_2$ ratio as indicator for VOC-NO_x-limitation. If the ratio is below 1, the system is VOC-limited, otherwise it is NO_x imited. If the ratio is close to 1 no clear conclusion will be possible.

3 Differential Optical Absorption Spectroscopy

3.1 Applications

The first spectroscopic measurements in the atmosphere were performed by the end of the 19th century. In 1925 Dobson applied an instrument which used the difference of ozone absorption at two wavelengths to determine the total thickness of the ozone layer.

In contrast to the measurements relaying just on two wavelengths, a certain wavelength interval is taken into account in the Differential Optical Absorption Spectroscopy (DOAS) [Platt et al., 1979]. In this method the concentration of the trace gases along the light path is determined by considering the small scale variations of the absorption cross section only. Beside O_3 many other trace gases, e.g. NO_2, HCHO, O_4, H_2O can be observed.

Nowadays a large variety of different DOAS instruments for different purposes exists. In principle two groups of Differential Optical Absorption Spectroscopy (DOAS) instruments can be distinguished: depending on the light source they are called active or passive systems. The references given in here indicate the most recent publications, the beginning of the active DOAS measurements reaches back to the 1970s [Platt et al., 1979].

Active systems emit a light beam from an artificial light source such as a Xe-lamp [e.g.: Mettendorf, 2005], a Laser [Hübler et al., 1984] or a LED [Kern, 2004]. The light is detected after it crossed the atmosphere along a well defined path.

Passive systems use natural light sources like the sun, the moon or some individual stars. Most passive systems observe scattered sunlight under one or more elevation angles. Compared to active systems the passive systems have no well defined light path. Their advantage is a high flexibility. They can be used on many different platforms ranging from ground based [Louban, 2005], aeroplanes [this work], balloons [Weidner, 2005] to satellite borne instruments [Beirle, 2004]. Ground based DOAS systems are a large specialised subgroup. While for stratospheric observation a zenith sky system is well sufficient, an instrument with different elevation angles (Multi-AXis-DOAS) [Sinreich et al., 2005] is best suited to retrieve profile information on trace gases. For plume studies an imaging DOAS instrument (i-DOAS) was developed recently [Lohberger et al., 2004 or Louban, 2005].

The instrument presented here was built to combine the profile information gained from a MAX-DOAS instrument with the high spatial resolution of aeroplane measurements.

3.2 The Measurement Principle

The measurement method used in this work is based on the fact that the absorption dI of light is proportional to the length dl of the light path through the absorbing medium, to the concentration c of the absorber and to the specific absorption cross section σ. The exact formulism is described by Lambert-Beer's[1] law:

$$dI(\lambda) = I(\lambda) \cdot c(l) \cdot \sigma(\lambda) \cdot dl \tag{3.1}$$

usually it is written in the integrated form

---

[1] Named after Johann Heinrich Lambert (1728 – 1777) and August Beer (1825 – 1863), the former discovered the absorption to be proportional to the length of the light path in the absorbing medium. The latter found the linear correlation between absorption and the concentration of the absorber.

$$I(\lambda) = I_0(\lambda) \cdot e^{-\int c(l)\cdot\sigma(\lambda)\cdot dl} \tag{3.2}$$

The dependency of the absorber is given by the specific cross section σ. In atmospheric measurements the absorbers are different constituents of the atmosphere, e.g. H_2O, O_3, NO_2 and HCHO. The examples mentioned here are definitely not the main constituents of the ambient air, usually only 1 to 100 parts per billion (ppb) air molecules are NO_2, HCHO or O_3. Nevertheless we focus on them due to their chemical importance (chapter 2).

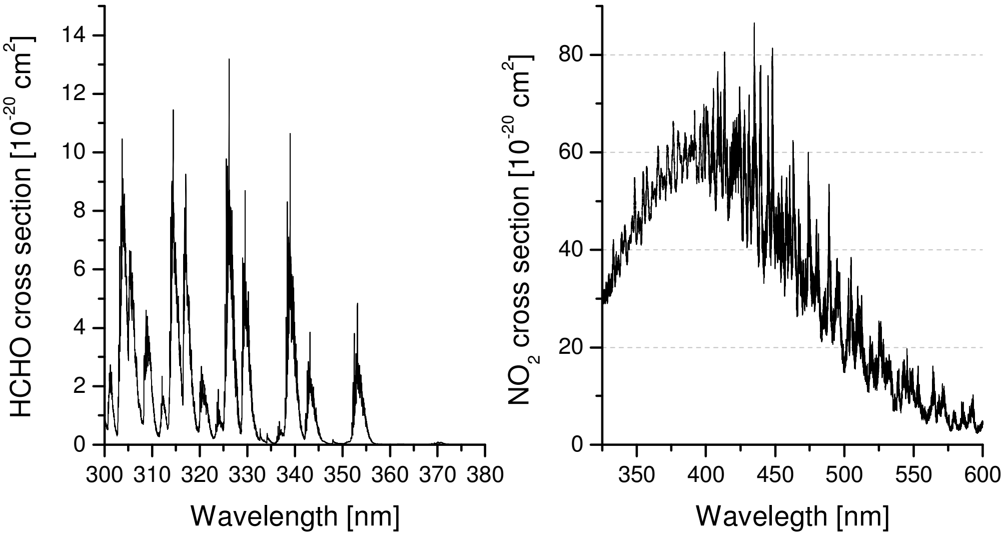

Figure 3-1: Cross sections for formaldehyde (left) [Meller and Moortgat, 2000] and nitrogen dioxide (right) [Voigt et al., 2002].

The cross sections of HCHO and NO_2 are shown in Figure 3-1, both show a characteristic absorption structure. The absorption is caused by electronic and rotational vibrational transitions in the molecules.

Besides the absorption of light caused by different trace gases, the initial intensity is reduced by scattering processes by molecules or particles (chapter 4.2.II and 4.2.IV). The extinction of light caused by the scattering processes is described in the above mentioned section. For the moment we describe the influence by extinction coefficients k for Rayleigh and Mie scattering depending on whether the scattering centres are small or large compared to the wavelength.

In total Lambert-Beer's law is written as:

$$dI(\lambda) = I(\lambda) \cdot \left(\sum_i c_i(l) \cdot \sigma_i(\lambda) + k_{Rayleigh}(\lambda) + k_{Mie}(\lambda) \right) \cdot dl \tag{3.3}$$

or again in the integrated formula:

$$I(\lambda) = I_0(\lambda) \cdot e^{-\tau(\lambda)} \tag{3.4a}$$

with

$$\tau(\lambda) = \sum_i \int_L c_i(l) \cdot \sigma_i(\lambda) \cdot dl + \int_L k_{Rayleigh}(\lambda) \cdot dl + \int_L k_{Mie}(\lambda) \cdot dl = \ln \frac{I_0(\lambda)}{I(\lambda)} \tag{3.4b}$$

here τ is the total optical density of the atmosphere. The index i numbers all the relevant gases absorbing light at this certain wavelength λ. The concentration c of most trace gases depends on the location and the altitude, also the Mie extinction coefficient is highly variable. The cross sections σ_i characterise the individual trace gases i but change with temperature and pressure. The Rayleigh extinction mainly depends on the air density.

3.2.I The DOAS Method

To retrieve the integrated concentrations along the light path the Differential Optical Absorption Spectroscopy (DOAS) is used [Platt, 1994]. The cross sections of the individual trace gases can be measured in the laboratory or taken from the literature and convoluted to the instrumental resolution. The total extinction, however, is influenced by many unknown parameters like scattering, which can hardly be retrieved. The absorption by the trace gases will be separated from their influence, if only the small band structures are considered (Figure 3-2). In the DOAS method this idea is applied to the spectra.

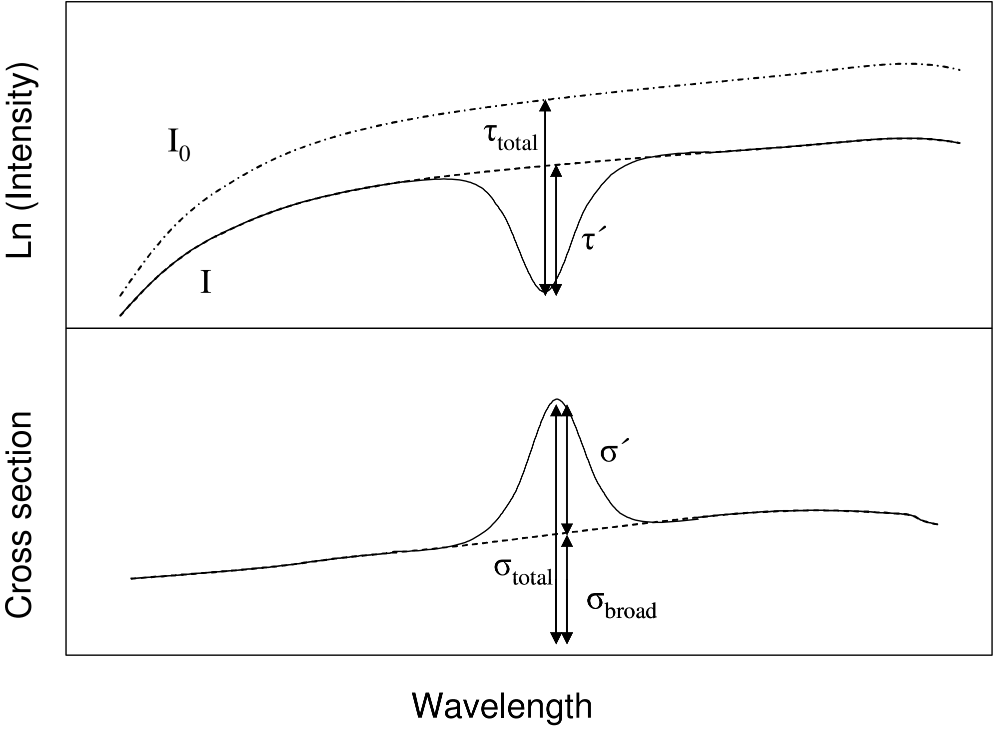

Figure 3-2: Upper panel: The total intensity I_0 is attenuated due to absorption; the measured intensity I shows a general reduction and a small absorption peak. The latter is used to derive the absorption caused by the trace gas.
Lower panel: Parallel to separation of small and broad band absorption, the cross section is split into a broad band and a small band part.
Adapted from [Stutz, 1996].

In case of the differential absorption spectroscopy the observed intensity is interpolated between the edges of one small absorption peak and only the difference to this interpolation line is considered (Figure 3-2). The method is based on the fact that both the total absorption τ_{total} and the small peak τ' are proportional to the integrated concentration along the light path. Mathematically this approach is realised by separation of broad band σ_{broad} and small band σ' absorption structures of the trace gases:

$$\sigma(\lambda) = \sigma'(\lambda) + \sigma_{broad}(\lambda)$$

The broad band absorption is usually approximated by adding a polynomial in the retrieval or both the spectrum and the cross sections are high band pass filtered. In Figure 3-3 the total and the differential cross sections are shown.

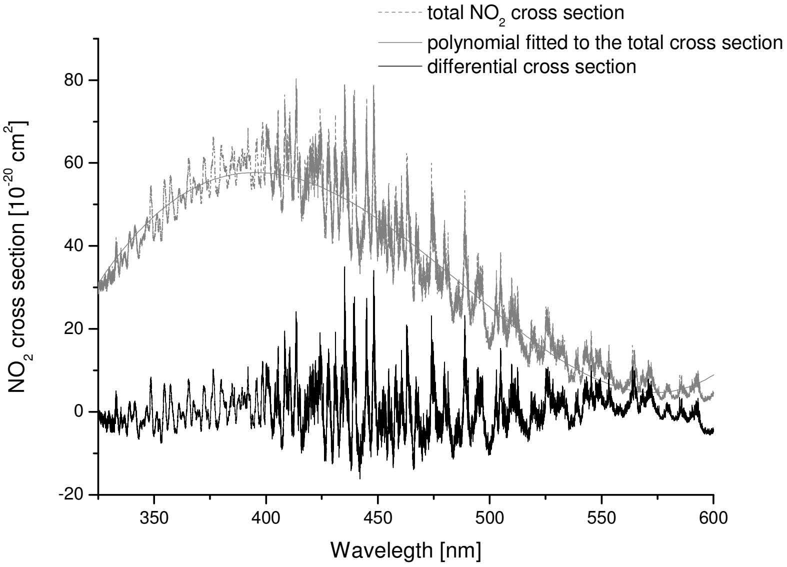

Figure 3-3: The broad band absorption structures are removed from the NO$_2$ cross section (Figure 3-1) and the small band structure σ´ remains (black line).

After separating the broad and small structures in the absorptions the optical density τ and Lambert-Beer's law is split accordingly:

$$\tau(\lambda) = \tau'(\lambda) + \tau_{broad}(\lambda) \tag{3.5a}$$

with

$$\tau'(\lambda) = \sum_i \int_L c_i(l) \cdot \sigma'_i(\lambda) \cdot dl \tag{3.5b}$$

and

$$\tau_{broad}(\lambda) = \sum_i \int_L c_i(l) \cdot \sigma_{broad,i}(\lambda) \cdot dl + \int_L k_{Rayleigh}(\lambda) \cdot dl + \int_L k_{Mie}(\lambda) \cdot dl \tag{3.5c}$$

According to equations (3.4a) and (3.5a) Lambert-Beer's law can now be written as:

$$\begin{aligned} I(\lambda) &= I_0(\lambda) \cdot e^{-(\tau'(\lambda)+\tau_{broad}(\lambda))} \\ &= I'_0(\lambda) \cdot e^{-\tau'(\lambda)} \end{aligned}$$

The intensity I´$_0$(λ) equals the initial intensity weakened by the broad band absorptions: $I'_0(\lambda) = I_0(\lambda) \cdot e^{-\tau_{broad}(\lambda)}$.

The differential optical density τ´(λ) is given by the logarithm of the ratio I´$_0$(λ) and I(λ):

$$\begin{aligned} \tau'(\lambda) = \ln\left(\frac{I'_0(\lambda)}{I(\lambda)}\right) &= \sum_i \int_L \sigma'_i(\lambda) \cdot c_i(l) \cdot dl \\ &= \sum_i \sigma'_i(\lambda) \cdot \int_L c_i(l) \cdot dl \end{aligned} \tag{3.6}$$

The last step will be possible, if we assume the cross section to be independent of the absorber's position r in the atmosphere. While this will be true for most tropospheric absorbers, this assumption is not really fulfilled, if the cross section depends on temperature and pressure (e.g. stratospheric Ozone). In this case a work around is usually used and two cross sections of the same trace gas with different temperatures are used. Nevertheless, we call the integrated concentration along the light path column density CD (or S) of the specific trace gas:

$$S = \int_L c(r) \cdot dl \tag{3.7}$$

3.2.I.a Measurement and Data Retrieval

The measurements of the spectra can be described by three separate steps. Beside the following description an overview is given in Figure 3-4.

At the beginning the light reaches the instrument with a certain intensity wavelength distribution I(λ), which is dominated by emission spectrum of the light source (Figure 3-4 a).

In the spectrograph the light is spectrally analysed. The spectral resolution of the spectrograph is dominated by the width of the slit and the grid of the spectrograph. Mathematically this process can be described as convoluting the intensity with the instrumental function H:

$$I^*(\lambda) = I(\lambda) * H(\lambda) = \int I(\lambda') \cdot H(\lambda - \lambda') \cdot d\lambda' \quad \text{(Figure 3-4 b)}$$

For the numerical analysis the spectrum is mapped on an electronic detector (CCD or PDA). Here the continuous function is split into several discrete values. Common detectors have about 1024 to 2048 pixels. The mathematical description of the discretisation is given by a number of integration procedures:

$$I^+(j) = \int_{\lambda(j)}^{\lambda(j+1)} I^*(\lambda') \cdot d\lambda'$$

Here the convoluted intensity is integrated across one pixel j of the detector. The complete spectrum is digitised in e.g. 1024 values (Figure 3-4 c). The function λ(j) is called dispersion function. It describes which wavelength interval is recorded by the individual pixels of the detector. Hence it is characteristic for the spectrograph detector combination. Usually it is approximated by a linear function or a polynomial of second or third order. Due the physical principles of the spectrographs the dispersion function is strictly monotonous in the definition interval. The dispersion function of our instrument is given in chapter 5.5.II.a. In real measurement the detector is fixed to the spectrograph and we can not distinguish between the steps 2 and 3.

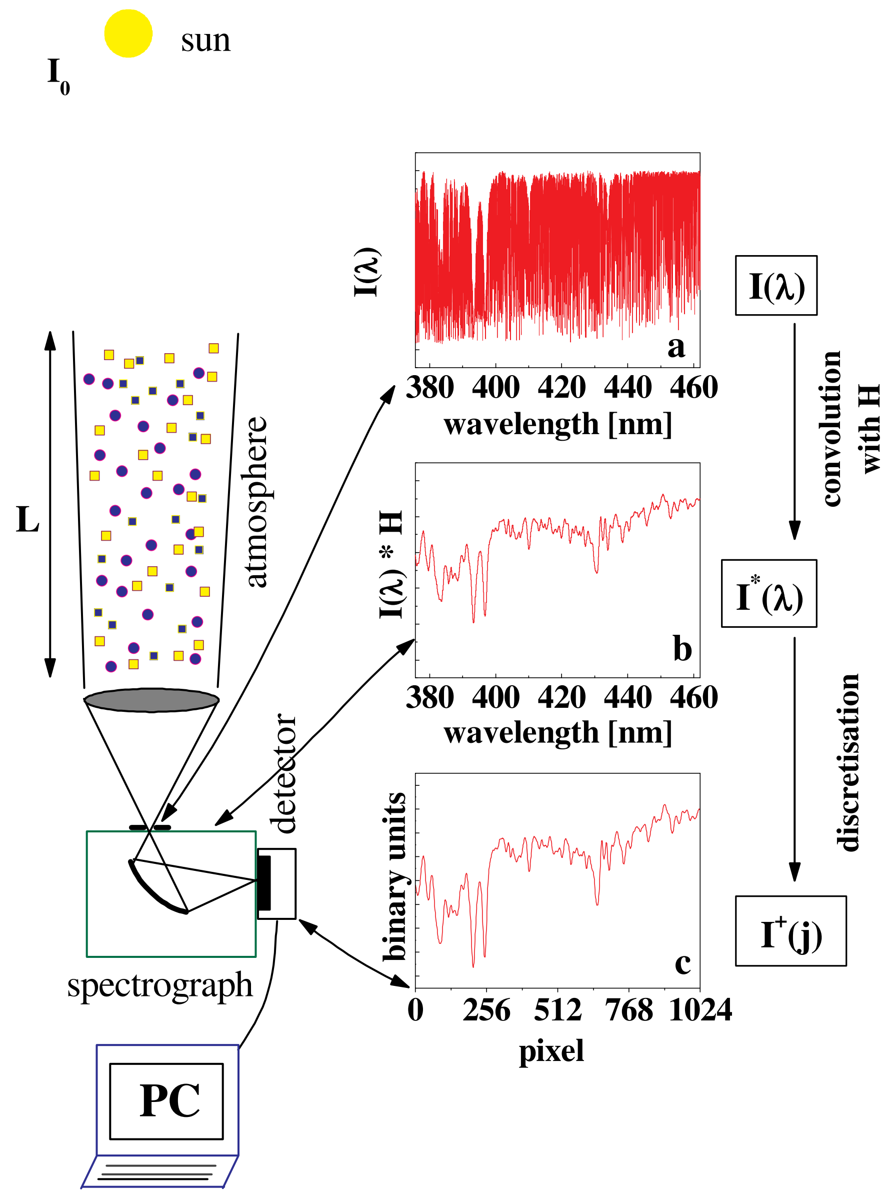

Figure 3-4: Systematic plot of the measurement procedure, adapted to stray light measurements from [Stutz, 1996]. In the sub pictures:
a) The high resolution spectrum was taken from [Kurucz et al., 1984],
b) convoluted with instrumental slit function,
c) convoluted and discretised with the detectors resolution.

In the analysis of the data the cross sections of several trace gases are fitted to the observed measurement spectrum. Usually the cross sections are not directly measured with the same instrument, but literature values are used and adapted to the instrumental properties. For this purpose they are convoluted with the instrumental function H: $\sigma^* = \sigma * H$, subsequently it is digitized using the same dispersion function $\sigma^*(\lambda) \mapsto \sigma^+(j)$.

In case of passive DOAS systems a special measurement spectrum is normally taken as reference I_0. To minimize the absorption structures in the reference in most cases a spectrum taken at noon is used. For our purpose, however, other criteria are more important (section 3.3).

3.2.I.b The Analysis Procedure

The cross sections have been convoluted to the instrumental resolution, the reference has been chosen, now all the data are prepared for the analysis. According to Lambert-Beer's law the following equation has to be solved for the CD_i for a certain number of pixels defined by the fitting window:

$$I^+(j) = I_0^+(j) \cdot \exp\left(-\sum_i \sigma_i^+(j) \cdot S_i - P(j)\right) \tag{3.8}$$

Compared to equation (3.4) an additional polynomial P(j) has been added to account for the broad band structures of the trace gases and for the scattering processes.

A linear least squares fit can be used to retrieve the column densities CD_i of the individual trace gases and the coefficients of the polynomial, as soon as the logarithm of the equation (3.8) is taken:

$$\ln(I^+(j)) - \ln(I_0^+(j)) = -\sum_i \sigma_i^+(j) \cdot S_i - P(j) \tag{3.9}$$

Sometimes the dispersion function is not constant in time, due to temporal variations of the spectrograph. Hence the spectra have to be recalibrated and the dispersion function has to be adjusted. In this case the complete fit is no longer linear and a Marquardt-Levenberg fit is used [Fayt and van Roozendael, 2001 and references therein].

The function to be minimized in the fit is obviously the difference between the right and the left hand of equation (3.9), squared and summed up for all m pixels of the fit window:

$$\chi^2 = \sum_{j=1}^{m} \left[\ln(I^+(j)) - \ln(I_0^+(j)) - \sum_i \sigma_i^+(j) \cdot S_i - P(j) \right]^2$$

The fitting routine WinDOAS [Fayt and van Roozendael, 2001] has been used to retrieve the data presented in this work.

3.2.I.c Residual Structure and Measurement Error

The measurement is influenced by the photon statistics and other sources of statistical noise, hence the right and the left term of equation (3.9) can never totally agree. The difference between the two terms is called residual structure or just residual:

$$res(j) = \ln(I^+(j)) - \ln(I_0^+(j)) - \sum_i \sigma_i^+(j) \cdot S_i - P(j)$$

The correlation between the residual structure and the observed spectrum will become evident if we assume two spectra taken immediately one after the other and the atmosphere did not change in between. In this case the sum and the polynomial vanish, and the two spectra differ by the observed noise N(j) only: $I^+(j) = I_0^+(j) + N(j)$

$$\begin{aligned} res(j) &= \ln(I^{+}(j)) - \ln(I_0^{+}(j)) \\ &= \ln(I_0^{+}(j) + N(j)) - \ln(I_0^{+}(j)) \\ &= \ln\left(\frac{I_0^{+}(j) + N(j)}{I_0^{+}(j)}\right) \\ &= \ln\left(1 + \frac{N(j)}{I_0^{+}(j)}\right) \\ &\approx \frac{N(j)}{I_0^{+}(j)} \end{aligned}$$

These equations show, that the relative noise of the individual spectra define the order of magnitude of the expected residual. Although we assumed the column densities S_i to be zero here, the same equations will hold, if the observed column densities are perfectly retrieved by the fitting procedure.

According to the definition the residual structure is an optical density, it can be used to determine the uncertainty of the fit. For example if the optical density of one trace gas is small compared to the residual the accuracy of this column density will be very low. Usually the residual is given as either the peak to peak value (PTP) or the root mean square (RMS).

$$PTP = \frac{\max(res(j)) - \min(res(j))}{average(res(j))}$$

$$RMS = \sqrt{\frac{1}{m} \cdot \sum_{j=1}^{m} res(j)^2}$$

Due to the photon statistics (Poisson), the PTP value usually is a factor of 6 higher than the RMS and the noise is dominated by the photon statistics. The magnitude of the noise also depends on the detector and is therefore explained in chapter 5.5.III. We will see later on, that the typical noise is of the order of 1 ‰. In this case the residual will be of the same order of magnitude.

To estimate the error of the fitting result two different possibilities will be introduced here. The first one is based on the fitting residual structure. The second approach uses the fluctuation in the retrieved column densities.

Details about the error estimation based on the residual structure are given by [Stutz and Platt, 1996]. The main idea is to use an ensemble of random spectra with peak to peak values of the same order as the residual and to use these spectra as input data for the fitting routine. Obviously the fit results in nothing but error. For each trace gas the average value of the ensemble should be zero and the width of the distribution gives the error of the column densities. If N_{rel} denotes the relative noise of the spectra, the error of the optical density will be given by:

$$\tau_{err} \approx \frac{N_{rel} \cdot 6}{\sqrt{m-1}} \qquad (3.10)$$

where m stands for the number of pixels in the fitting window. The factor six is an approximation resulting from the study quoted above. It differs for the individual trace gases and should in principle be defined for each DOAS instrument. The error in the column density is linear to the error in the optical density divided by the cross section.

In the following a brief example is given based on the HCHO retrieval for the first FORMAT campaign. The relative noise is about 1 ‰, the fitting window for formaldehyde expands from 323 nm to 368 nm. The HCHO cross section vanishes for wavelengths larger than 358 nm. The dispersion function of our instrument is linear with a slope of 0.083nm/pixel, so the number m of pixels in the fitting window equals $m \approx 421\ pixels$.

For formaldehyde the differential cross section σ' at 326.25 nm equals 6.8*10^{-20} cm^2/molec after it was convoluted to the instrumental resolution. So assuming a relative noise of 1 ‰ the error in the column density is given by:

$$\Delta S \approx \frac{n_{rel}\cdot 6}{\sigma'\cdot\sqrt{m-1}} \approx 4.3\cdot 10^{15}\ molec/cm^2$$

This number agrees quite well with the fit error given by the WinDOAS analysis software. For the data of 16/08/2002 the DOAS fit errors are of the order of 3 to 4*10^{15} molec/cm^2.

The second approach to determine the error is based on the assumption that the temporal variations in the observed trace gas are small compared to the temporal resolution of the instrument. In this case the high temporal fluctuations are dominated by the error. The data CD(t) of the measurement interval are smoothed CD_{smooth}(t) and the difference between the smoothed and the unsmoothed data can be used as a variance of the data. On average the difference vanishes and the width of the distribution equals the variation.

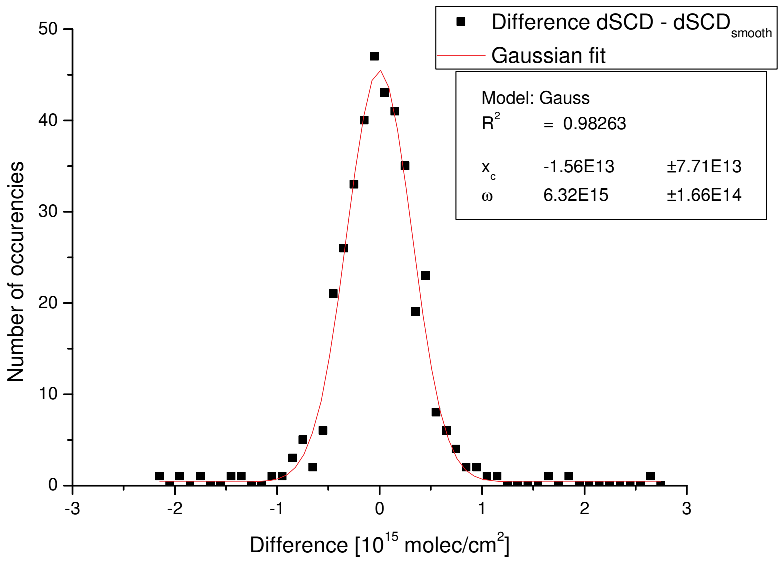

Figure 3-5: Frequency count of the difference dSCD(t)-$dSCD_{smooth}$(t) and a Gaussian fit. The centre of the fit is close to zero and the width equals 6.3*10^{15} molec/cm^2.

For the example of HCHO on 16/08/2002 (chapter 8.1) the frequency count for the telescope N2 (-16°) and the Gaussian fit are shown in Figure 3-5. The width ω of the Gaussian equals 6.3*10^{15} molec/cm^2, which equals an error of ±3.1*10^{15} mole/cm^2, which is in the same range as the error determined via the relative noise.

In section 3.3 an overview of the typical DOAS fit error for all trace gases observed with the AMAXDOAS instrument will be given, but first we will continue with the theoretical discussion of the DOAS method.

3.2.II Instrumental Effects

In the previous sections we assumed most steps in a series of measurement and data retrieval to be commutative. This however is only true in the sense of an approximation and normally leads to slight errors in the data retrieval, which will be discussed in the next two sections.

Therefore it is necessary to take a second, more detailed look on the mathematical description of the analysis to discuss the approximations.
The detected spectrum is given by:

$$I^{+}(j)=\left[\left(I_0(\lambda)\cdot e^{-\sigma(\lambda)\cdot S}\right)*H\right]^{+}(j)$$

In the analysis it is divided by a reference spectrum I_0:

$$\frac{I^{+}(j)}{I_0^{+}(j)}=\frac{\left[\left(I_0(\lambda)\cdot e^{-\sigma(\lambda)\cdot S}\right)*H\right]^{+}(j)}{\left[\left(I_0(\lambda)\right)*H\right]^{+}(j)}$$

And the fit of the column densities is done after the logarithm is applied:

$$\begin{aligned}\ln\left(\frac{I^{+}(j)}{I_0^{+}(j)}\right)&=\ln\left(\frac{\left[\left(I_0(\lambda)\cdot e^{-\sigma(\lambda)\cdot S}\right)*H\right]^{+}(j)}{\left[\left(I_0(\lambda)\right)*H\right]^{+}(j)}\right)\\&\approx\ln\left(\frac{\left[\left(I_0(\lambda)\right)*H\right]^{+}(j)\cdot\left[e^{-\sigma(\lambda)\cdot S}*H\right]^{+}(j)}{\left[\left(I_0(\lambda)\right)*H\right]^{+}(j)}\right)\\&=\ln\left(\left[e^{-\sigma(\lambda)\cdot S}*H\right]^{+}(j)\right)\\&\approx\ln\left(e^{-\left[\sigma(\lambda)*H\right]^{+}(j)\cdot S}\right)=-\left[\sigma(\lambda)*H\right]^{+}(j)\cdot S\end{aligned}\tag{3.11}$$

In the analysis two approximations are made. In both cases the convolution is assumed to be commutative with other mathematical operations. The following effects can also be elucidated by an operator formalism [Wenig et al., 2005].

3.2.II.a I₀-Effect

The absorption caused by a trace gas not only depends on the cross section and the column density, but it is also linear in the incident intensity I_0.
In Figure 3-4 a) the spectrum of the light I(λ) reaching the spectrometer is shown, a high variability is obvious. In the analysis only the detected (convoluted and digitized) signal $I^{+}(\lambda)$ can be used. The cross section was convoluted using the same instrumental slit function. Hence we indirectly assumed the detected (convoluted) light was absorbed by the trace gases. Or if we use the mathematical formulism in (3.11), it will be more obvious: in the second step the convolution and the multiplication were be exchanged:

$$\left[\left(I_0(\lambda)\cdot e^{-\sigma(\lambda)\cdot S}\right)*H(\lambda)\right]^{+}(j)\approx\left[\left(I_0(\lambda)\right)*H(\lambda)\right]^{+}(j)\cdot\left[e^{-(\sigma(\lambda)\cdot S)}*H\right]^{+}$$

As the real absorption depends on the initial spectrum $I_0(\lambda)$ the effect is called I_0-effect.
Practically this effect is small and can be further reduced by calculating a corrected cross section. A column density of the order of the expected values (e.g. $2*10^{16}$ molec/cm^2 for NO_2) is assumed for calculating a theoretical intensity I(λ) based on high resolution I_0 [e.g.: Kurucz et al., 1984]. Both $I_0(\lambda)$ and I(λ) are convoluted with the instrumental function and the logarithm of the ratio gives the response of the instrument to the assumed column density [Frieß, 1997]:

$$\sigma^{+}_{corrected}(j)=\frac{1}{S_{ass}}\cdot\ln\left(\frac{\left[I_0\cdot e^{-\sigma\cdot S_{ass}}*H\right]^{+}(j)}{\left[I_0*H\right]^{+}(j)}\right)$$

Only if the assumed column density perfectly matches the reality, the I_0-effect will be absolutely corrected by using this cross section, in the other cases the error is reduced.
The DOAS fit errors of the data presented here are much higher than the usual improvement (0.1 ‰ in the residuum [Frieß, 1997]) gained from a corrected cross section. Hence the I_0-effect was not taken into account here.

3.2.II.b Saturation

In the penultimate step of (3.11) we assumed the convolution and the exponential (logarithmic) function to be commutative:

$$\begin{aligned}\ln\left[e^{-(\sigma(\lambda)\cdot S)}*H\right]^{+}&\approx\ln\left(e^{-([\sigma(\lambda)*H]^{+}\cdot S)}\right)\\&=-(\left[\sigma(\lambda)*H\right]^{+}\cdot S)\end{aligned}$$

If the absorption is small, this error can well be ignored. For stronger absorber, however, the error is important. The same approximation can be deduced by replacing e^{-x} by $1-x$, which is known to be valid for small x:

$$\begin{aligned}\ln\left[e^{-(\sigma(\lambda)\cdot S)}*H\right]^{+}&\approx\ln[(1-(\sigma(\lambda)\cdot S))*H]^{+}\\&=\ln([1*H]^{+}-[(\sigma(\lambda)\cdot S)*H]^{+})\\&=\ln(1-[(\sigma(\lambda)\cdot S)*H]^{+})\\&\approx-[(\sigma(\lambda)\cdot S)*H]^{+}\end{aligned}$$

The approximation causes a non linearity of the observed optical density $\ln\left(\frac{I^{+}(j)}{I_0^{+}(j)}\right)$ to the column density. It is called saturation effect, as for very strong absorbers the observed optical density would not change even if the column density did.

3.2.III Passive DOAS Systems

In the description of the analysis we did not distinguish between active and passive systems. The spectrum of the absorbed light is of only secondary influence on the analysis (I_0-effect). In the following some details are shown where this influence is more important.
One aspect was already mentioned in the introduction of this chapter. The light path of an active DOAS system is well known, whereas the passive system integrates along an unknown light path through the atmosphere. The results of the passive DOAS instruments are hence called slant column densities (SCD, S) to consider this effect. For a better comparison with other measurements usually the vertical column density (VCD, V) is calculated. The following chapter (4) focuses on the calculation of vertical column densities, here only the main definitions are given:

$$V=\int_0^H c(z)\cdot dz$$

where z stands for the altitude, reaching from the ground up to the top of the atmosphere H and c again is the concentration of the trace gas. The vertical column density does not depend on the light path.
To convert a slant column to the corresponding vertical column the influence of the light path is calculated and expressed as air mass factor (AMF, A):

$$A = \frac{S}{V}$$

The air mass factors describe the sensitivity of the instrument for a trace gas under certain conditions in the atmosphere.

3.2.III.a Reference Spectrum – Differential Columns

In the DOAS analysis a reference spectrum I_0 is included. Usually a specially selected measurement spectrum is used for this purpose. However, if all the measurements are analysed relative to another spectrum, only the relative absorption will be gained. The absorption in the reference spectrum remains unknown. The analysis hence results in a differential column density instead of a total value. In the following it will be called dSCD,or dS:

$$dS_{measurement} = S_{measurement} - S_{reference}$$

Satellite instruments like SCIAMACHY can directly observe the sunlight and hence total slant columns can be retrieved directly.

3.2.III.b Ring Effect

Besides the elastic scattering processes (Rayleigh and Mie), inelastic Raman scattering (chapter 4.2.III) occurs as well: A photon with the wavelength λ has a different wavelength λ ± Δλ after the scattering process.

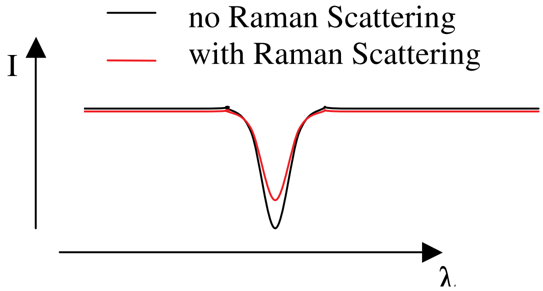

Figure 3-6: The Fraunhofer lines are filled in because of the Raman scattering.

If the intensity is a constant function of the wavelength, the Raman scattering will not change the spectrum. If there is a small absorption peak, then more light will be scattered from the edges to the centre of the peak than vice versa. This effect explains a filling-in of the Fraunhofer lines in atmospheric spectra. It was first observed by [Grainger and Ring, 1962] and explained by [Brinkmann, 1968]. It is named Ring effect after the discoverer.
As a consequence of the Ring effect it is impossible to remove the Fraunhofer absorption structures by dividing one measurement through another. The Ring effect changes with the most important measurement parameters. For example at large solar zenith angles the light path through the atmosphere is longer and the effect is hence stronger. Therefore the ring effect also depends on the relative azimuth angle between the detector's line of sight and the sun [Wagner et al., 2004]. In principle it might be used to derive additional information about

the length of the light path and hence the aerosol extinction. With the actual used Radiative transfer program (chapter 4.3) it is not yet possible.

A pseudo absorber is included in the DOAS analysis to account for the Ring effect a. Both measured and calculated Ring spectra are used. The measured Ring spectra however are influenced by the absorption in the atmosphere, which affects the data analysis [Wagner et al., 2001 b]. Therefore the calculated Ring spectra are recommended. The Ring spectra used here have been calculated using the WinDOAS analysis software.

3.3 Spectral Analysis

In the last sections the principle of the DOAS fit and the most important systematic and statistical errors were discussed. In this section some details concerning the retrieval of the presented data will be explained. The AMAXDOAS instrument consist of spectrometers optimised for either UV or vis. The vis-instrument was operated by our own, whereas the UV instrument belongs to our partners in Bremen. The following section focuses on the spectral analysis of the vis data, details about the uv-analysis can be found in Wang et al., [2005 a].

In the analysis a reference is included. Due to different instrumental functions (chapter 5.5.II.a) the reference was taken from the same viewing direction. Spectra observed in "clean air regions" are chosen for this purpose. For all lines of sight the reference spectrum is taken at the same time. For the SCIAVALUE campaigns (chapter 6.1) mountains or oceans were ideal reference regions. In case of the FORMAT campaigns (chapter 6.3 and 6.4) a spectrum observed in the south of Milano (outside the plume – chapter 8.1) was normally taken.

The main parameter of the spectral fit is the wavelength region. It is mainly given by the absorption cross section of the relevant trace gas (Figure 3-1).In the visible the fit region is divided in three sub-regions depending on the main absorber:

- For NO_2 the wavelength region from 420 nm to 444 nm is used including O_3 and H_2O as additional absorbers.
- For O_4 the strong absorption band around 477 nm is used, hence the fitting window ranges from 463 nm to 500 nm, here the absorption of O_3, NO_2 and H_2O have to be taken into account.
- The H_2O absorption in the O_4 fitting window is not that strong and hence a third fitting window has to be used, expanding from 490 nm to 530 nm. In this region the O_4 can be neglected whereas O_3 and NO_2 are important absorbers.

The references for the cross sections of the individual trace gases and the wavelength regions are listed in Table 3-A. The degree of the polynomial varies depending on the fitting window, the line of sight and the measurement campaign between 3 and 5. An additional offset was included in all fitting procedures.

In the first FORMAT campaign the UV-spectrometer failed and the vis-instrument was used for recording the data in the UV wavelength region (chapter 6.3 and 8.1).

- The fitting interval for the HCHO-fit expands from 323 nm to 368 nm. Apart from HCHO also O_3, NO_2 and O_4 show strong absorption structures in this wavelength region. So they are included in the fit, a polynomial of third degree was added as well as an additional linear offset.

Two examples of typical fits are shown below in Figure 3-7. The first part of the figure shows a fit typical of the SCIAVALUE II campaign. The spectrum and the reference were observed with the nadir telescope on 19/02/2003 with only 15 minutes time difference. In the fit the strong NO_2 absorptions are obvious, indicating a local pollution event north of the Alps, the reference was taken above the Alps, where clean air can be expected. The whole flight will be discussed in chapter 7.1.I.

The second fit shown below is applied to a spectrum observed during the first FORMAT campaign. The flight of 16/08/2002 will be discussed in detail in chapter 8.1. While the reference was taken south of Milano the spectrum was taken in the north-west when heading towards the town.

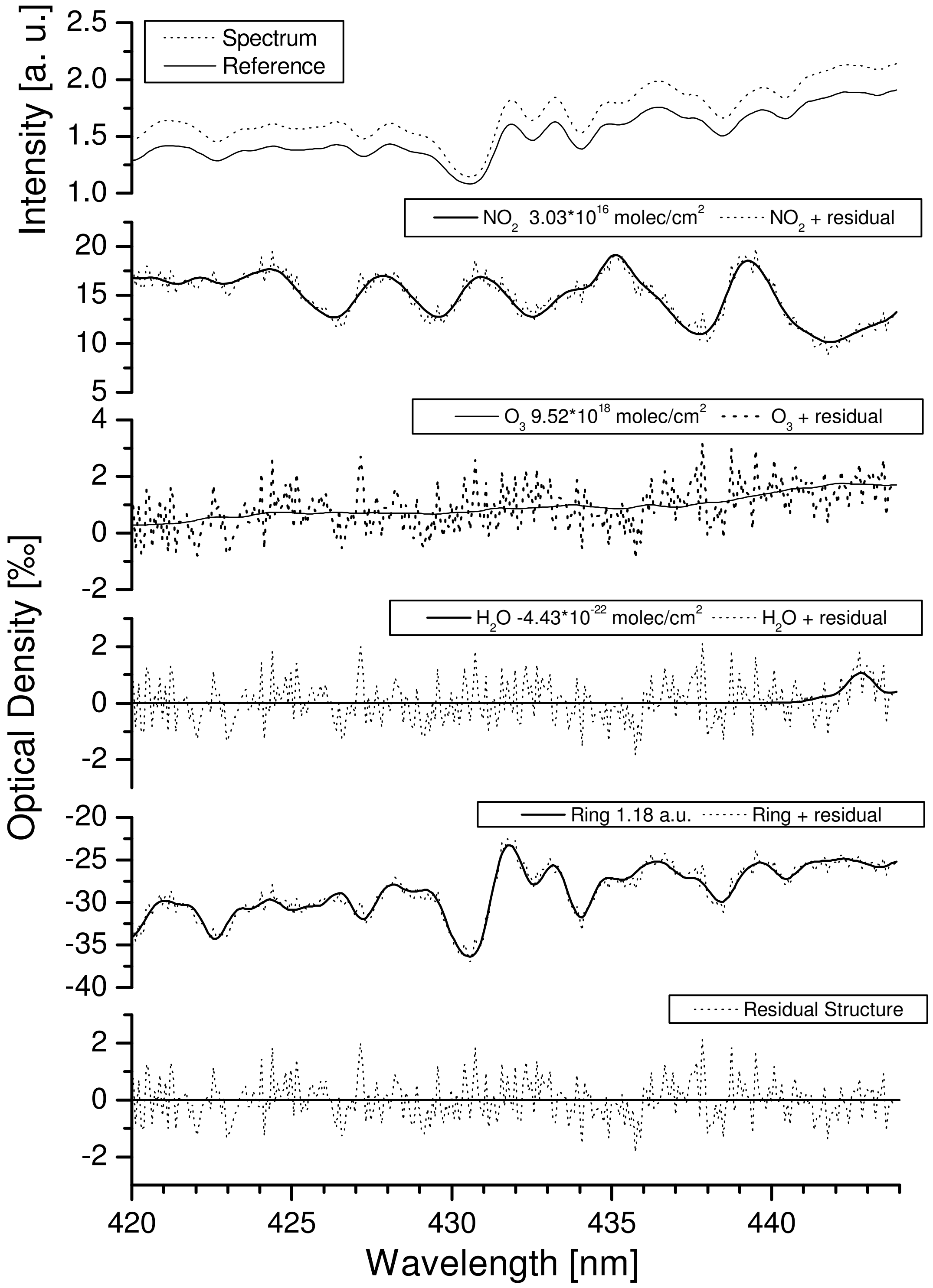

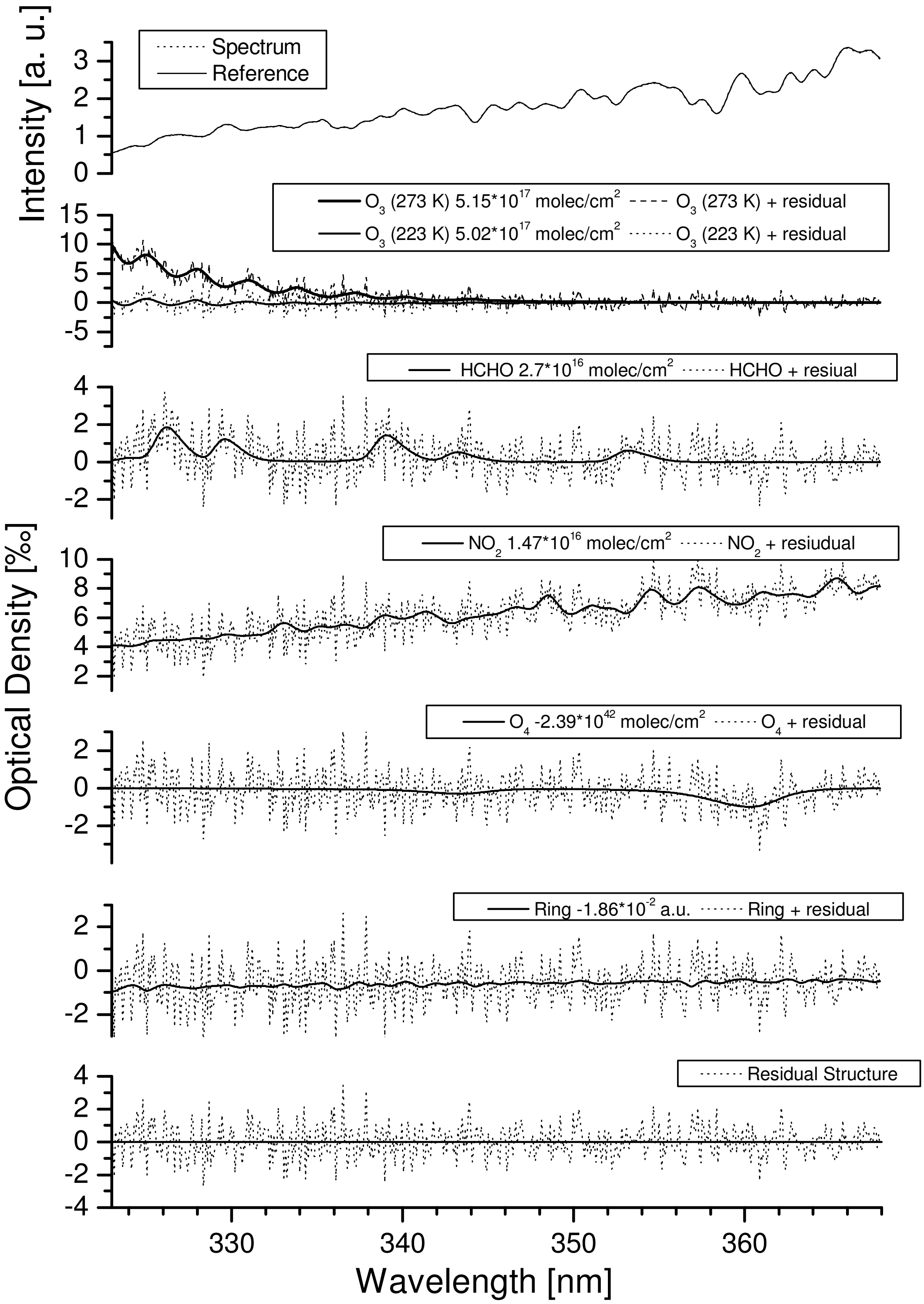

Figure 3-7: Typical fits of the AMAXDOAS vis-instrument, the observed dSCDs are mentioned in the figure.

The first picture shows an example fit of a spectrum recorded during the second SCIAMACHY validation campaign. The spectrum was taken on 19/02/03 at 8:14:30 UT north of Zürich, as reference a spectrum observed 15 minutes later over the Alps is used (chapter 7.1.I).

The fit shown of this page is applied to a spectrum taken during the flight on 16/08/2002 during the FORMAT I campaign. The spectrum was detected at 13:51:57 UT by the telescope "-16°". The reference was taken about 30 minutes earlier south of Milano (chapter 8.1.I).

Trace gas	**Fit interval**	**Cross Section**
HCHO	UV	Meller and Moortgat, [2000]
O_3, 223 K and 293 K	UV	Voigt et al., [2001]
NO_2	UV	Voigt et al., [2002]
O_4	UV	Greenblatt et al., [1990]
NO_2	vis	Voigt et al., [2002]
O_4	vis	Hermans et al., [1999]
O_3, 223 K	vis	Voigt et al., [2001]
H_2O	vis	Hitran atabase [Rothman, 1998]

Table 3-A: Overview of the literature cross sections used for the fit in the UV and vis wavelength region.

In 3.2.I.c the noise of the spectra and the error in the slant column densities were explained. An overview of typical measurement errors depending on the measurement campaigns (number of lines of sight and wavelength region), and the trace gas is given in Table 3-B.

	ΔHCHO [molec/cm^2]	**ΔO_3 [molec/cm^2]**	**ΔO_4 [molec^2/cm^5]**	**ΔNO_2 [molec/cm^2]**	**ΔH_2O [molec/cm^2]**
Wavelength range [nm]	**323 – 358**	**323 – 340**	**338 – 368**	**338 – 358**	
differential cross section [cm^2]	$6.80*10^{-20}$	$5.00*10^{-21}$	$4.40*10^{-46}$	$7.00*10^{-20}$	
FORMAT 1	$3.50*10^{+15}$	$1.17*10^{+17}$	$7.18*10^{+41}$	$4.51*10^{+15}$	
Wavelength range [nm]		**463 – 500**	**463 – 500**	**420 – 444**	**490 – 520**
differential cross section [cm^2]		$1.00*10^{-22}$	$6.20*10^{-46}$	$2.60*10^{-19}$	$1.30*10^{-25}$
FORMAT 2		$2.84*10^{+18}$	$4.59*10^{+41}$	$1.36*10^{+15}$	
SCIA-VALUE 1		$3.41*10^{+18}$	$5.51*10^{+41}$	$1.63*10^{+15}$	$2.92*10^{+21}$
SCIA-VALUE 2		$4.27*10^{+18}$	$6.88*10^{+41}$	$2.04*10^{+15}$	$3.65*10^{+21}$

Table 3-B: Overview of typical errors for the most relevant trace gases. These errors are given by the WinDOAS analyis, for most trace gases, they agree well with the typical noise of the measurement. The Error for the ozone slant column densities is underestimated. In the FORMAT I campaign no change in the tropospheric ozone can be observed.

3.4 Separation of tropospheric and stratospheric Signals

The analysis described above (section 3.3) results in differential slant columns dSCDs (section 3.2.III.a) of the total atmosphere. The signal of the reference spectrum is obviously zero. The observed signal is caused by the change in stratospheric slant columns and the change in the tropospheric signal. In the troposphere most of the NO_2 originates from local sources on the ground, therefore the signal is varying frequently. The stratospheric signal changes due to different stratospheric air mass factor with changing solar zenith angle and due to the latitudinal change of the stratospheric vertical column. The total change of the stratospheric slant column has to be subtracted from the total signal to gain the tropospheric column. In a sensitivity study three different ways of correcting for the stratospheric signal are compared:

1. The AMAXDOAS observes light from both zenith and nadir lines of sight. The nadir observations are most interesting for the tropospheric absorptions. In the zenith we would not expect to observe any influence of the tropospheric trace gases. Hence the zenith data might be used to estimate the stratospheric signal.
2. The geometrical approximation $1/\cos(\vartheta)$ with the solar zenith angle ϑ for the stratospheric AMF is used. We assume the latitudinal variations of the vertical column to be linear. Hence the stratospheric NO_2 column to be subtracted can be deduced:
   $$dS_{Strat} = (a + b \cdot \phi) \cdot \left(1 / \cos(\vartheta) \right) - (a + b \cdot \phi_{ref}) \cdot \left(1 / \cos(\vartheta_{ref}) \right)$$
   Where ϕ represents the latitude. The first part of the sum is the SCD at any latitude ϕ and the second part is the slant column at the reference place. The parameters a and b are defined by using the same approach for the SCIAMACHY total SCDs, where the reference contains no stratospheric absorption. Thus the vertical column as a function of latitude is derived from SCIAMACHY measurements. This method will be named “1/cos(SZA)”.
3. We assume the total variation to be linear and a linear function is fitted to the minima of the observed differential slant column densities.

An example showing the different correction types is given below (Figure 3-8). The data shown here where observed on 19/02/2003, the same flight as already mentioned in the example of the DOAS fit (Figure 3-7).

To use the zenith viewing telescope as reference, will overestimate the stratospheric columns in the polluted regions (e.g. 45° North). Although only a weak signal is observed in the zenith compared to nadir, the local variations are well detected by the zenith telescope as well. It cannot be recommended to use the zenith data to correct for the stratospheric absorbers. It will not be used in the following.

For most parts of the flight the other two methods differ by less than $0.5*10^{15}$ molec/cm^2 as can be seen in Figure 3-8. Only north of the Alps where the solar zenith angle varies around 74° ± 1° a larger difference ($1.6*10^{15}$ molec/cm^2) is observed. As it describes the reality better, we assume the 1/cos(SZA) method to be the correct one. Nevertheless for small solar zenith angles the errors introduced by the linear approximation can be neglected.

Later on (chapter 7.1.I) the specific data set will be used for the comparison with SCIAMACHY on ENVISAT. For this comparison it should be mentioned that the same problems of the separation of stratospheric and tropospheric columns occur for the SCIAMACHY data. So this study was made for both instruments and combined with a comparison of the slant columns (chapter 7.1.I.c). In addition to these two methods a third one is possible for the satellite data: a set of reference data observed over a clean region, i.e. the Pacific Ocean, is subtracted. The reference sector method is quite common when analysing satellite data on tropospheric trace gases e.g. [Beirle, 2004, Richter et al., 2004 and Hollwedel, 2005].

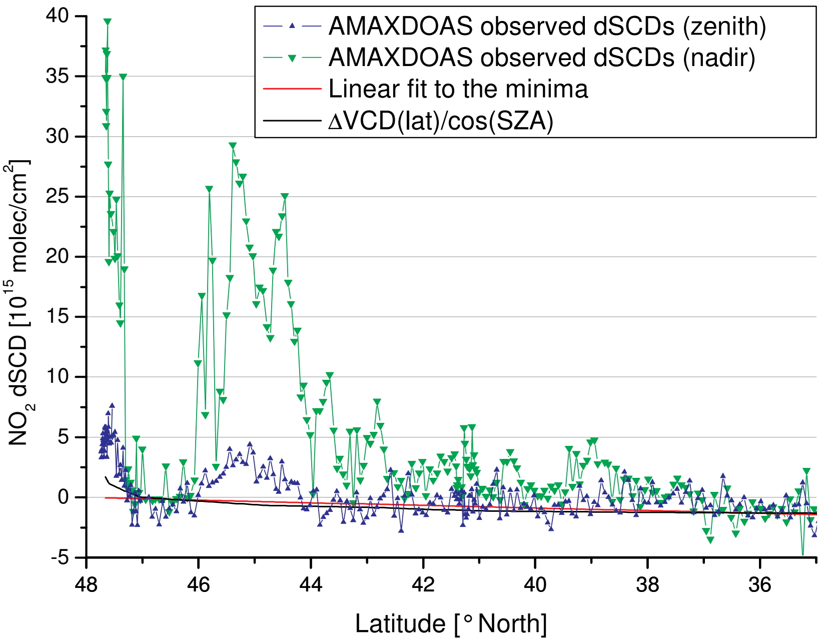

Figure 3-8: Observed dSCDs on 19/02/03 (nadir in green and zenith in blue) and the different methods of correcting for stratospheric absorption. The red line is for the assumption that the total variation is linear and black indicates the 1/cos(SZA) method.

Unfortunately the direct reference sector method is not possible for most airborne measurements. The range and the speed of the aeroplane limit the possible regions to a small region. For such an experiment it would be necessary to fly over both clean and polluted regions while the solar zenith angle must not change during the entire flight. Such flights are possible in the Polar Regions only.

3.5 DOAS Tomography

With the DOAS method the integrated concentration along a certain light path is measured. In the atmosphere, however, sometimes strong spatial variations in the concentrations are observed, especially for directly emitted tracers like SO_2 or NO_2 close to the source. These gradients are averaged by all integrating measurement methods like DOAS. Using several lines of sight in different directions the variations in the concentration can be detected and by mathematical inversion techniques the distribution can be retrieved. This is the principle of DOAS Tomography. In chapter 8.2.IV a reconstruction of three plume cross sections are discussed.

In the DOAS tomography both, measurements of column densities and numerical inversion are combined. The latter work however was carried by other investigators, thus only a short introduction is given in the following

3.5.I Principle of DOAS Tomography

In the DOAS tomography we have to distinguish between active [Pundt et al., 2005 a] and passive DOAS systems. The light paths of an active system are well defined. The number of light beams limits the inversions resolution. Using the new Multi beam DOAS instruments [Pundt and Mettendorf, 2005 a] up to 6 light paths can be realised simultaneously. With three instruments and a non simultaneous measurement the number can be further increased up to 40.

As this work concentrates on airborne measurement the principle of the reconstruction will be explained by an example of airborne plume observation. The flight altitude is assumed to be above the plume, this is not necessary for the airborne DOAS tomography but the explanation will be easier this way.
In Figure 3-9 an example measurement is illustrated. During the overpass different slant columns are observed along the different lines of sight. The high differential columns are shown in red. If no signal is observed, this will be indicated by a green line of sight. Cases of low SCDs are indicated by an orange line. As soon as a line of sight crosses the plume the observed SCD increases. It is obvious that the forward directed line of sight detects the enhanced values first.

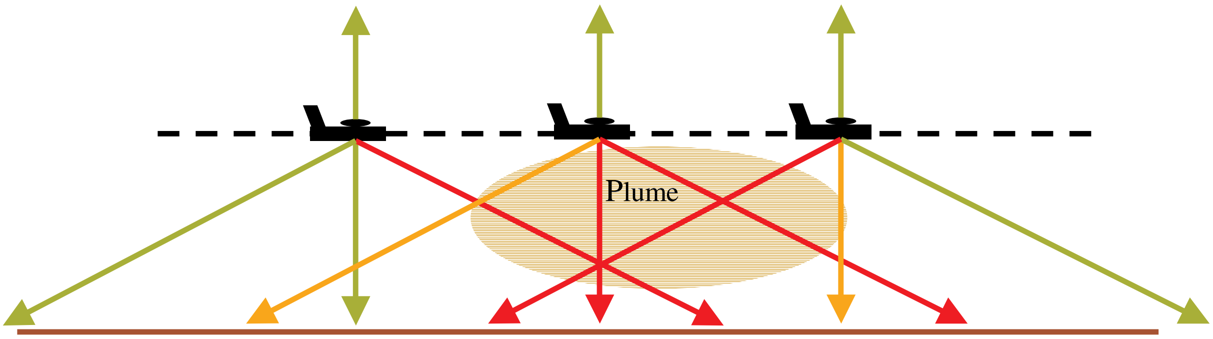

Figure 3-9: Measurement with the AMAXDOAS instrument above a plume. The colour scale in the lines of sight indicates the observed slant column. Green stands for no signal, orange for a low signal, and red for a high slant column density.

We assume that the time of the overpass is short compared to time scales of the atmospheric variations – in real measurements an overpass takes about 3 min (chapter 8.2.III). Although the atmosphere changes every second, this assumption can be made as the changes in the plume's shape are small compared to the resolution of the reconstruction. For the reconstruction the problem first has to be discretised and written as a mathematical problem.

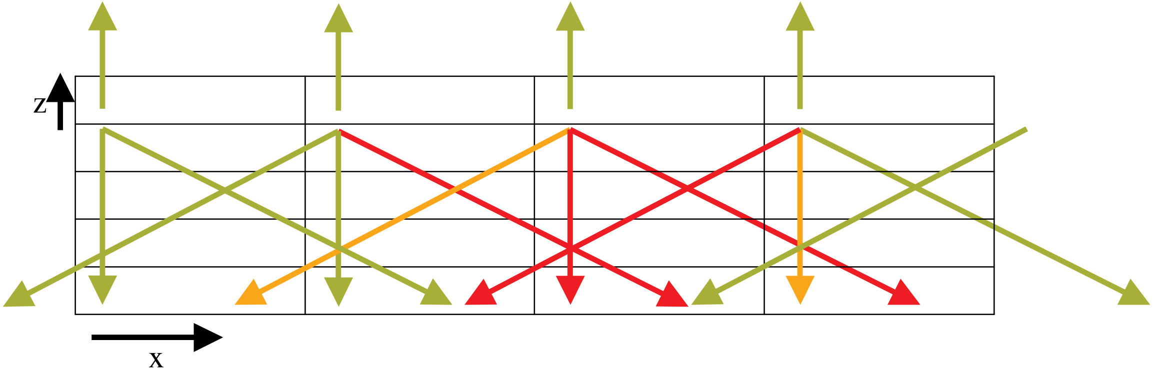

Figure 3-10: The observed dSCDs and a discrete grid is overlaid for the reconstruction. Compared to Figure 3-9 parts of two additional measurements at the edges are shown.

In Figure 3-10 the abstract version of the measurement is shown. The different lines of sight observe different slant columns according to the observed air masses. Instead of the time information of the measurement only the distance x is important here. In the background a discrete grid is shown. The aim of tomography is to determine the concentration in each box of the grid, based on the observed column densities. In the example discussed in chapter 8.2.IV we assume 4 boxes to be below the aeroplane and 11 above, reaching up to the mixing layer height. Here only 1 box is shown of above. In flight direction 12 boxes with 2 km length each are used. Perpendicular to the flight direction (horizontally) the boxes are infinite.

For a light path i crossing a box (x,z) the length inside the box is given by $l_{i,x,z}$. For this general overview we assume l is given by the geometrical light path. If $c_{x,z}$ is the concentration inside the box, the partial column density inside this box will be given by: $S_{i,x,z} = l_{i,x,z} \cdot c_{x,z}$. The total column density observed along this light path can be written as:

$$S_i = \sum_{x,z} l_{i,x,z} \cdot c_{x,z}$$

for the boxes not crossed by the light path the length l equals zero. For all lines of sight and all boxes the length l can be defined. This results in a vector equation in the form of:

$$\mathbf{S} = \mathbf{L} \cdot \mathbf{C}$$

where **S** is the vector of the observed column densities, **L** is the matrix given by the different light path in the boxes and **C** stands for the concentration in the boxes.
In the example we always assumed a set of box-like basis functions to describe the discrete concentration. This assumption is intuitive and can easily be understood. For mathematical reasons however it is not at all necessary. Other basis functions (e.g. bilinear) are possible as well. For the reconstruction it is important that the equation is still linear. Problems of this type are called discrete linear inverse problems. Now mathematical inversion methods are required to solve the equation (section 3.5.II).
Although the principle was explained using the example of airborne DOAS tomography we did not make use of any characteristic feature of the DOAS measurement, all we applied was Lambert-Beer law. The absorption depends linearly on the length of the "light path" inside the absorbing medium and the concentration. The same principle is used in the x-ray tomography as well. There the absorbing material is given by the different absorbers in the patient's body.
For passive DOAS systems the problem the number of observed light beams is limited. During 3 minutes about 6 measurements are performed with 10 slant columns each, this results in 60 lines of sight. The main problem of stray light measurements is that the light paths are not exactly known (chapter 4). Hence the sensitivity of one line of sight i to the concentration in the box (x,z) cannot be calculated by just using the geometrical length. In the next chapter (4.4.VII) two approaches to determine the sensitivity will be discussed in detail. For the moment we assume that a linear forward model **A** is given, with $\mathbf{S} = \mathbf{A} \cdot \mathbf{C}$. As the light is reflected on the ground or scattered in the air the number of light paths increases.

3.5.II Mathematical Inversion Techniques

As indicated above mathematical techniques are required to reconstruct the concentration distribution based on the observations
The problem to be solved is the matrix equation: $\mathbf{S} = \mathbf{A} \cdot \mathbf{C}$ If **A** could be inverted the would be solution rather simple: $\mathbf{A}^{-1} \cdot \mathbf{S} = \mathbf{A}^{-1} \cdot \mathbf{A} \cdot \mathbf{C} = \mathbf{C}$. However, normally the problem is ill-posed and it cannot be inverted. In these cases the least square of the differences is usually taken as solution:

$$(\mathbf{S} - \mathbf{A} \cdot \mathbf{C})^{\mathbf{T}} \cdot (\mathbf{S} - \mathbf{A} \cdot \mathbf{C}) = \min \tag{3.12}$$

The solution of the problem depends on the rank of the matrix **A** or on the number of measurements compared to the number of boxes. For example in x-ray tomography the numbers of measurements is by a factor of four higher than the number of boxes. In these cases no exact solution exists but only an approximation.

In the DOAS Tomography the problem is usually underdetermined. In our example we have about 60 lines of sight and crossing 12*15 = 180 boxes. Taking the scattering effect into account the number of light beams increases up to 170.

To solve the equation with 180 unknown parameters and with less than 180 measurements is in principle impossible as more than one solution exists. So some additional information has to be used. Usually a certain smoothness of the solution is required or the minimum norm solution $\mathbf{C}^{\mathrm{T}} \cdot \mathbf{C} = \min$ is assumed to be the best solution and negative results for the concentration are set to zero.

One might ask if a lower discretisation, using fewer boxes than measurements, will overcome this problem. In sensitivity studies similar to [Hartl et al., 2005] the grid used here was found to be optimal for the given problem. If the discretisation is too coarse the error introduced by discretisation itself is large compared to the error of the inversion. According to several well established criteria, like the integrated difference between the original concentration and the reconstructed one, an optimal grid has to be found.

To solve the equation (3.12) Row Acting Methods have been common in computerized Tomography [Laepple et al., 2004]. They are based on the idea that each row i of the equation $S_i = \sum_j \mathbf{A}_{ij} \cdot \mathbf{C}_j$ is given by one measurement point and defines a (n-1)-dimensional hyperplane, on which any existing solution must lie. The complete solution must hence lie in the intersection of all hyperplanes. Several methods (ART, SIRT, SART) to find the best approximation of the intersection are described in [Laepple, et al., 2004]. All of them project an initial a priori vector on the hyperplanes to find the intersection, or the best approximation to it. This leads to iterative process. The main difference between the methods is the question whether the projects on the hyperplanes are performed simultaneously or one after the other. For the airborne DOAS the Simultaneous Iterative Reconstruction Technique (SIRT) [Kak and Slanley, 1988] is used.

The grid shifting method [Verkruysse and Todd, 2004] has been modified and adapted to our purpose. For the grid shifting method several independent reconstructions are performed, each individual reconstruction is discretised by the original grid shifted by a fraction of one grid cell (1/n of the cell's width in both directions). In total n*n reconstructions are performed and finally averaged. The quality of the total reconstruction increases dramatically compared to the individual ones.

3.5.III Sensitivity Studies

Before the first FORMAT measurement campaign, sensitivity studies were performed to optimise the flight tracks for a fixed viewing directions and under a given distribution of a trace gas. It was found that a constant layer of a trace gas can hardly be detected due to the differential measurements. To minimize this problem, "dives" were included in the flight track. If the normal flight altitude was about 2000 m then the plane would go down to about 200 m and climb to normal flight altitude afterwards. When diving into or even through the layer additional information is gained. During ascent and descent however the flight conditions are rather unstable and this reduces the additional information. Moreover, the flight manoeuvre causes high costs in time and fuel. Nevertheless, it was used in the first FORMAT campaign.

In these first sensitivity studies scattering processes were ignored and only ground reflection was assumed. The plume width of 40 km in the lee of Milano was based on the result of a previous campaign (PiPaPo). The aim was to find the minimum numbers of dives necessary to determine the plume correctly. The results for one and two dives are shown in Figure 3-11. Independent of the number of dives, the reconstruction describes the input profile very well as long as no measurement noise is considered. However, if the noise is taken into account,

differences in the reconstructions will occur. If only one dive is performed some artefacts will be introduced as soon as the noise of the measurements will be considered. The retrieval is improved when two dives are flown with a distance of 40 km.
In the simulation we assumed a flight perpendicular to the wind direction, no aerosol and only ground reflection. The concentration distribution was reconstructed on a grid of 5*50 boxes covering an area of 2000 m*100 km.
No real flight was ever performed under such ideal conditions. Nevertheless the sensitivity studies demonstrate the possibilities and the restrictions of tomographic AMAXDOAS measurements.

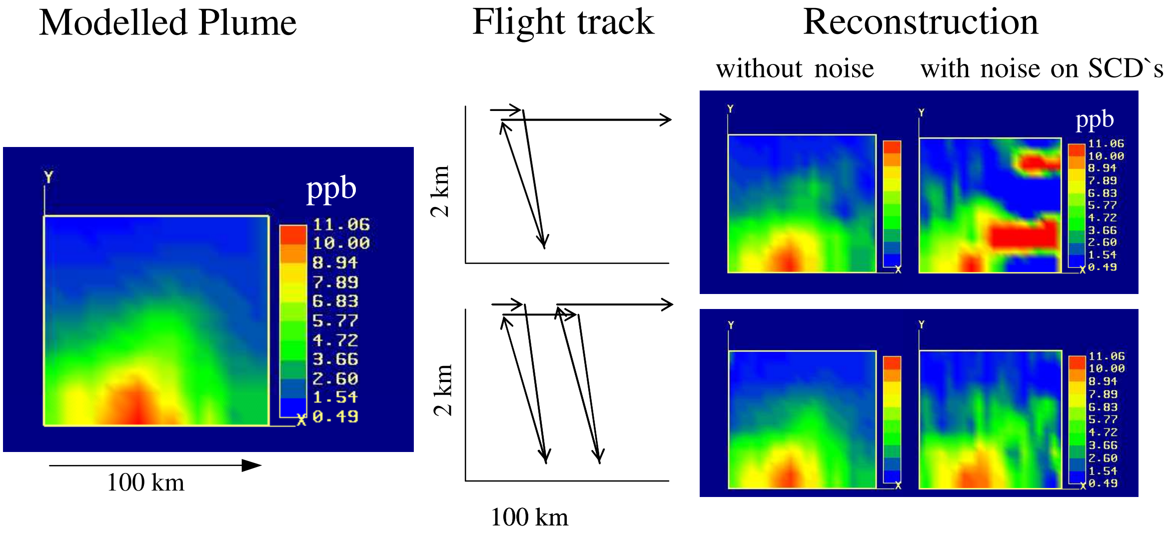

Figure 3-11: Sensitivity study concerning the influence of different flight tracks. The reconstructed concentration distributions shown here were smoothed (Thomas Laepple, private communication, May 2002).

For the real measurements we can use these studies to estimate the maximum vertical profile information retrieved from our measurements. If we only fly one dive or none at all, the retrieved profile will be worse.
For the second FORMAT campaign (chapter 6.4 and 8.2) the viewing geometry was optimized for smaller plumes originating from point sources like power plants or cement plants. In this case we are interested in the plume's shape and local excess concentration, hence a constant background can be neglected. Here no dives are necessary.
Finally, Figure 3-12 illustrates how individual box concentrations are, in principle, given by the measurement data for a typical reconstruction setup. Shown here is a measure for the Nullspace of **A** which, independent of the inversion technique, expresses whether concentration values are completely fixed by the data (value equals 0) or lie entirely in the Nullspace and have to be fixed by constraints or a priori information (value equals 1).
Profiles below the aircraft can be well determined from the measurement data alone. Above the aircraft, especially at higher altitudes, the information content of the measurement is rather poor.

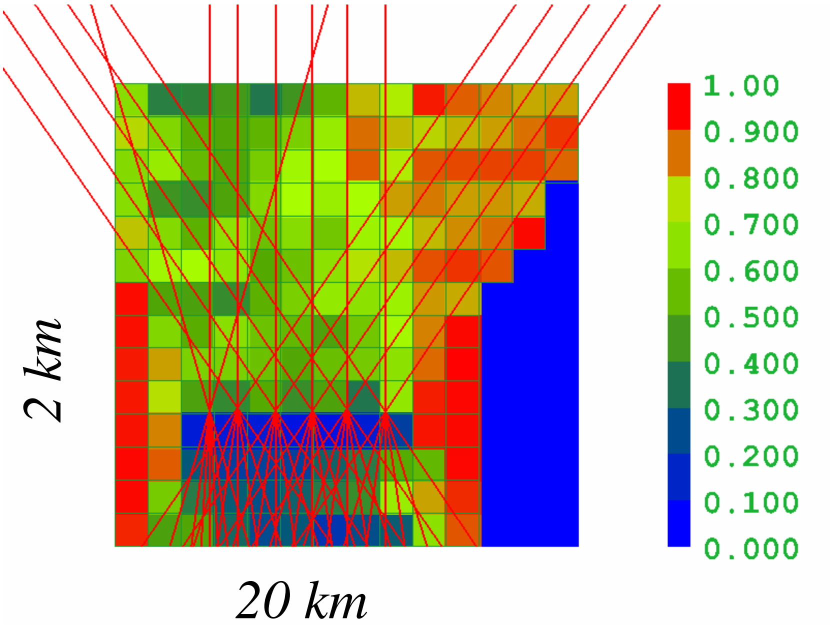

Figure 3-12: Information content for a typical airborne DOAS Tomographic measurement and reconstruction setting. The colour bar is a measure for the influence of a priori information. Red means the reconstructed profile is given by the a priori profile and blue indicates it is given by the measurement. Please ignore the blue area to the right, none of the observed light beams crossed this area and the respective boxes were excluded. Reflected and scattered light paths are not shown for clarity, in the analysis a single scattering approximation was used. (Andreas Hartl Talk, internal group meeting 14/06/05).

4 Radiative Transfer

The AMAXDOAS instrument observes scattered solar radiation. For all DOAS instruments (minimaxDOAS to SCIAMACHY) using scattered light the light path is not well defined. This principal difficulty can be resolved by using a radiative transfer model to simulate the light path through the atmosphere.

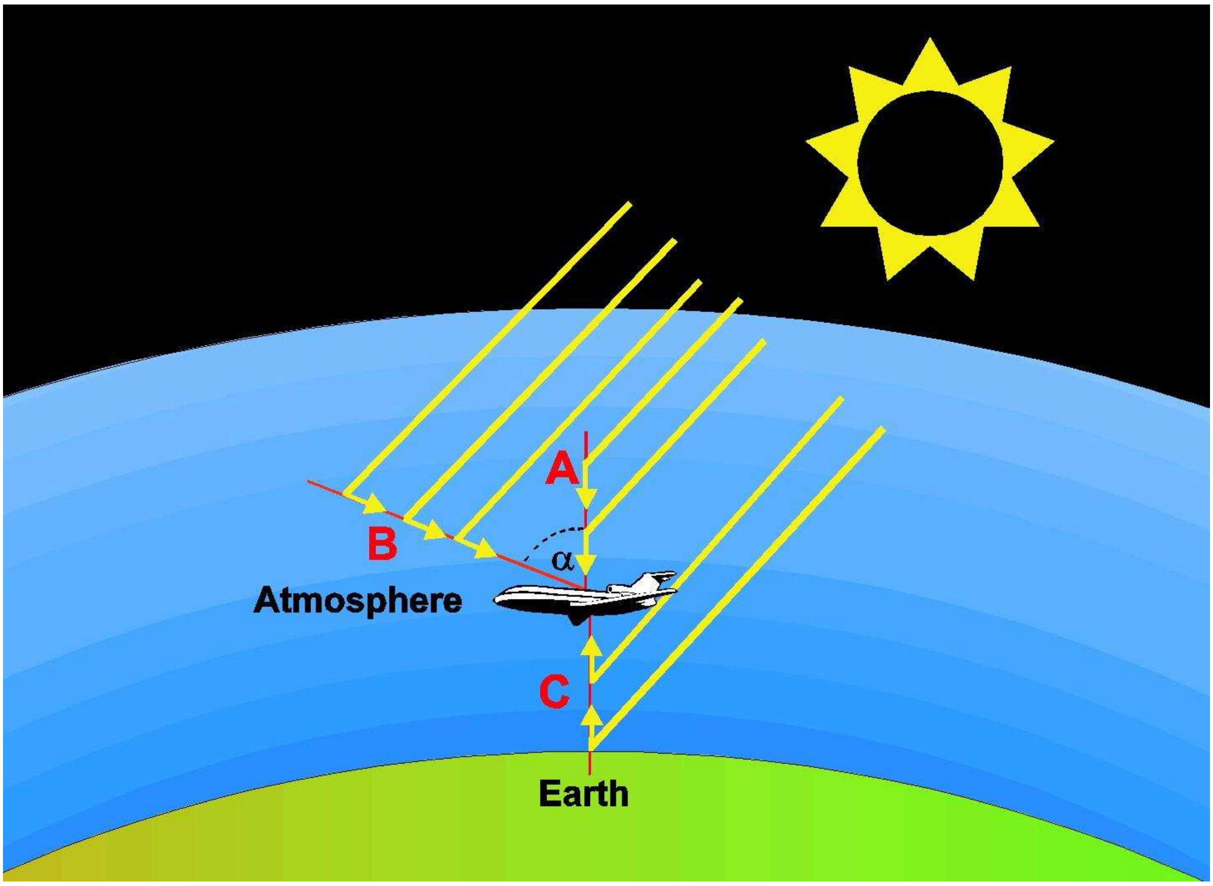

Figure 4-1: Different light paths for an AMAXDOAS instrument installed on an aeroplane. Here three different elevations are shown: A) Zenith, B) elevated telescope and C) Nadir. The light paths, through various altitude layers of the atmosphere, differ for the individual elevations [Wagner et al. 2001 a].

In Figure 4-1 the principal viewing geometry is shown neglecting the multiple scattering effects. The light originating from the sun crosses the atmosphere along different light paths until it is detected by the instrument. In this chapter the relevant quantities for the measurements are introduced, then the scattering effects are explained. A brief description of the model is given. The focus however, will be on some sensitivity studies and the explicit application to observed data.

4.1 Slant and Vertical Columns

The light path depends on many parameters like solar zenith angle, aerosol load, surface albedo and elevation angle of the telescope. The sensitivity of the measurement for a certain trace gas strongly depends on the distribution of the light paths and on the local distribution of the trace gas.

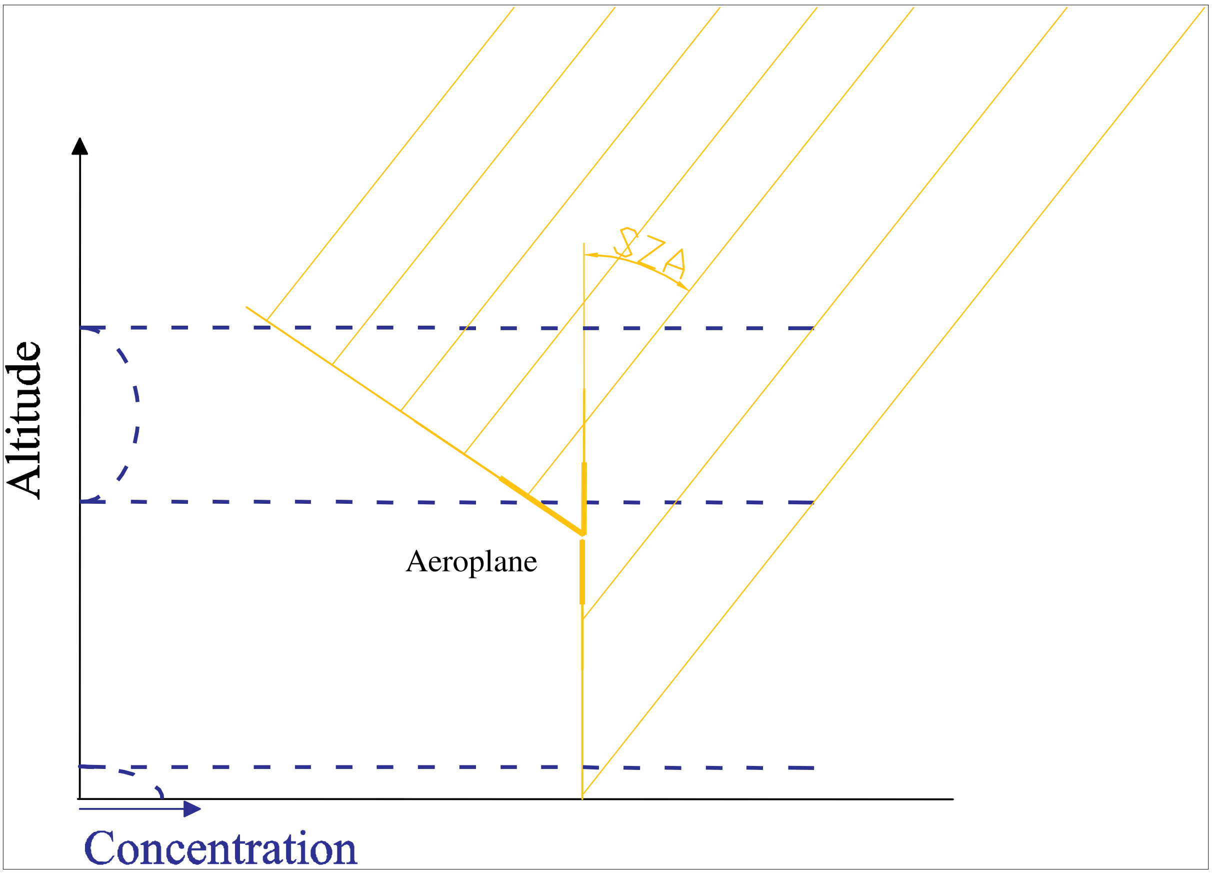

Figure 4-2: Diagram of different lines of sight (thick yellow) and the direct sunlight (yellow line) for the situation illustrated in Figure 4-1. At an altitude just above the flight altitude there is a layer of a trace gas (blue). The light observed by all telescopes is influenced by this layer. The light path through the trace gas is longest for the telescope with small elevation angel. For the second layer close to the ground the strongest signal is observed in the nadir. Multiple scattering (not shown in the sketch) leads to a weak signal in the other directions as well.

In Figure 4-2 three typical lines of sight are illustrated, zenith, nadir and a third one with a small elevation compared to the horizon. All telescopes with small elevation angles (± 30°) are defined as "elevated telescopes". Negative elevation is defined as "below the horizon". The elevation angle in our context varies between -90° and +90°.

In Figure 4-2 the effects of some of the important parameters are illustrated. Multiple scattering processes are not illustrated. If the Solar Zenith Angle (SZA) is larger, then the light path in the atmosphere gets longer and the slant column density (SCD) will increase. If the elevation angle is smaller (relative to the horizon) the signal along this line of sight will increase as well. As shown in Figure 4-2 this only holds, if the absorbing trace gas is located close to the detector. However, if the trace gas is situated at higher altitudes, the signal is independent of the elevation angle and dominated by the solar zenith angle. Due to the low density of scattering centres in high altitudes the incident light crosses the absorbing layer directly. Below the trace gas the light is scattered and finally observed by the instrument. If the layer of the trace gas is close to the ground, the slant column density for the upward looking telescopes will usually be small. This weak signal is caused by multiple scattering but for high ground albedo it can become important. From Figure 4-2 we would not expect it exists at all, whereas in the nadir it might well be observed.

Hence, the observed SCD depends on many parameters e.g. elevation of the telescopes or altitude of the trace gas layer and not only on the trace gas concentration. For a better comparison with other measurements usually the vertical column density (VCD) is calculated. It is defined in chapter 3.2.III as:

$$V = \int_0^H c(z)dz \tag{4.1}$$

where z stands for the altitude above ground, and *c* is the concentration of the trace gas. The upper limit H of the integral can be either the top of atmosphere if one is interested in total columns or the tropopause height, when we study tropospheric trace gases. It is obvious that the vertical column density does not depend on the light path.

To convert a slant column to the corresponding vertical column the influence of the light path and the corresponding parameters is calculated and expressed as air mass factor (AMF)

$$A = \frac{S}{V} \tag{4.2}$$

The air mass factors describe the sensitivity of the instrument for a trace gas under certain conditions in the atmosphere [Noxon et al., 1979 or Solomon et al, 1987].

If the trace gas layer is situated above the detector and most of the scattering processes occur at altitudes between the absorber and the detector, then a geometrical approach (Figure 4-2) of the AMF is possible and the AMF can be calculated as:

$$A \approx \frac{1}{\cos(\vartheta)} \tag{4.3}$$

This approximation leads to very good results for stratospheric absorbers when the solar zenith angle is smaller than 70° (the derivation to the modelled AMF is larger than 10 % for higher SZA). For tropospheric absorbers and especially for short wavelengths (which were observed with the AMAXDOAS instrument, 300 – 400 nm) multiple scattering processes contribute substantially to the measured signal and the approximation is no longer valid.

A more sophisticated quantity than the AMF is the Box AMF, A_{Box}. It is defined as the ratio of SCD to VCD within a particular altitude layer. The Box AMFs hence describe the sensitivity of the instrument for a trace gas in a certain layer. The tropospheric AMF introduced above is a special case of a Box AMF, the altitude layer in this case encompasses the complete troposphere.

The name “Box AMF” indicates that it might be used to calculate the respective AMF for boxes in a fully 3-dimensional grid. In this work the radiaditve transfer program “Tracy” (section 4.3) was not used to calculate 3-dimensional Box AMFs, but 2-dimensional Box AMF were well calculated (chapter 3.5.I and 4.4.VII). Although the general idea of Box AMFs will be explained by an example of a 1- dimensional case the same holds for 2 and 3 dimensions. If we know the Box AMFs for all layers and the corresponding trace gas profile, we will calculate the SCD:

$$S = \sum_j A_{Box,j} \cdot V_j = \sum_j A_{Box,j} \cdot c_j \cdot \Delta z_j \tag{4.4}$$

here *j* denotes the altitude layer Δz. In the last step we assumed the concentration c to be constant throughout the respective layer, hence the vertical column can be calculated as $V_j = c_j \cdot \Delta z_j$. The same equation can be regarded as an inverse problem. For a given set of SCDs a set of concentration has to be found, in a way that:

$$S_i = \sum_j A_{Box,j,i} \cdot \Delta z_j \cdot c_j \tag{4.4}$$

where i corresponds to different measurements of the same air mass. This is achieved by using several lines of sight. The same equation can be written as vector equation.

$$\mathbf{S} = \mathbf{A} \cdot \mathbf{zC} \tag{4.5}$$

here **S** and **zC** are the vectors given by the measured SCD and the vertical columns. The Box AMF are now written in a matrix called **A**. The solution C of this problem is the vertical concentration profile.

Hence the important outputs of any ray tracing program are the AMFs or the Box AMFs for the observed trace gases. A brief description of the radiative transfer program "Tracy" is given in 4.3. For the modelling of the respective quantity a detailed knowledge of the most relevant processes is essential.

4.2 Scattering Processes and Extinction

Here an overview of the scattering processes is given. The main topics on which we will concentrate are:

- How can we approximately describe the surface reflection?
- Concerning scattering in the atmosphere, how much of the incident light is scattered? The answer to this question depends on the scattering process, the wavelength, the number of scattering particles and the cross section of the scattering process.
- Relative to the incident light, in which direction is the light scattered? Here the answer is given in form of a phase function – which gives the distribution of the scattered light around the scattering centre with respect to the original direction. It can be regarded as the probability of light being scattered in a certain direction.
- Does the energy (wavelength) change with respect to the incident light? The two most important scattering processes Rayleigh and Mie are elastic scattering processes. Raman scattering is inelastic.

The refraction of light due to the differences in pressure and temperature in the atmosphere is a well known phenomenon and will not be discussed. It is taken into account in the simulation, but it is not of mayor relevance for the understanding of any measurement. The interested reader may refer to standard literature on atmospheric science e.g. [Roedel, 1991].

As indicated in the last section we have to distinguish between several types of scattering processes, depending on the size and the composition of the scattering centre. In addition to the atmospheric scattering process, the light is also reflected on the earths surface. Depending on the flight altitude the surface reflection can become very important.

4.2.I Surface Reflection

Reflection on the earth's surface mainly depends on the surface properties. For the normal situation we assume that the reflected intensity is isotropic and hence independent of the direction of the incident light. A surface which reflects the light as diffuse as mentioned is called Lambertian.

Normally not all of the incoming light is scattered back. The incoming intensity has to be weighted with the cosine of the incident angle relative to the normal of the surface. The reflected intensity is integrated over the scattering hemisphere. The ratio of these two intensities is defined as surface albedo. It depends on the surface type and the wavelength. The example values given in Table 4-A were taken from Feister and Grewe, [1995].

Wavelength [nm] Surface	300	400	500	800
Loam	0.041	0.08	0.13	0.269
Grass	0.016	0.022	0.035	0.587
Concrete (dry)	0.096	0.161	0.215	0.266
Snow (2cm)	0.623	0.672	0.680	0.745

Tabelle 4-a: Albedo values of different surfaces and different wavelengths, values taken from Feister and Grewe, [1995].

4.2.II Rayleigh Scattering

Rayleigh's theory of scattering is based on the idea that light as an electromagnetic wave induces an electromagnetic dipole in the molecule. This dipole oscillates with the frequency of the wave and parallel to the lights electronic field. According to the theory of an oscillating dipole (Hertz), it emits an electromagnetic wave. Let us assume the oscillation is in Z-direction, then the dipole does not emit in this direction, and the emission is circular around this axis. This means it is completely independent of the direction of the incoming light but depends strongly on the polarization of the light. In Figure 4-3 a) and b) the emission characteristics of a Hertz dipole are shown for both directions, parallel to the E-field of the dipole a) and perpendicular to it b): $E_{parallel} \propto \cos^2 \vartheta$ and $E_{perpendicular} \propto const$

For comparison with standard literature concerning the Hertz dipole the reader has to keep in mind the definition of the angle ϑ. In our case it is defined relative to the direction of the incoming light, in the classical electrodynamics it is defined relative to the dipole axis.

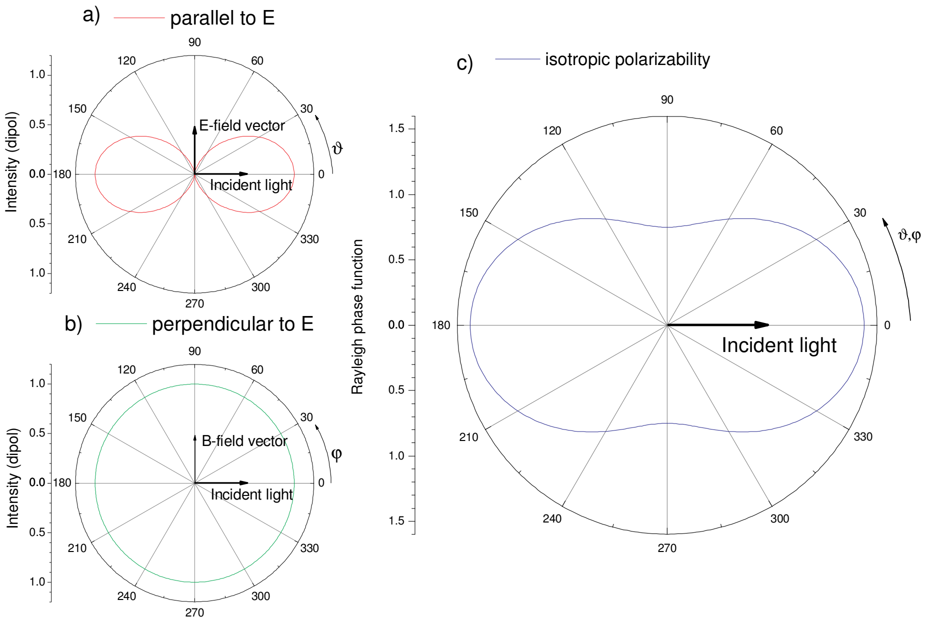

Figure 4-3 Phase function of the Rayleigh scattering process:
a) and b) Electromagnetic field of a Hertz dipole parallel or perpendicular to the E-field.
c) Rayleigh phase function of unpolarised light.

Of course this explanation only holds for completely polarised light. Light is non-polarised normally and the induced dipoles oscillate in any directions perpendicular to the direction of the incident light. The phase function of the Rayleigh scattering processes can be regarded as superposition of all these induced Hertz dipoles. The total phase function (Figure 4-3 c)) usually used to describe the Rayleigh scattering is:

$$\theta_{Rayleigh}(\vartheta) = \frac{3}{4} \cdot (1 + \cos^2(\vartheta)) \tag{4.6}$$

The phase function Figure 4-3 c) shows two main directions in which the light is scattered, backwards and forwards, whereas perpendicular to the incoming light directions less light is scattered

The total power emitted by a dipole is proportional to the frequency to the power of 4: $P \propto \omega^4$. As the emitted power equals the absorbed power, the cross section of the Rayleigh scattering process is proportional to $\omega^4 \propto \frac{1}{\lambda^4}$.

Up to now we assumed the scattering centres of the air to be polarisable, for the real atmospheric conditions the polarisability ε of the air has to be taken into account.

The complete Rayleigh cross section is given by:

$$\sigma_{RS} = \frac{8 \cdot \pi^3 \cdot \varepsilon^2}{3 \cdot \varepsilon_0^2 \cdot \lambda^4} \tag{4.7}$$

$\varepsilon_0 = 8.85 * 10^{-12}$ F/m^2.

4.2.III Raman Scattering

Raman scattering is the only inelastic scattering process described here. For the Rayleigh scattering the incident light induces an oscillating dipole in the molecular electron cloud. The molecular structure with the electron clouds allows the excitation and de-excitation of rotational and vibrational states. In both cases the scattered photons exchange energy with the scattering molecules.

The cross section of the Raman scattering depends on the excitation states involved but in general it shows the same λ^{-4} dependency as Rayleigh scattering. Compared to Rayleigh scattering the cross section is about 3% [Haug, 1996] for 488 nm. So for the scattering itself the influence is small. The main importance of Raman scattering is the Ring effect for passive DOAS measurements (chapter 3.2.III.b).

4.2.IV Aerosol Scattering

For the Rayleigh scattering we assumed the scattering particle to be small compared to the wavelength, otherwise the wave would not induce a dipole. If the particle is approximately of the same size or larger than the wavelength, the interaction of the incident light can be described as diffraction. Many small particles in the air (aerosols) are larger than the wavelength of the observed light. Due to the different origins of the aerosols e.g. sea spray, desert dust or soot they differ in magnitude and shape. Apart from coarse dust and ice crystals, most aerosol particles can be assumed to be spherical or to be embedded in spherical liquid droplets. The optical properties of such aerosols can be accurately described by the Mie theory. The basic effect observed can be compared to the diffraction of light at a pinhole. In the scattered light a strong maximum in the forward direction is observed and depending on the size and the refraction index several smaller maxima can be seen.

An analytical description of the phase function is much more complex than in the case of Rayleigh scattering and will be omitted here. Numerical calculations of the phase function were carried out recently [Sanghavi, 2003]. For an ensemble of aerosols the Henvey-Greenstein approximation of the phase function is often used:

$$\theta_{Mie,HG}(\vartheta) = \frac{1-g^2}{(1+g^2-2\cdot g\cdot\cos\vartheta)^{3/2}} \tag{4.8}$$

here g represents an asymmetry coefficient. This quantifies the anisotropy of the phase function. It is obvious that the phase function is constant in case $g=0$. For usual aerosols observed in the atmosphere g is in range of 0.6 to 0.8 (Christoph von Friedeburg, private communication, May 2003). Most microscopic characteristics like size, size distribution and refraction index of the aerosol are combined in this single parameter.

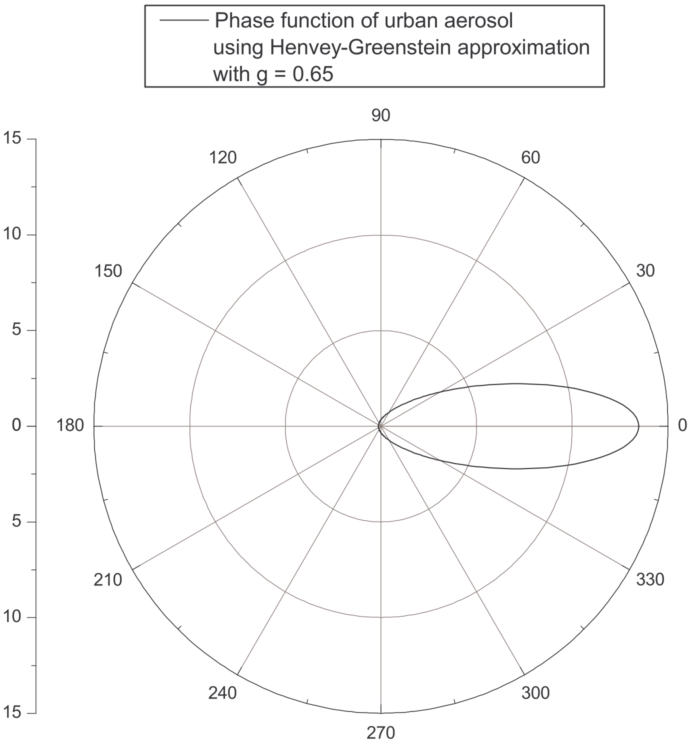

Figure 4-4: Phase function for Mie scattering. Here an urban aerosol type was chosen and the phase function was calculated with the Henvey-Greenstein approximation.

In Figure 4-4 a phase function is shown in the polar plot. Here the asymmetry coefficient equals 0.65 which is typical value for urban aerosol and a wavelength of 440 nm. The strong enhancement in the forward direction is obvious in this plot, and only little light is scattered in the perpendicular or backwards directions. Both phase functions shown in Figure 4-3 and Figure 4-4 are normalised to: $\int\Theta(\varphi,\vartheta)\cdot d\varphi\cdot\sin\vartheta\cdot d\vartheta = 4\pi$. Hence the figures may directly be compared, the peak in the forward direction is higher by a factor 10 for aerosol scattering than for Rayleigh scattering.

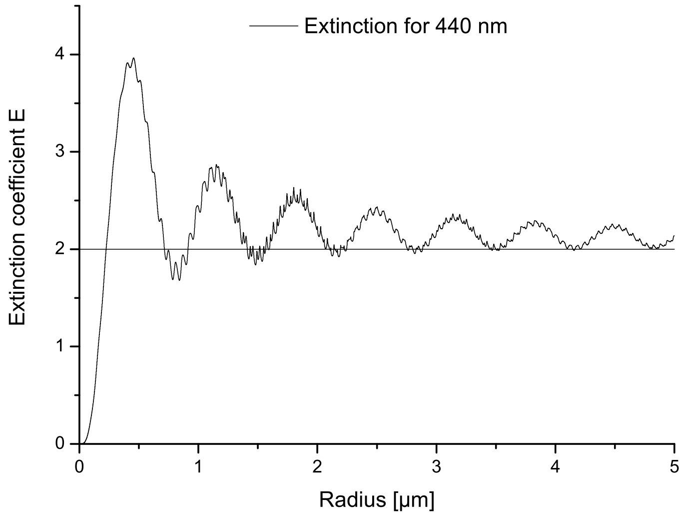

Figure 4-5: Extinction coefficient based on the Mie theory, here a wavelength of 440 nm, the radius ranges up to 5 µm (Suniti Sanghavi personal communication, February 2005).

For the cross section the geometrical cross section is multiplied by the extinction efficiency Figure 4-5:

$$\sigma_{Mie,App}(\alpha) = E(\alpha)\cdot\pi\cdot r^2 \tag{4.9}$$

here $\alpha = \frac{2\cdot\pi\cdot r}{\lambda}$ denotes the size parameter. For large particles $\alpha > 100$ (in Figure 4-5 $r > 5\ \mu m$), E(α) can be approximated by 2.

Usually there is a mixture of many aerosols with a size distribution depending on the origin and the age of the aerosol. The total extinction hence is given by:

$$K_{ext}(\lambda) = \int_0^\infty \pi\cdot r^2\cdot E(\alpha(\lambda,r))\cdot n(r)\cdot dr \tag{4.10}$$

The size distribution of the aerosols is described by a log normal distribution, for particles larger than 0.1 µm it can be approximated by a r^{-s} law with s of the order of 4 or 4.5. The macroscopic extinction only depends on λ and can be written as:

$$K_{ext}(\lambda) = const\cdot\lambda^{-(s-3)} \approx const\cdot\lambda^{-1.3} \tag{4.11}$$

This macroscopic extinction has the unit of an inverse length (usually km^{-1} is used) and describes both effects caused by the aerosol the absorption of light as well as scattering.

In clouds usually water drops with radii between 5 and 20 µm are observed. According to Figure 4-5 the extinction is constant as a function of the radius and is independent of the wavelength for used UV-vis wavelength region (not shown). Therefore the scattering probability and hence the light path enhancements (section 4.5.II) in the cloud is the same for the wavelengths in the UV-vis region [van de Hulst, 1957].

4.2.IV.a Absorption

As already mentioned the aerosols do not only scatter but partly absorb the light. The fraction of light absorbed by the aerosol is given by the single scattering albedo. It is defined in the similar way as the surface albedo, it equals 1 for white aerosols (all the light is scattered) or 0 for black aerosol.

Typical values of the single scattering albedo at 440 nm in urban aerosols vary between 0.9 and 0.98 depending on the aerosol type and the location [Dubovik et al., 2002].

4.2.IV.b Total Extinction

The aerosol extinction coefficient calculated above can be directly used to retrieve the visibility in the atmosphere. For the further analysis we assume that the aerosol extinction is dominant compared to the Rayleigh extinction. However, the visibility depends on many human influences like health of the observer's eye. A more accurate number to define the influences of aerosols on the light is the length a light beam has crossed until only 1/e of the initial intensity is observed. The intensity is weakened according to Lambert-Beers law:

$$I(l,\lambda) = I_o(\lambda) \cdot e^{-K(\lambda)\cdot l} \tag{4.12}$$

here K is the extinction coefficient. The path length l_e, where the intensity equals 1/e, is given by:

$$l_e(\lambda) = \frac{1}{K(\lambda)} \tag{4.13}$$

Nevertheless for practical reasons the visibility l_{vis} is still important, it can be approximated by:

$$l_{vis} \approx \frac{3.9}{K} \tag{4.14}$$

A detailed explanation of this approximation using the fact that human eye can observe intensity differences as small as 2 % is given by [Roedel, 1991]. The visibility is of course calculated for the visible wavelength range, whereas the extinction coefficient is wavelength dependent. The observed visibility can be attributed to a certain aerosol load. However depending on the wavelength, there are several aerosol extinction coefficients describing the same aerosol load. For a better understanding an example is given here.

The visibility is 5 km using the equations 1.14 and 1.11 it follows that the extinction coefficient for the visible wavelength (580 nm) equals:

$K(580\ nm) \approx 0.8\ km^{-1}$

$l_e(580\ nm) = 1.25\ km$

If the $\lambda^{-1.3}$ law is assumed, in the UV region the same aerosol load will lead to an extinction coefficient of:

$K(360\ nm) = 1.5\ km^{-1}$

For our measurement, these values define a maximum of the aerosol extinction coefficient, as the minimum visibility for the flights under visual flight rules (VFR) is 5 km. During the FORMAT campaigns the visibility was never as bad as 5 km, 5.1 km was the worst ever observed (section 4.5.III).

For the pure Rayleigh case the extinction in the visible range varies between 0.046 km^{-1} for 400 nm and 0.0029 km^{-1} for 800 nm [Roedel, 1991]. Following the dependency of $\sigma \sim \lambda^{-4}$ the extinction equals 0.031 km^{-1} at 440 nm, and for the UV wavelength of 360 nm as used above it is 0.07 km^{-1}. This limits the visibility to $vis \approx 125\ km$ for blue light (440 nm).

4.3 Radiative Transfer Modelling

At our research group a full spherical and 3-dimensional ray tracing program (Tracy) was developed recently [Friedeburg, 2003]. For most of the radiative transfer simulation presented in section 4.4 this program Tracy was used in the version from 12/07/2004, which was the latest version available. Only for the 2-dimensional Box AMF (section 4.4.VII) an internal bug caused a crash and the older version 15/03/04 had to be used. In the new version some bugs were repaired, but unfortunately some new ones occurred. In the following a brief description of the model is given, from a user point of view.
Tracy is able to read trace gas (maximum 10) and aerosol extinction profiles for a defined altitude lattice and calculate the most relevant quantities like AMF for the trace gas and for O_4 and Box-AMF for different telescopes looking in different elevations (maximum 10). In addition to these crucial parameters it delivers some helpful information on the scattering altitude, the part of light reflected on the ground, the portioning of Rayleigh to Mie scattering. This output is often very useful for the interpretation of the AMF and for debugging the program.
The basic idea of Tracy is to simulate the light path of many photons from the sun to the observer. As the optical path is reversible it uses the other way round starting at the detector and following a possible light path through the atmosphere to the sun. A large number of individual photons are simulated in finally the main quantities are averaged. A single photon path is weighted by its intensity, which might be reduced due to, e.g. aerosol absorption or ground reflection. Details about the algorithm are described in [Friedeburg, 2003].
For the calculation of the AMF the following formula [Solomon et al., 1989] is used:

$$A(\lambda) = \frac{\ln\left(\dfrac{I_0(\lambda)}{I(\lambda)}\right)}{\tau_{Vertical}} \tag{4.15}$$

here $I_0(\lambda)$ represents the intensity if no trace gas is taken into account and $I(\lambda)$ is the intensity if the trace gas is taken into account. Comparable to the vertical column the vertical optical density is given by: $\tau_{Vertical} = \int \sigma(z) \cdot c(z) \cdot dz$.

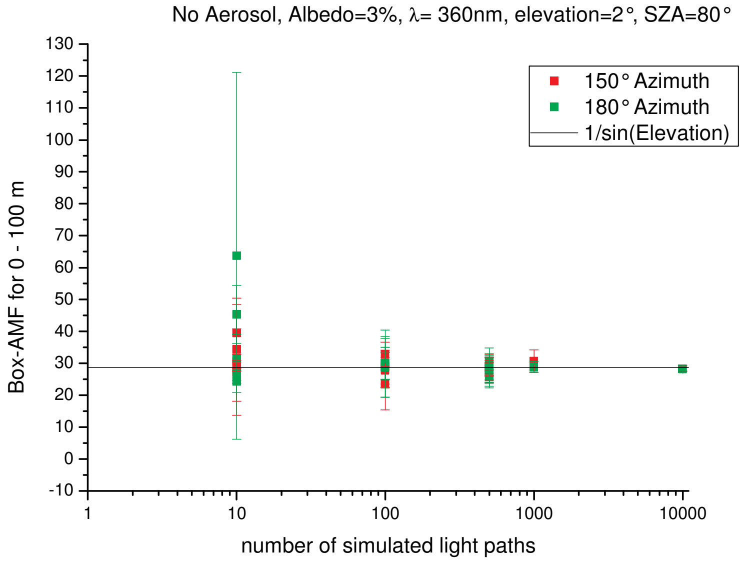

Figure 4-6: Dependency of the AMF on the number of photons. For 10, 100 and 500 runs 5 AMFs where simulated, the variations are much higher if only a few light paths are simulated. For the 1000 and 10000 only one was simulated.

With Tracy the accuracy of the AMF depends on the number of simulated light paths. In Figure 4-6 it is shown, that the variations decrease with increasing number of light path. If only 500 light paths are simulated the variations are too high, for 10000 photons the error is smaller than 10%. The AMFs for this figure were calculated assuming a ground based detector.

The time needed to calculate an AMF is linear to the number of simulated path ways, for 10000 photons and one line of sight it takes about 1 h using a Pentium® 4M-1.8Ghz processor. The AMF presented in this work are normally based on 10000 simulated light paths.

In almost all institutes (e.g. IUP-Bremen, BIRA, KNMI), where passive DOAS system are used, Radiative transfer programs for the calculation of AMF have been developed. The stratospheric AMFs as used in chapter 7.2 were calculated with the Bremenian model SCIATRAN (Rozanov et al., 2001).

4.4 Sensitivity Studies

The AMFs are a good way to express the sensitivity of the instrument under certain fixed or changing conditions. The main question concerning the sensitivity of the AMAXDOAS are:

- How sensitive is a downward looking DOAS instrument concerning changes in the flight altitude when a tropospheric absorber is observed?
- The next question might concern the clouds, between the aeroplane and the absorber. How does a thin layer of clouds influence the sensitivity?
- What happens if the mixing layer height decreases? Can we detect some absorbers in a small mixing layer of 200 m height, when the aeroplane is in 11600 m altitude?
- For the elevated lines of sight the dependency, of the relative solar azimuth angle is an interesting question. This study was performed assuming the AMAXDOAS is installed on a smaller aeroplane and flying in lower altitudes (chapter 5.10.II). Although, these sensitivity studies were performed for an aeroplane at low altitudes, the general dependencies are very similar for an aeroplane at high altitudes.
- Aerosol extinction influences the light path. How do the AMFs for different elevation angles change depending on the extinction coefficient?
- When flying at low altitudes the terrain elevation might influence the observed signal.
- For the tomographic inversion, the sensitivity in different distances from the detector and different altitudes are investigated. Here the 2-dimensional Box AMFs were simulated.

4.4.I Flight Altitude Studies

In this study we fixed most parameters in radiative transfer modelling. The solar zenith angle was fixed to 75°. The ground albedo was set to 5 %. We assume the observed trace gas (NO_2) is situated in below 2000 m with strong maximum between 1000 m (Figure 4-7). The aerosol extinction is illustrated in the same figure.

As the Falcon (chapter 6.1.II) rapidly reaches an altitude of about 7000 m after the take off, the altitude range studied is between 6600 m and 11600 m, lower and higher flight altitudes were ignored. In chapter 7.1.I.f we discuss an example, where the flight altitude changes in this range.

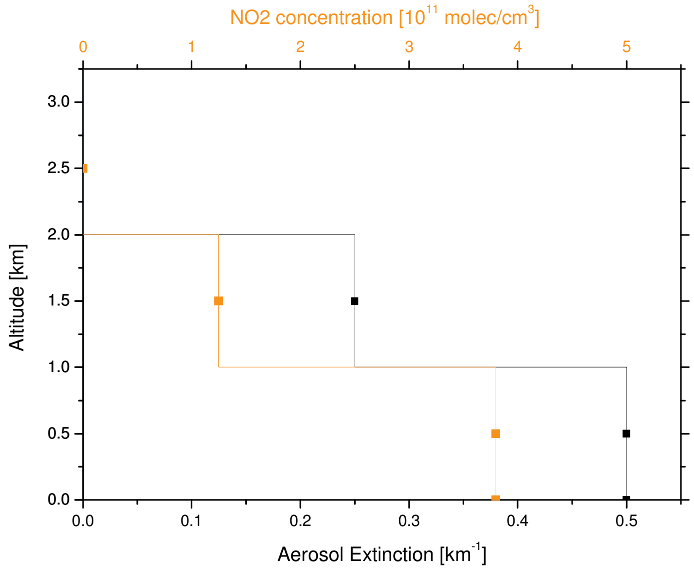

Figure 4-7: Aerosol and NO_2 profile as input for the simulation of the AMF.

When observing a trace gas in the lowest level of the atmosphere we would expect the sensitivity to decrease with flight altitude. The interesting question is how large is the effect of the flight altitude and can we ignore this effect when a certain altitude has been reached. In Figure 4-8 the AMFs for tropospheric NO_2 are shown for different flight altitudes. NO_2 was concentrated in the lowest km. As expected the AMF decreases with flight altitude. For flight altitudes lower than 8000 m the difference to the standard cruising altitude of 11600 m is up to 30 %. If the flight altitude varies between 10000 m and 12000 m, the relative change in the AMF will be low.

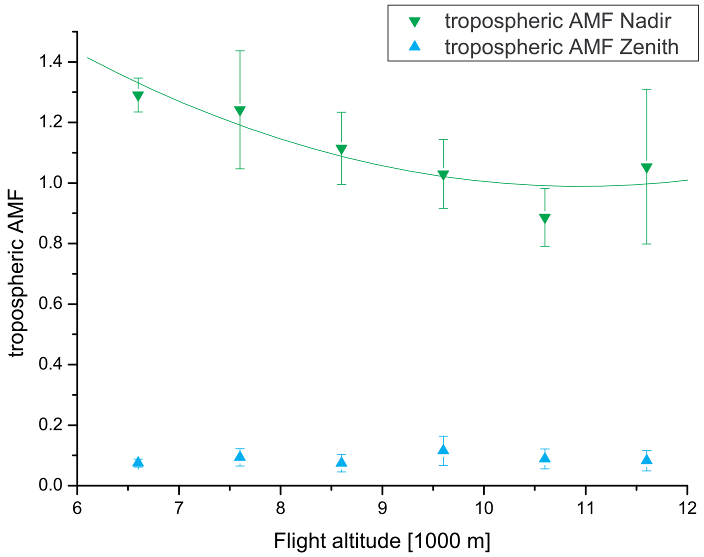

Figure 4-8: AMF for tropospheric NO_2 for different flight altitudes.

A similar effect can be observed for the O_4-AMFs (not shown here). They vary between 3 and 2.5 for the different flight altitudes.

Although the signal of any tropospheric absorber in the telescope directed to the zenith is very low the AMF is shown in Figure 4-8. A significant change according to the flight altitude cannot be observed. Here a relative stronger influence on the O_4-AMF is expected and observed. The AMF varies between 0.75 and 0.4.

4.4.II Influence of Clouds on tropospheric NO_2-AMF

The influence of clouds is not straight forward, even if the clouds are not optically thick, and the NO_2 is believed to be below the clouds. If clouds partly cover the field of view between the detector and the absorber the sensitivity will decrease rapidly. However more complex situations are possible where the clouds are thick and the trace gas is in the cloud or just above. In these cases the sensitivity can even be enhanced. Such situations were observed with AMAXDOAS on board the Falcon and were analysed and discussed in detail by [Wang et al., 2005 a]. In section 4.5.II an enhanced light path inside a thick cloud is studied.

We concentrate on the assumption that the NO_2 layer is below the clouds in a layer of 1000 m thickness. The vertical aerosol optical thickness can be called low (0.22). The clouds are situated below the aeroplane in 6000 m above the ground level.

In TRACY a cloud is implemented as Lambertian reflector covering a defined percentage of the sky. The cloud albedo was set to 0.9 and 10 % of the incident light crossed the cloud. This means the clouds simulated in this study do not absorb any light. The results are used for a specific observation from 10/03/2003 (chapter 7.1.II) where the assumption of bright clouds seems reasonable. As the data of the flight are of special interest for the validation of tropospheric NO_2 columns of SCIAMACHY, AMF for both instruments were simulated.

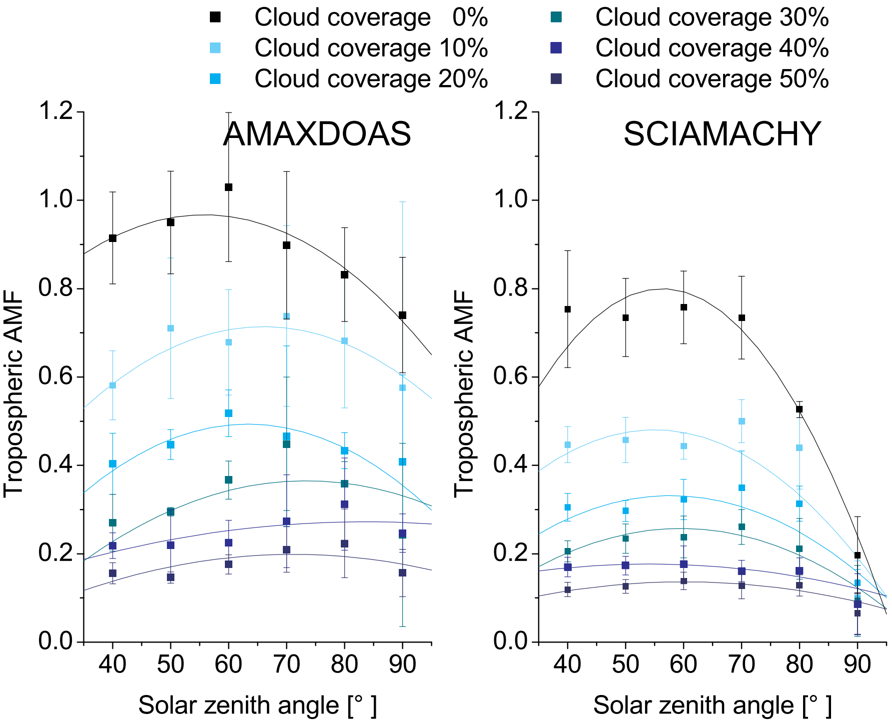

Figure 4-9: AMF for different cloud coverage for AMAXDOAS (left panel) and SCIAMACHY(right panel). The cloud coverage varied between 0% and 50% for a SZA range of 40° to 90°.

Figure 4-9 shows the AMF for tropospheric NO_2 when changing the cloud coverage between 0 % and 50 %. As expected the sensitivity for both airborne and satellite instrument decreases with increasing cloud coverage. For cloud coverage of 50 % the AMF is of the order of 0.1. So the observed slant column is only 10 % of the real vertical column. For higher cloud coverage both instruments seem to be more or less insensitive to tropospheric NO_2.

Comparing the sensitivity of both instruments it is obvious that the AMFs for AMAXDOAS are higher than those of SCIAMACHY. The difference will be about 20 %, if no clouds cover the field of view and about 10 % if the cloud coverage is 10 %.

Such a difference between the two instruments is expected due to the different altitude of the observing instruments. One has to keep in mind that about 20 % of the atmosphere is above the standard flight altitude of the Falcon. Above the simulated clouds we assumed no NO_2

hence the signal decreases for both AMAXDOAS and SCIAMACHY. For cloud coverage of 100 % we would expect the signal is close to zero for both instruments. When increasing the clouds both signals are more and more influenced by the bright clouds and observe less of the tropospheric pollution. This explains why the difference between the AMF for AMAXDOAS and SCIAMACHY decreases with increasing cloud coverage.

For higher cloud coverage influence of the light reflected at the clouds surface increases. Hence the relative influence of the Rayleigh scattered light decreases. The generally observed difference in the sensitivity of the two instruments is caused by the Rayleigh scattering events taking place between the flight altitude and the top of the atmosphere.

4.4.III Mixing Layer Height

In this section we will discuss the effects of a varying mixing layer height. The information presented here is important for a SCIAMACHY validation study based on the observations during the flight on 19/02/2003 (chapter 7.1.I.b) and [Heue et al., 2005]. Here different independent sources of information were used to describe the atmospheric conditions during the flight as realistic as possible. The flight crossed the Po-Valley where the highest slant columns were observed. According to soundings from Linate (Mi) and San Pietro (available at the University of Wyoming http://weather.uwyo.edu/upperair/sounding.html, checked 06/11/2005) the mixing layer height (MLH) was about 200 m above sea level (ASL) during night which can therefore be regarded as minimum. Other observations in the same region but in different years assume a MLH of 200 m to 600 m above ground level (AGL) [Petritoli et al., 2004]. The vertical aerosol extinction was derived from the Aeronet data in Ispra, (http://aeronet.gsfc.nasa.gov, March 2005) and equalled 0.3 for most of the day.

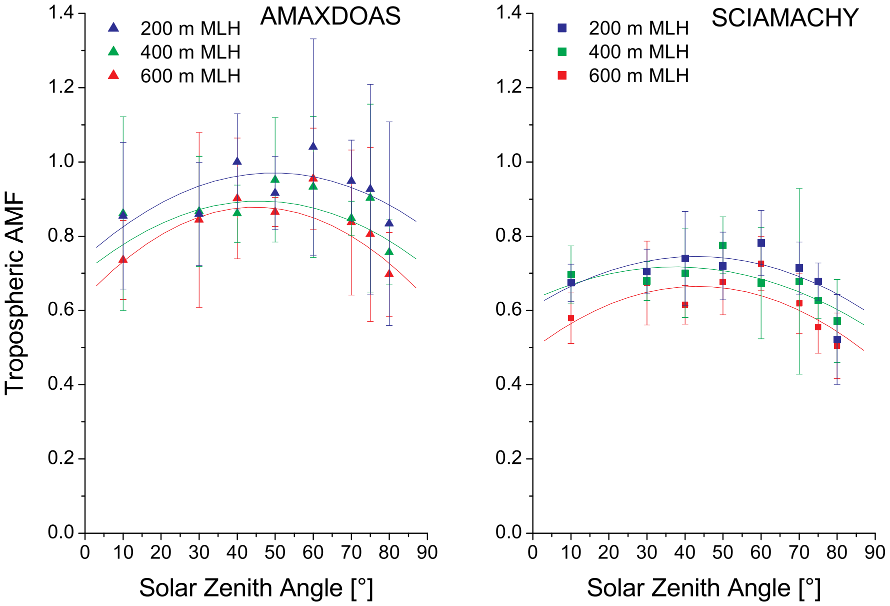

Figure 4-10: Tropospheric NO_2 AMF for different MLHs for AMAXDOAS (left) and SCIAMACHY (right).

Based on this information AMFs were modelled for three different mixing layer heights (200, 400 and 600 m) and a constant total vertical aerosol extinction of 0.3. As it was again part of a validation activity the AMFs for SCIAMACHY were calculated as well.

The difference between the AMF for AMAXDOAS and SCIAMACHY discussed above can be observed here as well (Figure 4-10). The basic finding is that for lower mixing layer heights the AMFs are lower as well. This can be expected, as more light is scattered to the observer above the NO_2 layer. Between 600 m and 200 m mixing layer height, the difference in the AMAXDOAS AMF is about 11% at a solar zenith angle of 60°. Besides the high aerosols load the main reason for this small effect is, that the NO_2 and the aerosols were assumed to have the same mixing layer height.

4.4.IV Solar Azimuth Dependency

The AMAXDOAS instrument observes light from different elevation angles, up to now only nadir was discussed. For the elevated lines of sight the relative position to the sun is important. As only two elevated telescopes were used on board the Falcon, we will discuss this effect in lower altitudes assuming the AMAXDOAS is installed on the small Partenavia aeroplane (chapter 5.10.III) as in the FORMAT I campaign (chapter 6.3). The flight altitude was 1100 m.

In this case we assume a high aerosol load and concentrate on short wavelength, as the main topic of the project was to retrieve the distribution of formaldehyde. The wavelength used for this study was 360 nm, the telescope was elevated 3° relative to the horizon and the solar zenith angle was 42°. Both sun and the instrument's line of sight are defined by the two angles, each:

- solar zenith angle (SZA),
- solar azimuth angle (SAA, φ) and
- elevation angle (α),
- instruments azimuth angle (θ).

Both azimuth angles are defined relative to north, i.e. 180° solar azimuth means the sun is in the south (12:00 LT) and 180° instrumental azimuth means the instrument is directed to the south. The difference between the two absolute azimuth angles is defined as relative azimuth angle ($\theta_{rel} = \theta - \varphi$). If the relative azimuth is 0, the detector will be directed towards the sun. The angle will be positive, if the sun is left of line of sight and negative in the other case. In case it is 180° the sign is irrelevant.

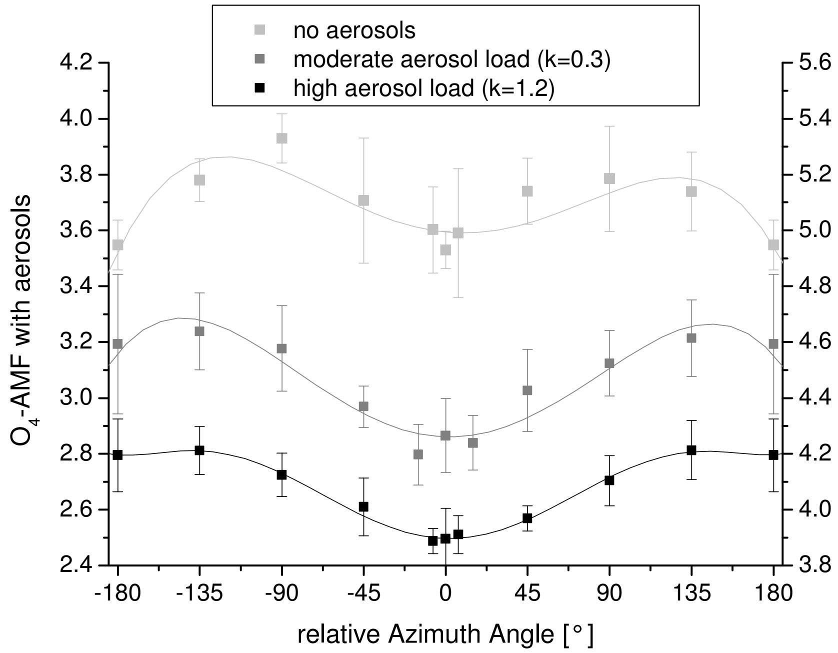

Figure 4-11: O_4-AMF for different aerosol loads as function of the relative solar azimuth angle. For a pure Rayleigh atmosphere two minima are observed, at 0° and 180°. In case aerosols are included only one minimum remains.

In Figure 4-11 the O_4-AMF for different aerosol loads are shown. In all cases the model reproduces the expected symmetry quite well. In the case of a pure Rayleigh atmosphere two minima are observed at a relative azimuth angle of 0° and of 180°. It is obvious that the light path is short when the detector is directed towards the sun (0°). For the opposite direction (180°) the observed effect is caused by the symmetry of the Rayleigh phase function (Figure 4-3). The observed minima however are not as strong as might be expected from the phase function. The phase function varies between 0.75 perpendicular to the direction of the incident light and 1.5 in the parallel direction. The O_4-AMFs vary between 5.2 and 5.0. Similar observations for ground based measurement were also described in [Wagner et al., 2004].

Due to the strong forward preference in the Mie Scattering process (Figure 4-4) the second minimum will be weaker or will vanish totally, if aerosols are included. For the Mie scattering process a stronger dependency might be expected. But if the aerosol load is high, the total number of scattering processes will increase as well, hence the information about the position of the sun is lost. The reader might remember a summer day with a high aerosol load, the “air seems to be bright” irrespective of the direction. According to the TRACY simulations about 4 (4.2 ± 0.2) aerosol scattering events will occur in the high aerosol load and about 2 (1.9 ± 0.1), if the moderate aerosol load is assumed.

The difference between the maxima and the minima has an almost constant value of 0.2. According to our discussion above, we would expect it to change, what is not observed in the model. The used phase function did not change the observed effect, although we increased the forward peak by a factor of two (not shown). One reason might be that in the model as well as in real measurements the detector must not be directed direct to the sun. Therefore the effect of changing the relative azimuth angle should be used very carefully, if at all, to derive the aerosol profile information, from O_4 measurements.

4.4.V Aerosol Extinction

The AMAXDOAS instrument observes scattered sunlight under different elevation angles. The different lines of sight are affected differently by aerosol scattering. This might be used to retrieve some information about the aerosol extinction profile, in a similar way as it is done in ground based measurements [e.g. Wagner et al., 2004 and Heckel et al., 2005].

Flying close to the mixing layer height the influence of aerosol scattering will strongly depend on the elevation angle of the line of sight. In the zenith the absolute influence is very small. The AMF for the upward directed telescopes (+11°, +3°, +2°) will be strongly affected, if the aeroplane is inside the aerosol layer. As long as the visibility is large compared to the flight altitude, the AMF for nadir will not change dramatically. Radiative transfer simulations will help to quantify the influence on all telescopes, including those directed to any other downward directions as nadir. The O_4-AMF were simulated for different aerosol extinction profiles. As this study is part of the data retrieval for the FORMAT I campaign, the realistic parameters for a selected flight (chapter 8.1) were chosen, i.e. wavelength of 360 nm, flight altitude 1100 m, elevation angles as described in chapter 5.10.II, SZA 39° and relative SAA 90°.

The simulated AMFs are illustrated in Figure 4-12. In the undisturbed Rayleigh atmosphere the AMF for the lines of sight -1° to +3° are extremely high. The line of sight -1° might theoretically reach the earth surface in 62 km distance (the curvature of the earth not taken into account), for the small wavelength however the Rayleigh scattering reduces the light path. For the flat upwards elevations (+2° and +3°) a similar AMF is simulated, the small decrease is caused by less scattering centres above the aeroplane compared to below. The same explanation also holds for the line of sight +11°. For the other downward telescopes a geometrical approach $A_{geom} \approx \frac{1}{\sin(\alpha)} + \frac{1}{\cos(\vartheta)}$ might in principle explain the observed trend.

The observe magnitude, however, does not agree with this approximation, e.g. $AMF_{geom.}(-16°) = 4.9$, $AMF_{sim}(-16°) = 2.77$, the difference again is caused by the strong Rayleigh scattering at this wavelength. Hence, only part of the light observed by the telescope is reflected at the surface. For the nadir line of sight the geometrical approximations equals 2.2, which will in good agreement with simulations, even if aerosols are included and additional scattering processes occur.

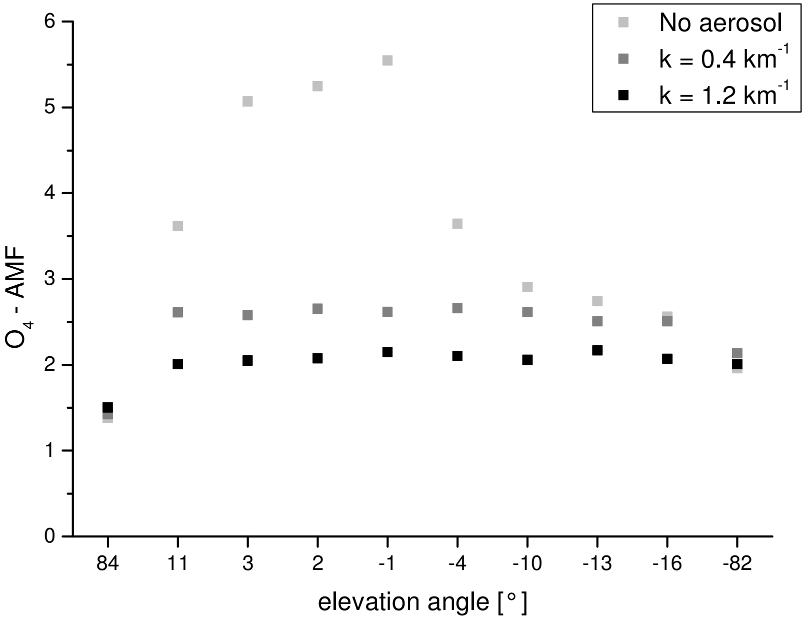

Figure 4-12: O_4-AMF for pure Rayleigh atmosphere (light grey), moderate aerosol extinction (grey) and strong extinction (black). Both aerosol profiles were assumed to be constant up to 1400 m.

From ground based MAX-DOAS a slight increase for the zenith with increasing aerosol extinction is expected [Wagner et al., 2004]. Here, however no significant increase can be realized in the simulated data, compared to the quoted study the aerosol load might already be too high or the aerosol layer is not mighty enough (300 m above the detector).

In case the aerosol extinction is introduced to the simulation, all AMFs decrease, except for nadir and zenith. In the telescopes directed close to the horizon the effect is strongest. The length of the light path is reduced by the additional scattering centres. The light is partly shielded from the surface by Rayleigh scattering as discussed above for the downward directed telescopes. Including additional scattering centres, as given by the aerosols, this effect is enhanced, therefore the AMF are even lower than before and the difference between the different lines is reduced. It completely vanishes for high aerosol extinction.

4.4.VI Terrain Level

In the last section we prepared the retrieval of aerosol information for a special flight around Milano. However this preparation is not yet completely finished, as we concentrated on the aerosol extinction only. If we fly in constant flight altitude of 1250 m (ASL), the different terrain elevation between the Po river (50 m) and the foot hills of the Alps (up to 400 m) might also affect the observed O_4 column densities. For the selected flight only a smaller altitude range (100 – 200 m) is of interest. Hence we concentrate on the two terrain altitudes: 50 m and 250 m to cover the interesting altitude range.

In contrast to the flight altitude studies in section 4.4.I, the flight altitude and the air density and related parameters were changed according to the terrain level. The discretisation grid was not changed.

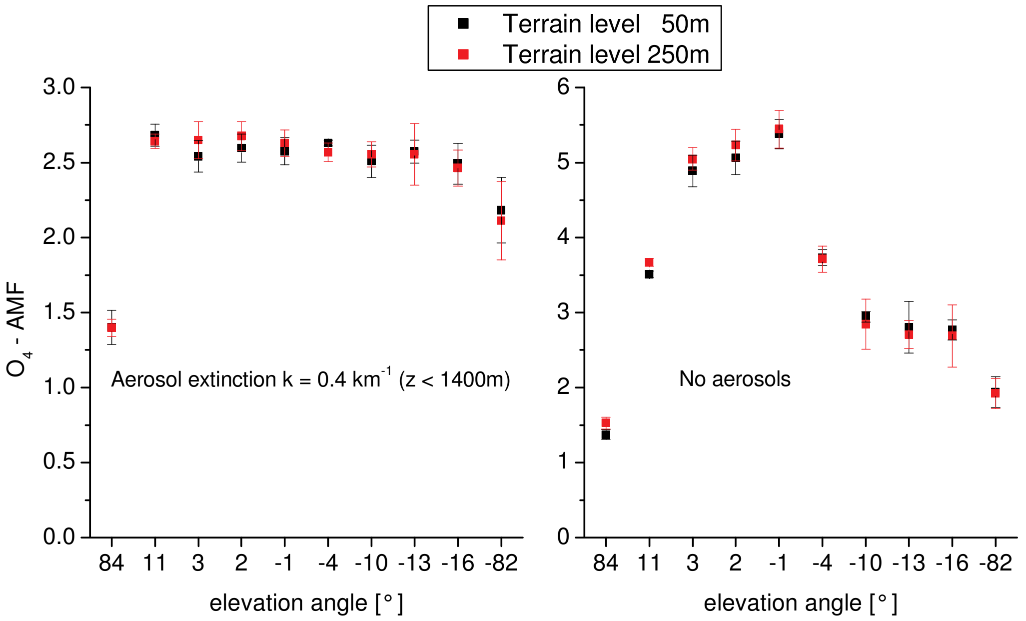

Figure 4-13: O_4-AMF for different terrain levels 250 m in red and 50 m in black. In the right figure the pure Rayleigh atmosphere is shown and in the left we used the same moderate aerosol load as in the last section. The aerosol altitude of the aerosol extinction 1400 m was measured relative to the ground level. In this figure the standard errors of the AMFs are given, which are realistic for most cases, but sometime underestimate the real deviation of the simulations.

The vertical column densities changes by ±2 % relative to the value for the average altitude (150 m) of $1.22*10^{43}$ molec^2/cm^5. Compared to the errors of the AMFs (10 %) this deviation can be ignored.

The AMF are shown in Figure 4-13. In case no aerosols are considered, a small effect for the upward directed telescopes is observed, but within the errors they agree well. On the left panel the O_4-AMF, with a moderate aerosol taken into account, is shown. These AMFs are not affected by the different terrain level. Hence for the detailed study (section 4.5.III) an average terrain level of 150 m ASL is used.

4.4.VII Two-dimensional Box AMFs

If the horizontal variations of a trace gas are very high, e.g. in the plume of a point source, it will not be possible to derive a vertical profile. Besides the interesting challenge is to retrieve the 2-dimensional distribution (chapter 8.2.IV). However with a 1-dimensional Box AMF, depending on the altitude only, this aim is far out of reach. For the tomographic retrieval (chapter 3.5) such 2-dimensional Box AMF are essential.

For the simulation of the Box AMF, the flight parameters of the flight on 26/09/2003 (chapter 8.2) were used. The flight altitude was 660 m above ground, the solar zenith angle 55° and the relative azimuth angle can be approximated by 90°. The viewing direction of the telescope is described in chapter 5.10.III. For the albedo as usual 4 % were assumed, the wavelength was set to 440 nm. Around the aeroplane's position a grid with 2 km grid element width and 100 m grid elements height was set. If the distance is larger than 12 km in front of the aeroplane, only one large box will cover complete hemisphere. Also behind the plane a large box will be introduced, if the distance is larger than 2 km.

In **Figure** 4-14 the geometrical set-up including the lines of sight and the boxes are shown.

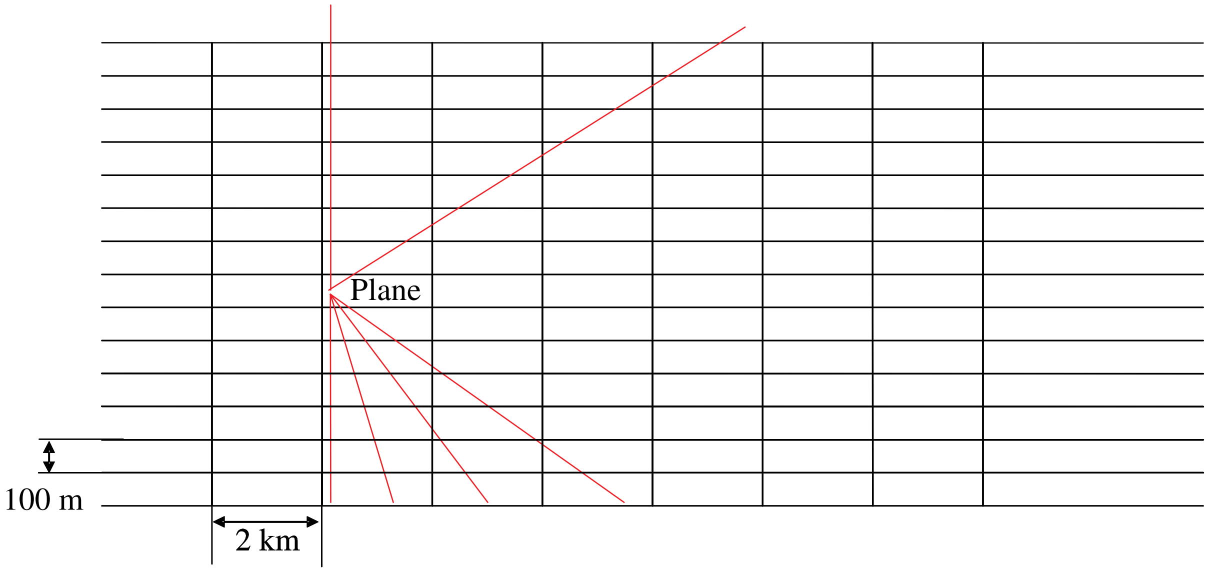

Figure 4-14: Relative position of the aeroplane in the box lattice. The Box AMFs were simulated assuming the plane to be close to the edge of the box. To study the influence of light from "behind" the plane, the AMF for another column of small boxes was simulated.

The aeroplane is situated at 660 m above ground and set close to the edge (20 m) of the grid box. To study the influence of the light scattered from behind the aeroplane one column of small boxes was introduced behind the plane.

In Figure 4-15 the Box AMFs are shown as colour plot, the dots are positioned in the centre of the respective box (except for the large boxes which are shown in -5 and 15 km). Here only the telescopes directed in "flight direction" are shown, the telescopes directed to the back were simulated as well. As the AMF are symmetrical to the position of the aeroplane ($\theta_{rel} = 90°$) these AMFs are not shown in Figure 4-15. The highest sensitivity is observed close to the aeroplane along the slant lines of sight, e.g. "+7°" or "-7°".

Figure 4-15 shows a 2-dimensional projection of a 3-dimensional problem. The sun can be assumed to be at the reader's position and in the 2-dimensional projection it is above the aeroplane.

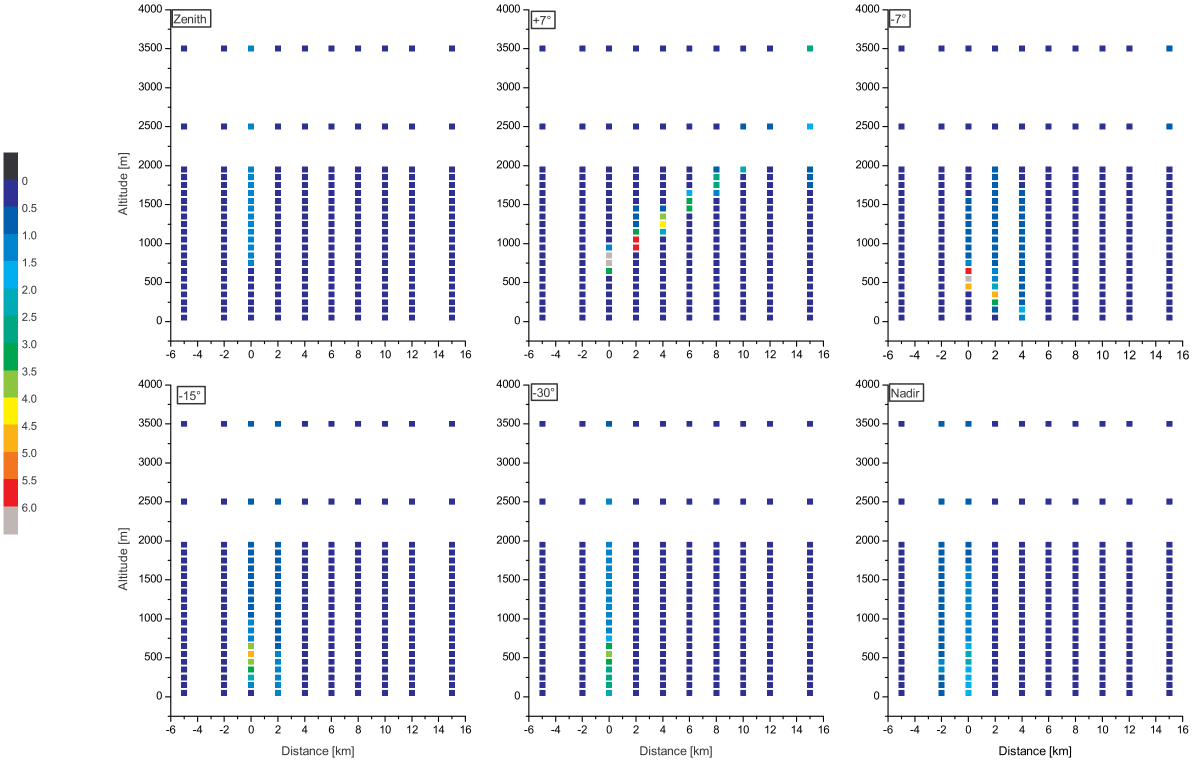

Figure 4-15: 2-dimensional Box AMFs simulated for a flight altitude of 660 m. For the distances larger than 2 km behind the plane and 12 km in front only one large box is assumed, hence the respective AMF are shown in a larger distance. Most of the lines of sight can be clearly identified (e.g. +7° or -7°).

These data were calculated for comparison with a single scattering approach. Before comparing them to any other data a consistency check is crucial. The best way is to compare the Box AMF with the total AMF by integration across the boxes. The first step is to calculate 1-dimensional Box AMF, by integrating across one altitude layer. In Figure 4-16 the 1D Box AMF are shown.

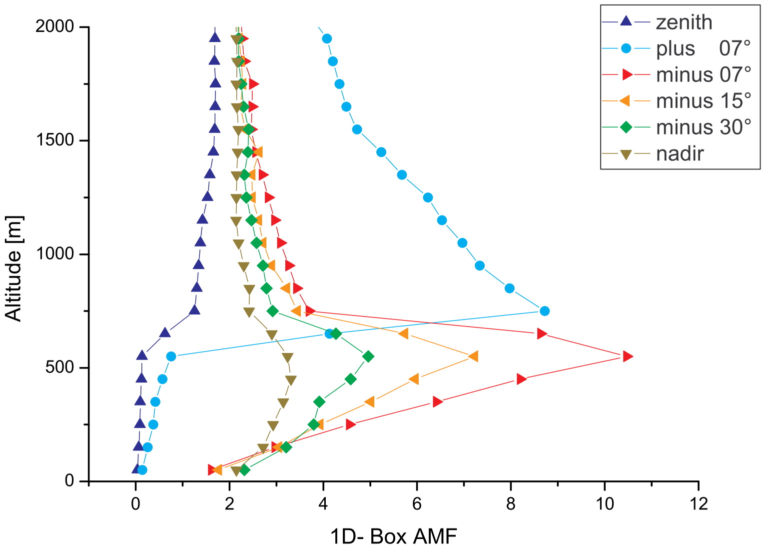

Figure 4-16: The integrated 2D-Box AMF can be seen as 1D-Box AMF.

With Tracy we can calculate both the 2D Box AMF and the total AMF simultaneously – using the same discretisation grid. According to the definition of the Box AMF, these two are related to each other by the following equation:

$$A = \frac{S}{V} = \frac{\sum_j A_{Box,j} \cdot c_j \cdot z_j}{\sum_j c_j \cdot z_j}$$

The same trace gas profile c_j as used in the simulation must be used to calculate AMF based on the Box AMF.

Both sets of AMFs are shown in Figure 4-17. The comparison shows that the AMFs differ by up to 30%. In general it seems the AMF are overestimated by the Box AMF, hence we can assume most of the Box AMFs are overestimated as well. However no conclusion concerning a certain Box AMF is possible.

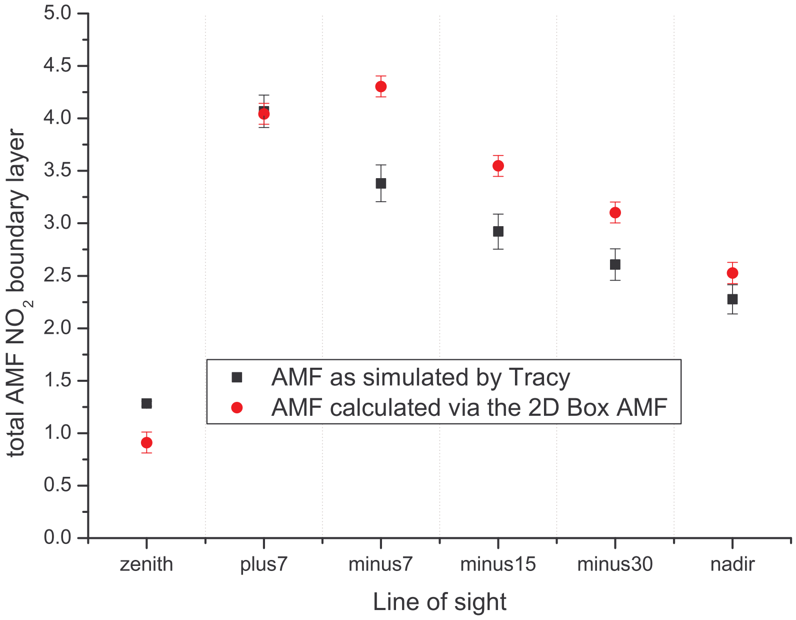

Figure 4-17: For boundary layer NO_2 the AMF are calculated directly and via the Box AMF. Both quantities were calculated with TRACY.

The reason for this large difference between AMF and Box AMF is not fully understood but whenever Box AMFs are simulated by Tracy this effect can be observed. The same effect is observed when 1-dimensional Box AMF are calculated (Tracy bug report, Attachment). Even if the problem for the 1-dimensional Box AMF cannot be resolved, a work around will be found easily. Instead of using the standard Tracy Box AMF the trace gas profile is split into several layers and used as independent traces gas profiles in the simulation. (Tracy bug report). This work around however is not possible for the 2-dimensional Box AMFs as using a 2-dimensional traces gas distribution is not implemented in Tracy up to now.

Hence for any comparison between the 2D Box AMF from Tracy and any other data it has to be kept in mind that it can only be qualitative and we have to be very cautious when comparing “correct” numbers

4.4.VII.a Single Scattering Approximation

The 2-dimensional Box-AMF we discussed in the last section will be compared to an analytic single scattering approximation. The approximation is used for the tomographic inversion.

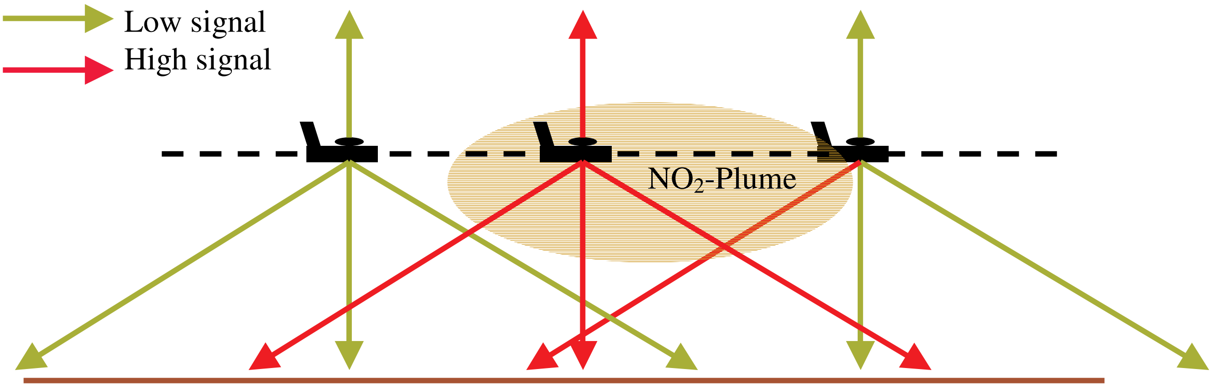

Figure 4-18: Sketch of the aeroplane crossing the plume. Three different positions are shown here, where different lines of sight observe the plume.

For the reconstruction a grid parallel to the flight direction was used (chapter 3.5.I). For the calculation of the Box-AMF we first concentrate on the 2-dimensional concentration field. If $\mathbf{c}_{x,z}$ is the concentration distribution, than the next step is to calculate the matrix $\mathbf{A}_{\alpha,x,z}$ a linear forward model with:

$$S_{\alpha,x} = A_{\alpha,x,z} \cdot c_{x,z} \tag{4.16),}$$

where α stands for the lines of sight, observing the SCD at a given position x. The matrix A will be calculated below, by comparing the equations (4.16) and (4.5) the relation between the Matrix A and the Box-AMF are obvious: The altitude of the box is treated in a different way in both equations: $A_{\alpha,x,z} \cdot z_{\alpha,x,z} = A_{Box,\alpha,x,z}$

The forward model matrix **A** describes the response of the instrument to a certain concentration at a certain position in the box. The relevance of the position is obvious from Figure 4-18, if the telescope is directed in flight direction it is insensitive to any absorber located behind the plane.

To find the appropriate forward model a simplified radiative transfer with a single scattering approximation is used. The model can be described as follows:

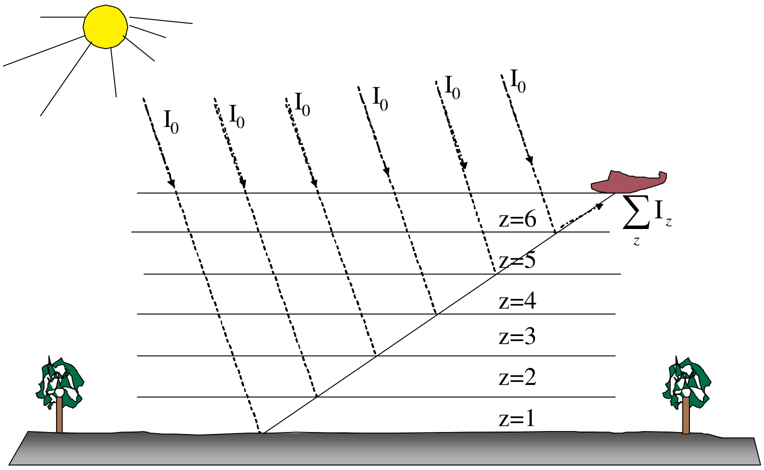

Figure 4-19: Single Scattering approximation for the light observed by the telescope.

For the moment we will concentrate on one telescope i and will not subscript it in the following steps. As long as the line of sight is of no importance this can be done and the index will be reintroduced later on.

At the top of the model the light has the intensity I_0, the light is scattered in different altitudes into the observing telescope. Along the way (l) from the top of the model to the detector some extinction (coefficient K) due to aerosol and Rayleigh scattering occurs as well as molecular absorption (chapter 4.2). The light observed by the telescope i originating form a certain layer z can be approximated by: $I_z = I_0 \cdot e^{-K \cdot l_z} \cdot p_z$, the factor p_z describes the probability the light is scattered into the detector.

The total intensity observed by the telescope directed to α can be calculated by taking into account all layers z:

$$I_\alpha = \sum_z I_{\alpha z} = I_\alpha \cdot \sum_z w_{\alpha z} \,. \tag{4.17}$$

The weighting factor $w_{\alpha z}$ introduced here equals the relative intensity observed by the telescope scattered in the layer z, for z = 0 the albedo scattering is taken into account.

The assumption about the albedo and the aerosol extinction are the same as in the previous section (4.4.VII): 4 % Albedo and 0.16 1/km aerosol extinction between ground and 1700 m altitude.

The weighting factors w were calculated with the radiative transfer simulation “eagle” (Christoph von Freideburg private communication)

In the same way as the intensities are summed up to the total intensity the slant columns are added to the observed signal:

$$S = \sum_z w_z \cdot S_z \tag{4.18}$$

The partial slant columns S_z are given by the concentration observed along the light path l_z: $S_z = \int_{l_z} c(x,z) \cdot dl$

The concentration field c(x,z) can be written as a discrete sum which is given by the used gird:

$$c(x,z) = \sum_{x,z} c_{x,z} \cdot b_{x,z} \,, \tag{4.19}$$

where $b_{x,z}$ represents the set of basis functions in the grid, be $b_{x,z} = \delta(x,z)$ the well known Kronecker δ function.

The slant column observed by the telescope directed to α is hence given by:

$$S_\alpha = \sum_z w_{\alpha,z} \cdot \int_{l_{x,c}} \sum_{x,z} c_{x,z} \cdot b_{x,z} \cdot dl \tag{4.20}$$

It follows by the definition of the grid that the concentration c is constant inside one box, so the integral is simplified to: $\int_{l_{ik}} \sum_j c_j \cdot b_j \cdot dl = \sum_j c_j \cdot \int_{l_{ik}} b_j \cdot dl$, and the observed SCD is given by:

$$S_\alpha = \sum_{x,z} A_{\alpha,x,z} \cdot c_{x,z} \,, \tag{4.16}$$

now the matrix **A** can be calculated:

$$A_{\alpha,x,z} = \sum_{z} w_{\alpha,z} \cdot \int_{l_{x,z}} b_{x,z} \cdot dl \tag{4.21}$$

The matrix element is given by the light path inside the box weighted with the intensity.
For the telescopes directed upwards all scattering processes close to the aeroplane are neglected and the geometrical ratio of path length to box height is used as Box AMF. It is mainly given by $1/\sin(\alpha)$, with α as elevation angle. The intensity weight is the same for all lines. For the zenith telescope the AMF is constant and equals one for all boxes situated above the plane. The maximum Box AMF for the telescope directed to 7° equals $1/\sin(7) \approx 8.2$, smaller values are caused by light paths crossing only parts of the box.
For those boxes not crossed by any light path the weighting equals zero. For example if the elevation is -7°, then the weighting below the aeroplane close to the ground vanishes.

4.4.VII.b Comparison between Single and Multi Scattering Approximation

The two different approaches to calculate the Box AMFs may now be compared to each other. As mentioned above only a very qualitative comparison is useful here.
The best way to illustrate the comparison is a colour map as we used for the Box AMFs themselves. In Figure 4-20 the absolute differences for the lines of sight directed to the ground are shown. In general a good agreement is observed, but the AMF for some boxes show large deviations. With respect to the large uncertainties in the Tracy Box AMFs, the observed differences will not be discussed in detail here.

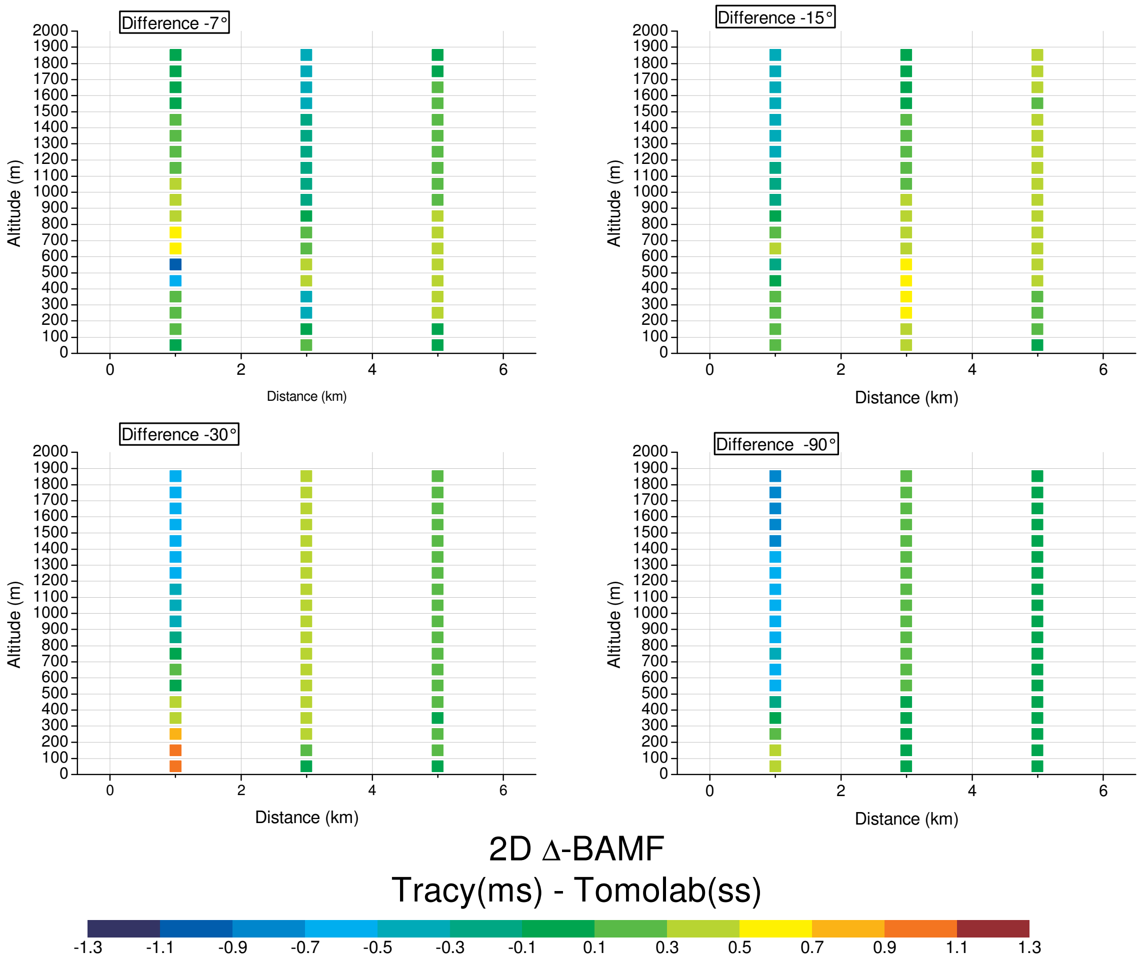

Figure 4-20: Absolute difference between the multiple scattering and the single scattering Box-AMFs for the four downward directed lines of sight. In general the agreement is good (green squares), but also some disagreement is observed (red or blue).

The difference relative to the Tracy simulation is shown in Figure 4-21. High deviations higher than 60 % mostly occur at larger distances to the aeroplane. In most of these cases the Tomolab Box AMF is zero.

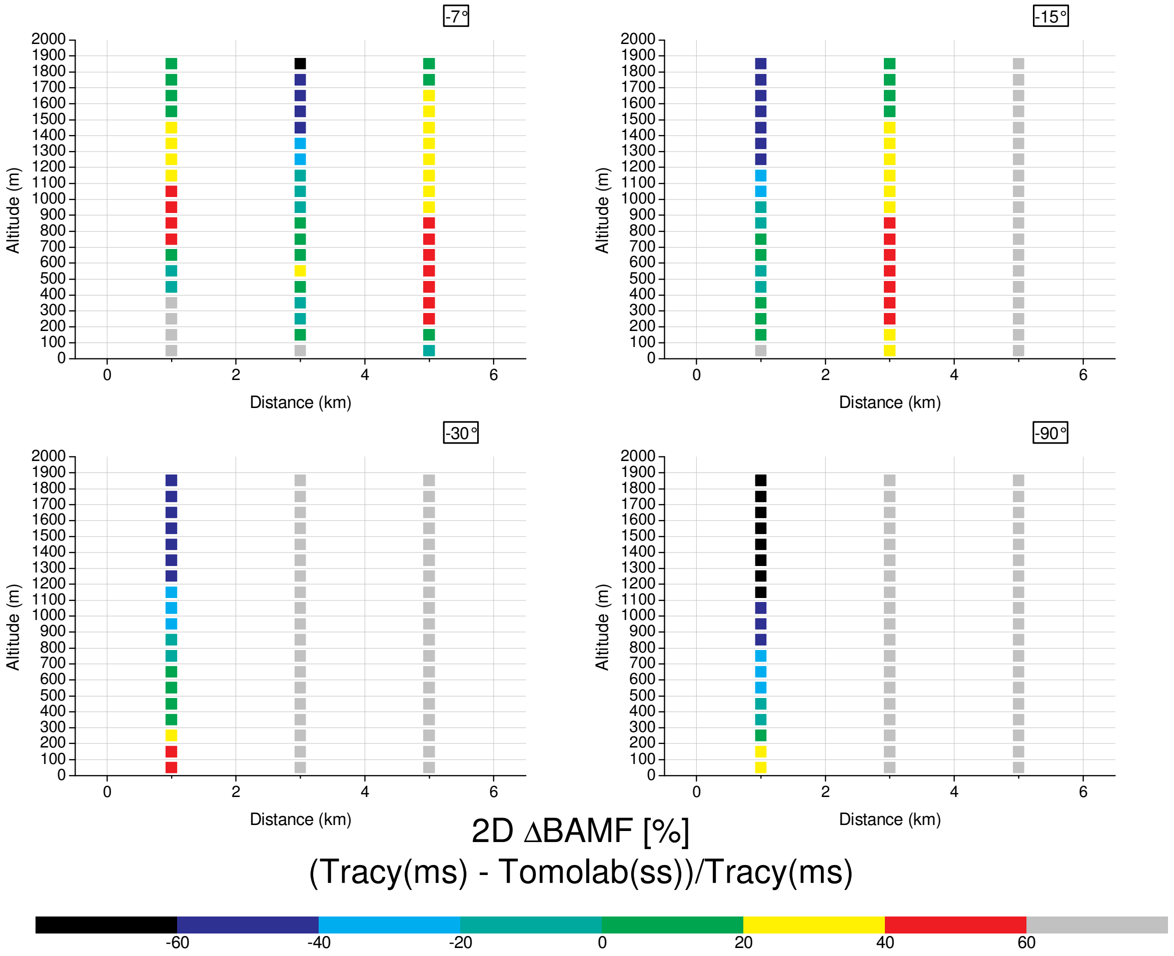

Figure 4-21: Relative difference between the two sets of Box AMFs.

Due to the observed bug in Tracy the question whether the straight forward simulation describes the reality well enough can not be solved. As both simulations might be wrong it is best to use the single scattering approximation and approximate the introduced error. A comparison of 1D Box AMF between Tomolab and SCIATRAN showed a good agreement when the single scattering approximation was used in SCIATRAN as well.

To get correct Box AMF for a 2-dimensional lattice seems to be impossible at the moment but will be in the near future as soon as the next version of Tracy is finished and validated. As long as it is not finished the single scattering approximation seems to be good.

4.5 Applications

The sensitivity studies in section 4.4 mostly describe the principle behaviour of the observed slant column densities due to changes in certain observation parameters. In most cases the parameters vary within a realistic range. In this section individual observations and the cause for the observed quantities are discussed in detail.

4.5.I Langley Plot

The stratospheric absorption of the reference spectrum is not known, this was an advantage for the retrieval of the tropospheric column (chapter 3.4). Here the stratosphere had to be subtracted any way, but it is the main challenge for the retrieval of stratospheric columns.

Following the definition of the AMF (section 4.1) the differential slant column (chapter 3.2.III.a) is given by:

$$dS = V \cdot A - S_{ref}$$

This equation describes a linear function dS(A) – as long as the slope (V) is constant. Hence the missing parameters (SCD_{ref} and VCD) can be retrieved by plotting the dSCDs against the AMFs. This method is usually referred to as Langley plot.

For NO_2 the assumption of a constant VCD is not fully correct, as it photodissociates very quickly, therefore the photo stationary state depends on the incident radiation and the solar zenith angle. This means the stratospheric concentration and the vertical column density depends on the SZA. The difficulty is to find an appropriate interval where the AMF changes strong enough and the vertical column can be assumed to be constant.

The approximation for the AMF ($A \approx {}^{1}\!/_{\cos(\vartheta)}$) is not valid for SZA values larger than 70°.

For one flight on 04/09/2002 (chapter 7.2.I) a Langley plot is made for an interval of solar zenith angles between 86° and 88.5° assuming that the NO_2 concentration does not change too much in this period. According to [Bösch et al., 2001] the photolysis rate of stratospheric NO_2 changes only slightly in this range of the solar zenith angle, hence we can assume this to be the case for the stratospheric NO_2 as well.

For zenith and nadir the solar azimuth angle is obviously irrelevant. As the detected light is scattered below the absorbing layer the AMFs are similar for both these viewing directions. The differences in the simulated AMFs are below 5% for the SZA below 94°.

For an elevated telescope (+2°) however, the azimuth angle might have a large effect. In Figure 4-2 we assumed the relative azimuth angle to be large and the observed light is mainly scattered below the trace gas layer, hence we expect the AMF to be similar to the ones for nadir and zenith. However, this simplification does not hold in real measurements, the AMFs are definitely higher (~10 %). The AMF for this line of sight strongly depends on the relative azimuth angle and changes by up to 36 %. For the retrieval of the total vertical column only nadir and zenith data are considered.

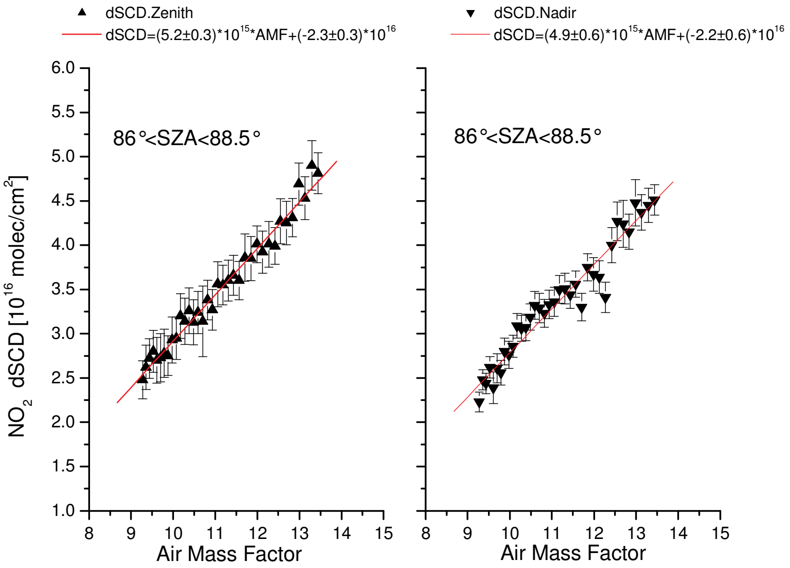

Figure 4-22: Langley plots for zenith and nadir dSCDs for 04/09/2002.

Although a small range of the solar zenith angle is used a deviation from the linear function can be seen Figure 4-22. The observed vertical column density is approximately $5*10^{15}$ molec/cm^2 and the slant column in the reference equals $2.2*10^{16}$ molec/cm^2. In chapter 7.2.1 the total vertical column along the flight will be discussed and compared to other measurements.

4.5.II Light Path Enhancement inside a large Cloud

Inside big clouds the light path is often enhanced due to multiple scattering. On the flight from Nairobi to Yaoundé (25/09/2002) the Falcon had the bad luck to cross a thick cloud around 8:30 UT.

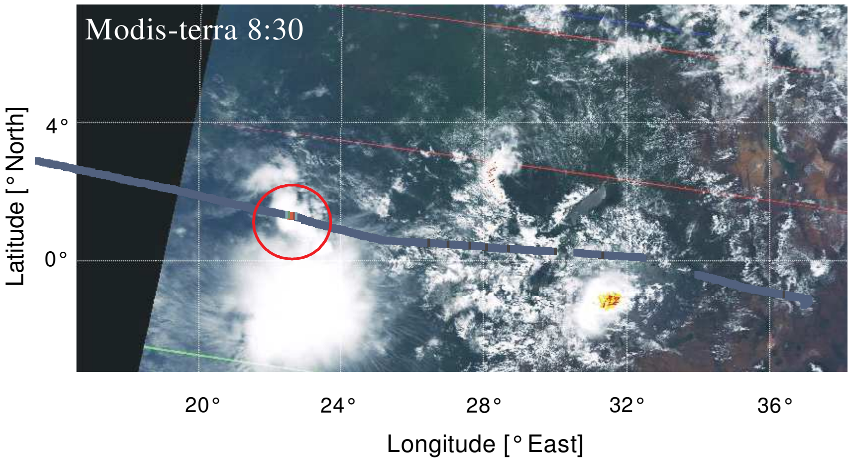

Figure 4-23: Satellite image (MODIS Terra) of eastern central Africa. The Falcon passed by a big storm in the east; in the west she crossed a dense cloud field (red circle) (satellite image: http://modis-atmos.gsfc.nasa.gov/images/index.html, March 2005).

The cloud is a smaller part of large cloud system as can be seen in Figure 4-23. At this time the position of the Falcon was: 1° 15' 46''N, 22° 38' E which is over the central Congo basin. The image was taken at the same moment the Falcon crossed the cloud.

In the log I reported that, there were thick clouds below and above the aeroplane before entering the cloud. The cloud itself is mentioned as heavy turbulences, the operators were asked to fasten the seat belts again and stop working for a few minutes. The aeroplane was totally surrounded by the cloud.

Of course this cloud was also observed by the other instruments on board. The backscatter ratio of the OLEX is shown in Figure 4-24, around 8:30 UT a rapid decrease is observed:

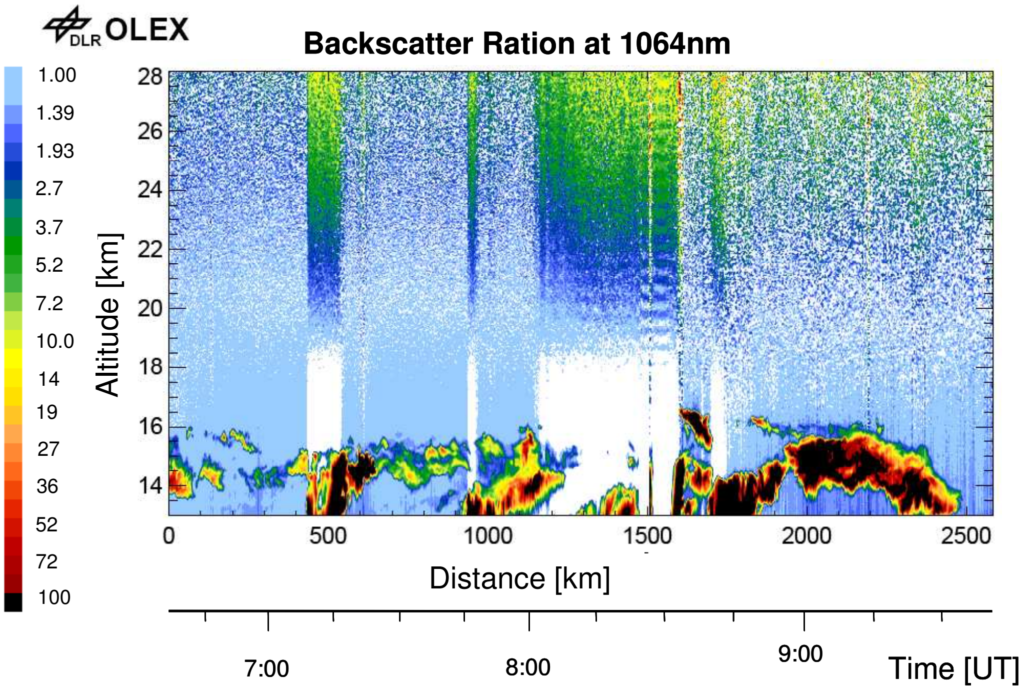

Figure 4-24: Backscatter ratio observed by the OLEX instrument on 25/09/2002 (Andreas Fix, private communications, 25/03/2003). The white stripes indicate that no light is scattered back from higher altitudes. Mostly such effects were caused by clouds in the flight altitude or just above e.g. 7:15 or 8:30 UT.

The backscatter ratio of a LIDAR instrument gives the ratio of the observed light to the emitted light. According to Andreas Fix the rapid decline might be due to thick clouds located just above the aeroplane or around it. The altitude scale in Figure 4-24 starts at 13 km (ASL) which is about 2 km above the flight altitude.

4.5.II.a Measurement Results

During the short period when the Falcon crossed the cloud a strong increase in the absorptions in most trace gases is observed in all lines of sight. As some heavy turbulence had been crossed before one of the telescope shutters (-2°) was blocked for this part of the flight. Within a few minutes the O_4 slant column increases up to $5.04*10^{43}$ $\text{molec}^2/\text{cm}^5$. In Figure 4-25 (left) the observed O_4 data from all (active) lines of sight are shown. The observed enhancement is very similar for all lines of sight, this agrees with my personal expression that the aeroplane was totally surrounded by the cloud. The dSCDs of O_4 and H_2O for the Zenith line of sight are shown in Figure 4-25.

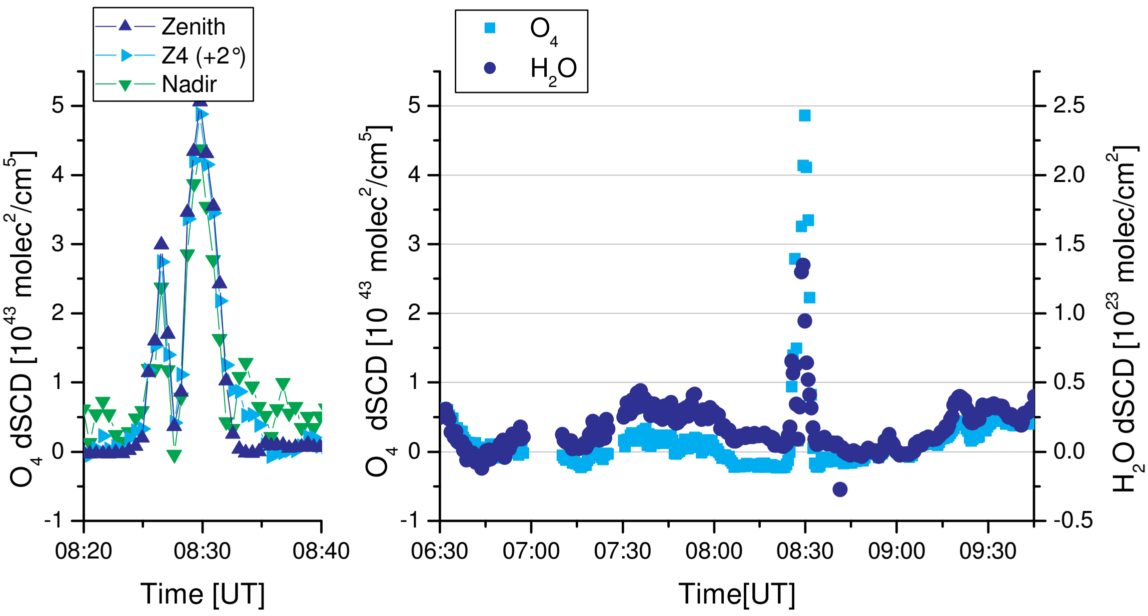

Figure 4-25: Left panel: Observed O_4 dSCD for all lines of sight during the cloud cross section. The different absorption in the reference are subtracted.
right panel: O_4 (light blue and left scale) and H_2O (dark blue and right scale) dSCDs from the Zenith viewing telescope. At the same time as the O_4 enhancements are observed a similar effect can be made out in the H_2O.

Similar effects have been observed from ground based measurements when clouds cross the instrument's field of view [Erle et al., 1995 and Wagner et al., 2002].
An overview of the differences in the observed SCD caused by the cloud is given in Table 4-A, the observed increase of NO_2 and O_3 dSCD is discussed in chapter 8.3.I.

	NO_2 [10^{16}]	O_3 [10^{18}]	H_2O [10^{23}]	O_4 [10^{43}]
Zenith	7.00 ± 0.05		1.31 ± 0.1	5.04 ± 0.1
Zenith (UV)	11.5 ± 1.2	8.70 ± 0.4		
Nadir	6.30 ± 0.1		1.31 ± 0.1	4.4 ± 0.2
Nadir (UV)	9.40 ± 3	8.00 ± 0.8		
Z4 (+2°)	6.20 ± 0.2		1.39 ± 0.1	4.7 ± 0.1

Table 4-A: Overview on the differential slant columns caused by light path enhancement. The data are in molec/cm^2 except for O_4 which is in molec^2/cm^5.

4.5.II.b Retrieval of the Light Path Enhancements

Based on the observed increase in the column densities (Figure 4-25) we will estimate the light path inside the cloud. First we will discuss the necessary mathematical basis and start to estimate the light path inside the clouds afterwards.
The approximation of the cloud parameters will be done in three steps. The simplest approximation of using an average scattering altitude gives a first guess of the quantities we are interested in. In a second step, a more detailed discussion of the cloud, we will use a set of different cloud bottom and cloud top heights and reduce the number of possible solutions. Finally we will use two trace gases O_4 and H_2O to find a most possible approximation of the real conditions in the cloud. The approximated light path will be used to retrieve the average NO_2 mixing ratio inside the cloud in chapter 7.3.
Based on the assumption that the concentration of some of the observed gases is known the rapid increase can be used to approximate the average length of the light path in the cloud.

For the concentration profiles we referred to standard literature profiles [Thomas and Stammes, 1999 and references therein (AFGL-TR-86-0110, tropical)].

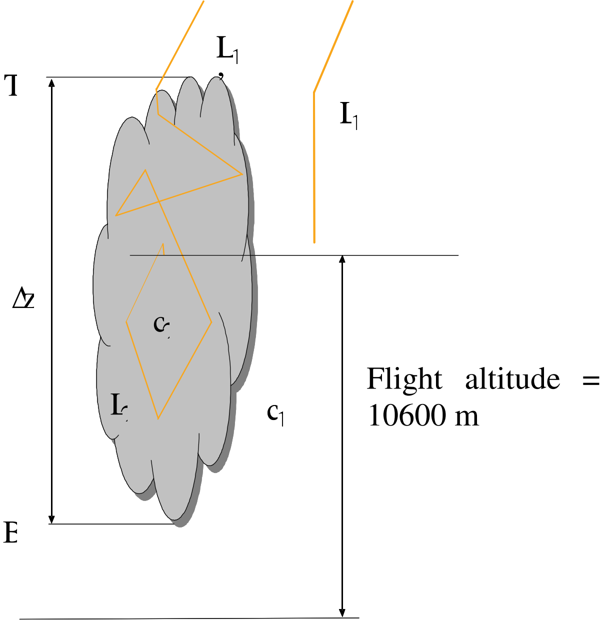

Figure 4-26: Sketch of the cloud and simplified light path inside. The clouds altitude can be assumed to be around 10600 m. The cloud extends over an altitude range Δz from the cloud bottom height (B) to the cloud top height (T).

In Figure 4-26 the most relevant parameters of the cloud for the later analysis are introduced. Outside of the cloud the concentration c_1 is observed, resulting in a slant column density:

$$S_1 = \int_{L_1} c_1(l) \cdot dl \tag{4.22}$$

The slant column inside the cloud is mainly given by:

$$S_{cloud} = \int_{L_2} c_2(l) \cdot dl \tag{4.23}$$

The light path L_2 inside the cloud is longer due to multiple scattering and the concentration c_2 inside the cloud might be different. The observed signal however is still influenced by the light path L'$_1$ outside e.g. above the cloud by stratospheric absorbers:

$$S_2 = \int_{L_2} c_2(l) \cdot dl + \int_{L'_1} c_1(l) \cdot dl$$

For the approximation: $L_1 \approx L'_1$ the observed dSCD is given by the concentration in the cloud and the respective light path.

$$dS = S_2 - S_1 \approx \int_{L_2} c_2(l) \cdot dl \tag{4.24}$$

For the moment we assume the concentration profile c to be the same inside and outside of the cloud. For O_4 this is no restriction, whereas for NO_2 and O_3 this is probably wrong. The NO_2 will be discussed later on when the light path is approximately known.

We assume the average light path per altitude interval in the cloud to be independent of the altitude: $r(z) = r = \frac{\Delta l}{\Delta z} = const$. The introduced ratio r(z) is comparable to a Box AMF for boxes inside the cloud. The real distribution is not known and very variable depending on the cloud parameters [Funk, 2000]. As soon as some more information about the cloud is available it can be used to estimate the length of the light path more accurately. Formula (4.24) can be written as:

$$\begin{aligned} dS &= \int_L c(l) \cdot dl \\ &= \int_B^T c(z) \cdot r \cdot dz \\ &= r \cdot \int_B^T c(z) \cdot dz \end{aligned} \tag{4.25}$$

with r as defined above. If <L> stands for the average light path in the cloud and Δz is the cloud thickness, the formula can be written as:

$$dS = < L > \cdot \frac{1}{\Delta z} \cdot \int_B^T c(z) dz \tag{4.26}$$

If c(z) is known, this can be used to approximate the average light path. To get a first approximation of the average scattering altitude and length of the light path this formula is written in a linear form:

$$dS = < L > \cdot \frac{1}{\Delta z} \cdot \int_B^T c(z) \cdot dz = < L > \cdot < c > \tag{4.27}$$

where $< c > = \frac{1}{\Delta z} \cdot \int_B^T c(z) \cdot dz$ is the average concentration in the cloud.

Due to first term analysis for all altitude intervals [B, T] one altitude z_{av} exists with: $c(z_{av}) = < c > \; and \; z_{av} \in [B,T]$ this z_{av} is referred to as average scattering altitude.

A first approximation of the scattering altitude and the light path enhancement can be retrieved by: $< L > = \frac{dS}{c(z_{av})}$, as shown in Figure 4-27. Here the observed O_4 dSCD is divided by the square of the O_2 concentration for several altitudes. A short example is best suited to explain the viewgraph: According to Table 4-A the O_4 dSCD in the zenith equalled $5.04 * 10^{43}$ molec^2/cm^5. The concentration of O_2 in the tropics in 9 km altitude is $2.05 * 10^{18}$ molec/cm^3. The light path inside the cloud for 9 km average scattering altitude would be 120 km.

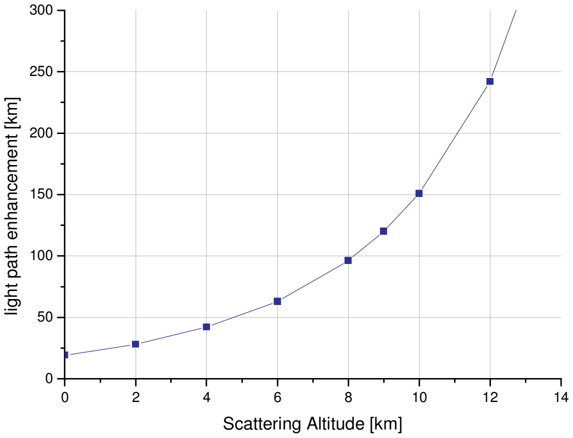

Figure 4-27: Light path enhancements for different average scattering altitudes based on the observed O_4 dSCD.

To get an estimate on the light path enhancement and the scattering altitude from Figure 4-27 additional information is crucial. For example we can assume a realistic light path enhancement is of the order of 130 km ± 40 km [Erle et al. 1995], so the average scattering altitude is between 8 and 10 km. This of course depends strongly on the individual clouds is only given as an example to demonstrate the various quantities.
To retrieve more accurate information we will focus on certain altitude intervals, defined by the cloud base height and cloud top height. Based on the observed dSCD for O_4 the average light path in the cloud can be calculated for a set of the cloud base height (B) and cloud top height (T). In addition the cloud top is known to be above 10600 m, therefore we assume a minimum of 11000 m. Also the maximum cloud base is known to be below the flight altitude hence we use 10000 m as maximum.

The ratio light path to cloud thickness $R = \frac{<L>}{\Delta z}$ (similar to AMF_{cloud}) can be used as criterion whether the retrieved light path in the cloud is reasonable or not. According to private communication with Thomas Scholl (April 2005), this ratio depends on the cloud optical thickness and it is of the order of 10 to 20. In Table 4-B possible solutions for the equitation (4.4) are listed. Here both realistic and non realistic results are shown and marked by different colours.

B – T [km]	10 – 14	8 – 14	7 – 14	6 – 14	4 – 14	2 – 14
<L> Zenith [km]	235	177	154	134	101	76.6
<L> Z4 (+2°) [km]	218	165	144	125	94.3	71.4
<L> Nadir [km]	204	155	135	117	88.3	66.8
R= <L>/Δz	54.72	27.65	20.6	12.09	9.46	5.97

Table 4-B: Example of different light path enhancements for the assumed parameters B (cloud base) and T (cloud top). The realistic values are marked in red, the less realistic values are written in black.

B – T [km]	6 – 16	6 – 15	6 – 14	5 – 14	6 – 13	5 – 13	6 – 12	5 – 11
<L> Zenith [km]	157	145	134	116	123	107	113.2	90.7
<L> Z4 (+2°) [km]	147	135	125	107	115	100	105	84.6
<L> Nadir [km]	137	117	117	102	107	93.7	98.4	79.2
R= <L>/Δz	14.71	15.1	15.66	12.09	16.44	12.55	17.57	14.13

Table 4-C: Most realistic values of the light path enhancements inside the cloud.

In Table 4-C some possible solution in the studied range of cloud altitude and cloud thickness are shown. The range for the cloud top height is between 11 and 16 km and is limited by the Tropopause height (~16 km). In contrast to this, the cloud base altitude seems to between 4 and 7 km – no solution was found with 8 km bottom altitude. The light path in the cloud strongly depends on the altitudes assumed for the cloud bottom and cloud top and varies between 80 km and 170 km, the extremes are not shown in Table 4-C.

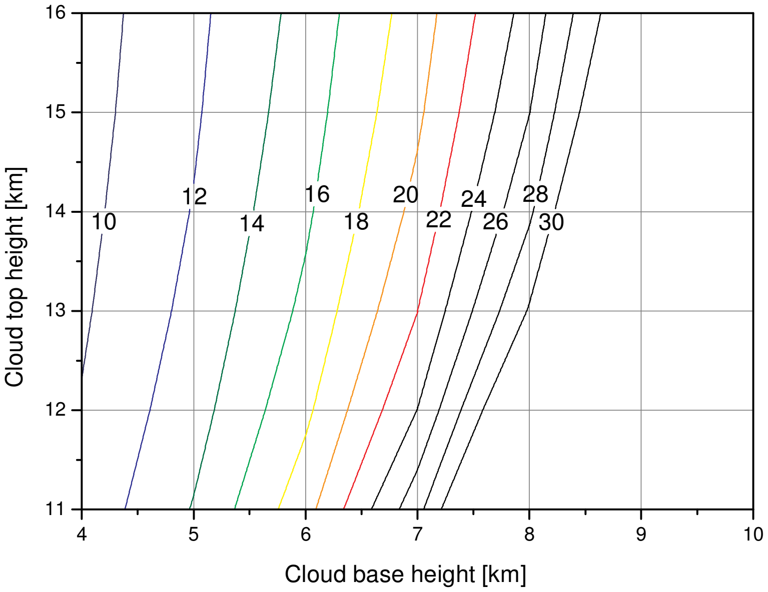

Figure 4-28: Contour plot of the ratio R=<L>/Δz. The cloud base height (abscissa) and cloud top height (ordinate) define the cloud thickness (Δz). The light path is given by the observed dSCD and the integrated O_4 concentration. It only depends on the cloud base height and the cloud top height.

The range of possible solutions is shown in Figure 4-28. The light path was calculated for several cloud base heights and cloud top heights. Each of these pairs belongs to a certain light path and a cloud thickness, e.g. for a cloud base height of 7.2 km and a cloud top height of 16 km the cloud thickness is obviously 8.8 km The ratio shown in Figure 4-28 is 20, therefore the light path equals $< L > = R \cdot \Delta z = 176\ km$.

There is still a large variety of possible solutions, so a second trace gas with a known profile might be useful to reduce the number of possible solutions. As NO_2 and O_3 are strongly influenced by convective transport from the boundary layer or inflow of stratospheric air masses, these two trace gases are not useful here. In the cloud water vapour might be used; the relative humidity in the cloud can be approximated by 100 %.

The light path inside the cloud should be the same for both O_4 and H_2O and of course the criterion ($10 \le R \le 20$) mentioned above is still valid. So we calculate the light path based on the water vapour as we did for O_4 and compare these two light paths. In Figure 4-29 the difference between the calculated light paths for O_4 and H_2O is shown as a function of cloud base height and cloud top height. The difference between the two equals zero for the real light path and cloud parameters. The area where both light paths agree within 15 km is marked in green. The expected light path is about 150 km long and considering an error of 10 % leads to an interval of ± 15 km. According to the discussion above the ratio between light path and cloud thickness is expected to be in between 10 and 20, the area is marked as hatched.

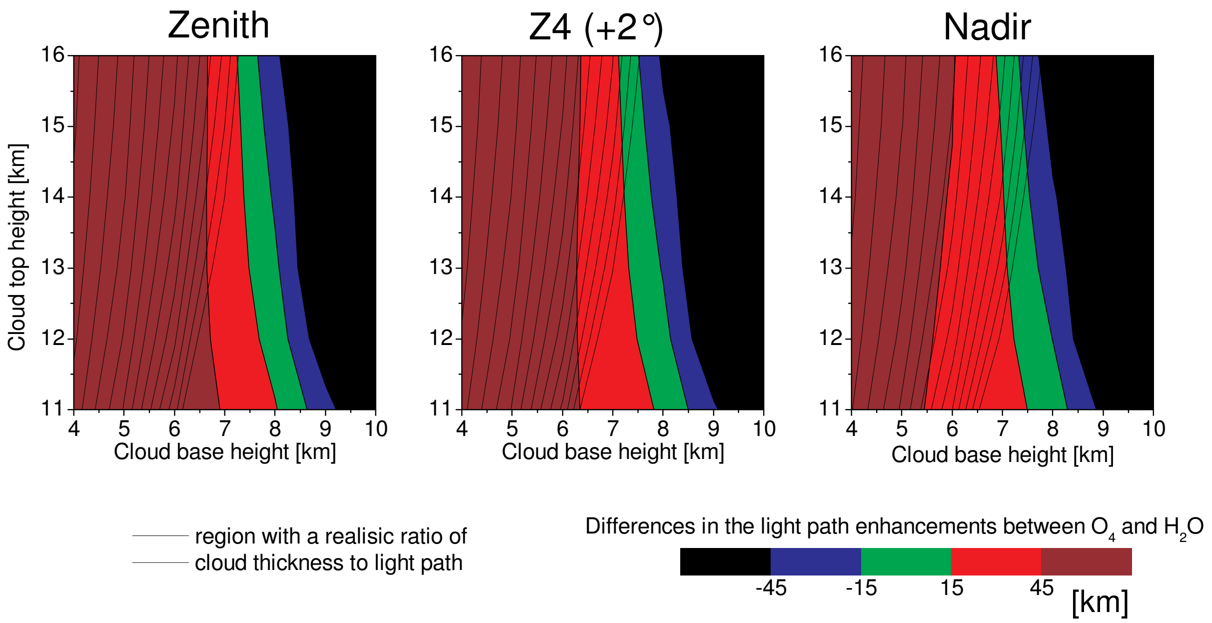

Figure 4-29: Difference between the light path inside the cloud calculated via O_4 and H_2O concentration. The agreement is marked by the green area – the difference is less than 15 km. The hatched area indicates the ratio R=<L>/Δz between 9 and 21 (Figure 4-28).

By studying Figure 4-29 the best solution can be found for both realistic ratios of path length to cloud thickness and similar path lengths for O_4 and H_2O. It is given by a cloud base height of 7.2 km and a cloud top height of 16 km. The light path equals 190 km for the zenith viewing direction, 178 km for Z4 (+2°) and about 167 km for the nadir.

With a ratio between light path and cloud thickness of 20 this solution is close to the limit, however the analysed cloud top height of 16 km seems to be reasonable compared to the cloud top height observed by the OLEX (Figure 4-24) for the neighbouring clouds.

Extrapolating Figure 4-29 by eye the reader might think of further solutions with a smaller ratio and a good agreement between the light paths based on O_4 and H_2O. This might well be possible and we cannot exclude it. But a cloud top altitude of 16 km is already close to the tropopause and to extend the analysis into this region is rather tricky and might easily cause some errors.

4.5.III Retrieval of a varying Aerosol Extinction Profile around Milano

The principle influence of aerosols on the sensitivity of the instrument was discussed in section 4.4.V. To estimate the aerosol profile based on real measurement, is the focus of the following section. Based on the different sensitivity of the individual lines of sight the aerosol extinction profiles are retrieved for eight selected positions including the reference. Using a simulated O_4 SCD of the reference location, the SCDs for the other locations can be calculated by adding the measured dSCD to the simulated reference. These SCDs can then be compared to modelled simulation. By the comparison of the eight measurement points and all lines of sight the aerosol parameters can be estimated.

The presented method can be applied to other data sets as well. However, it was only used for this single flight on 16/08/2002 (Chapter 8.1) due to the enormous efforts necessary to retrieve the aerosol extinction. Moreover it depends on many parameters of the selected flight.

4.5.III.a Observed Data

From the spectral analysis only differential slant columns are retrieved (chapter 3.2). In chapter 8.1 the HCHO and NO_2 results are used to estimate the local mixing ratios and the formaldehyde flux. The observed O_4-dSCDs as a function of the position are shown in Figure 4-30.

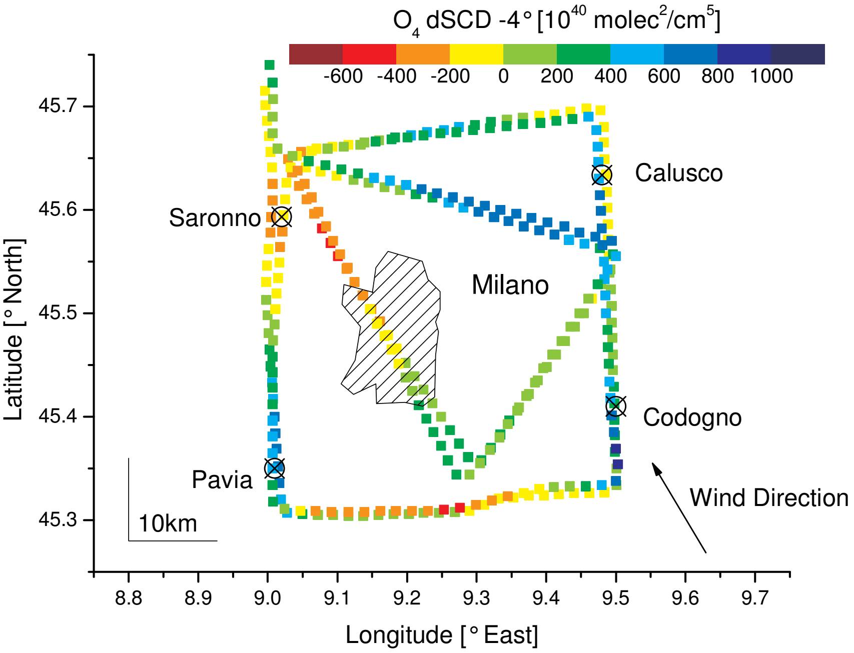

Figure 4-30: O_4 dSCD along the flight. North west of the town strong O_4 absorptions are observed, indicating a high aerosol extinction. In the south and the east lower absorption indicate lower aerosol extinctions.

Lower O_4 values indicate higher aerosol load, therefore a reverse colour bar is used to map rather the aerosol extinction than the O_4 values. The highest aerosol content is observed north-west (lee) of the town, whereas in the southern and eastern legs of the flight low values are observed. The analysis results of O_4 as function of time are shown in Figure 4-31. The result for NO_2 and HCHO are presented and discussed in chapter 8.1.

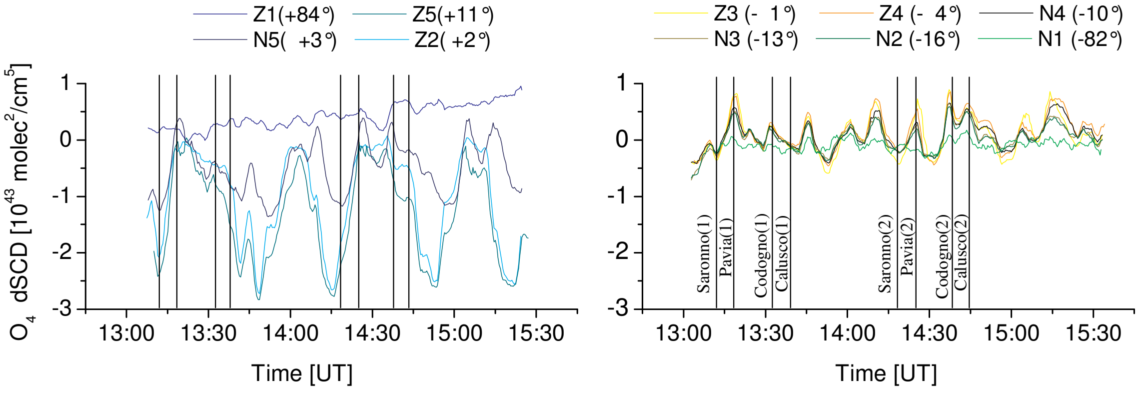

Figure 4-31: Right panel: O_4 dSCDs observed by the upward looking telescopes, including the times of the overpasses.
Left panel: O_4 dSCDs observed by the telescopes directed downwards, the overpasses are marked, for the labels refer to the right panel.
In the data for +3° and +11° rapid decreases are observed between Calusco and Saronno, during these periods the aeroplane headed west and the mentioned telescopes were directed towards south east, with a small relative azimuth angle.

Four locations (Figure 4-30) were chosen for a detailed investigation of the aerosol and later on the HCHO VCD is studied in detail at theses places (chapter 8.1.I.a): Saronno (45.61°N / 9.02°E), Pavia (45.36°N / 9.0°E), Codogno (45.4°N / 9.5°E) and Calusco (45.64°N / 9.48°E). All the locations were over-flown twice with more than 1 hour time difference. Therefore they have to be regarded as eight independent points. From now on they will be referred to as measurements points, neglecting the measurements performed along the way for the moment. Pavia (1st overpass), which is situated in the South-west of Milano, was taken as reference location. As the reference used in the DOAS analysis was not exactly taken from Pavia but from a region close by, the dSCDs from Pavia were subtracted.

For the simulation of the AMF it is important that we chose measurement points with a similar relative solar azimuth angle. As can be seen in Figure 4-31 (right panel) in the lines of sight N5 (+3°) and Z5 (+11°) very low O_4 dSCDs ($-2.4*10^{42}$ molec^2/cm^5) were observed during the periods when the plane headed west. During these periods these two telescopes had relative solar azimuth angle of 0° ± 5°. For the future analysis it is important to stress out that a similar effect is not observed in the downward directed telescopes, although the flight leg between Pavia and Codogno these telescopes also had a small relative azimuth angle. Tracy can in principle simulate this effect a quantitative result is difficult here (section 4.4.IV). The relative solar azimuth angles in the measurement stations were about 280° (=-80°) for Saronno and Pavia and 70° for Codogno and Calusco relative to the backward looking telescope. The influence of small changes in the relative azimuth angle is small (Figure 4-11). Nevertheless for the detailed simulation in the measurement points it has to be considered.

Below the flight altitude (1100 m) no clouds were observed. However, some clouds developed close to the flight altitude over the mountains edge between Lecco and Como (45.8° North) and in the south over the Apennines. High above the flight altitude some thin cirrus clouds were observed, which were neglected in the actual analysis, although a slight influence cannot be excluded.

4.5.III.b Retrieval of the Aerosol Extinction

For the retrieval of the aerosol load four layers were used in the lowest 2000 m. As the sensitivity is highest close to the flight altitude, we used the following boxes: 0 – 600 m, 600 – 1000 m, 1000 – 1400 m and 1400 – 2000 m. Above 2 km a standard lattice with box heights between 1 km and 5 km depending on the altitude is used. The top of atmosphere in the model was set to 100 km in total 48 discrete layers were used. The aerosol extinction above the lowest four boxes was not changed throughout the simulation. It decreased exponentially with altitude and vanishes above 20 km.

The O_4 profile is well known and depends on the temperature and pressure only [Greenblatt et al., 1990]. We assume that the observed changes in the dSCDs were caused by changes in the aerosol extinction profile. This approach is well established to retrieve aerosol profile information from ground based MAX-DOAS measurements [e.g.Wagner et al. 2002, Hönninger et al., 2004, Wagner et al., 2004].

The measured dSCD are divided by the vertical column density to retrieve differential air mass factors:

$$dA_{loc,i}^{mes} = \frac{dS_{loc,i}^{mes}}{V} = \frac{S_{loc,i} - S_{ref,i}}{V} \tag{4.29}$$

where loc stands for the location and ref for the reference (i.e. Pavia) and i numbers the lines of sight. Based on the temperature and pressure data in Bresso and the midlatitude summer standard atmosphere [Thomas and Stammes, 1999] we calculated the total vertical column density of O_4: VCD(O_4) = $1.22*10^{43}$ molec^2/cm^5.

In the simulation the air mass factors for the reference and the measurement locations are simulated, the changes in the relative azimuth and the SZA are taken into account. The aim of this step is to minimize the following function,

$$\begin{aligned} F_i &= \left| dA_{loc,i}^{mes} - (A_{loc,i} - A_{ref,i}) \right| \\ &= \left| dA_{loc,i}^{mes} + A_{ref,i} - A_{loc,i} \right| \end{aligned} \qquad (4.30)$$

for all the lines of sight i, and the seven remaining locations loc by changing the aerosol extinction profiles. Actually we added the simulated AMF of the reference $A_{ref,i}^{sim}$ (Figure 4-32 lower left panel) first and retrieved an AMF ($A_{loc}^{mes} = dA_{loc} + A_{ref}^{sim}$) which is compared to the simulated AMF for the same location (Figure 4-32). Depending on the location between 2 and 8 sets of O_4-AMFs were simulated. In total about 40 sets were taken into account – not included the sensitivity studies presented in section 4.4.

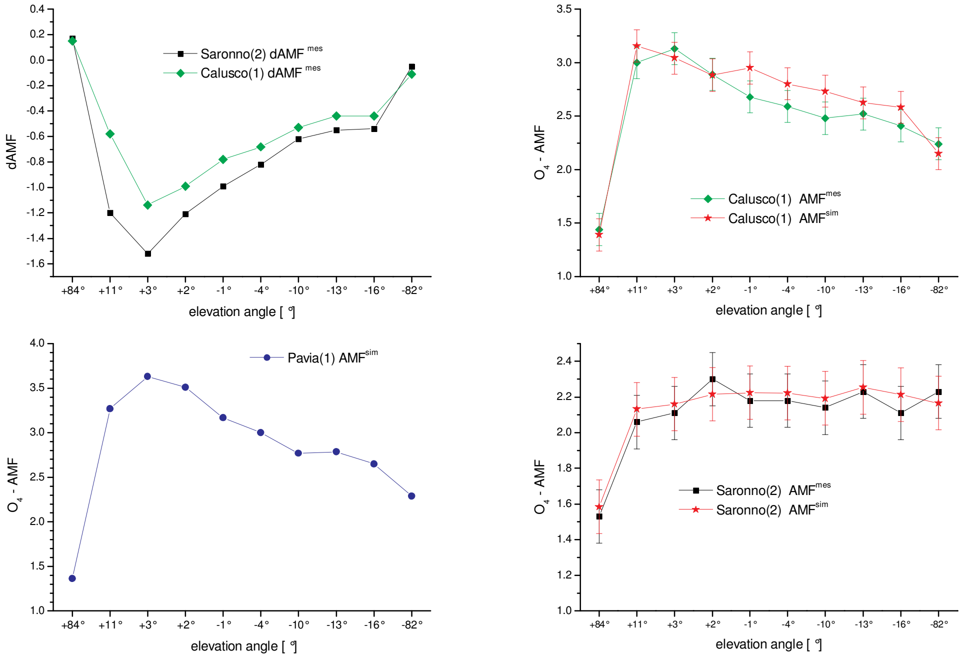

Figure 4-32 Left up: dAMF for all ten telescopes for two measurement locations: Calusco(1) and Saronno(2), left down: simulated AMF for Pavia.
Right: After the simulated AMF for the reference was added to the observed dAMFs (green and black squares) these AMFs are compared to simulated (red-star) AMFs for the same locations. The assumed profiles are shown in Figure 4-33. The situation in Codogno is illustrated in Figure 4-34.

It is obvious that several combinations of AMF for the reference and one measurement location might solve this problem. Therefore some a priori information is included. The visibility is used as indicator to estimate the maximum aerosol extinction. The minimum visibility necessary for a flight under visual flight rules is 5 km, this can be attributed to an extinction coefficient of 0.8 km^{-1}. The reader has to keep in mind this holds for the visible wavelength region (580 nm), in the UV (360 nm) the same aerosol load causes an extinction of coefficient of about 1.5 km^{-1} (section 4.2.IV.b).

For three measurement points, the aerosol profiles retrieved by this analysis are shown in Figure 4-33. The other aerosol profiles are not shown for clearness of the viewgraph. For the first overpass of Saronno the extinction coefficients are also in the range of 1.5 km^{-1} and for most other location they vary between the values retrieved for Calusco(1) and Pavia(1), i.e. about 0.4 km^{-1} to 0.6 km^{-1}.

In Saronno the profile decreases slightly with the altitude up to the mixing layer height and rapidly afterwards. This is in good agreement with our observations, that the visibility increased enormously when the plane reached the edge of the mixing layer (see also chapter 8.2.II). In the less polluted areas the aerosol extinction profiles decrease almost linear with altitude.

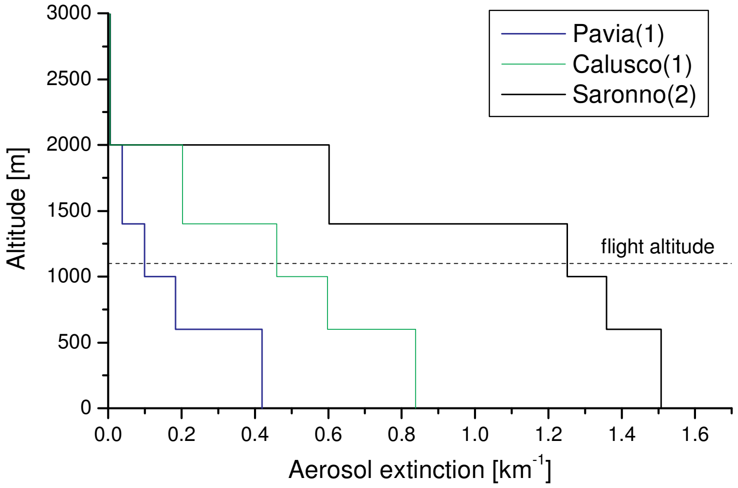

Figure 4-33: Aerosol extinction (360 nm) profile for two locations (Saronno and Calusco) and the reference (Pavia). The dotted line indicates the flight altitude; most of the aerosol seems to be situated below the aeroplane as expected when we assume the flight altitude to be close to the top of the mixing layer.

The AMF for 10 lines of sight in 7 locations and the reference were simulated and a reasonable agreement was observed between the measurements and the simulation. Slight variations in the aerosol load cannot be excluded but they will cause no significant changes in the Box AMF. The influence of changes in the aerosol extinction profile is illustrated in Figure 4-34. Here for the position of Codogno (2nd overpass) three different profiles are shown together with the respective O_4-AMFs. The AMF of all ten lines of sight will be enhanced, if the aerosol extinction is reduced (black and blue line). If more aerosols are assumed to be above the aeroplane, the AMF for the upward directed telescopes will decrease. The assumed changes in the aerosol profiles are rather small, compared to the influence on the different lines of sight.

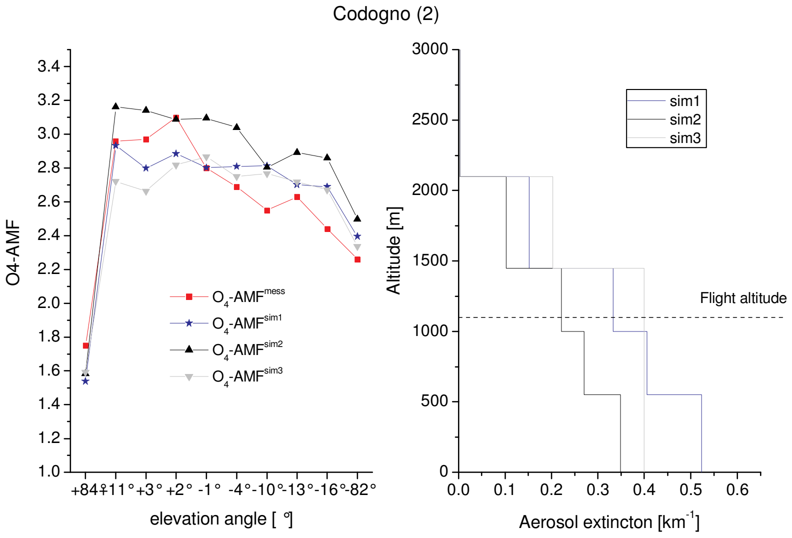

Figure 4-34: O_4-AMF (left) for three different aerosol extinction profiles (right). If a lower aerosol profile is assumed, the simulated O_4-AMF will be bit too high (black line). If the extinction close to the flight altitude is too high, the AMF for the upward directed telescope will decrease (grey line). The blue lines fits best to the measurement and the assumed background.

4.5.III.c Comparison to other Data

The aerosol extinction profile can be compared to in situ measurements performed by Wolfgang Junkermann [Junkermann, 2005] in his microlight on the same day. Due to restrictions of the VFR-airspace around Milano no particle measurements are available in the interesting area. Only over the mountains edge the microlight was allowed to climb to altitudes above 2000 ft. In the mountains the mixing layer height follows the terrain to a certain degree hence we expect it to be higher in this region compared to Milano. So a direct comparison is not useful especially when the large spatial variations are considered.

Nevertheless the aerosol measurement is shown in Figure 4-35 for two different sizes of aerosols. These data were observed close to the mountains, between Como and Alzate (see map Figure 6-6). The profile has a strong maximum in 800 m altitude and decreases slightly up to 1600 m. Afterwards it decreases rapidly and nearly no particles are observed at altitudes higher than 1900 m.

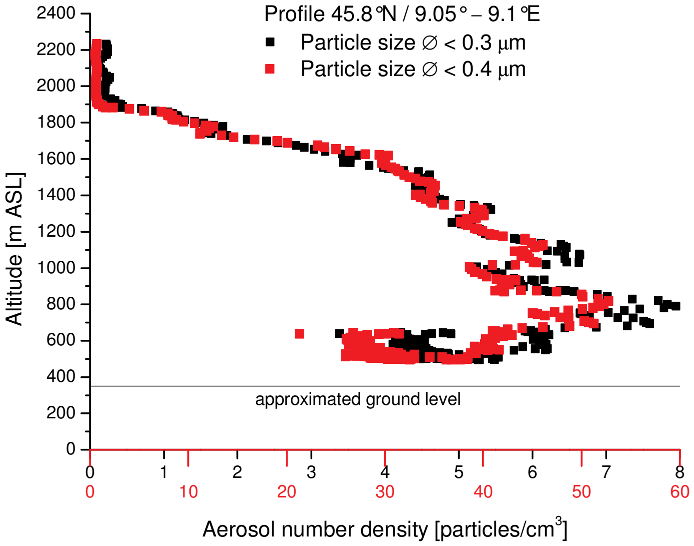

Figure 4-35: Aerosol profiles measured by Wolfgang Junkermann on 16/09/2002 close to the mountains north of Milano (private communication, file date: 24/09/2004). In red the number density of particles with a diameter smaller than 0.4 µm are shown. In black only the fraction with a diameter smaller than 0.3 µm is given. The ground level in this area is between 300 and 400 m ASL, hence below 500 m no measurements were performed.

Besides the principle difficulty of a comparison some common patterns are observed: The decrease with altitude seems to be similar to our findings in Saronno and the mixing layer height was retrieved correctly in the used discretisation. The strong maximum observed in the in situ measurements might be a local effect.

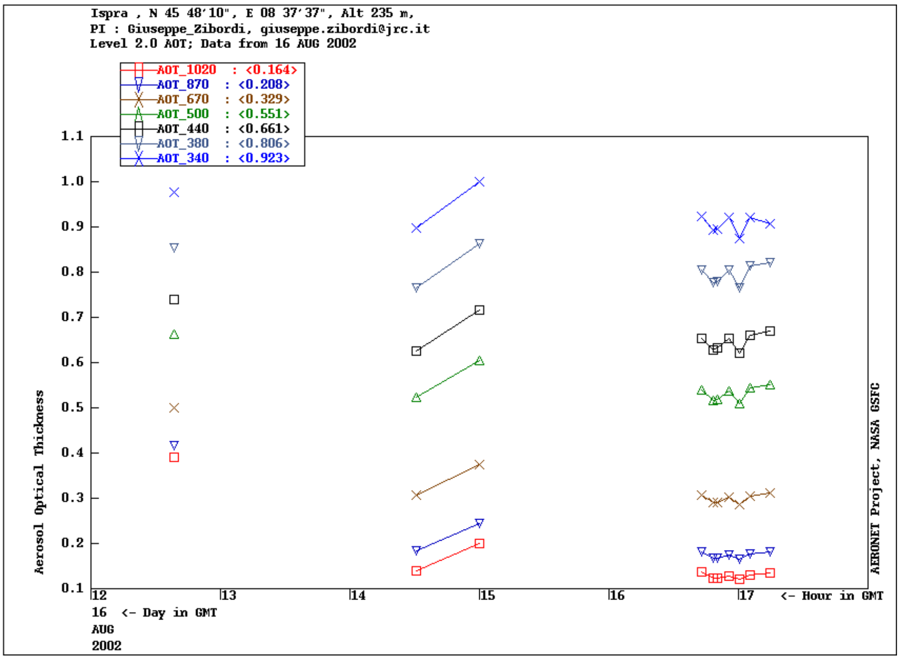

Figure 4-36: Aerosol Optical Thickness in Ispra (~ 80 km north-west of Milano). In the UV wavelength range (380 nm) the AOT is close to 1.

In addition we can substantiate the retrieved aerosol extinction profile by comparison with the AERONET data of this day in Ispra (Zibordi, http://aeronet.gsfc.nasa.gov, 03/03/05). Although Ispra is far-away from Milano (80 km north-west) in the foot hills of the Alps, the AERONET data give us the order of magnitude of the vertical aerosol extinction (Figure 4-36). In the interesting wavelength range 340 nm to 380 nm the aerosol optical thickness is only little less than 1.

The vertical aerosol extinction along the flight around Milano varies between 0.5 in Pavia (1) and 2.6 in Saronno (1 & 2) outside the highly polluted regions the vertical extinction is about 1. We cannot expect the aerosol load in the highly polluted areas around Saronno to agree with the observation in Ispra. In the regions with moderate aerosol extinction (Calusco) they agree quite well.

5 Description of the Instrument

The Airborne Multi AXis DOAS instrument was designed to observe air masses above and below the aeroplane under different elevation angles (up to 10 can be realised). Scattered sunlight in the wavelength range from 320 nm to 560 nm is observed by two different spectrometers optimised for either the UV or the visible wavelength range. The first one was optimised for the UV region covering the interval from 320 nm to 440 nm. The other spectrometer was built for the visible region (400 nm to 560 nm).

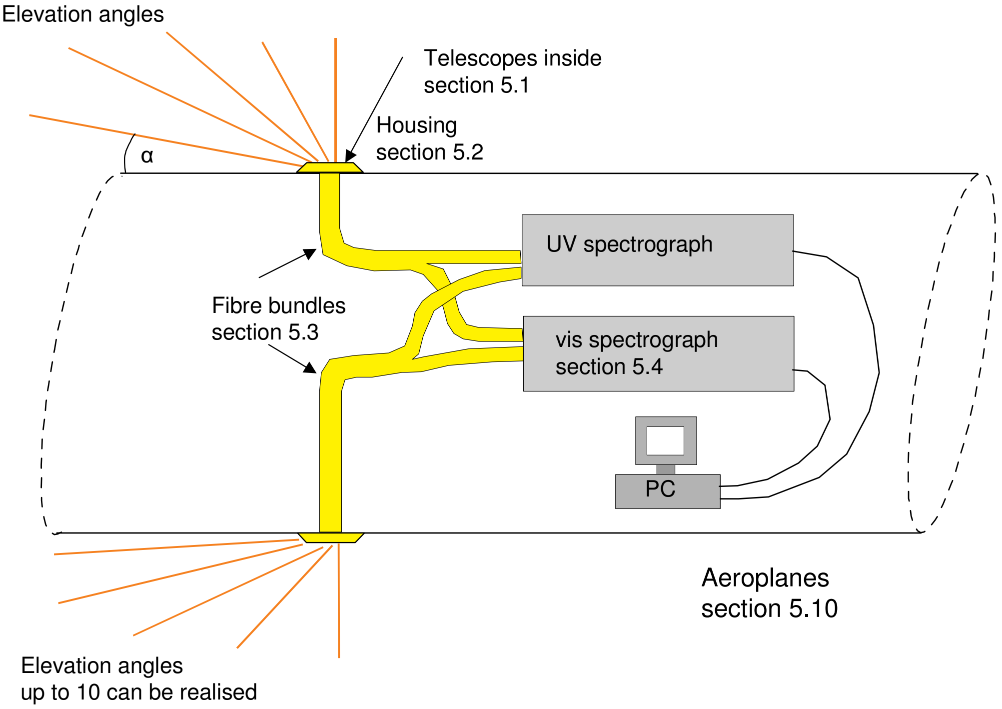

Figure 5-1: Overview of the instrumental set-up. Ten pairs of telescopes are installed in small housings outside the aeroplane. Quartz fibres lead the light to spectrographs, where it is analysed and detected by a CCD camera [Wagner et al., 2001 a].

An overview of the AMAXDOAS instrument is shown in Figure 5-1. The sunlight scattered in the atmosphere or reflected on the ground is observed by 2 x 10 telescopes (section 5.1). These telescopes are mounted in small housings (section 5.2) outside the aeroplane. Bundles of quartz fibres (section 5.3) guide the light to either the UV or the vis spectrograph (section 5.4), where it is spectrally analysed and detected by a CCD camera (section 5.5). The CCD cameras detect the light from all viewing directions simultaneously. The images taken by the CCD cameras are added during the integration time and are saved afterwards by a PC (section 5.6) for later analysis (chapter 3.3).

It should be pointed out, that not only the spectrographs and the CCD cameras exist for both wavelength regions but almost the complete set-up exist in a double version beginning from the telescopes, finishing with the PCs.

The total signal per line of sight on the detector depends on the intensity and on the number of fibres used per telescope. For the flight in high altitudes only few lines of sight can be realised, due to the weak signal in zenith and nadir compared to the signal of the elevated lines of sight. In Table 5-A (p 77) a detailed list of the elevation angles is given.

In the following I will describe the single parts of the instrument following the way of the light starting with the telescopes until it reaches the detector. Finally the signal is saved on the PC. After the description of the AMAXDOAS instrument itself, the used aeroplanes and the installation of the instrument is described. Later on some suggestions for the future of airborne DOAS instrument are given. Finally the SCIAMACHY instrument on the ENVISAT satellite is described briefly as one of the main scopes of the AMAXDOAS instrument was the validation of this instrument.

5.1 The Telescopes

The telescopes are 121 mm long and have a diameter of 19 mm, the lenses inside the telescopes are made of quartz glass and have focal length f of 42 mm at 330 nm. The distance between the fibres and the lens equals the focal length of the lenses. The aperture α of the telescopes is hence ideally given by the diameter d of the fibre bundles and the focal length f of the lens:

$$\tan\frac{\alpha}{2}=\frac{d}{2\cdot f} \tag{5.1}$$

Here d is 0.4 mm and f equals 42 mm resulting in an aperture of 0.54°, as can be seen in Figure 5-2. The long telescope tube does not limit the aperture but reduces additional stray light. The lenses and the distance to the fibres were chosen in a way that the aperture of the fibres is optimally used to observe a maximum input of light.

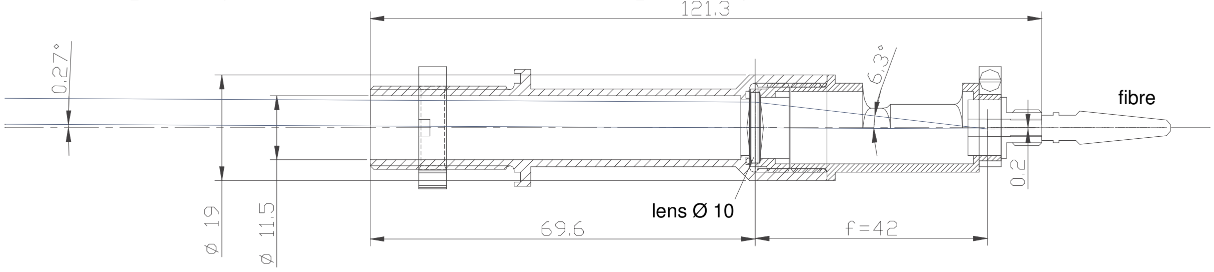

Figure 5-2: Sketch of the telescope including the fibre. The diameter of the fibre bundle is 0.4 mm. The aperture of the telescope is 0.27°.

As already mentioned the complete AMAXDOAS instrument consists of two combined systems, one for the UV and one for the vis region. Two telescopes (UV and vis) are used as one pair, directed in the same viewing direction and connected by two aluminium bridges. This system was chosen for several reasons, compared to the alternative of using only one telescope.

As can be seen the aperture is linearly proportional to the diameter of the fibres. Therefore combining the fibres of the ultra-violet and the visible region in one telescope would results in a larger aperture. To keep the aperture small would mean to use larger telescopes. However due to the restrictions of the aviation authorities this was impossible.

Using a couple of telescopes allows separating the fibres of UV and visible light completely. Compared to one bundle being split at the end the construction of two similar bundles is easier and therefore cheaper.

In case of direct sunlight entering the telescopes the instruments have to be protected from possible damage caused by the intensive radiation. Therefore a shutter technique was invented that automatically closes the affected telescopes, while all the others remain open and a restricted measurement is still possible. The shutter mechanic was installed between the two telescopes as shown in Figure 5-3:

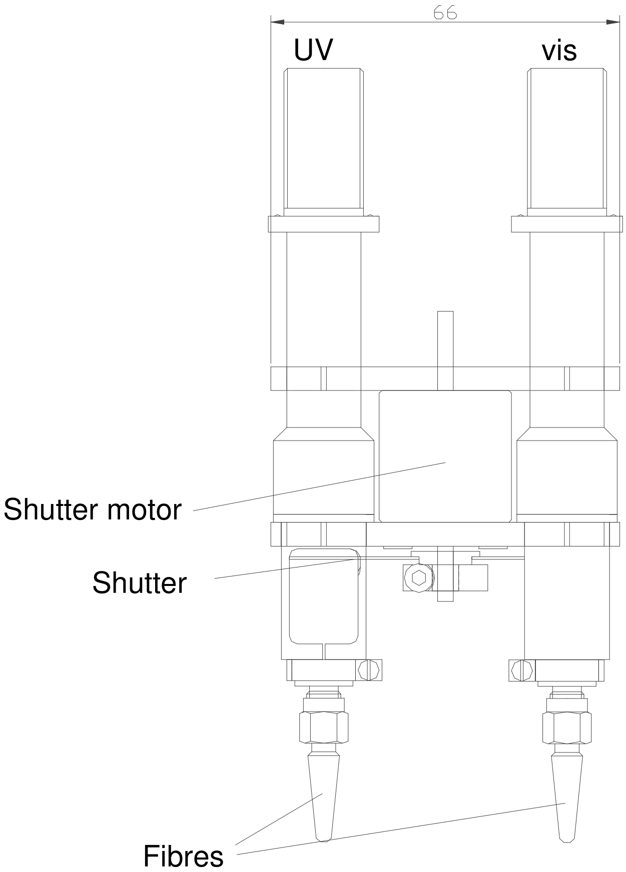

Figure 5-3: One pair of telescopes. Between the two telescopes a small motor is installed for closing the shutters in case of direct sunlight, the shutter can be turned by 90°.

Small photo sensors, installed in the housing parallel to the telescopes, will notice all cases of direct sunlight. In Figure 5-4 they are not visible for most of the telescopes, only in zenith it can be seen. They are built of photodiodes and connected to a controlling unit inside the aeroplane, which closes the shutters within a second. For security the total aperture of the sensors (~5°) is much larger compared to the telescopes.

During the SCIAVALUE campaigns (chapter 6.1) direct sunlight was observed for several times. In most cases the zenith telescopes were shut when flying close to the equator. But also in the polar region some cases were observed when the Falcon headed south towards the sun here mostly the telescopes elevated by -2° closed. In the FORMAT campaigns (chapter 6.3, 6.4) no such case was observed. As the workshop of the institute must not be asked to build small series of ten or more equal parts, the telescopes were built by the company IML[1] south of Heidelberg.

Due to the pressure difference between the plane's interior and the atmosphere outside, every part had to be tested whether it resists the resulting forces. If parts of the instrument broke during flight, this would cause large damage and a rapid loss of pressure inside the aeroplane. For the ceiling of the housings this was no problem, here the experiences of our workshop and of the DLR flight department was enough, but no one had any experiences with 2 mm thin quartz lenses. Hence a test was necessary, the pressure difference was assumed to be 1000 hPa in the maximum, which is a rough approximation including a security factor of 1.5. The resulting force on the lens of 1 cm diameter is given by $F = \Delta P \cdot \pi \cdot r^2 = 7.85\ N$. A corresponding mass of $F / g < m = 1\ kg$ was put upon the lens inside the telescope and it did not break.

---

[1] IML Instrumenta Mechanik Labor GmbH, Grosser Stadtacker 2, 69168 Wiesloch.

5.2 The Telescope Housings

Before going back to the fibres and following the way of the information, a small paragraph about the housing of the telescopes is added. While the telescopes have to be outside the aeroplane, the rest of the instrument is inside. The quartz-fibres and electrical cables connect the telescopes with the rest of the instrument.

Two sets of housings were built during the AMAXDOAS project. The first set was built for the SCIAVALUE campaigns and to optimize the viewing geometry a second one was built for the second FORMAT campaign. For the first FORMAT campaign the housings existing for SCIAVALUE were used and turned in the way suited best for this campaign.

To find the optimal setup for the different lines of sight a theoretical study was performed [Bruns et al., 2004 and Bruns, 2004]. For AMAXDOAS measurements at 10000 m altitude the best lines of sight to retrieve profile information are given by the following angles (relative to the horizon):-90° (nadir), -8°, -5°, -2°, +2°, +5°, +8°, +90° (zenith). Two backward looking lines at ±5° were added to these 8 lines of sight. The backward directed telescopes are tilted relative to the flight direction, otherwise it would be directed to the empennage (Figure 5-5). The standard pitch angle[2] of the aeroplane (4° for the Falcon) has to be considered during the construction of the telescope housings. The AMAXDOAS was once used with this original set-up, but it turned that the intensity was too low for reasonable integration time. So the set-up used for the Falcon campaigns consists of four telescopes only (Table 5-A).

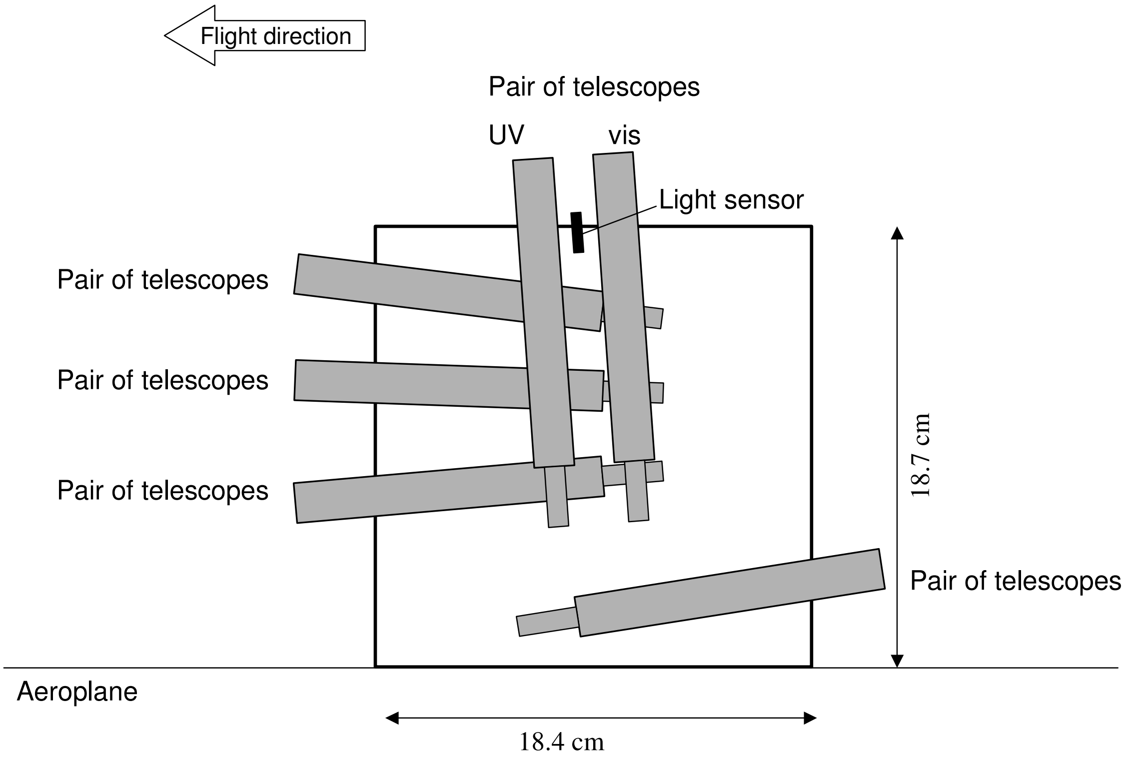

Figure 5-4: Side view of the telescopes housing. In the zenith both telescopes (UV, vis) are shown, while for the other elevation angles in this perspective only one telescope is visible. Between the telescopes the sensor for the shutters is mounted in the housing (shown for zenith only). The angle relative to the housings are enlarged to demonstrate why the lowest forward telescope has to be tilted relative to the flight direction.

A sketch of the upper housing of the SCIAVALUE campaigns (chapter 6.1) is shown in Figure 5-4 and in Figure 5-5. The housings are 187 mm high and the inner diameter was 184 mm. Compared to the length of the telescopes (~ 118 mm including the plug of the fibre)

---

[2] Definition of the pitch angle is given in the list of abbreviations.

the housings are rather small, especially as the fibres bending radius has to be considered. The bending radius of the fibres equals 400 times the diameter of the fibre's core. In our case this results in a radius of 6 cm.

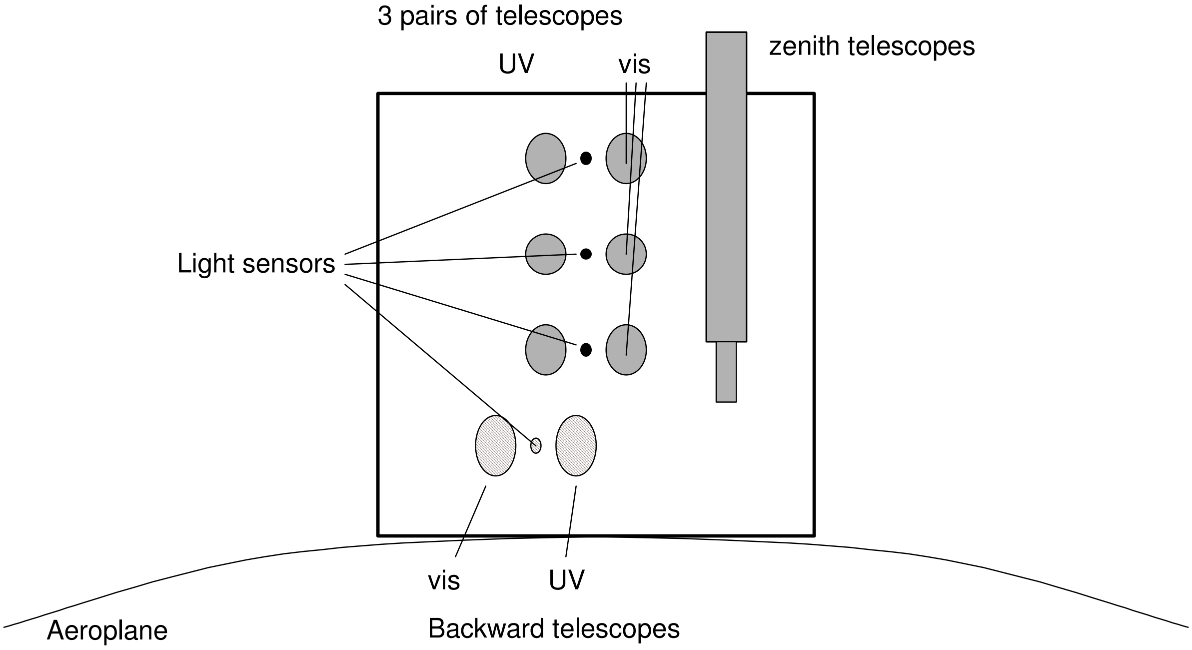

Figure 5-5: Front view of the telescope housing. The telescopes are tilted relative to the flight direction, to avoid looking to the empennage or to the hull, therefore they are not centred in the figure.

As the AMAXDOAS was built to fly in high altitudes (~35000 ft[3]), a heating was installed inside the housings (not shown in Figure 5-4). The heating is based on the principle of a hairdryer, a small ventilator ventilates hot air. As ventilator an old unused CPU cooler was used and two heating elements, 2*2 cm² and 50 W, heat up the air in front of the cooler. This heating system worked fine in the mid latitudes and the Tropics, in the Artic however it was not always sufficient to deice the telescopes. For future instruments this system might be improved by directly ventilating the optics. The realised elevation angle for the individual measurement campaigns is shown in Table 5-A:

measurement campaign	**number of lines of sight**	**elevation angles**	**fibres**
SCIAVALUE I, II and EUPLEX	4	+90°, f +2°, f -2°, -90°	former test Figure 5-9 left
FORMAT I	10	b+84°, f+11°, f+3°, b+2°, b-1°, b-4°, b-10°, b-13°, b-16°, f-82°	CO 5+5 Figure 5-9 centre
FORMAT II	10	+90°, f+7°, b+7°, f-7°, b-7°, f-15°, b-15°, f-30°, b-30°, -90°	CO 7+3 Figure 5-9 right

Table 5-A: For the individual campaigns different geometrical setups are used. In this table an overview of the realised elevation angles is given. The angles are relative to the horizon and the letter f or b indicates whether the telescope is directed forward or backward.

---

[3] 1 ft = 0.30479 m. Usually the approximation is used: Altitude in feet *3/10 = Altitude in meters.

5.3 The Fibres

The fibres are made of quartz to minimize the extinction in the UV wavelength region. The diameter of the fibre equals 150 µm for the core, 165 µm for core plus cladding and 180 µm including the coating as well. The number of fibres used per telescope depends on the elevation angle and the measurement campaign (Table 5-A).

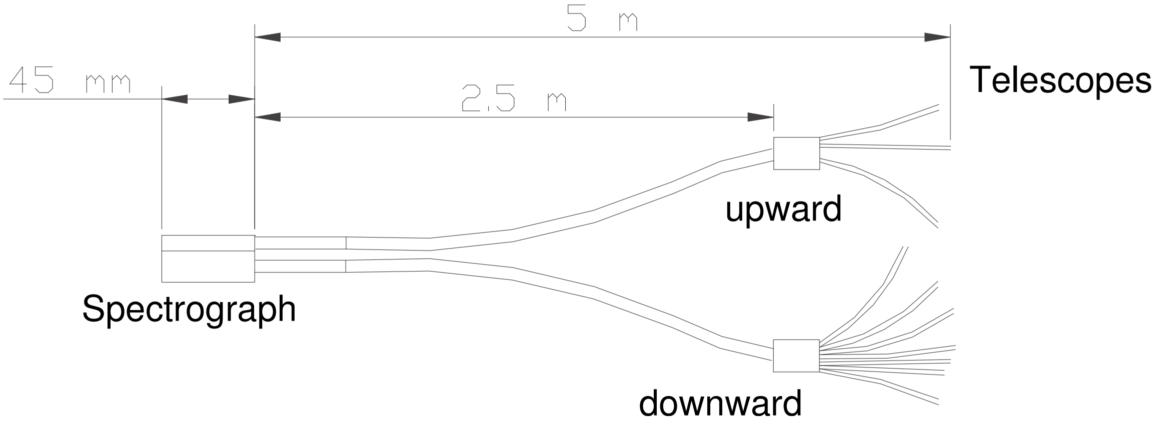

Figure 5-6: Sketch of one fibre bundle (here the one used for FORMAT II). The bundle consists of an upward and a downward part. They can be separated at the spectrographs end. Each part splits up according to the number of telescopes used in the upper or lower housing (here 3 above and 7 below).

For the AMAXDOAS different fibre bundles exist but they are all designed in a similar way (Figure 5-6). Towards the telescope a standard SMA-plug (diameter 3.17 mm) is used. The diameter of the fibre bundle itself depends on the number of fibres, due the tolerances of the production the minimum diameter is 0.4 mm (Figure 5-7).

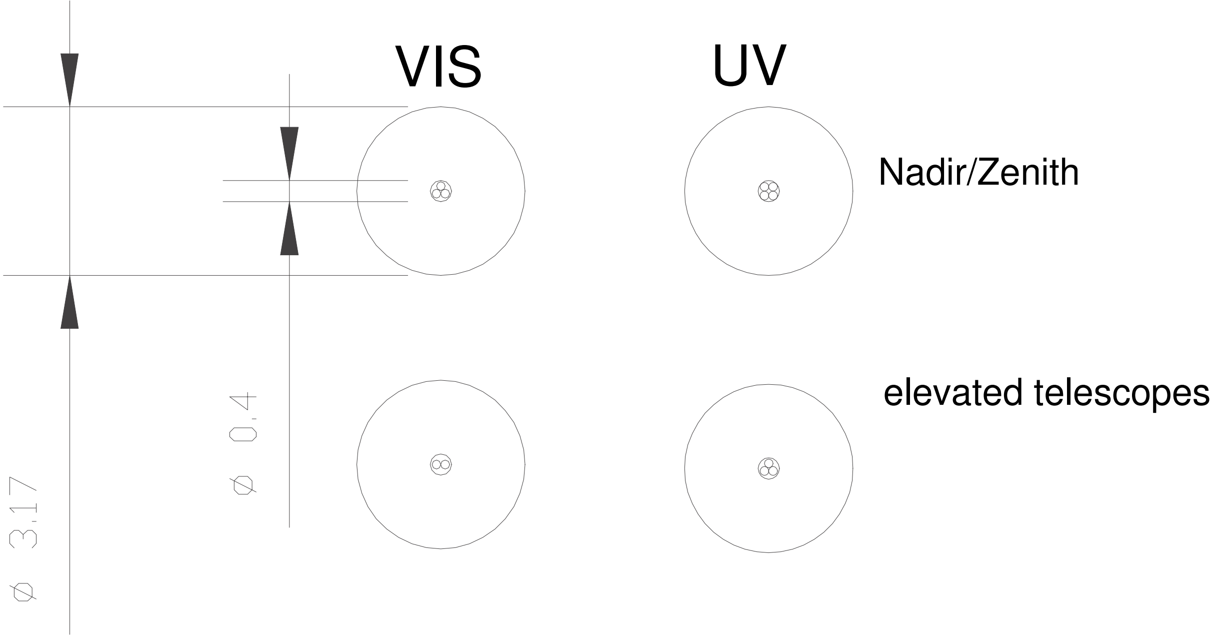

Figure 5-7: View on the fibres at the telescopes end (here FORMAT I or II). For nadir and zenith more fibres are used as they were observed to be rather dark, compared to the elevated lines of sight.

A rectangular plug was used towards the spectrometer, which can be divided in two parts (Figure 5-8). This was a great challenge for the engineers of the fibre optic companies. However, it is necessary as the fibres have to be fixed to the telescopes in advance before the housing was installed on the aeroplane. The ensemble of electrical cables and optical fibres was lead inside the aeroplane through the ceiling or the bottom of the aeroplane and the housing was installed outside of the aeroplane.

At the spectrometers end, the fibres should be as close together as possible, if they belonged to the same viewing direction and they should be as good as possible separated, if they do not. For this reasons the coating was removed towards the spectrograph's end. So the distance was reduced to 165 µm between the centres of two fibres. If the fibres do not belong to the same line of sight, two additional dead fibres, without coating and cladding, will separate them (Figure 5-8 and Figure 5-9).

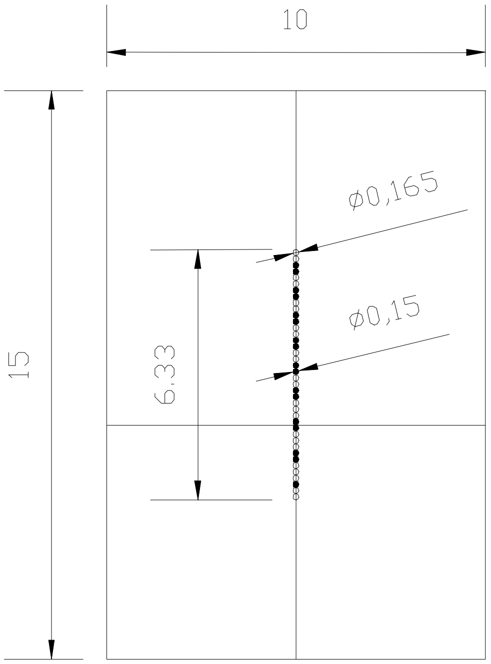

Figure 5-8: Plan of the socket for the spectrograph's end. The total socket has the dimensions of 10*15 mm. The black line close to the centre indicates where the socket can be divided. Here the bundle for the FORMAT II campaign is shown: seven lines belong to downward looking telescopes and three to upward directed ones. The fibres extend over 6.33 mm, so the total CCD-chip is used.

At the beginning of the AMAXDOAS project 2000 m of quartz fibres with the numerical aperture of N.A. = 0.11[4] had to be bought, because this was the minimum the company (Loptek[5] Berlin) offered for such special cases. The numerical aperture is defined as sine of the acceptance angle γ: $N.A. = \sin(\gamma)$. The acceptance angle of the fibre hence equals: $\gamma = 6.3°$ as shown in Figure 5-2, this special numerical aperture was used because it fits best to the aperture of the telescopes' lenses, where $\gamma_{telescope} = 6.68°$. The spectrograph's aperture $F/\# = 1:4 \Rightarrow \gamma_{spectrograph} = 0.5 \cdot \arctan(F/\#) = 7°$ also fits very well to the fibres and the telescopes (details on the spectrograph refer to 5.4). The different quantities for the individual parts are listed in

	Lenses	Fibres	Spectrograph
Half aperture α/2	6.68	6.3	7
Numerical aperture	0.12	0.11	0.125
F/#	10:42	Not defined	1:4

Table 5-B: Aperture (acceptance angle) of different parts of the optical system.

The fibres' acceptance angle is the smallest aperture in this system, to minimise the stray light in the spectrograph.

---

[4] The aperture of different optical components is given in different quantities, i.e. the aperture angle, the numerical aperture or F number. Here the quantities used by the various companies are given.

[5] Loptek Glasfasertechnik GmbH & Co.KG, Oberlandstrasse 13 – 14, 12099 Berlin.

Within the last years several bundles of fibres were built:

a) One test bundle “test” using only two viewing directions with 20 fibres per viewing direction.
b) One bundle with ten viewing directions, five directions for above and five for below, produced by Loptek “Lo 5+5”.
c) One bundle with ten viewing directions, five directions for above and five for below, produced by Ceram Optec[6] “CO 5+5”.
d) One bundle with ten viewing directions, seven directions for below and three directions for above (Figure 5-6), produced by Ceram Optec “CO 7+3”.

The fibres’ configuration of individual bundles used in the different measurement campaigns are shown in Figure 5-9.

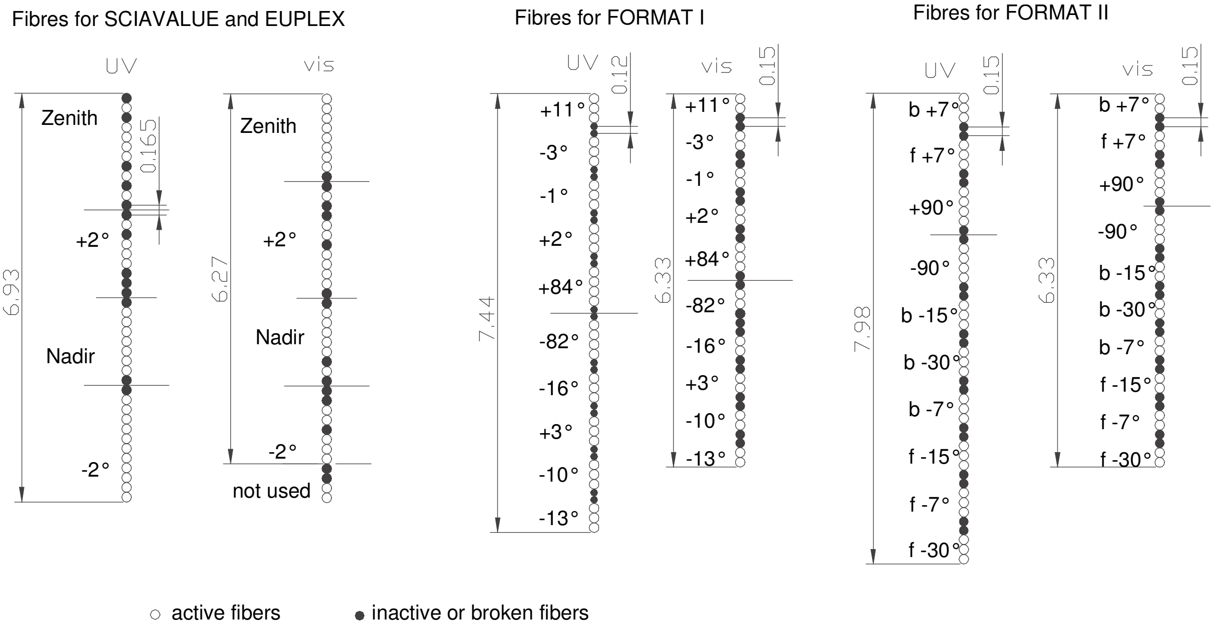

Figure 5-9: Fibre bundles used in the individual campaigns by the UV and the vis instrument. The bundle used in the SCIAVALUE and EUPLEX campaign (left) was made of the former test bundle and had some broken fibres in between. The separation between the different telescopes is therefore marked by additional lines. The fibres for the first FORMAT campaign (centre) and for the second FORMAT campaign (right) consisted of ten different lines of sight, separated by two dark fibres each.

In the test bundle many fibres were broken. Later it was transformed to a four viewing directions bundle, which was used in the SCIAVALUE campaigns (Figure 5-9 left). The broken fibres were used as separator of the different lines of sight, so the plug at the instruments end did not have to be changed.

The first bundle with ten viewing directions “Lo 5+5” was used for the above mentioned test with ten lines of sight on board of the Falcon. Unfortunately it was of poor quality, because it was one of the first constructions of this type ever built. Many fibres broke and repairing such a bundle is as expansive as buying a new one – as long as the fibres are still available.

The bundle “CO 5+5” was used in the FORMAT I campaign in August 2002 (Figure 5-9 centre).

The last bundle “CO 7+3” was especially built for the improved design of the instrument used in the FORMAT II campaign in September 2003 (Figure 5-9 right).

As each bundle is about 7 m long (only the last one CO 7+3 was shorter) and consists of one part for the UV and one for vis, by the end of 2003 all the 2000 m bought at the beginning were consumed for the instrument.

---

[6] Ceram Optec GmbH company of biolitec group, Siemensstrasse 44, 53121 Bonn.

5.4 *The Spectrometer*

The spectrometer has to fulfil some special characteristics as all lines of sight are imaged on the same CCD array and read out simultaneously. The most important characteristic is the imaging quality. This does not only mean that the light of different lines of sight must only be detected in the corresponding area of the detector, but also the spectral resolution of different lines of sight must be comparable. Only with such a spectrograph, it is possible to use a CCD camera and to detect several lines of sight simultaneously. The Acton 300i was found to suit best for our applications, because it has the required imaging quality and is small enough to be used inside an aeroplane.
The Acton 300i is a Czerny-Turner type spectrometer [Czerny and Turner, 1930] with a focal length of 300 mm and the aperture is given by $F/\# = 1:4$. This fits quite well to the aperture of the fibres and the telescopes (section 5.3).

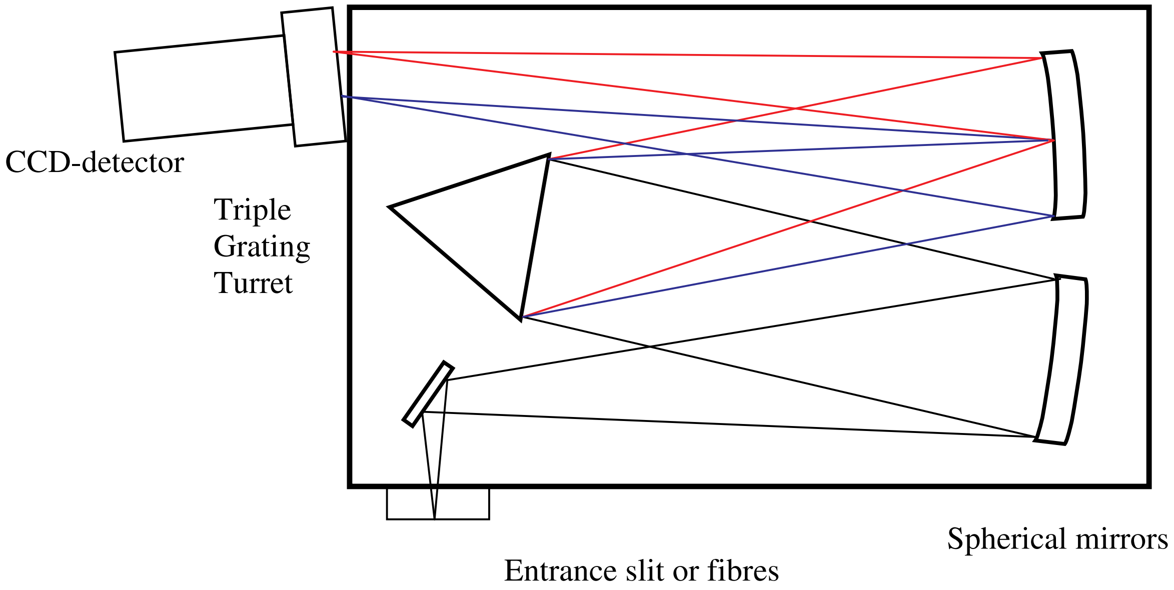

Figure 5-10: Schematic of the spectrograph (adapted from Acton product information, www.actonresearch.com (March, 2005)).

A schematic of the spectrograph is shown in Figure 5-10. The principle of a Czerny-Turner spectrograph is illustrated as well but will not be discussed in detail here. The detector is tilted relative to the spectrograph. The imaging quality of the spectrograph will be best, if the detector is tilted by about 15°. The images of each line of sight have a small and constant width, but the spectral resolution changes with the wavelength. The resolution will be constant, if the detector is not tilted at all. In this case the imaging quality is too poor to distinguish between the individual lines of sight. As a compromise between constant resolution and good imaging quality the detector was tilted by about 8°. So the imaging quality is good in the central area of the CCD-chip (Figure 5-12). In the same region the slit function is rather constant. As the resolution depends on the complete system it will be discussed below (section 5.5.II.a).
The Acton 300i spectrographs are provided with a grating turret which allows choosing the optimal grating (out of three) for the current application. Besides, the turret can be turned to optimise the spectral range. During the campaigns the gratings must not be turned and therefore the power supply for the gratings was turned off, so the spectra are comparable from one flight to another.

The dispersion of the spectrographs, i.e. the relation of the wavelength to the position on the detector, $d\lambda/dx$ is mainly given by the number of lines per millimetre of the grating, g:

$$\frac{d\lambda}{dx} = \frac{1}{f \cdot m \cdot g} \tag{5.2}$$

where f is the focal length and m, the order of diffraction, equals 1. The focal length of the spectrometer equals 300 mm, our grating consists of 500 lines/mm, hence the dispersion equals 6.6 nm/mm. The maximum resolution of the spectrometer is given by the dispersion multiplied by the size of the smallest unit (pixel) on the detector. The pixel size of the detector is 13.5 µm, this leads to 0.89 nm/pixels. The resolution of the complete system is dominated by the width of the entrance slit.

The gratings are optimised for a certain wavelength, it is called blaze wavelength. Here the highest intensity compared to the incoming intensity is detected. An overview of the characteristics of the used instrument is given in Table 5-D (p 89).

Optical instruments of high precision always have to be kept at constant temperature, because the thermal expansion of the different materials inside otherwise causes an error in the later analysis. To keep the spectrometers at constant temperature a heating with 50 W (conventional heating slide from Conrad electronics) was fixed on the walls to stabilise the temperature at 39° C. The temperature was measured automatically and a small thermostat controlled the power supply for the heating slide. In addition the temperature was read out via an AD-converter and stored on the computer as well. A temperature curve is shown in Figure 5-11. It was measured during the flight on 19/02/2003 from Oberpaffenhofen via Basel to Tuzeur (chapter 6.1.III and 7.1.I). Due to the resolution of the AD-converter no measurements are possible until the temperature reaches 35° C. The gradient of the curve can be used to approximate the heating rate to 7.5° C/h. If the temperature of the spectrograph is 23° C at the beginning, it will take about 2 hours until the temperature reaches 39° C and up to 1 hour until it is stable (± 0.1° C). On board the aeroplane the spectrometers were surrounded by special isolation foam (Wulfmeyer[7], Material gem. DAN1247-01) and surrounded by a metal box.

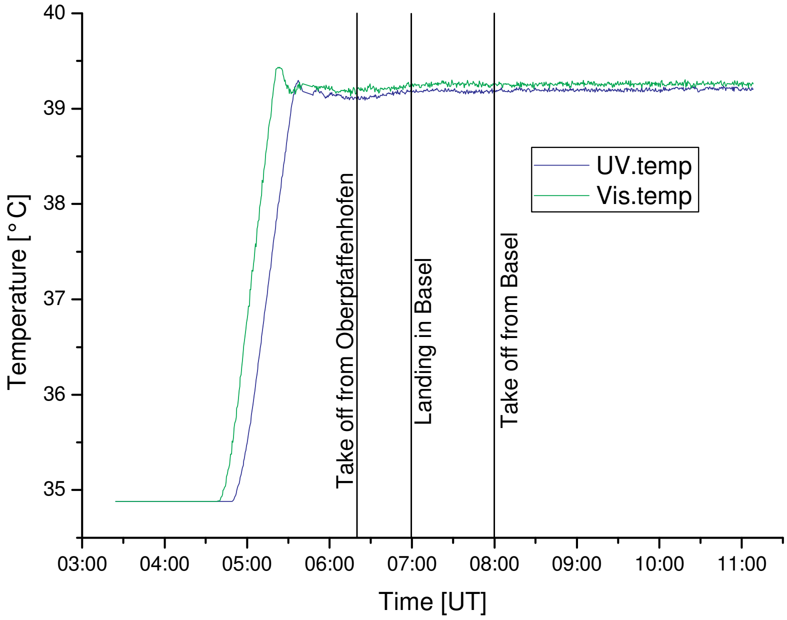

Figure 5-11: Temperature of the spectrographs during the flight on 19/02/2003. At the beginning the heating rate is constant 7.5° C/h.

---

[7] Rudolf Wulfmeyer Aircraft interior GmbH & Co.KG, Frankenring 15, 30935 Langenhagen.

A spectrometer of this type was already used for similar applications like the MAX-DOAS on the research vessel "Polarstern" [Boßmeyer, 2002]. Here the unfortunate experience was made that a so-called cross evaluation is not possible. The cross evaluation is the idea of using one reference from the zenith with only little tropospheric absorption for the analysis of all the other lines of sight with high tropospheric absorptions. Such evaluations have been made before with scanning MAX-DOAS instruments [Hönninger et al., 2004]. It turned out that the optical properties (slit function and dispersion) of the different lines of sight are too different in the used set-up. The instrument used on board the Polarstern in Winter 2001/2002 was very similar to our AMAXDOAS instrument.

5.5 The CCD-detector

One idea of the AMAXDOAS is to measure different lines of sight simultaneously. Therefore a 2D-CCD camera with 2048 x 512 pixels was used as detector and the different lines of sight were imaged to different areas on the CCD chip. Figure 5-12 shows an example image of the vis-CCD taken in the FORMAT II campaign in September 2003.

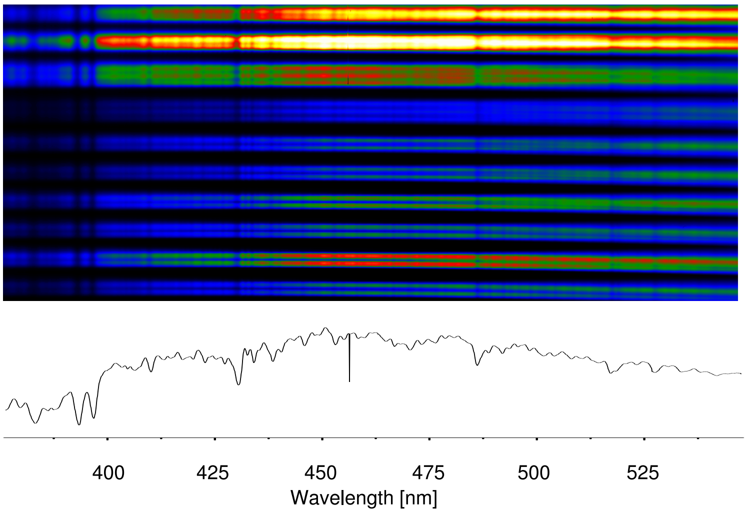

Figure 5-12: Picture of the CCD camera taken during a flight in the FORMAT II campaign. From the top to the bottom ten lines can be identified belonging to the ten telescopes. The spectrum shown below corresponds to the zenith viewing direction (3rd from top). There is a bad pixel at about 466 nm at pixel 962.

This picture shows the ten different lines of sight imaged on different areas. The number of fibres used per different LOS can clearly be identified (3 for Zenith and Nadir and 2 for the other ones). In addition, the bad pixel at the position 962 (466 nm) can be made out in the spectrum. Another typical characteristic of the instruments can be realised: The different lines of sight observe different intensities. There is no permanent intensity difference for the different lines of sight. It strongly depends on the flight altitude, the ground albedo and the relative solar angles (flight direction).

5.5.I Principle of CCD Cameras

A Charge Couple Device (CCD) consists of an array of picture elements (in our case 2048 x 512 pixels), which convert the incident light into an electronic signal. The principle here is the same as for a digital camera, the main difference is the way the data are read and digitized. Before we concentrate on reading the signal the principle of detecting the light will be explained.

Each pixel is made of four layers (Figure 5-13), one metal, one isolator (SiO_2), one P- and one N-doped silicon layer. Together they are usually called a MOS (Metal Oxides Silicon) capacitor.

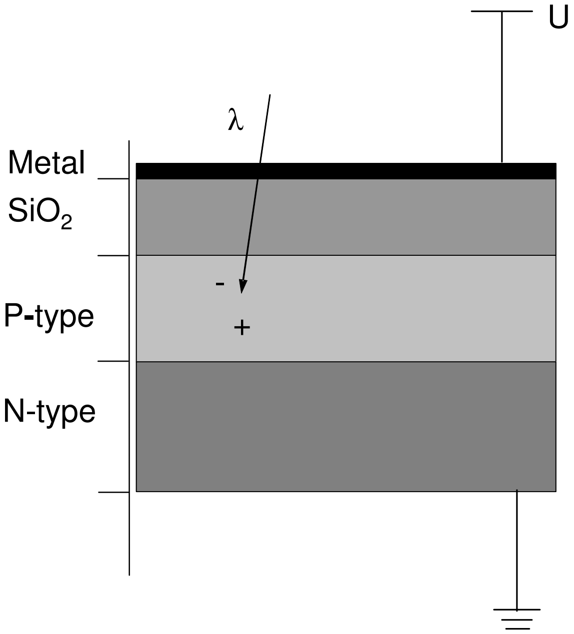

Figure 5-13: Cross section of a CCD-pixel. The incoming light produces an electron (-) and a hole (+). The hole is refilled by the electrons in the N-type while the electron remains in the P-type until the readout procedure.

A positive voltage between the N-layer and the metal produces a potential well for electrons in the P-layer. The photoelectrical effect leads to the creation of electron-hole-pair. Holes and electrons are separated by the potential well. The holes are refilled with electrons from the N-doped silicon, whereas the electrons are stored in the potential well, until they are read out. The number of electrons per time interval is given by the flux of the incident light and the quantum efficiency of the CCD-chip.

The quantum efficiency depends on the type of the CCD and the wavelength. As shown in Figure 5-14 the quantum efficiency is normally better in the visible range than in the UV. To improve the efficiency in the UV special techniques like fluorescent coatings or back illuminated (BU) CCDs are used.

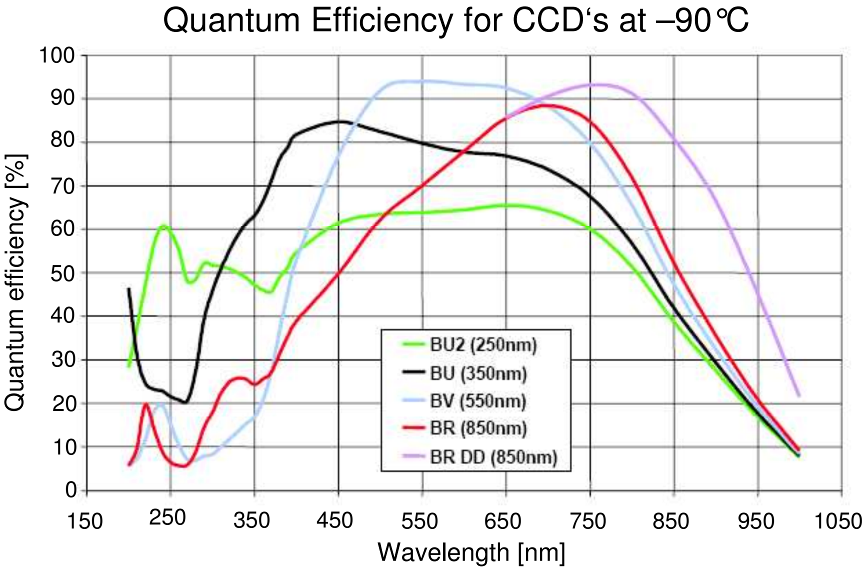

Figure 5-14: Quantum efficiency for different types of CCD cameras produced by Andor technology. The vis camera is of the type BU (350 nm) (www.lot-oriel.com, 10/10/2005).

For different CCD-types provided by Andor[8] technology the quantum efficiency as function of the wavelength is shown in Figure 5-14. For measurements in the wavelength region 400 nm to 500 nm the type BU (black line) is best, as the quantum efficiency is both relative high and constant. This type of camera was used for the AMAXDOAS vis instrument.
In addition some electron-hole-pairs are created by thermal excitation. These electrons are later read out together with the signal. This additional signal is called dark current and gives an additional offset to the signal which has to be subtracted. To reduce this effect the CCD of the vis instrument is cooled down to -30° C – for the UV instrument it was -40° C. For our instrument the dark current is of the order of 0.01 counts per pixel and second (Figure 5-20 p 89).
The maximum capacity of the MOS capacitor is called full well capacity. It is defined by the maximum number of electrons stored by each pixel. The full well capacity depends on the type of the CCD chip and the pixel size. It equals 80000 electrons per pixel for our instrument.

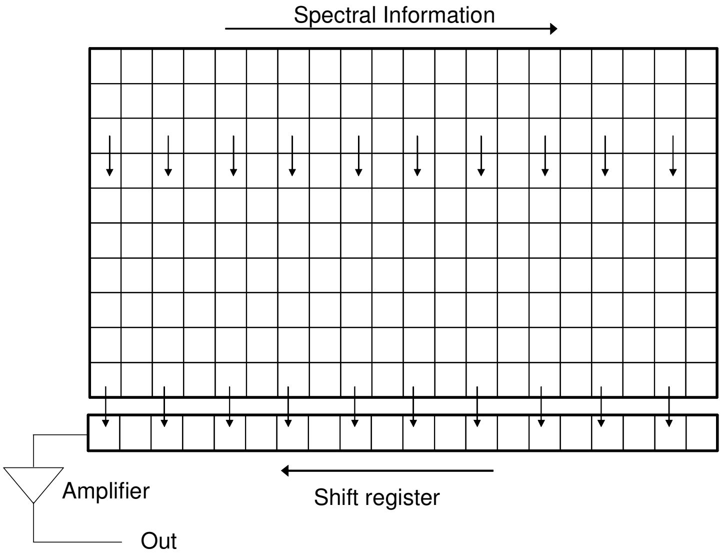

Figure 5-15: Drawing of the readout procedure. The first line is shifted to the shift register and the others move up. The shift register is read out via an amplifier and digitised for the later analysis.

In Figure 5-15 the principle of the readout procedure is shown. A series of electrodes, installed parallel to the lines, covers the CCD array. The stored charges are moved along the columns by “clocking” the electrodes (www.lot-oriel.com, 10/10/2005). In Figure 5-16 this process is shown schematically. All signals are moved simultaneously. The lowest line is transferred into the shift register and all the other lines above move down one line. The pixels in the shift register are read out one by one. The shift register also has a series of electrodes, perpendicular to the lines. If the first pixel read, the others will move up one place then the second pixel will be read. When the first line is finished, the second line is shifted to the shift register. The complete procedure is repeated until the last pixel is read. Depending on the chip size and the digitising frequency it takes between 0.5 s and 4 s, in case of the vis-camera it took 1 second.

---

[8] Available at: LOT-Oriel GmbH & Co. KG, Im Tiefen See 58, 64293 Darmstadt.

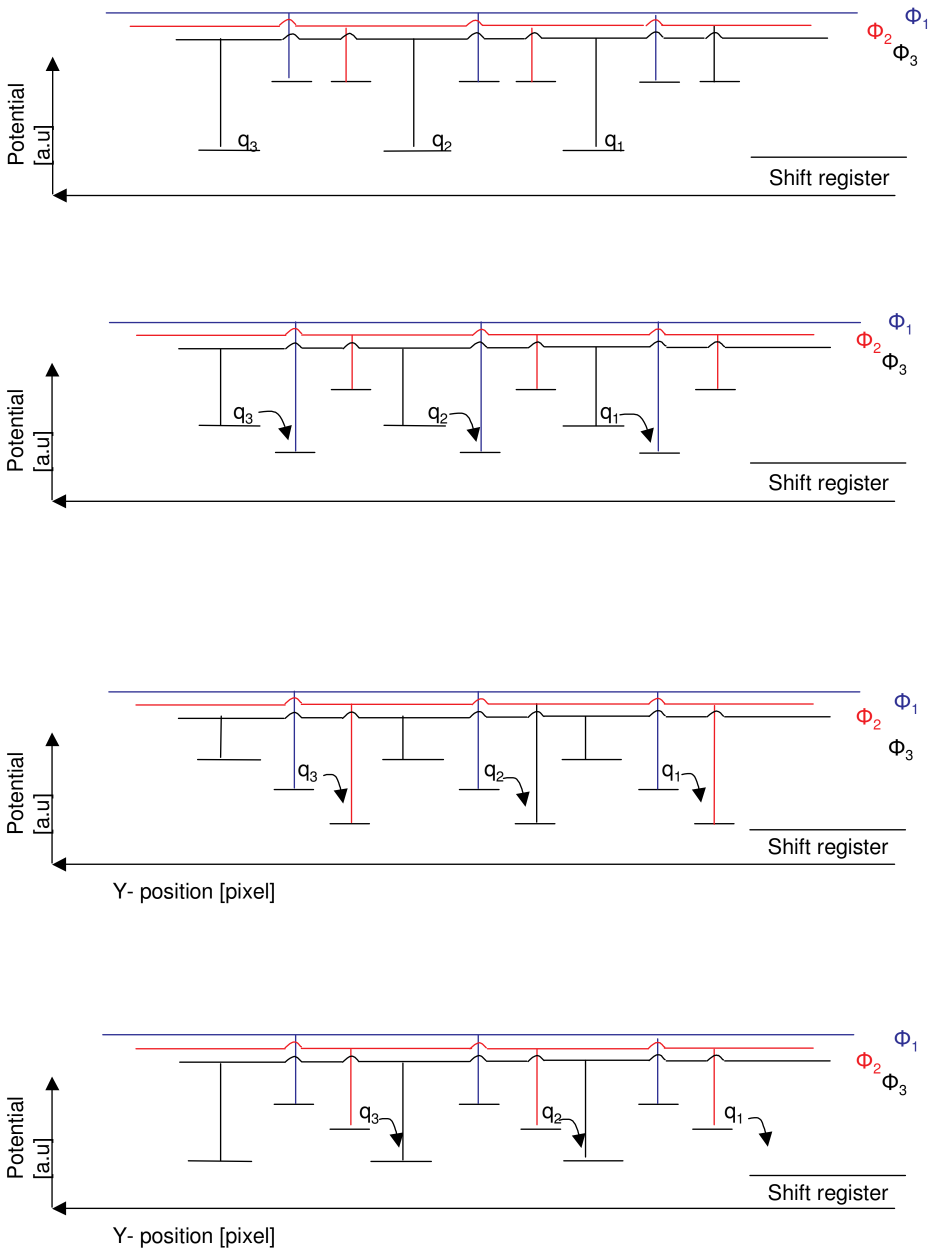

Figure 5-16: Diagram of the charge transfer process during the readout. Between the pixels (longer lines) two electrodes define the potential. At the beginning the charges (signals) q_n are stored in the individual pixels. By clocking the electrodes the charges are moved towards the shift register (adapted from Marti und Plettl, 2005).

During the readout procedure (section 5.5.I) the charge, related to the detected signal, is shifted from one pixel to the other until it reaches the shift register and is finally digitized. Depending on the position of the pixel the signal is shifted up to 512 + 2048 = 2560 times, or just twice. During the shifting processes the charge transfer efficiency (CTE) does not equal 1, i.e. some electrons are not shifted and are lost. For a normal camera the CTE is of the order of $CTE \approx 1 - 10^{-6}$ and is constant for all charges transferred (section 5.5.IV).

5.5.II Characteristic of the used CCD

The UV-instrument was mainly operated by our partners in Bremen. For a description of the UV-camera refer to [Bruns, 2004]. The CCD-camera used for the vis-instrument is an ANDOR DU-440-BU, its chip (Marconi, CCD 42-10) consists of 2048 x 512 pixels each

13.5 x 13.5 µm large, so in total it measures 27.6 x 6.9 mm. During measurement it is cooled down by a Peltier element to -30° C to minimize the dark current. The heat originating from the warm side of the Peltier element is removed to the cabin of the aeroplane by a small ventilator. As there is more than one instrument inside the plane and all of them are cooled in a similar way, the air inside the cabin was too warm to cool down the camera any further without an additional power supply, producing additional heat.

5.5.II.a Dispersion and Slit function

After each flight, an HgCd lamp was hold in front of each individual telescope to calibrate the spectra. The other telescopes were closed during the calibration measurements to avoid additional light to be observed by the CCD. The used lamp emits several sharp lines at well known wavelengths in both the visible and UV region (Table 5-C).

UV				vis					
340.3	346.6	361	365	404.6	407.8	435.8	467.8	479.9	508.5

Table 5-C: Lines of the mercury cadmium lamp used for the calibration. Here the maxima of the emission lines in nm are listed for measurements in air (Marco Bruns, private communications, September 2002).

The aim of the calibration measurements is not only to get the wavelength calibration (Figure 5-17) but also to get the instrumental slit function, which is the response to the sharp peak of a single emission line (Figure 5-18).

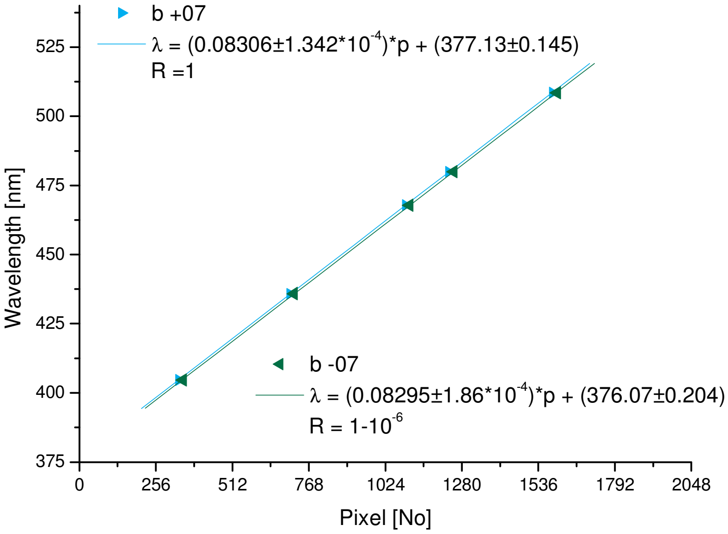

Figure 5-17: The wavelength calibration for the visible-instrument retrieved from a measurement during the FORMAT II campaign on 17/09/03. Only two out of ten calibration fits are shown here to keep the figure clear. The two LOS were chosen due to their slit function, ub07 (upward backward 7°) is imaged on the top of the CCD, whereas db07 (downward backward 7°) is imaged in the centre (fourth from bottom in Figure 5-12)

The dispersion of the spectrograph equals 6.6 nm/mm (section 5.4), the pixels of the camera extend over 13.5 µm and therefore the theoretical value of the dispersion equals 0.089 nm/pixel. As we did not use the blaze wavelength of the spectrometer a slight difference can be expected. As illustrated in Figure 5-17 the dispersion varies slightly depending on the line of sight, the approximated average of all calibration measurements is 0.083 nm/pixel.

The slit function is used in the DOAS analysis to convolute the cross section of the individual trace gas to the instrument's resolution. In some cases it can be approximated by a Gaussian function. Compared to the width ω given in ORIGIN the full width of half maximum as used in WinDOAS equals:

$$w_{FWHM} = \omega \cdot \sqrt{2 \cdot \ln(2)} \approx \omega \cdot 1.177$$

The difference seems to be small, however recent studies showed that an error in the slit function as small as this can be detected in the DOAS analysis (Kai Uwe Mettendorf, private communication, April 2004).

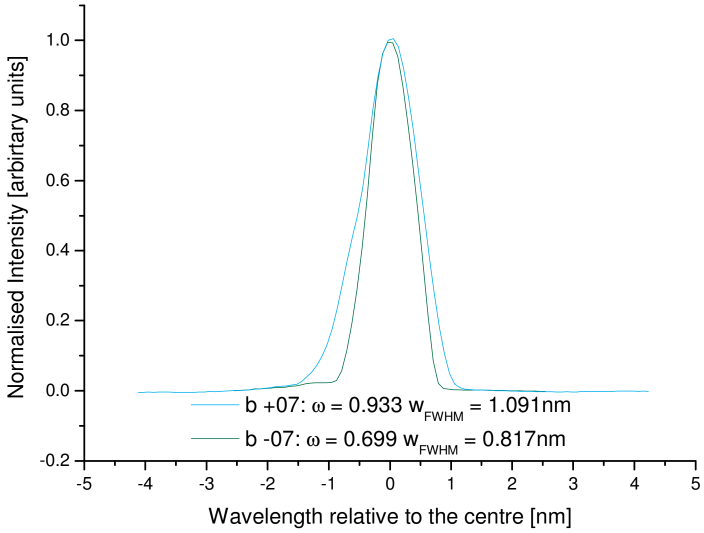

Figure 5-18: The best and the worst slit function observed during FORMAT II (17/09/2003). The fibres were arranged to have a better resolution for the downward looking telescopes.

Figure 5-18 shows two slit functions as measured during the FORMAT II campaign. As the most interesting trace gases are observed below the aeroplane, the resolution for the downward looking telescopes was generally better as for the upward looking. For the other campaigns the slit functions are comparable and are therefore not shown here.

In section 5.4 we mentioned a wavelength dependency of the slit function, which is caused by the optical system of the spectrograph. As example for three different central wavelengths the slit functions are shown in Figure 5-19. The shown slit functions were measured during the SCIAVALUE II campaign and belong to the nadir telescope.

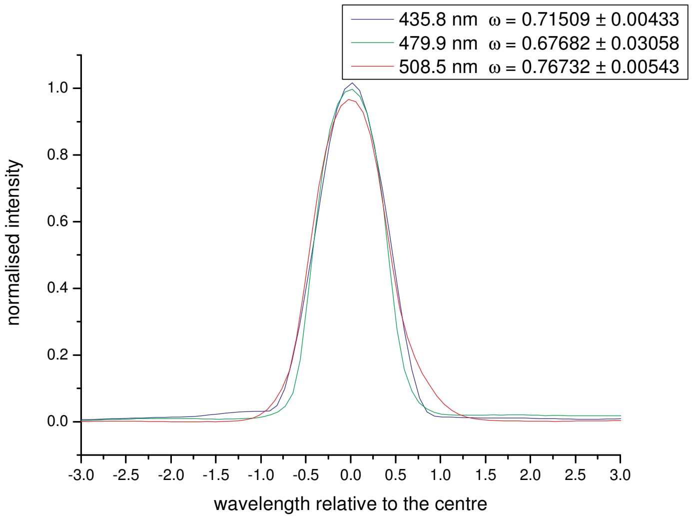

Figure 5-19: The slit functions of three different central wavelengths. The width varies only slightly in the wavelength interval of 70 nm. The complete chip covers an interval of 160 nm.

The spectral resolution is dominated by the width of the entrance slit. The AMAXDOAS instrument does not use an additional entrance slit and the light coming from the fibres is directly led to spectrograph. The diameter of the fibres measures 150 µm, hence a perfect image also has the same diameter on the CCD-chip. According to the pixel size of 13.5 µm the image is about 11 pixels wide. Therefore the resolution will equal 0.9 nm, if the dispersion is a constant with 0.83 nm/pixel.

As discussed above the dispersion and resolution depends on the line of sight as well as on the grating and the spectrometer, so to conclude this section an overview of the characteristics is given in Table 5-D:

	UV	Vis
Grating [lines/mm]	600	500
Blaze wavelength [nm]	300	560
Dispersion [nm/pixel]	0.11	0.083
Pixel size [µm]	20	13.5
Resolution fwhm [nm]	0.7	1.0

Table 5-D: Characteristics of the both AMAXDOAS instruments. Data of the UV-instrument were taken from [Bruns, 2004].

5.5.II.b Dark Current and Offset

A small offset is added to the signal before the complete signal is digitised and transferred to the computer. In addition to this offset the dark current occurs as described in 5.5.I.

For the DOAS retrieval this offset has to be subtracted in advance. Traditionally the offset and the dark current are measured before or after the measurements. Typically these measurements were taken before each flight; the most accurate results can be obtained under laboratory conditions. Extended tests of the camera were performed before the instruments were installed on the aeroplane for the first campaigns [Glück, 2002]. In Figure 5-20 the dark current is shown for different temperatures. For temperatures higher than -25°C, the dark current increases exponentially with the temperature.

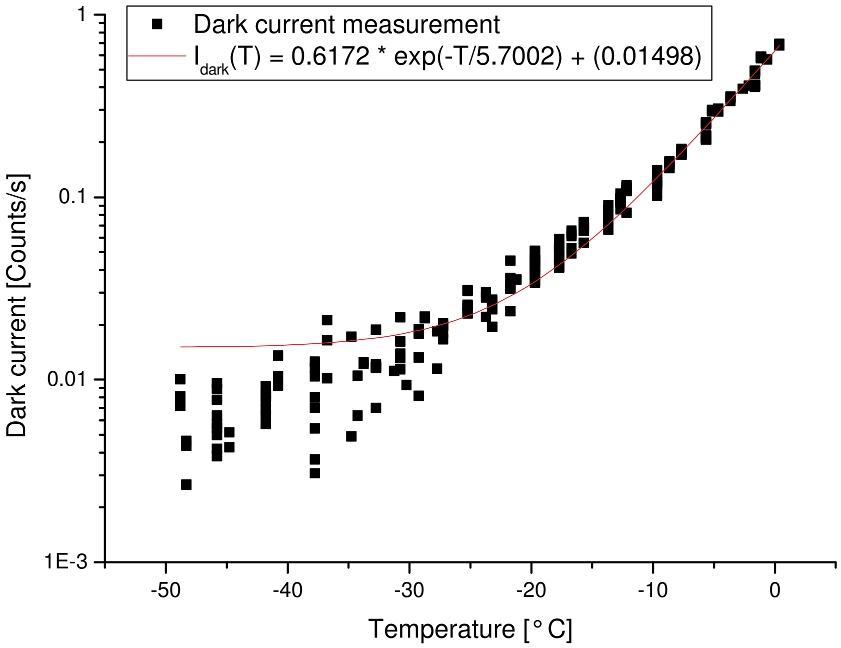

Figure 5-20: Dark current as a function of the detector temperature. For this measurement the dark signal was observed for 3 minutes. The variations for low temperatures (T<-25°C) are mainly due to the logarithmic scale.

Using a CCD camera, there is a better way to correct for the offset, the dark current and the stray light simultaneously [Sinreich, 2003]. Dark zones are used to separate the individual lines of sight from each other (Figure 5-12). Here the three components mentioned dominate the signal. The dark current and the offset are the same as in the illuminated parts (ignoring some small CCD-internal variations). If an average of the dark areas is subtracted, the offset and dark current will be perfectly removed.

5.5.II.c Stray Light

When subtracting the signal in the unilluminated areas as background, the stray light in these regions has to be considered, especially as the stray light in these zones might be different from the stray light superimposed to the signal. In the dark areas most light originates from diffused stray light in the system. In addition some light is scattered from the neighbouring illuminated parts, compared to them the signal is less than 2 % in the centre of the chip and less than 10 % towards the edges. An error of 10% in the stray light correction is very large and leads to wrong data in the DOAS retrieval, however the complete system is set up in a way that the most interesting part of the CCD chip is not affected by this effect. So a vertical (y-direction) average over the dark areas is used to subtract the background signal, whereas in the x-direction the spectral information of the stray light is kept.

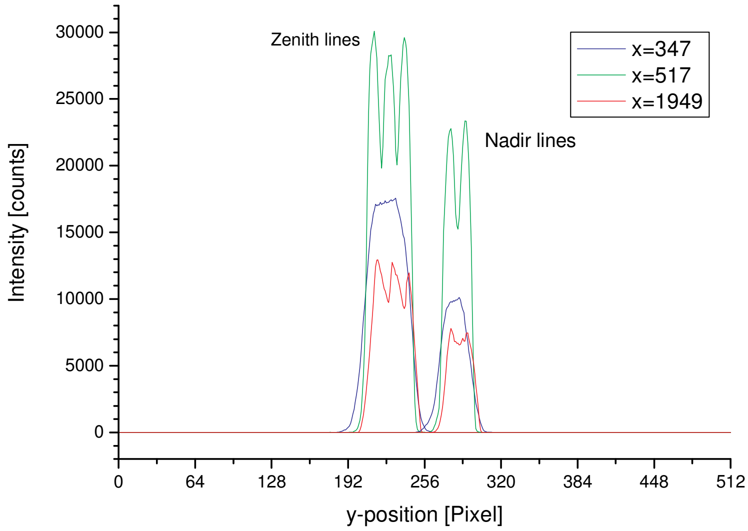

Figure 5-21: Calibration measurements are one excellent opportunity to estimate the stray light. Here the intensity cross section for three peaks is shown, for two neighbouring signals on the CCD (nadir and zenith from 16/08/2002). While in the centre beginning from pixel 517 the individual fibres of the one telescope can be separate very easily this is impossible towards lower wavelength (position 347).

The regularly performed calibration measurements are ideal to study the influence of the stray light, as most of the CCD chip is dark and the observed light can easily be attributed to one of the observed spectral lines (details are described in 5.5.II.a). In Figure 5-21 three cross sections for nadir and zenith telescope are shown, the lines were chosen with respect to the position on the CCD chip and the observed intensity. Close to the centre the individual fibres corresponding to one line of sight can be separated, towards the edges of the chips this impossible. For the Estimation of the maximum error introduced to the spectra, this region is of special interest (Figure 5-22).

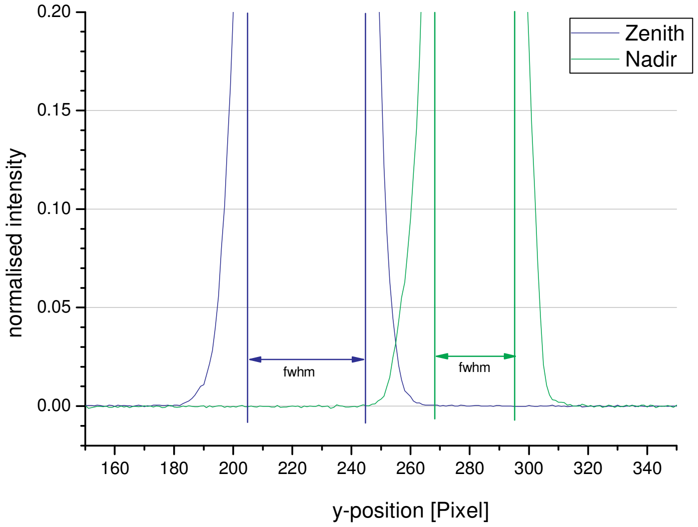

Figure 5-22: Detail of Figure 5-21 concentrating on the shortest wavelength. In contrast to the former figure the observed signal is normalised to maximum. The width of the signal is shown additionally, it was used for the calculation of the integrated signal.

In this worst case region the stray light signal between the lines is about 5 % of the maximum. Therefore the maximum error in the signal introduced by subtracting is 10 % (five from each neighbouring signal). In the centre of the chip the error is far lower (≤ 1 ‰).

A correct background (offset + dark current + stray light) for the complete chip is subtracted when the lines of sight are separated by more than two small inactive fibres. For the Falcon the back ground correction worked far better than for the Partenavia, due to the different fibre bundles (Figure 5-9).

The total signal varies with the relative solar azimuth angle and hence depends on the flight direction. Therefore for each individual image the stray light is corrected separately.

5.5.III Noise and Detection Limit

The optical density of the trace gases retrieved by the DOAS algorithm (chapter 3.2) is of the order of 1 ‰. If the noise in the measured spectra is larger than the optical density, then the trace gas will not be detected. Hence it is important to get an estimate of the noise and therefore to determine the measurement errors of the most interesting trace gases.

The noise in the observed spectra consists of three main fractions: For good spectra the most relevant part is caused by the photons statistics N_{ph}. The second noise which is also part of the signal is caused by statistical fluctuations in the offset and the dark current N_{bg}. The dark current depends on the CCD-temperature, for higher temperatures also a higher noise in the dark current is observed. As long as the camera is cooled down to -30°C the dark current noise is negligible. Moreover, the dark signal depends on the exposure time and with an increasing dark current the noise in the dark current increases as well. For the typical measurements this effect is negligible Also during the readout and digitisation some noise N_{dig} is introduced to the signal. The total noise influencing the signal is given by:

$$N_{tot} = \sqrt{N_{ph}^2 + N_{bg}^2 + N_{dig}^2} \tag{5.3}$$

For a more detailed discussion it is useful to concentrate on the noise in the electrons instead of the observed counts. The counts s are linear to the number of electrons: $s = \alpha \cdot n_{electrons}$

The noise in the photoelectrons is proportional to the square root of the observed photoelectrons ($N_{ph} = \sqrt{n_{photoelectrons}}$), the other two fractions are almost constant and independent of the signal. Hence for large signals they can be neglected and the total noise is dominated by the square root of the detected photons.
The relative error n_{tot}/signal is most important for the retrieval, it is mainly given by:

$$N_{rel} \approx \frac{N_{ph}}{n_{photonelectrons}} = \frac{\sqrt{n_{photonelectrons}}}{n_{photonelectrons}} = \frac{1}{\sqrt{n_{photonelectrons}}} \propto \frac{1}{\sqrt{signal}} \tag{5.4}$$

Hence for spectra with higher signal the noise and therefore the detection limit are lower.
To calculate the relative noise it is important to know how many photoelectrons are produced in the detector. The full well capacity of the camera pixel is 80000 electrons. If the average pixel is saturated by 50 % and 24 pixels per scan are added up, the relative noise per scan will equal 1 ‰. To improve the relative noise several scans are added. If we add for example ten spectra, the noise will be reduced by factor of $\sqrt{6} \approx 2.5$ and the noise will be less than 0.4 ‰. As one scan takes about one second, the horizontal resolution will decrease, if scans are added.
For the calculation of the noise we assumed the signal to be about half of the maximum signal. However, as the different lines of sight are observed by the same CCD and the integration time is dominated by the brightest LOS, this assumption is not always correct.

5.5.IV A former Error of our CCD-Camera

The following section concerns an error, which occurred on the used CCD-camera and was detected and described by the Institute für Umweltphysik in Bremen and Heidelberg in spring 2002 [Heue et al., 2002] and afterwards corrected by the manufacturer. According to the company it should not occur again in any of their cameras. Up to now it was not reported again by any user of CCD-cameras in the DOAS groups in either of the two universities.
The position of a weak peak signal was shifted compared to strong signals (Figure 5-24). It was observed when the sharp emission line of mercury lamp was detected with different exposure times.
The test was repeated for several emissions lines, without moving the grating turret. To check for optical effects, which might also lead to asymmetric slit functions, several positions on the CCD chip were used. The position of the lamp relative to the fibre was kept constant as well, so a shift caused by different illumination angles can be excluded. The experimental set-up is shown in Figure 5-23.

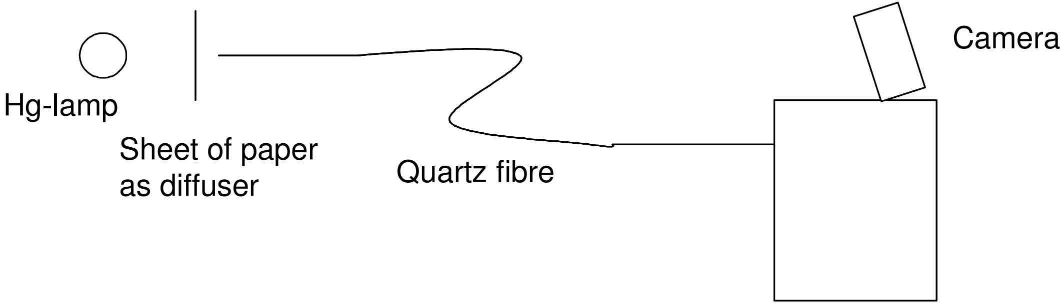

Figure 5-23: Set-up of the tests performed for CCD-failure. The sheet of paper was folded several times to reduce the detected intensity.

For short exposure times the detected signal is small (about 150 counts for 0.011 seconds). The position of the detected peak centres obviously changes between the low and the high signal (Figure 5-24). The shape of the detected signal changes as well, the high peaks could be assumed to be Gaussian, the lower ones however, had a long tail towards the larger channels.

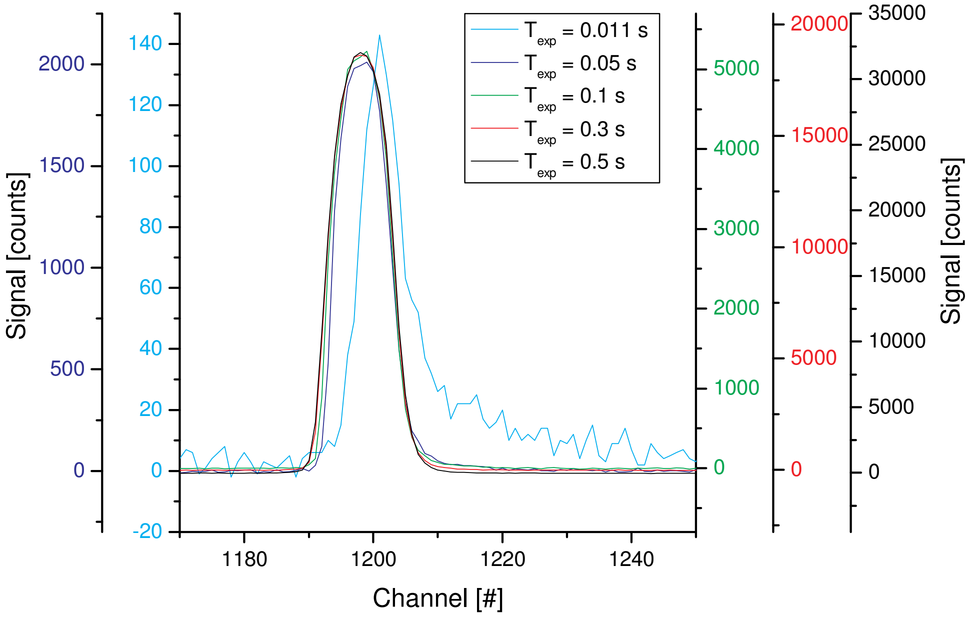

Figure 5-24: An Hg-line (546 nm) was detected with different integration times. For short integrations time (blue lines and left scales) the position of the peak is shifted to higher pixel numbers compared to longer integration times (other colours and right scales) [Heue et al., 2002].

This effect was strongest for signals lower than 2000 counts. In Figure 5-24 the dark blue line has about 2000 counts in the maximum and here a slight shift can be observed as well.

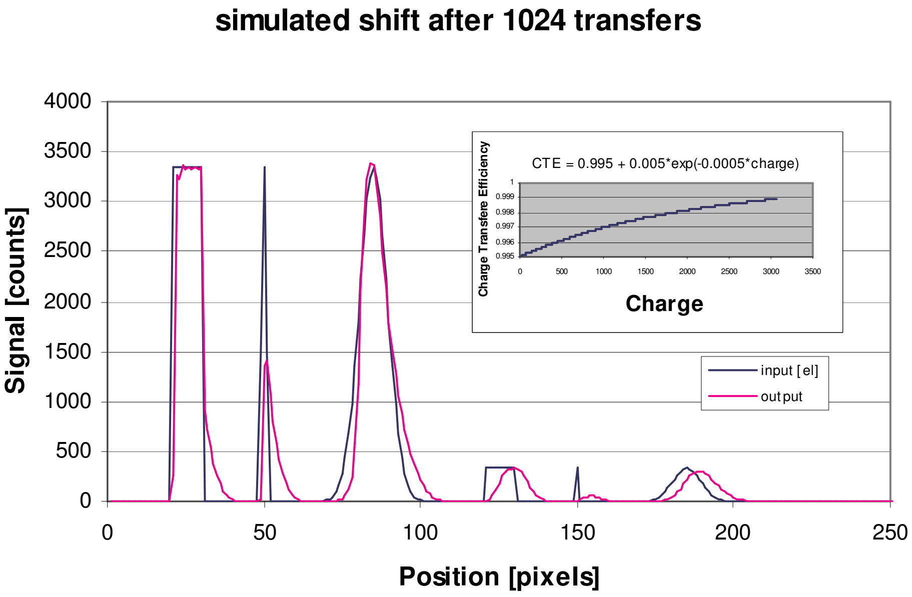

Figure 5-25: Computer simulated shift with a charge depending CTE. For small signals the peaks are clearly shifted, whereas the strong peaks are not shifted. Compared to Figure 5-24 the tails of the peaks in the signal can be observed in both the measurement and the simulation.

The error was called charge transfer efficiency (CTE) error. Several tests lead to the conclusion the reported error might be caused by an unstable CTE. A simple computer simulation showed all the observed effects might be explained with a CTE, which depends on the charge. For the simulations an exponential CTE was assumed, $E = 0.995 + 0.005 \cdot e^{-0.0005 \cdot q}$ In Figure 5-25 the result of the simulation is shown. The input distribution is shown in blue and was shifted 1024 times with the CTE shown in the small figure. As can be seen the magenta curve shows the same structure as observed by the CCD. The small peaks are shifted and the large peaks are tilted (Figure 5-24).

The error was corrected by the manufacturer in June 2002, the exact reason was not published, “Wrong setting in the electronic”. However, the camera worked well for the measurement campaigns beginning in August 2002 (chapter 6).

5.6 The Computer and Measurement Program

As space and weight are limited inside aeroplanes, a smaller computer was bought (Conerto III[9]: 133 Mhz CPU, 256 MB ram, 80 GB hard disc). Besides the size it was a normal PC with a USB-port, a serial port and two PCI-slots. The PCI-slots are necessary as the interface of the camera uses a PCI card.

Together with our partners in Bremen, we bought three computers – one was bought in spare just before the company stopped the production. It turned that out the third computer was essential, because the one bought for the visible CCD-camera did not work with this camera and the corresponding card. Several operating systems and several versions of the camera operating software were tried. Even the dealer of the camera tried several settings without any success. In the end there was no other choice than using the spare computer “Sparky” instead of the original “Daedalus” – “Ikarus” would have been a more telling name with respect to the many crashes it had.

Due to the troubles with the computer the most stable version of a measurement routine was used and a small macro was written based on the official operating software “Andor-MCD”. All attempts using the same software as used for the similar MAX-DOAS instrument failed.

The well established idea to calculate the exposure time for the next measurement based on the last measurement was used:

$$T_{n+1} = \frac{70\% \cdot S_{saturation}}{S_n} \cdot T_n$$

where n is the number of the last measurement performed and n+1 belongs to the following measurement and “S_n” stands for the maximum counts of the measurement n. If the maximum of the counts reaches the threshold of 70 % saturation level ($S_{saturation}$), the exposure time is reduced by a factor 3 to avoid over saturation. Usually the exposure time changes when the plane changes the flight direction because with a change of the relative azimuth angle to the sun the maximum intensity changes as well.

The integration time was fixed to 20 seconds so the number of scans performed during one measurement varies. Usually about 8 to 10 scans were performed. The usual exposure time is about 0.3 seconds and the camera needs 1 second per picture for the readout procedure. A period of 8 seconds is needed for storing the image and calculating the new exposure time. Although the system is slowly it has worked quite stable, which was not sure at the beginning due to the troubles with the computers.

---

[9] ICO Innovative Computer GmbH, Zuckmayer Str. 15, 65582 Diez-Lahn.

5.7 Geographical Position and Slope Parameters

To get good spectra is a difficult task but they will be completely useless if the geographical position and slope parameters are not recorded as well. Like for many parts of the instrument we have to distinguish between the instrumental set-ups during the SCIAVALUE and the FORMAT campaigns.
In the first case all this information is delivered to the scientist on board the Falcon by the plane's computer and can be read via a serial port and stored to the computer. Due to the problems with Daedalus, the flight data were stored to the UV-computer "AMAX".
As the Partenavia is owned and run by an association for hail protection and is only used part time for scientific flights, the owners do not offer such a service. So during the FORMAT campaign a handheld GPS (Garmin) and commercial gyroscope[10] (Crossbow – VG600CA-200) delivered the additional information. The gyroscope was read out with a high frequency (80 data points/sec), this needs quite a lot of CPU-time, therefore a third computer – a personal notebook – was used to read out this data, whereas the PCs concentrated on their main work, taking and storing the images of the CCD cameras. Only the geographical position data were stored to the vis computer – Sparky.
If you use two or three computers simultaneously to store datasets independently which belong together in the end, you will have to make sure that the system clocks of the computers are synchronous. Before each flight the operators checked the computer times and synchronized them by hand with the time given the by GPS-instrument. This can be assumed to be correct. From one day to the other they normally differ by less then 3 seconds.

5.8 Power Supply

On board of the aeroplane the electrical power is no problem as along as the engines are running. Both aeroplanes have been equipped with additional generators (28 V), so there was always enough power for the instruments. At this point it might be interesting to know how large the power consumption of the AMAXDOAS is. Just adding the power of all the instruments approximates a maximum consumption to 1.4 kW. The approximation obviously overestimates the true consumption as most instruments do not need their maximum power all the time. Independent measurements in 2002 at the DLR in Oberpfaffenhofen and at Avionik[11] in Straubing observed an average consumption of 400 W while the instruments were running under stable conditions. During the booting of the system peak values of about 1 kW occur.
The problems occur when the aeroplane's engines do not run. For the AMAXDOAS it is essential to keep the chips of the CCD camera at constant cool temperature (section 5.5.I) and the spectrograph to a constant level (~ 40° C). Whereas the spectrographs' heating may be switch out for a short time (0.01 s – when changing from ground power to board power) this is impossible for the CCD. Even the short lack of power forces the computers to shut down and the CCD cooling is switched off.
For the operating modes three cases have to be considered:

1. The aeroplane supports the instruments with electrical power.
2. There is no power available at all.

---

[10] The gyroscope was rent for the duration of the campaign from the company CMT-GmbH, Mühlfeld 32, 82211 Herrsching.

[11] Avionik Straubing, Flugplatz Wallmuehle, 94348 Atting. This company helped us installing the AMAXDOAS on board of the Partenavia.

3. The plane is inside a hangar or stands very close to it, so the usual 230 V AC is available and extension cables can be used.

The first case is standard during the flights, and is no problem for the instruments.
The second case is the largest problem, because here the batteries have to be used to run the instruments. As soon as power from the aeroplane is available the instruments have to switch to this supply without shutting down. The batteries must be recharged during flight. For this situation a special recharging instrument (Hoffmann Messtechnik[12] – special instrument) was built to supply the instruments with uninterruptible power.

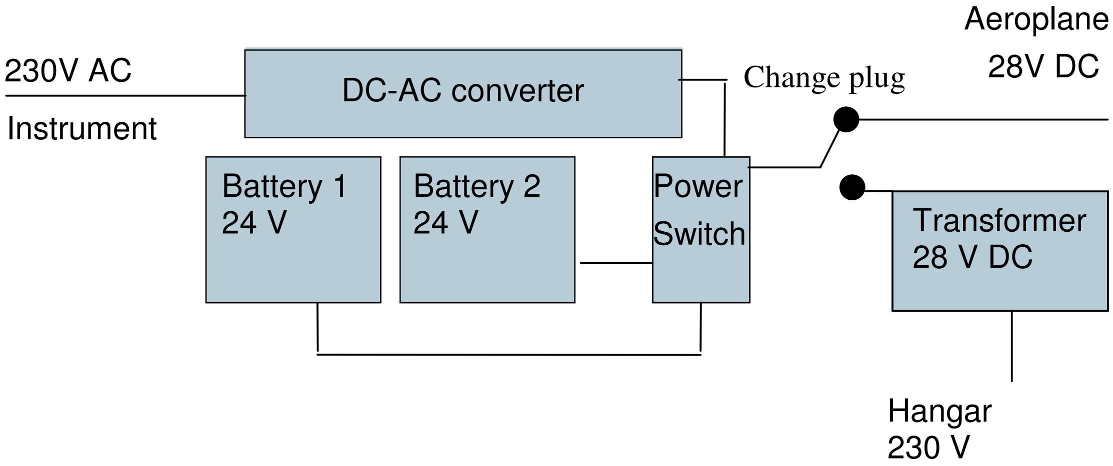

Figure 5-26: Overview of the power supply for the instrument. The instrument is running on 230 V AC and the plane supports the instrument with 28 V DC. The converter is supported by the aeroplane operation team. The power switch is used to support the instruments while no power is available using the batteries and recharges them as soon as possible. To use 230 V from the hangar directly for the instrument will be possible only if the system can be shut down in between.

For the third case two sub cases can be thought of, the whole aeroplane is supplied with external power or an extension can be used to supply only one instrument inside the plane.
Normally at larger airports systems can be rented to support the aeroplane with power (28 V DC) but they are very expensive. We made this bad experience in Lugano[13] (2002), during the FORMAT II (2003) campaign a small system was rented from Avionik for 4 weeks.
On board of the Falcon an additional power generator has been installed. Before take-off and during the short refuelling stops this was used to supply the instruments with electrical power.
For the case the aeroplane stood close to a hangar and we wanted to run only our instruments a small transformer is used to transform the 230 V AC to 28 V DC. It has a maximum output of 400 W which is well enough for the standard use but to low for booting the system. The power switch had to be disconnected from the aeroplane and connected to the transformer. The additional power was supported by the batteries during this period. More details about the different systems of the power supply, depending on the aeroplane are given in section 5.10.

5.9 Instrumental Racks

Inside the aeroplanes the instruments themselves were stored in specially designed racks. The racks were built to keep the instruments in place even in a case the plane crashes and the

---

[12] Hoffman Messtechnik GmbH, Schloss-Straße 32, 69231 Rauenberg.

[13] In Lugano (2002) we paid 4078 SFr, (~2720 €) for the 10 flights in 3 weeks. In 2003 we paid 300 € for renting a small system for 4 weeks – the difference equals two monthly net incomes of the author.

acceleration is of the order of $9 \cdot g$. The important aspect is not to protect the instruments but the crew from large and heavy parts of the instruments flying around in the cabin.

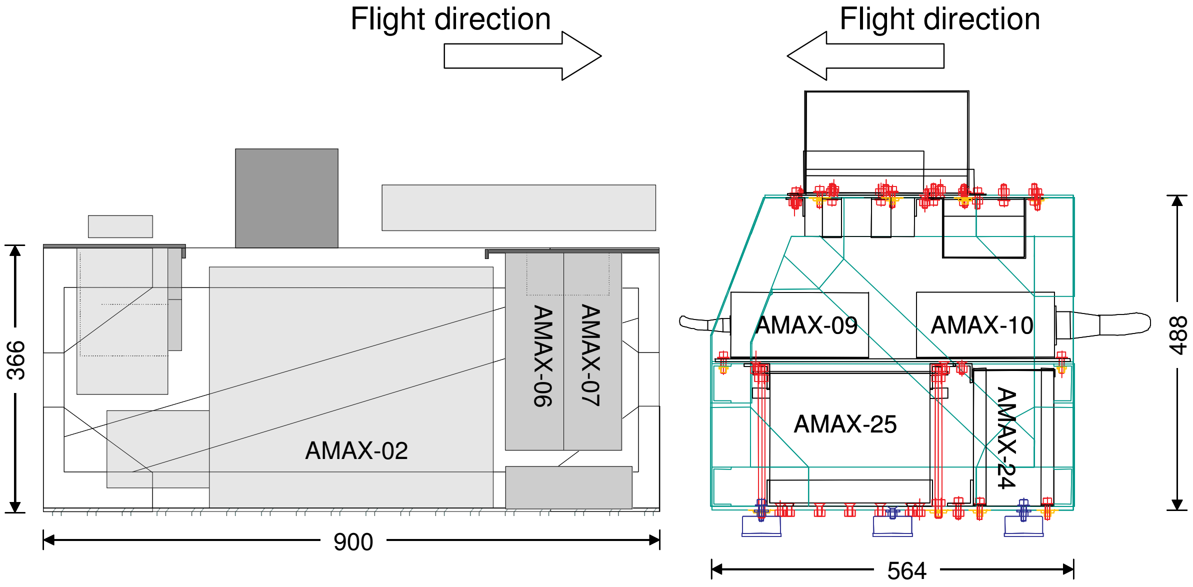

Figure 5-27: Overview graphs of the instruments in the racks.
In the left panel the instrumental rack is shown, here the spectrometers (AMAX-02) and the computers (06 & 07) are stored.
In the right panel you see the "power rack" with the batteries (25), the charging instrument (24) and the DC/AC converters (09 & 10).

In Figure 5-27 the instruments are shown inside the racks. In the rack shown ion the left all measurement instruments were stored, i.e. the spectrographs with the cameras and the computers. The power supply consisting of the batteries, the power switch and the converters is fixed in the rack shown on the right.

5.10 Aeroplanes and Installation

The AMAXDOAS instrument was installed on two different aeroplanes, depending on the aims of the measurement campaigns (chapter 6). For the validation of the SCIAMACHY instrument (section 5.12 and chapter 6.1) the Falcon F-20 of the Deutsches Zentrum für Luft und Raumfahrt (German aerospace agency) D-CMET was used.

The measurements in the boundary layer were performed with the Partenavia PA 68 (D-GITY), which is owned by the Landkreis Rosenheim.

5.10.I The AMAXDOAS instrument on Board of the Falcon

Three remote sensing instruments were installed on the:

- a LIDAR from the DLR (OLEX),
- a SUbmillimeter Radiometer (ASUR) from the University in Bremen,
- the AMAXDOAS by the Universities of Bremen and Heidelberg.

The operators themselves described details about the instruments in the overview paper [Fix et al., 2005]. The mission was called SCIAMACHY VALidation and Utilization Experiment (SCIAVALUE).

The Falcon D-CMET is equipped with several standard sensors for meteorological parameters like pressure, temperature, wind speed and direction. All these data are stored together with the time and flight parameters i.e. slope angle, altitude and speed and can be used for the scientific purpose.

Figure 5-28: Photo of the Falcon on the airport in Mahé. When the plain is outside the hangar for longer periods, the upper housing has to be protected from rain (blue plastic bag). The lower housing is visible next to the stairway. (Also the Falcon is not waterproof – the blue basket stood inside for this purpose)

The aeroplane's wingspan is 16.3 m and the length is 17.2 m, the average cruising speed during the campaigns was 430 knots or 800 km/s. Depending on the traffic and the weight the flight altitude during the campaigns varied between 30000 and 40000 ft (9143 m to 12191 m). In Figure 5-29 an overview of the instruments on board of the Falcon is given. As can be seen, the AMAXDOAS is surrounded by the ASUR in the back and the OLEX instrument in front. Figure 5-30 is a photograph taken from the back of the aeroplane during the campaign, here all the instruments can be seen. In the front of the cabin, between the OLEX and the plane's wall a small (50 cm * 120 cm) way was left free. Therefore the instruments had to be installed in the order from back to front, and the OLEX had to be last, closing the way for the instruments – not for the operators and their luggage.

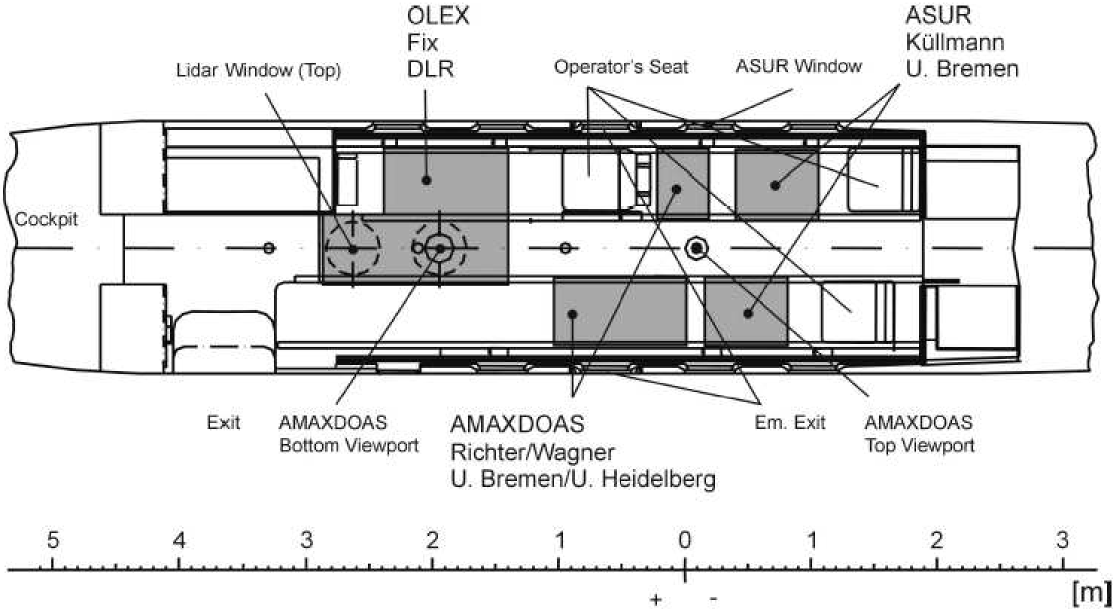

Figure 5-29: Ground plan of the Falcon and the three instruments used for the SCIAVALUE campaign. As can be seen the AMAXDOAS is in between the ASUR and the OLEX instrument [Fix et al 2004].

Figure 5-30: Photo taken inside the Falcon during one flight. The two large racks on the right and the left in the front of the picture belong to the ASUR, on the left in front of the ASUR the AMAXDOAS measurement rack is visible. The OLEX Rack is the one in the background of the picture behind its operator Andreas Fix.

5.10.I.a Power Supply on Board of the Falcon

As mentioned in section 5.8 the plane is without power during the refuelling process. A fuelling process takes about 20 min not including the taxi to the fuelling stations, so the batteries had to be big enough to support the instrument for 60 minutes in the minimum: $1.4\ kW \cdot 1\ h = 1.4\ kWh$ and $1.4\ kWh / 24V = 58\ Ah$.

As we know the consumption of 1.4 kW is overestimated, the total capacity of the batteries is slightly smaller: $2 \cdot 27\ Ah = 54\ Ah$. The batteries must be suitable for use on an aeroplane. We used "Hawker[14] 24-27h".

At first glance 1 hour seems to be a long time period, but several aspects of security cannot be neglected, i.e. the batteries are in good shape at the beginning of the campaign, but towards the end their output decreases and the performance of batteries depends on the temperature – to our surprise the only problems with the batteries occurred in the polar regions, not in the tropics.

The different temperature not only affected the battery performance, but also directly influenced the power consumption of the instrument. In the Tropics, the temperature in the aeroplane was high (~27° C), in the north the plane was in a heated hangar (~20° C), so in the tropics less energy is needed for heating the spectrographs. The difference can be calculated by multiplying the power of the spectrographs (100 W for both) with one hour (heating rate 7.5° C/h – section 5.4).

The cooling of the CCD is affected only to a weaker degree, by the ambient temperature. A similar calculation as above shows that the difference is less than 10 Wh.

However, these numbers are small compared to the energy stored in the batteries: 1400 Wh.

The main reason is that different operators worked with the instrument on both legs. Different operators had different ways in running the instrument and therefore power the consumption varied. The heating of the spectrographs takes one additional hour. If only parts of the

---

[14] Hawker GmbH, An invensys company, Dieckstrasse 42, 58089 Hagen.

instruments are running this will not affect the batteries, the heating can well be supported by the small transformer. If, on the other hand, all instruments are running or even additional ones, e.g. for a backup of the data, then additional power from the batteries will be needed. So the conclusion that the batteries performed better in the tropics might be wrong.

5.10.I.b Housings for the SCIAVALUE Campaigns

The housing for the SCIAVALUE were already discussed in section 5.2, hence here mainly a more detailed plan (Figure 5-31) and two photos of the housings are shown (Figure 5-32). During the SCIAVALUE campaigns only only 4 of 10 telescopes were active: ±2° and ±90° . The other telescopes were mounted in the housings but were not used. If the telescopes were removed, this would have reduced the weight by (2*3*200 g), but the remaining holes in the housings would have to be closed (including the proof for the aviation authorities). The aviation authorities limited the weight for instruments outside the aeroplane to 5 kg, our housings fulfilled this limitation within 10 % error.
For completeness it should be mentioned that these two small housings outside the aeroplane cause a lot of turbulences and therefore influence the flight performance of an aeroplane as large as the Falcon. According to private communications with the pilots the additional fuel consumption can be approximated to be 10% - in other words the maximum flight distance is reduced by 10%.

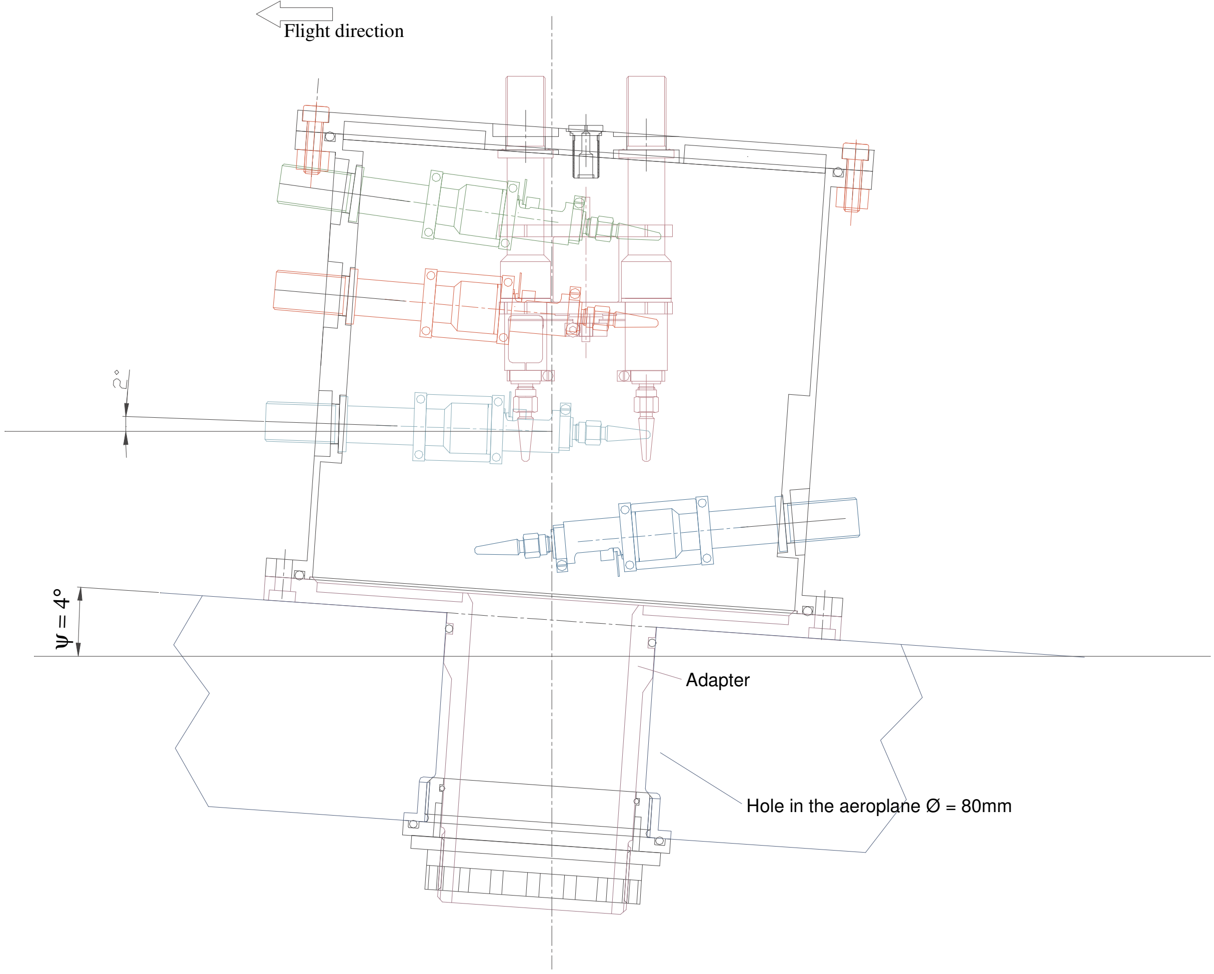

Figure 5-31: Detailed plan of the upper telescope housing (compare to Figure 5-4). Here the situation on the Falcon is shown.

Figure 5-32: The housings installed on the Falcon. Left photo: upward direction and right photo: downward direction. Due to dirt raised by the front wheel, the downward telescopes must be cleaned with alcohol from time to time (right picture).

5.10.II The AMAXDOAS Instrument on Board of the Partenavia

The AMAXDOAS was installed on the GITY. This aeroplane is officially operated by the Landkreis Rosenheim and is normally used for hail protection [Hagelabwehr, 1996]. The plane is financially supported by an organisation for hail protection. A special contract with the IMK-IFU allows an additional use for scientific flights. The Partenavia PA 68 is a motor plane with two engines. The wing span is about 12 m, the total length is about 10.5 m including a nose boom which had once be installed for exact wind measurements, but is not active any more. The average cruising speed during our measurements was 130 knots or 240 km/h.

Figure 5-33: The aeroplane on the airfield in Lugano (2002 FORMAT I campaign).

Every instrument installed on an aeroplane should be as light as possible. Light has to be seen relative to the maximum take off weight (MTOW) of the aeroplane. The AMAXDOAS instrument as it was installed on the Falcon had a total weight of 250 kg, the MTOW of this aeroplane is about 20 tons. The maximum take off weight of the Partenavia equals 1990 kg, as sum of the empty plane, the pilot, the operator and the fuel. The empty plane has a weight of 1450 kg, the instrument 250 kg, the pilot and operator 85 kg each, in sum this means 120 kg fuel. The typical consumption with the housings outside was about 70 l/hour and the maximum flight duration would be 1.2 hours (including spare fuel for 30 min according to the flight restrictions). This means to perform longer measurement flights the instrument's weight has to be reduces dramatically. “Each gram is important” (private communications Georg

Vogl the pilot, every evening throughout the campaign during dinner). Hence large parts of the instruments were removed (Figure 5-34 compared to Figure 5-27). In total about 85 kg were spared. The equivalent of this weight equals more than one additional hour of measurement flight.

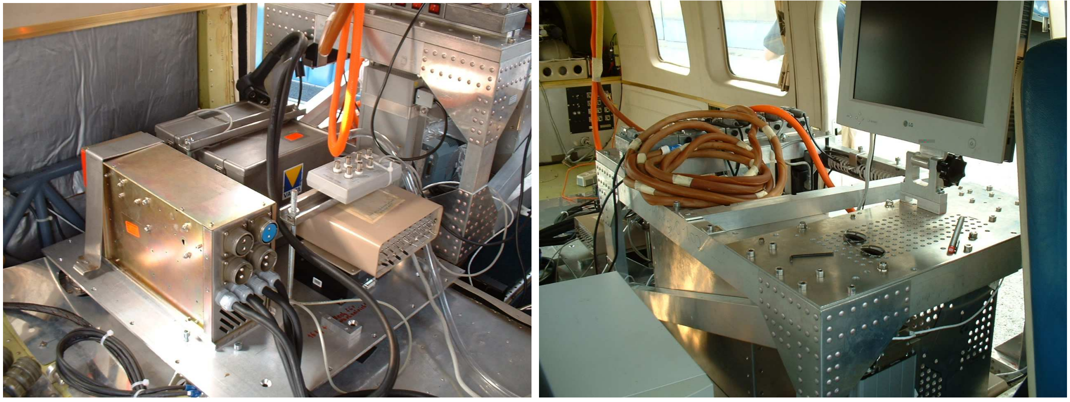

Figure 5-34: The instruments used during the first campaign inside the GITY. These pictures were taken during uninstalling. During the measurement flights the quartz fibres and cables were stored and fixed between the rack and the wall.

5.10.II.a Power Supply for the FORMAT I Campaign

One battery was removed and large parts of the "power rack" were uninstalled. This reduces the maximum time where the instruments can be used with batteries to half an hour. The DC/AC converter is installed in the Partenavia so it was no longer part of this rack, the transformer (AC/DC) was found to be no longer necessary.

5.10.II.b Housing for the FORMAT I Campaign

For the first FORMAT campaign the same housings as for SCIAVALUE (Figure 5-4) were used and adapted to the new task. The measurement of the formaldehyde distribution was the aim of this campaign. Formaldehyde is directly emitted or develops as a secondary pollutant. In both cases it is situated mainly in the boundary layer. So the housings were turned in a way that most of the telescopes are directed downwards. The best way to achieve this was to look backward with most of the telescopes. In Figure 5-35 the lower dome is shown as it was used in the first FORMAT campaign. The upper dome was turned in a way that the following viewing direction were realised: f+11°, b+84°, b+2°, b-1° and b-3° (not shown here).
The heating inside the housing was not necessary as the main flight altitude was below 2000 m where the temperature was about 10°C.

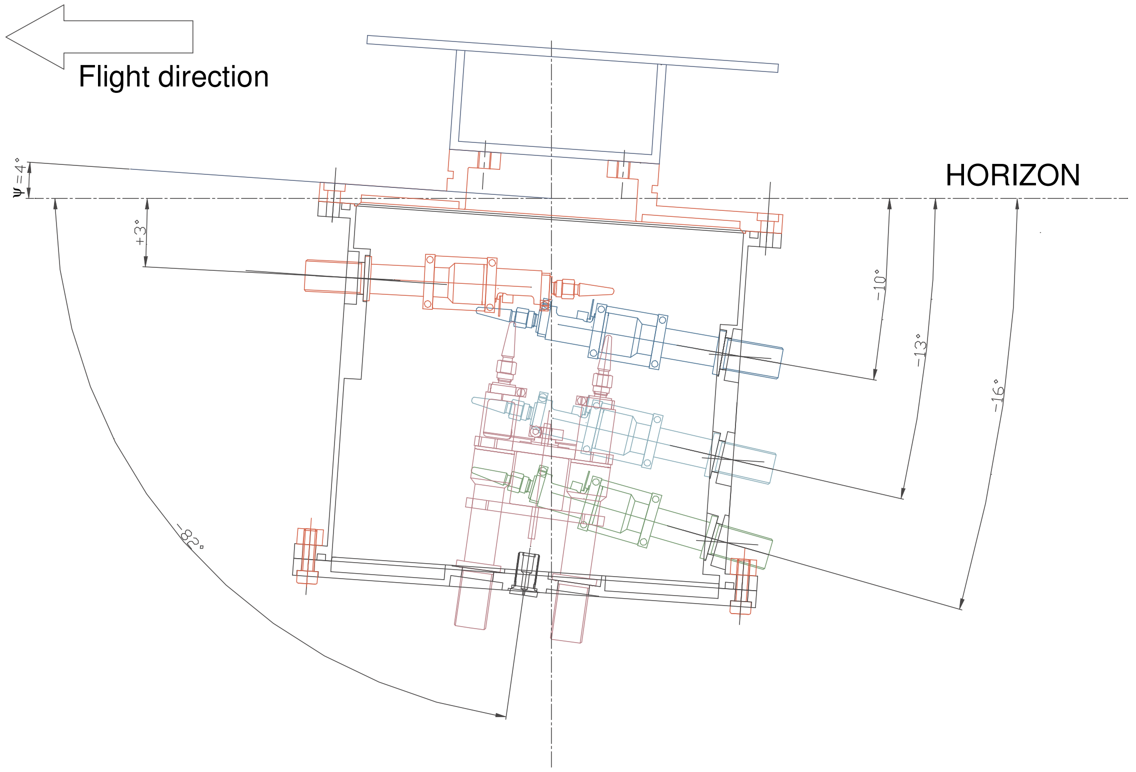

Figure 5-35: Figure of the lower dome as it was turned in the first FORMAT campaign. An average pitch angle of 4° was observed in the campaign.

These housings caused heavy turbulences in behind. The turbulences reduced the maximum range of the aeroplane and interfered with the empennage. The largest problem however was realized after the end of the campaign: The adapter of the upper housing was damaged. In the worst case this would have caused a complete loss of the upper housing, if it had been broken. It is obvious that the aeroplane might crash if the cables and fibres are entangled in the empennage.

5.10.III The FORMAT II Installation

For the second FORMAT campaign the same aeroplane was used as for the first one, but based on the experiences of the first campaign we had to build completely new housings. In addition this opportunity was taken to improve the viewing geometry.

In the observed SCD of several flights in the first campaign (e.g. 16/08/2002 – chapter 8.1) close to the cement works of Calusco, we realised that a more symmetric viewing geometry would be of great advantage. For the viewing directions several theoretical studies were performed basing on the tomographic inversion program TOMOLAB [Laepple et al., 2004].

Whereas for the SCIAVALUE campaigns the retrieval theory was mainly based on Rodger's theory, to retrieve a vertical profile of different independent lines of sight without using the fact that some of the light paths cross each other, for the FORMAT campaigns a more tomographic approach was used (Chapter 3.5).

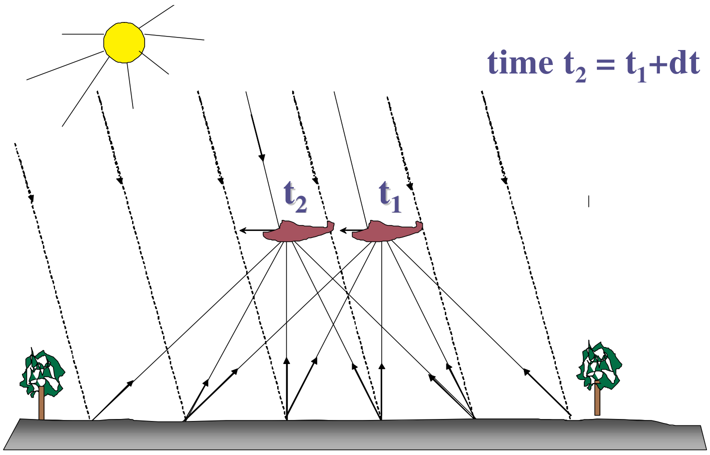

Figure 5-36: Systematic sketch of the tomographic approach for the lines of sight [Pundt, 2003].

At a time t+Δt some lines of sight observe the same air masses as other LOS did at the time t, assuming that the atmospheric conditions did not change within the interval Δt. In Figure 5-36 a sketch of the system is shown. As can be seen in the figure it is important that the lines of sight intersect as often as possible.

Most of the pollutants are emitted close to the ground (0 – 300 m AGL), and when flying in the boundary layer height, the sources can be assumed to be below the aeroplane. To observe the mixing process close to the source is a major task of the tomography-project [Pundt, 2003]. Seven of ten telescopes are now pointing into the air below the aeroplane. A symmetrical set up turned out to be best suited for this task (Bing Chao Song, personal communication, April 2003) and so the new angles were defined as: b,f-7°, b,f-15°, b,f-30° and -90°, relative to the horizon and parallel to the flight direction. The upward telescopes point to the direction b,f+7° and +90°. The letters b and f stand for forward and backward respectively (Table 5-A).

5.10.III.a Power Supply for the FORMAT II Campaign

For the FORMAT II campaign an even lighter variation of the power supply was built. Instead of the heavy NiCd-battery, two lighter Pb-jelly batteries were used and instead of the recharging instrument a normal charging instrument and two large diodes were used. All these small changes sparred about another 10 kg. Compared to first FORMAT campaign the instrumental rack was shifted back by about 15 cm to improve the performance of the aeroplane.

Normally, a better performance is achieved by high costs; in this case the cost we had to pay was less performance of the batteries. In the Falcon the instrument could run for about one hour, in the Partenavia this time was reduced to half of the time. But on the other hand this time was well enough as the fuelling was normally done at the end of a flight day, and even if a refuelling was necessary the most important instruments ran for more than 30 min without additional power, whereas the refuelling only took 10 minutes.

5.10.III.b Aerodynamic Housing

Thin sheet steel (2 mm) was bent into an "aerodynamic" shape, and the telescopes were put inside on small adapters made of thinner sheet steel. In order to reduce the turbulences caused by the sharp edges on the sides, winglets were added.

Figure 5-37
a) upper left panel: The new housing for the upward looking telescopes, two holes in a new panel for the aeroplane and a small box for the forward looking telescope. The backward looking telescope is placed outside the centre, so the signal is not influenced by the empennage.
b) upper right panel: Me working on the downward looking housing.
c) lower panel: Seven downward looking telescopes inside the new housing. The complete system including the winglets is about 800 mm long and 300 mm high. About 1/3 of the dimensions are caused by the winglets.

5.11 Future Developments

In principle the instruments worked successfully as is demonstrated in the chapters 7 and 8. However, each instrument can be further improved. In this section some disadvantages will be discussed and some ideas for improvements will be presented.

5.11.I Cross Evaluation – Scanning System

Originally the AMAXDOAS was built to separate the tropospheric and stratospheric column in a more direct way. The plan was to analyse the spectra taken with the nadir telescope using a reference from the zenith. However due to the different instrumental functions corresponding to the different regions on the CCD-array this was impossible in the actual implementation. Although this problem was discovered just before the measurement

campaigns there was not enough time to rebuild the instrument including the time the authorities need to check the licence for the flights.
How can the instrumental principle be changed to fulfil the requirements of separating stratosphere and troposphere in a direct way?
After the problem of the cross evaluation occurred in the ground and ship based instrument a new instrument for this purpose was invented. Here the advantages of both ideas the scanning method and the parallel Multi AXis DOAS were combined in one instrument. Several telescopes (three in the actual instrument) are connected to stepper motors and all of them scan from the zenith to the lowest elevation angle (Figure 5-38). As all telescopes are directed to the zenith this can be used as a reference in the analysis. So on one hand we got the advantage of the scanning instruments, on the other hand compared to the scanning instruments the time resolution is much better as several telescopes are scanning.

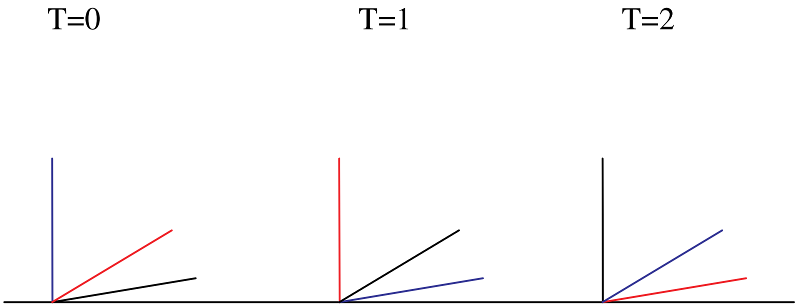

Figure 5-38: Principle of the Multi Axis scanning system. Three telescopes (indicated by the colours) scan different elevation angles simultaneously. So most elevations angles are covered at any time and all telescopes do a zenith measurement for the reference.

For the AMAXDOAS such a system is principally possible as well. This would allow a direct comparison of the zenith with the other elevation angles. Obviously it is not possible to use two separate housings below and above the hull, because this contradicts the aim of comparing nadir data to zenith. A small winglet situated at the side of the hull would be one solution, as shown in Figure 5-39.

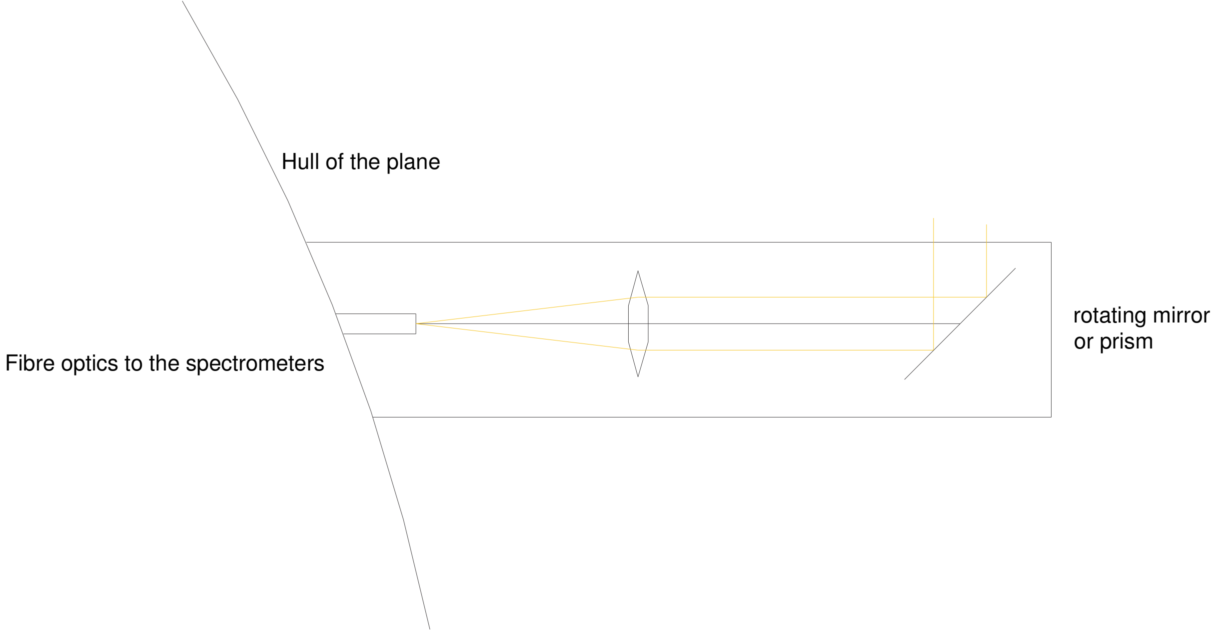

Figure 5-39: Sketch of a small winglet situated at the side of the aeroplane, the mirror is turnable and so the same optics can be used to observe the zenith and the nadir.

5.11.II Measurement Software and Computer

One computer used for the AMAXDOAS instrument did not run stable, hence the spare computer often controlled the visible instrument. A script based on the official operating software was used to control the measurement. This solution was very slow and a lot of time was spent to calculate the exposure time for the next measurement. Other operating software as used for the ground based data could not be used as the system was even more instable during the tests.

Although the exact reason of these break downs is not known, the fact that the camera worked with other computers like “Sparky” indicates the problem is caused by the computer. If the instrument is further improved a new computer will be a “cheap” and efficient way, however it has to fit to the limited space available.

If the measurement routine is faster, this will be used to improve the spatial resolution or to reduce the detection limit. However we have to keep in mind that the readout of one scan takes one second and this is the major limitation when reducing the measurement time.

5.11.III Expanding the Wavelength Region

Encouraged by the large success of methane observations [Frankenberg et al., 2005] with SCIAMACHY infra-red data, the idea of using an infra-red DOAS instrument on board of an aeroplane was developed. The focus of an infra-red instrument on an aeroplane would of course be the nadir observation, as the scattering cross section in the infra-red is too small to observe a for reasonable signals in the zenith.

Depending on the wavelength region additional trace gases could be observed by extending the wavelength region to the IR. Carbon dioxide would be an interesting tracer for plume studies as most point sources like power plants emit of CO_2 which is a quasi inert tracer to estimate the turbulent mixing. Hence both aspects chemical reaction and turbulent mixing can be separated.

5.11.IV Airborne Imaging DOAS

With an Imaging DOAS instrument a 2-dimensional map of the trace gas distribution can be retrieved. Hence, it would be a good choice for several airborne DOAS measurements like plume studies. The principle of the instrument is described in detail by Lohberger et al., [2004], here a very brief description is repeated and the possible adoption of such an instrument to airborne measurements is illustrated.

The entrance slit of an imaging spectrograph is illuminated directly (no fibres only a lens) by the scattered and reflected radiation. Due to the imaging quality of the spectrograph a 1-dimensional section of the trace gas distribution parallel to the entrance slit can be retrieved. In the direction perpendicular to the entrance slit the spectral information is mapped on the CCD camera. Depending on the camera the trace gas information for several pixels (e.g. 512) is retrieved by the analysis. To obtain a full 2-dimensional image the system has to be turned around an axes parallel to the entrance slit (usually a mirror is used instead). An alternative to the rotation would be to moved the whole system perpendicular to the direction of the entrance slit. This can easily be realised in an aeroplane (Figure 5-40).

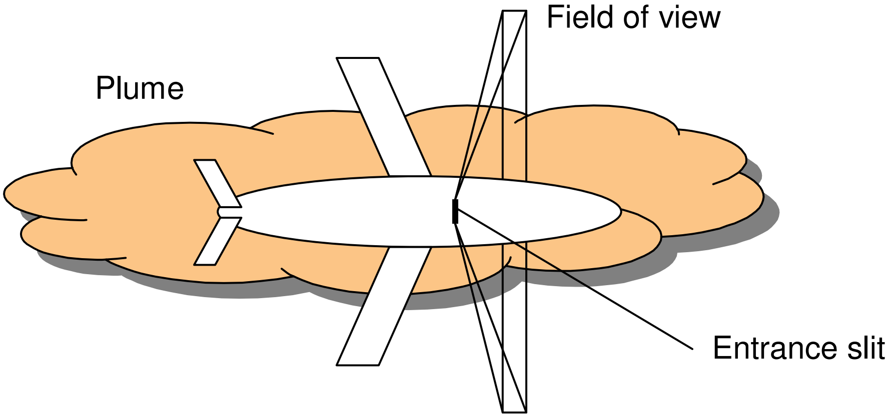

Figure 5-40: Sketch of an airborne imaging DOAS instrument.

5.12 SCIAMACHY on ENVISAT

During two campaigns AMAXDOAS was used for the validation of the SCIAMACHY instrument on board of the ENVISAT satellite. The satellite was launched on 01/03/2002[15]. Since then it orbits the earth in about 800 km altitude. The orbit is polar and sun synchronous from north to south during daytime and the satellite crosses the equator every day at 10:00 local time.

The SCIAMACHY instrument is an 8 channel spectrometer designed for measuring the sunlight in the UV, visible and near infra-red region (240 – 2380 nm). Depending on the channel the resolution varies between 0.22 and 1.48 nm. The NO_2-columns are retrieved in the wavelength region of 425 to 450 nm (channel 3) where the resolution of the instrument is 0.44 nm. Like the AMAXDOAS it observes the light scattered or reflected in the earth atmosphere and at the surface respectively.

Measurements are performed alternatingly in nadir and limb direction, changing every 2 minutes. Within 7 minutes the same air mass is observed first in limb viewing mode and afterwards in the nadir mode. With this method the stratospheric column and the total column are measured independently. At the beginning and at the end of each orbit, solar and lunar occultation measurements are also performed.

The horizontal resolution of the instrument in the nadir is 30 x 60 km^2. Global coverage is achieved after 6 days [Bovensmann et al.,1999].

---

[15] The satellite was launched from the ESA space centre in Kourou, French Guyana, at about 2 AM central European time. Hence it was still 28/02/02 LT in Kourou. Both dates are mentioned in the literature.

6 Measurement Campaigns

The AMAXDOAS instrument participated in four measurement campaigns and in a fifth one as a hitchhiker. Two campaigns were performed in the framework of the FORMAT Project in July / August 2002 and September 2003; two were carried out for SCIAMACHY validation and are referred to as SCIAVALUE. The first SCIAVALUE campaign was in November 2002 and the second in February / March 2003. In January / February 2003 the AMAXDOAS was already installed on the Falcon and therefore took part in the EUPLEX campaign.
In this chapter mainly a short overview on the campaigns and the flights is given, in addition some parameters e.g. meteorological data are explained.

6.1 The SCIAVALUE Campaigns

6.1.I Aims of the SCIAVALUE Campaigns

The new European research satellite ENVISAT was launched into space on 01/03/2002 (Chapter 5.12). In the last three years since the instruments are running many interesting results were gained [e.g. Frankenberg et al., 2004 or Beirle, 2004].
World wide an enormous work was done for the validation of the SCIAMACHY instrument, among them were many ground based stations from Ny-Ålesund and Kiruna in the North via the Tropics (Nairobi, Paramaribo) to the Antarctic (Neumayer Station). One DOAS instrument on board of the research vessel “Polarstern” cruised all the way from Bremerhaven to the Antarctica. Numerous balloons were launched from various starting points such as Kiruna, France, Brazil. Two airborne measurement campaigns were flown covering a large latitudinal and longitudinal range. The missions and its results are described in a special issue in Atmospheric Chemistry and Physics [editors: Burrows and Platt, 2004].
For the validation of SCIAMACHY, an aeroplane was used in addition to the balloons, the ground and ship based instruments, because of its long range allowing flights in less populated regions and over highly polluted regions as well. The campaigns extended from the Arctic regions to central Europe and south crossing northern Africa and afterwards to the east over the north of central Africa to the Seychelles.
The other two instruments on board of the Falcon (chapter 5.10.I) observed stratospheric air masses to compare the profiles of several trace gases (O_3, BrO, N_2O, and aerosols) with the respective SCIAMACHY product. The AMAXDOAS was the only instrument on board observing tropospheric air masses as well. The total and the tropospheric columns for NO_2 and O_3 were the main scopes of the AMAXDOAS measurements during the SCIAVALUE campaigns. In addition other tracer like BrO, OClO, O_4 and H_2O were measured.
The validation of the SCIAMACHY data product with our results is discussed in the following chapter (7). The individual steps of the analysis are compared in detail: The slant column densities, the air mass factor retrieval and the vertical column densities. The retrieval of the AMF is usually based on some assumption concerning the atmospheric parameters like trace gas profile or mixing layer height (chapter 4.4). For the comparison the most realistic parameters are considered to retrieve the optimum agreement between the two measurements and the real atmospheric conditions.

6.1.II The SCIAVALUE I and II Measurement Flights

During the SCIAVALUE campaigns 2 * 14 + 1 = 29 flights[1] were performed, starting from Oberpfaffenhofen (Headquarter of the DLR - about 80 km southwest of München), see Table 6-A [Fix et al., 2004].

The flights were divided in to two mayor legs (Figure 6-1), one leading to the north: Kiruna (Sweden), Ny-Ålesund (Norway), Reykjavik (Iceland) and Sondre-Stromfjord (Greenland). The other leg led to the south, via Palma de Mallorca (Spain) in 2002 or Tozeur (Tunisia) in 2003 and Yaoundé (Cameroon), Nairobi (Kenya) to Mahé (Seychelles), and of course all the way back. For all the flights the observed total VCD is shown in the attachments. In the polluted regions the nadir data are more interesting and hence illustrated. Outside Europe the zenith data were used. Case studies for specially selected flights are discussed in chapter 7.

Date Time	Orbit	Crossed Orbit Index	Flight Leg	Comment
Northern Part				
03/09/02 8:00-10:30	2667	10,11,12	Oberpfaffenhofen, Kiruna	
04/09/02 16:00-19:30	2685, 2686	7,5	Kiruna, Kiruna via Ny-Ålesund,	Chapter 7.2.1
05/09/02 10:00-13:00	2696, 2697	10,11	Kiruna, Keflavik	Bad data in between (2° West)
06/09/02 12:50-15:00	2712, 2713	10, 11	Keflavik, Kangerlussuaq	
07/09/02 12:30-14:30	2726, 2727	10	Kangerlussuaq, Keflavik	
07/09/02 18:20-22:00	2730	Solar Occ. 61.8° lat., 351.9° lon.	Keflavik, Oberpfaffenhofen	No measurement for half the flight, SZA > 92°
Southern Part				
15/09/02 9:15-11:00	2839	12	Oberpfaffenhofen, Mallorca	Bad data over the Alps
17/09/02 5:45-15:30	2867	13-17	Mallorca, Yaoundé	Chapter 7.2.II
18/09/02 8:30-11:30	2880, 2881	17,18	Yaoundé, Nairobi	
19/09/02 5:00-7:30	2894	18,19	Nairobi, Mahé	
24/09/02 6:30-8:30	2966	17,18	Mahé, Nairobi	
25/09/02 6:30-9:45	2981	17,18	Nairobi, Yaouné	Dense Cloud chapters 4.5:II and 7.3
26/09/02 5:30-15:00	2996	13-16	Yaoundé, Mallorca	
28/09/02 9:30-11:00	3025	11,12	Mallorca, Oberpfaffenhofen	Enhanced NO_2 over the Mediterranean

Table 6-A: Summary of the validation activity during the SCIAVALUE I campaign in September 2002. The orbit index is related to limb observation [Fix et al., 2004].

---

[1] During each campaign 14 flights were performed and one local flight in addition (19/03/2003).

Date	Orbit	Crossed Orbit Index	Flight leg	Comment
Southern Part				
19/02/03 8:00-10:30	5086	11	Basel, Tozeur	Chapter 7.1.I and Heue et al., [2005]
20/02/03 7:30-15:00	5100	xx	Tozeur, Niamey, Yaoundé	
23/02/03 8:30-13:45	5142	16	Yaoundé, Entebbe, Nairobi	No data between Entebbe and Nairobi
24/02/03 9:00-15:00	5156	17	Nairobi, Mombasa, Mahé	
26/02/03 6:30-9:00	5184	17	Mahé, Nairobi	Over heating computer failed no data
28/02/03 7:45-12:00	5214	16	Nairobi, Douala	Thunderstorm in Yaoundé, alternate Duala
01/03/03 4:15-11:30	5229	13-16	Douala, Niamey, Tozeur	No data between Duala and Niamey
03/03/03 8:30-12:20	5258	11	Tozeur, Oberpfaffenhofen	Enhanced NO_2 close to the French coast
Northern Part				
10/03/03 9:45-12:45	5358	9, 10	Oberpfaffenhofen, Kiruna	Chapter 7.1.II
12/03/03 7:30-11:15	5387	7, 8	Kiruna, Kiruna via Ny-Ålesund	
13/03/03 9:30-13:15	5402	9	Kiruna, Keflavik	
14/03/03 12:00-15:45	5417 5418	9 9	Keflavik, Kangerlussuaq	
15/03/03 13:00-15:00	5433	xx	Kangerlussuaq, Keflavik	
17/03/03 10:30-14:15	5459	xx	Keflavik, Oberpfaffenhofen	High NO_2 SCD close to Frankfurt a.M.
19/03/03 7:15-11:00	5487	10, 11	Oberpfaffenhofen, Oberpfaffenhofen	Wang et al., 2005 a

Table 6-B: Summary of the validation activity during the SCIAVALUE II campaign. The orbit index is related to limb observation, xx SCIAMACHY was not active [Fix et al., 2004].

In total a latitudinal cross section from Ny-Ålesund to Yaoundé of more than 80° was flown. The longitude along this cross section varied for less than ± 10°. In Figure 6-1 the individual flight tracks are illustrated:

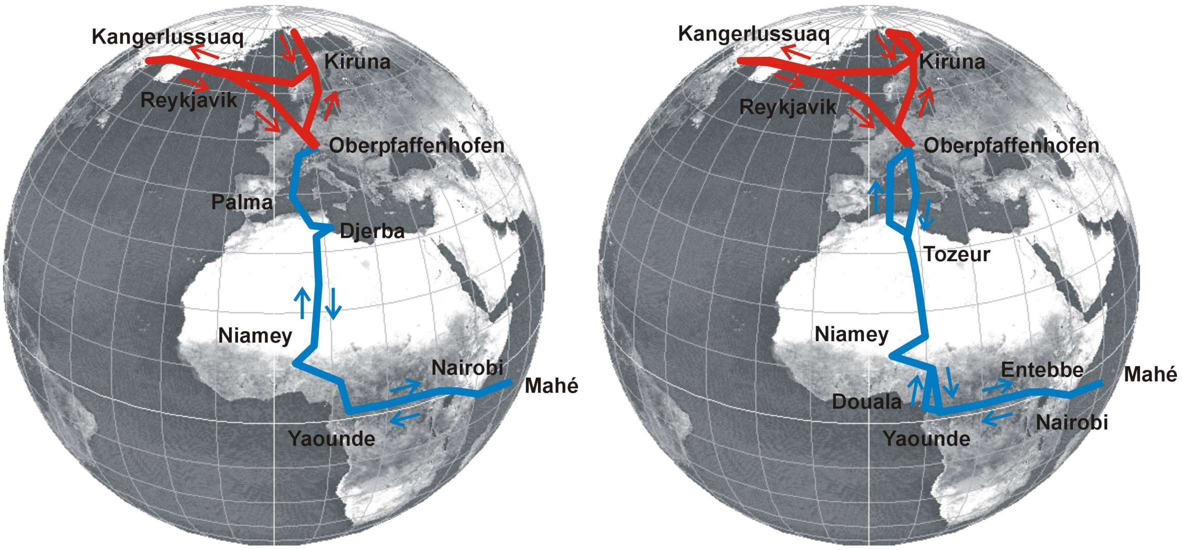

Figure 6-1: Flight tracks of the campaigns. In red the northern flights are shown and in blue the southern flights [Fix et al., 2005].

6.2 The EUPLEX Campaign

The AMAXDOAS took also part in the European Polar Stratospheric Cloud and Lee wave EXperiment (EUPLEX), although it was not originally planned to do so. The EUPLEX campaign was in January, February 2003, just before the second SCIAVALUE campaign. The other two instruments (chapter 5.10.I) for the SCIAVALUE campaign were part of the EUPLEX project, and the place for the AMAXDOAS was not occupied by any instrument. So The AMAXDOAS was installed on the Falcon before the EUPLEX campaign started.

The advantage of taking part in an interesting project for the AMAXDOAS is obvious. For the other groups, the advantage is mainly given by the fact that the OLEX must be outside the plane when installing the AMAXDOAS (chapter 5.10.I). This would have caused a lot of additional work and would have cost the corresponding time (2 days in the minimum). The main advantage was that the spared time could be used to wait for better weather conditions in Kiruna.

Due to the lack of people and money, the AMAXDOAS was not operated by ourselves, but by one of the colleagues working on the other instruments on board. At this time of the year the solar zenith angles are very high, the nights are long and the times of daylight conditions are very short. In the end, there was only one flight (26/01/2003) where the AMAXDOAS really measured. All the other flights were performed during night time.

Nevertheless this flight is well worth to be mentioned as we observed OClO, along this flight. The results of this flight have already been published by our colleagues in Bremen [Wang et al. 2003] or will be published soon [Wang et al, 2005 c]. The main results will be summarised in chapter 7.4.

6.3 The FORMAT I Campaign

6.3.I Aims for the FORMAT Project

FORMAT is the acronym for “FORMaldehyde As a tracer for photo oxidation in the Troposphere”. This already describes the aim of this research project: studying the photo chemistry of ozone formation and of the precursors such as formaldehyde. The chemistry is discussed briefly in chapter 2. The FORMAT project was an international project with partners from six European countries (www.nilu.no/Format) and was funded by the European Union. As already mentioned (chapter 5.10.II and 5.10.III) two measurement campaigns were performed for this project. Greater Milano (Figure 6-2) is an ideal research area to study the chemistry of ozone formation. About 4 million people live and work within this area. The mountains in the north and more far away in the west and the south often prevent an exchange of air masses, so the evolution of photochemical summer smog can be observed over longer periods. The incoming irradiance on a typical summer day is strong enough to drive photochemical reactions.

Figure 6-2: Map of greater Milano including the three ground measurement stations (Claudia Hak, personal communications, April 2005). As can be seen from the map, north of the town there are many suburbs e.g. Monza, Saronno, whereas the south is of agricultural character.

During the campaigns aircraft and ground based measurements were performed. About 20 ground-based instruments to study several trace gases were installed north (Alzate) and south (Spessa al Po) and on the edge of the town (Bresso), they are labelled in Figure 6-2.

In addition to the Partenavia two other aeroplanes took part. One microlight (D-MIFU) owned and operated by the Fraunhofer-Institut für atmosphärische Umweltforschung (IMK-IFU) in Garmisch-Partenkirchen was equipped with a Hantzsch instrument to measure HCHO, a particle counter for aerosol properties and a radiometer to measure actinic fluxes. Details about the instruments are given by Junkermann [2005]. For the Paul Scherrer Institut (PSI) Villigen, Switzerland, the MetAir motor glider (HB-2335) ,a Dimona HK-36TTC-ECO, measured various trace gases especially HCHO and about 30 different VOCs. Details about the instruments and additionally measured parameters (e.g. wind speed) are posted in the internet (www.metair.ch, 13/10/2005). In the first campaign the Dimona could not participate, because it had a bad crash just a few weeks before the campaign started. The pilot was not injured badly but the plane was broken into two parts.

6.3.II Conditions during the FORMAT I Campaign

The AMAXDOAS participated in the FORMAT I campaign from 29/07/2002 till 18/08/2002. The mid of August is the main holiday season in Italy (Ferragosto). In this period a lot of companies close for holidays, the cities are relative empty and quiet. Also both airports in Milano: Bresso for small planes like ours, and the large Linate airport were closed. At Linate the holiday season was used to rebuild the runway. As Milano Bresso was closed our aeroplane's home base was in Lugano in southern Switzerland (15 min flight to edge of Milano). The fact that both airports were closed had the good effect that only few aeroplanes flew around Milano. So the controllers were not too busy and we were allowed to fly at the mixing layer height of about 1200 m. Normally the maximum flight altitude in this sector is 2000 ft above sea level.

The weather conditions were not stable (Figure 6-3). At the beginning there was a short period of sunny conditions (1 flight). The second flight had to be interrupted as a heavy thunderstorm ended this period of fine weather. As most aeroplanes are not waterproof, the GITY got very wet inside. The large humidity damaged the UV CCD camera and the spectrograph was removed the next day – until the following SCIAVALUE campaign in September 2002 it was repaired again. As the aim of the campaign was to study the formaldehyde distribution, the grating of the vis-spectrometer was turned. So the wavelength range was changed from 370 – 540 nm to 317 – 488 nm. The resolution was improved after the next flight, but was still far less than it had been with the UV – instrument.

The time between 1st August and 11th August was mainly used to remove the damaged CCD-camera and optimise the vis instrument as far as possible to perform measurements in the UV. In this time it was very cloudy and sometimes even rainy so only one flight was performed. In the time from the 12th August to 16th August, the weather was very good, after the rainy days the viewing conditions were excellent on the first day, but got worse from day to day.

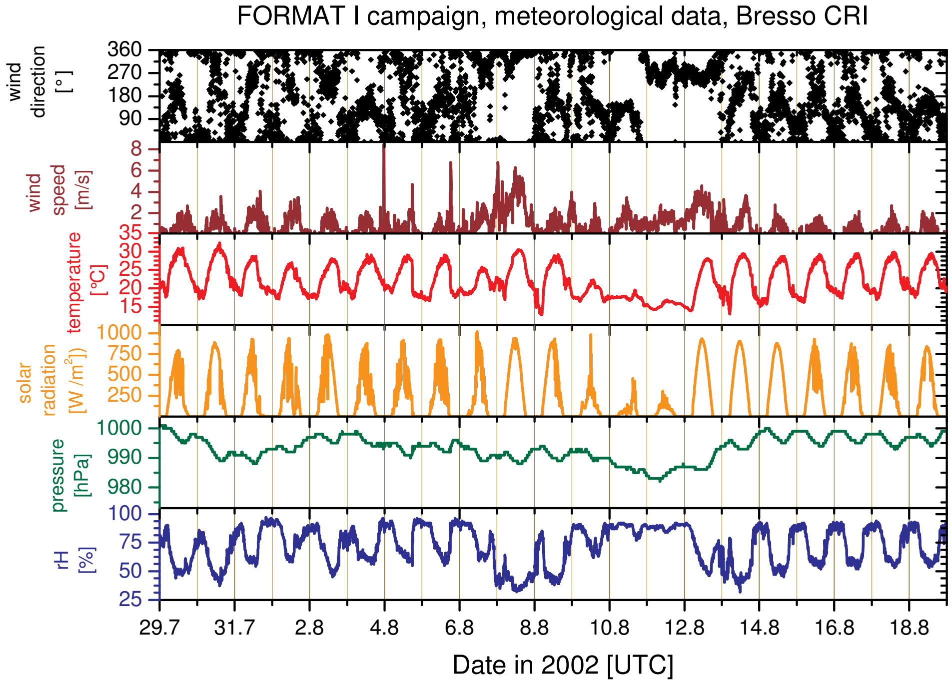

Figure 6-3: Measurement data of the meteorological parameters as observed in during the campaign in Bresso. Clearly the rainy days on the evening of 31/07 and 10 – 11/08 can be made out by the high relative humidity and the rapid decrease in solar radiation and temperature. During days mostly southern wind are observed and during nights it changes to northern direction (Claudia Hak, private communication, file date: 22/08/2005)

The constantly fine weather between 12/08/2002 and 18/08/02 led to an increase in formaldehyde and ozone as shown in Figure 6-4 (Claudia Hak personal communication, file date: 14/04/2003).

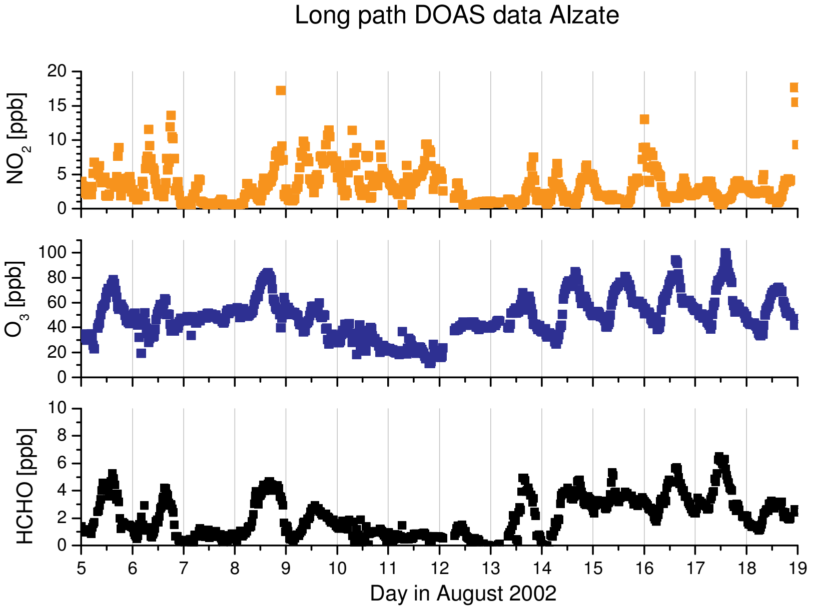

Figure 6-4: Ground based Long Path DOAS data from Alzate (north of Milano) indicating how the summer smog developed in the time between 13th and 19th August (Claudia Hak personal communication file date: 14/04/03).

6.3.III FORMAT I Measurement Flights

Table 6-C gives an overview of all flights of the first FORMAT campaign. In addition to the date and some short information about the flight track (See also attachments), the used instruments and some comments about the weather condition are given.

An overview of the HCHO and NO_2 dSCD for one line of sight (-16°) is given in the attachment. The formaldehyde distribution around the town is studied for the flight on 16/08/2002 (chapter 8.1).

Date Time	Flight track	Spectrometer	Weather
29/07/2002 8:45-10:20 Monday	Alzate	UV/Visible	Very few clouds
31/07/2002 9:30-12:00 Wednesday	Big F: Pavia, Alzate	UV/Visible	Some clouds at the beginning, rain during landing
05/08/2002 9:12-10:48 Monday	Big F: Pavia, Alzate	Visible (bad resolution)	Clear sky, clouds in the south, turning north of them Bad viewing conditions
12/08/2002 12:34-15:07 Monday	Big F: Pavia, Alzate	Visible	Very few clouds, turbulences, very clear viewing conditions
13/08/2002 12:48-15:22 Tuesday	Big F: Pavia, Alzate	Visible	No clouds, very clear viewing conditions – worse than the day before

Date Time	Flight track	Spectrometer	Weather
14/08/2002 10:05-11:37 Wednesday	U-round Milano	Visible	Very few clouds, clear viewing conditions – worse than the day before
14/08/2002 13:00-15:24 Wednesday	3 x Box around Milano	Visible	Very few clouds, clear viewing conditions – as the flight before
15/08/2002 10:54-13:26 Thursday – Assumption of Mary	Voghera, cross Milano	Visible	Good viewing conditions, first large clouds develop, burning factory south east of Milan downtown
16/08/2002 12:56-15:37 Friday	Two times (box around and triangle over Milano)	Visible	Smog over Milano – some small clouds, larger ones in the south, many cirrus clouds above flight level, not constant in time
18/08/2002 10:13-11:55 Sunday	Box around crossover Milano	Visible cooling failed	Smog over Milano – some small clouds in the South, more clouds in the North

Table 6-C: Overview of the FORMAT I measurement flights. The UV-camera was damaged by the rain on 31st July – later on only the visible camera was running.

6.4 The FORMAT II Campaign

6.4.I Conditions during the FORMAT II Campaign

The first FORMAT campaign (section 6.3.II) was strongly affected by the holiday season, therefore the second campaign was shifted to September 2003. The AMAXDOAS participated in the time between 14/09/2003 and 27/09/2003. At this time the holiday season was over, the factories were running and both airports were operated. As both airports were fully operating, the air traffic was very heavy and we were no longer allowed to fly above 2000 ft. This time the Partenavia stayed at Bresso airport (Figure 6-5) which is “ideal” for our purpose. It is situated on the edge of the town, and operated by the local aero club. Most of the other planes stationed here are about the same size of the Partenavia. Next to the airport, is the area of the Italian Red Cross (Croce Rossa Italiana), where our colleagues operated the ground based instruments [Hak et al., 2005].

Figure 6-5: Photo of the Bresso airport, the area of the CRI is situated next to the airport left of the runway.

The summer 2003 was very dry in Italy, the Po river had less water than usual and some of the power station situated on the banks of the Po were closed in July as there was not enough water. However, in September when we measured they were running again.

The end of September is harvest in northern Italy, where rice and wheat is cultured. After the harvest the stubble fields are traditionally burned. The fires are an additional source of air pollutants, like aerosols and direct emissions of HCHO and SO_2.

Figure 6-6: Photo of some burning fields as seen south west of Milano close to the refinery of Sannazzaro (17/09/2003).

During the campaign the weather was mostly sunny. Beginning from the 14/09/2003 until the 22/09/2003 there was sunshine every day, no clouds were observed and the temperature in Bresso varied between 10°C during night-times and 30°C in the afternoon as illustrated in Figure 6-7 (Claudia Hak private communication, file date: 03/02/2004).

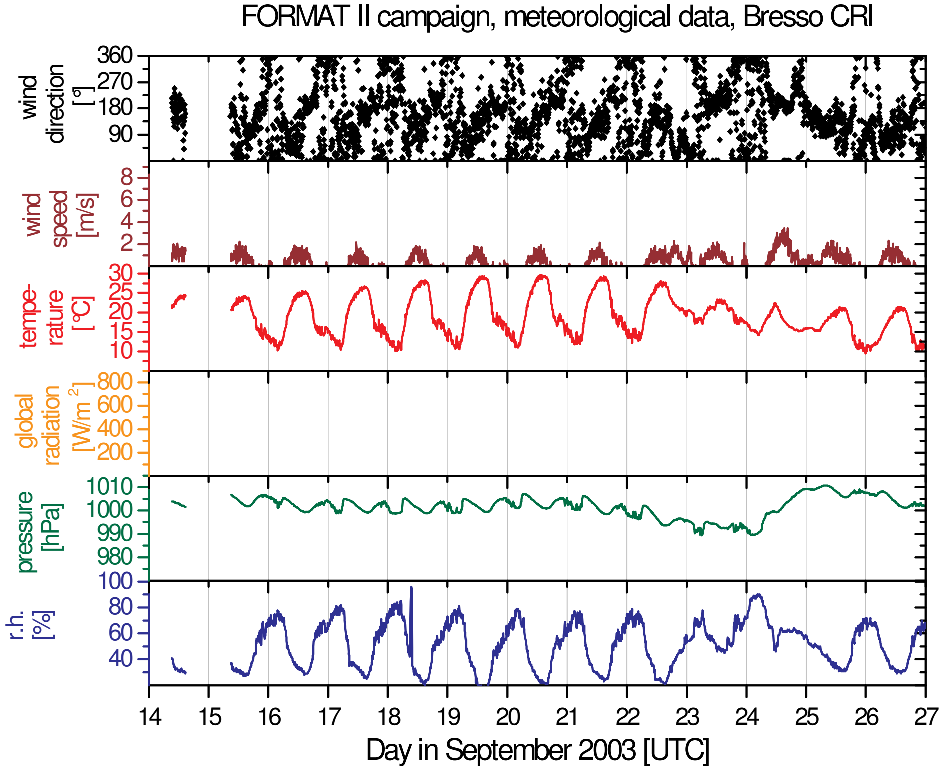

Figure 6-7: Time series of the most relevant meteorological parameters. The radiation measurements failed after 13/09/2003 (Claudia Hak, personal communications, file date: 03/02/2004).

In the following three days the weather got worse and it was cloudy again. After 24/09/2003 the sun was shining again and only very small clouds were observed. Based on the weather forecast the time was used for four more flights until 27/09/2003. After this day bad weather was forecasted and we finished our activity on 27/09/2003. It should be mentioned that the forecast was right and no more flights would have made sense afterwards.

The time series of the NO_2, O_3 and HCHO mixing ratios observed in Bresso are given in Figure 6-8 (Claudia Hak, personal communications, 17/04/2005).

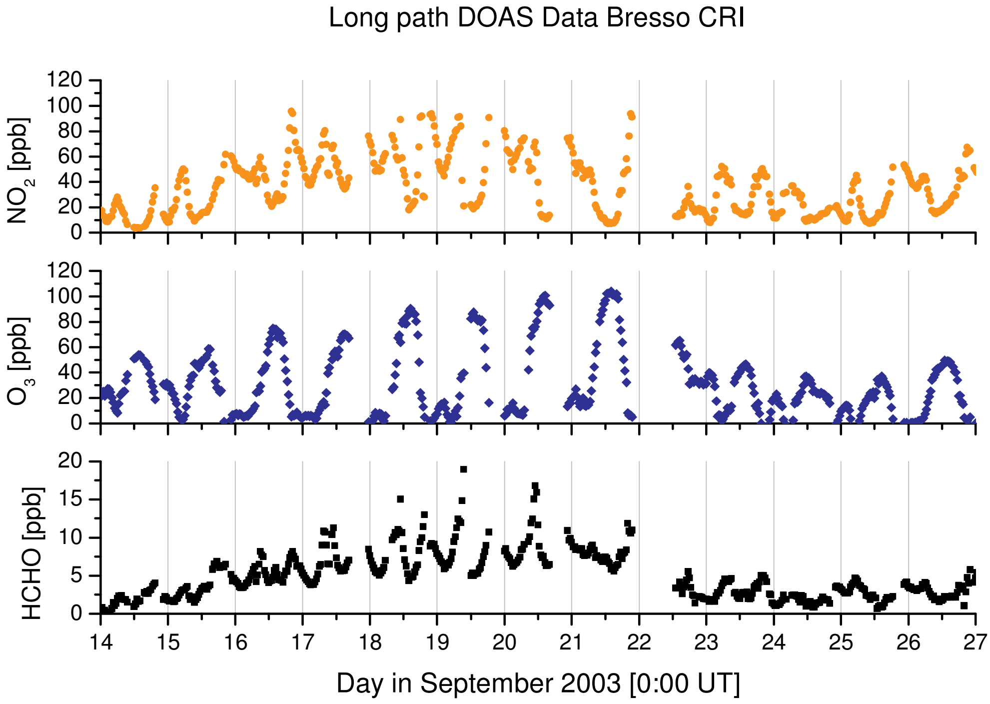

Figure 6-8: Data from Long Path DOAS observations during the FORMAT II campaign in Bresso (Claudia Hak, private communication, file date: 17/04/2005). In the period from 14/09/2003 to 21/09/2003 the mixing ratios of ozone and formaldehyde increased from day to day. After 22/09/2003 they decreased rapidly and remained low until the end of the campaign.

6.4.II FORMAT II Measurement Flights

In the second FORMAT campaign flights across the city centre of Milano were no longer allowed, and the maximum allowed flight altitude was strictly limited to 2000 ft. This is one reason why we focused on the second aim of the FORMAT project: to estimate the emission strength of single point sources like refineries, power plants or cement works. An overview is given in Table 6-D:

Date Time	Flight track	Weather conditions	Comments
14.09.2003 11:18 – 12:59 Sunday	Pavia, Spessa, Boxes around Cremona refinery	No clouds	No vis data, instrument did not run
16.09.2003 10:30 - 12:11 Tuesday	Box: Pavia, Codogno, Calusco, Saronno, Pavia, three boxes around Sannazzaro refinery	No clouds, low winds observed (smoke, or flags) various directions.	At 10:35 the UV instrument stopped, many agricultural fires in the southern part.
17.09.2003 10:30 – 12:30 Wendesday	Box: Pavia, Codogno, Calusco, Saronno, Pavia, three boxes around Sannazzaro refinery	No clouds, low winds observed (smoke, or flags) various directions.	Many agricultural fires in the southern part.

Date **Time**	**Flight track**	**Weather conditions**	**Comments**
18.09.2003 11.51 -13:46 Thursday	two times box: Pavia, Codogno, Calusco, Saronno	Bad visibility, as usuall around Milano. No clouds	Passed Calusco, in lee and luff, with one hour difference
19.09.2003 12:20 – 14:30 Friday	Big F: Pavia-Saronno-Alzate	No clouds	Trouble with CCD cooling. Higher flight alitude in the North
20.09.2003 9:58 – 12:11 Saturday	Box around and cross over Milano	Very hazy	The only flight with flight altitude higher than 2500 ft close to Milano
25.09.2003 12:50 – 15:20 Thursday	Pavia, Mantova, Montagnana, Mantova, Pavia	Few small clouds, no clouds in the area of interest.	In the area of Montagnana a comparison flight was made with the Dimona
26.09.2003 8:50 – 11:21 12.38 – 15:01 Friday	Pavia, Mantova, Porto-Tolle, Reggio nell'Emiglia, Sermide,Ostiglia (powerplants) Montagnana, Mantova, Calusco	Small clouds at the beginning of the flight	No vis data until Mantova – computer crashed. Fueling stop in Reggio nell' Emiglia. In the area of Montagnana a comparison was made with the microlight
27.09.2003 Saturday	Pavia, Mantova, Porto-Tolle, Sermide, Ostiglia, Mantova, Spessa, Pavia	Some clouds at the coast.	One scan following the Po-river to the coast. This flight was made for SCIAMACHY –validation

Table 6-D Overview over the FORMAT II flights, the weather was much better than in FORMAT I, and longer flights to the Adriatic coast (Porto-Tolle) were made. Both spectographs worked during the whole period – with some short failures. The Gyro and the GPS devices are not listed here. But in general they also worked fine.

During the first part of the campaign we mainly concentrated on the area around Milano. In the last three days four flights were performed to study the distribution of HCHO and NO_2 all along the Po from Milano to the Adriatic coast. As the airspace around Milano was strictly limited, the opportunity was used to combine the long range flight with a vertical scan which is possible only east of Verona. The most interesting result of the campaign was gained on the 26/09/2003 when studying the emission plumes of two power plants situated on the river banks of the Po. The SO_2 emissions are published in [Wang et al., 2005 b] the publication for the NO_2 distribution is preparation [Pundt et al, 2005a] and is presented in chapter 8.2.
An overview of the observed dSCD for one line of sight (-7°) is given in the attachments.

7 Results of the SCIAVALUE Campaigns

The validation of SCIAMACHY was one of the main aspects of the AMAXDOAS activity [Heue et al., 2005]. The AMAXDOAS instrument can separate the tropospheric from the stratospheric column of NO_2. In a first part of this chapter we will compare SCIAMACHY tropospheric columns to AMAXDOAS columns. Due to the similar measurement principle, both slant and vertical columns can be compared. However most of the flights led over unpolluted areas over which a comparison of tropospheric columns is less useful (comparing zero to zero), hence we concentrate on flights over central Europe.

The comparison of stratospheric columns is possible in remote regions as well, and will be discussed for flights where no tropospheric NO_2 is expected.

A brief description of the SCIAMACHY instrument and its mission was already given in chapter 5.12. The analysis of the SCIAMACHY data is not described in this work depending on the scientific product the retrieval is described in [Richter et al., 2004] or [Beirle, 2004].

Perpendicular to the flight direction SCIAMACHY scans an area of 960 km divided in 16 sub-pixels of 60 km each. In flight direction the pixels measure 30 km. For the comparison all the AMAXDOAS data across the corresponding SCIAMACHY pixel are averaged.

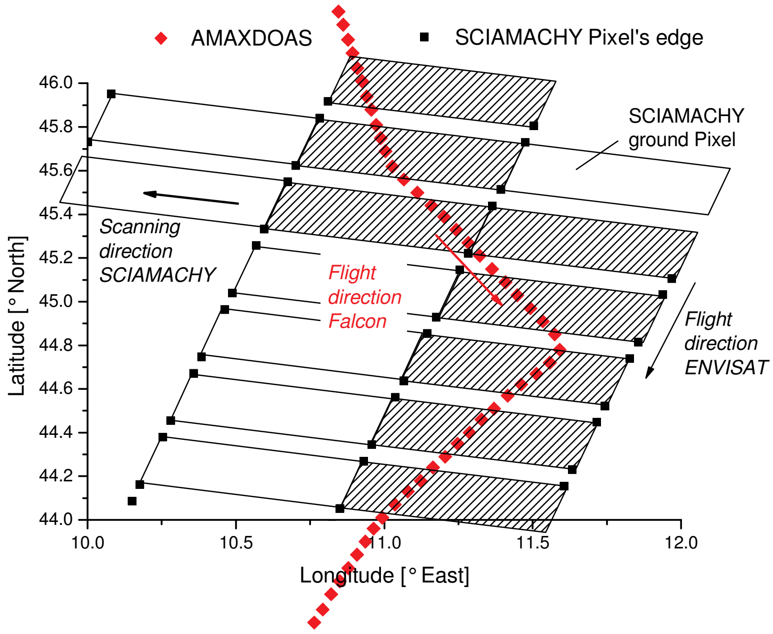

Figure 7-1: SCIAMACHY ground pixel and the flight route of the Falcon on 19/02/2003 for the same region (Po basin). The AMAXDOAS ground pixels are 6.6 km long and 400 wide, hence the shown squares are only a very rough approximation.

In Figure 7-1 the SCIAMACHY pixels covering the Po basin and the AMAXDOAS measurements along the flight on 19/02/2003 are shown. The SCIAMACHY measurements taken into account for further comparison (section 7.1.I) are marked as hatched.

The AMAXDOAS measurement in the gaps (about 6 km wide) between two SCIAMACHY pixels were not ignored but assumed to belong to the closest SCIAMACHY pixel. Nevertheless it is still obvious from the Figure 7-1 that averaging cannot completely solve the problem of different spatial resolution. The difficulties originating from the different spatial resolution depend on the local gradients. Most of anthropogenic NO_x is emitted by point sources like power plants or by the people living in towns. It is obvious that SCIAMACHY cannot resolve every power plant (chapter 8.2), especially not in a highly polluted area. But what about a town's plume – can this be resolved by SCIAMACHY?

For the large town of Milano (~5 million inhabitants including the suburbs) the plume is about 20 km wide (chapter 8.1), therefore SCIAMACHY stills observe highly polluted and “clean” air together in many ground pixels. This effect leads to a smoothing of local trace gas concentrations.

7.1 Validation of tropospheric Nitrogen Dioxide Columns

For the validation of tropospheric NO_2 columns it is essential to chose flights where polluted and unpolluted area were observed and SCIAMACHY measurements were performed simultaneously, hence the best flights were those crossing central Europe (chapter 6.1.II). Unfortunately not all spectra measured by the SCIAMACHY instrument have been provided to the scientific community by the ESA up to now.

- 19/02/2003 from Basel to Tozeur crossing the Po basin.
  SCIAMACHY data from Andreas Richter via personal communication 14/04/2004 the retrieval is described in [Richter et al., 2004].
- 03/03/2003 from Tozeur to Oberpfaffenhofen crossing Marseille.
  No tropospheric NO_2 data from SCIAMACHY are available.
- 10/03/2003 from Oberpfaffenhofen to Kiruna crossing the Ruhrgebiet.
  SCIAMACHY data from Steffen Beirle via personal communication 2.12.2004 described in [Beirle, 2004].
- 19/03/2003 local flight from Oberpfaffenhofen, crossing the Netherlands, Belgium and Luxemburg.
  No tropospheric NO_2 data from SCIAMACHY are available.

There are no tropospheric NO_2 columns from SCIAMACHY available for September 2002, neither in Bremen nor at KNMI or in Heidelberg.
From nine interesting flights suitable for a comparison of tropospheric columns there are only two were SCIAMACHY and AMAXDOAS data are available. For both data sets a comparison is shown, the first (19/02/03) will be discussed in detail [Heue et al., 2005]. The second flight (10/03/2003) is discussed less detailed. Some arguments of the previous discussion (19/02/2003) hold here as well and it is not necessary to discuss all of them in detail again. A first comparison between these data sets is already given by Heue et al, [2004].
For both studies (19/02/2003 and 10/03/2003) we first compare the tropospheric slant columns, then we try to find the most realistic settings to calculate the tropospheric AMFs and conclude the comparison with a validation of the “Near Real Time” data-products.
As the AMFs have a large influence on the results, the comparison of both slant and vertical column is shown. This allows us to separate the influences of the slant column and the AMF calculations. According to [Boersma, et al., 2004] and [Heland et al. 2002] the errors introduced by the uncertainties of the AMF are can even exceed 50 %.

7.1.I 19/02/2003 from Basel to Tozeur

The plane took off in Basel at about 8:00 GMT, flew south east towards the Alps and crossed the Alps, the Po basin, the Mediterranean and reached northern Africa where we landed in Tozeur to fly across the Sahara desert the next day. The flight track is shown in Figure 7-2, besides the Italian peninsula and the snow caped Alps, some details can be made out here e.g. The Schwarzwald and the Apennines (also snow capped), and the region of Lago di Garda and the Adige valley (less snow).

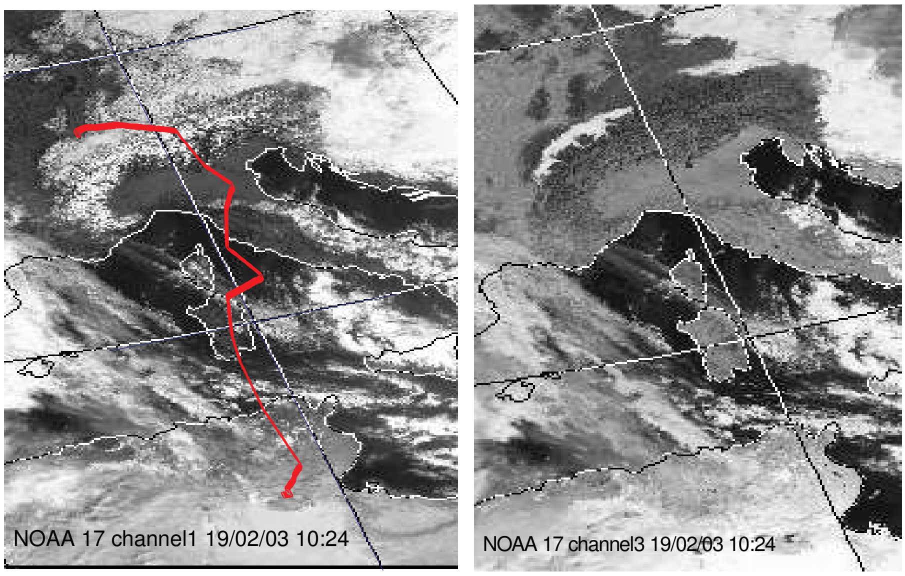

Figure 7-2: Satellite image of the cloud coverage (19/02/2003) (www.sat.dundee.ac.uk/auth.html, 24/02/2005). Channel 1 visible (right) and channel 3 short wave infra-red (left). The flight track was overlaid in red.

7.1.I.a Cloud Coverage along the Flight

Before discussing the measurement results in detail we will check the weather conditions on this day along the flight track. According to our log we observed dense clouds between Basel and the Alps. These dense clouds can be seen in the satellite image (www.sat.dundee.ac.uk/auth.html, 24/02/2005). In Figure 7-2 some smaller cloud east and south of Sardegna can be realised, which were also reported in the log. The Po basin was very hazy on this day as reported in the log. The haze seems too thin to be observed from the NOAA satellite in the visible or the infra-red channel.

Often O_4 is used as an indicator for clouds and light path enhancements and to approximate the aerosol extinction [Wagner et al., 2004 and chapter 4.5.II or III]. In Figure 7-3 the observed O_4 dSCD is shown, here an offset was added to account for the absorption in the reference spectrum. In the simulation many effects like different surface albedo, clouds or changes in the temperature between Basel and Tozeur were neglected as well as the flight altitude during ascent and descent.

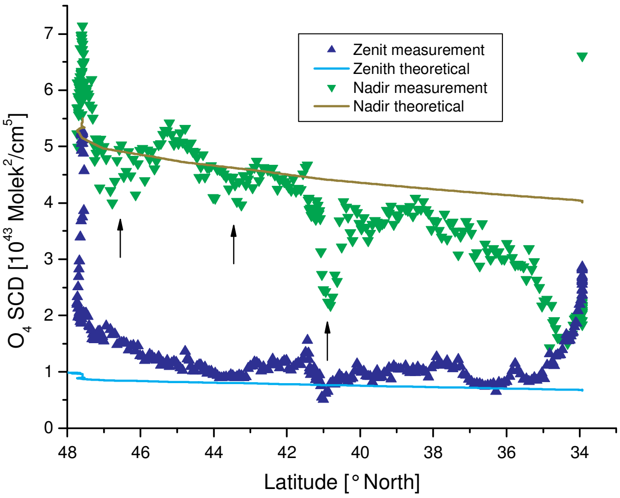

Figure 7-3: simulated and measured O_4 SCD. An offset was added to the measured dSCD to compensate the reference's SCD. In the zenith a strong influence of the flight altitude is observed during ascend and descend. In nadir other effects like ground albedo and ground elevation is super positioned to this altitude effect. Also the cloud coverage is more important here.

The observed dSCDs in the nadir show some strong structures around 8:30 UT, 8:50 UT and at 9:20 UT. The first two can be attributed to the Alps and the Apennines respectively. The strong and rapid decrease at 9:20 UT was caused by the dense and high clouds north-east of Sardegna. When flying over the mountains strong variations in the O_4 were detected. Here the conditions change rapidly between snow capped mountains and dark valleys.

Between the Alps and the Apennines over the Po basin no clear structures are observed, hence we can assume the conditions like the aerosol load and albedo in the basin to be relative homogenous. In the Po basin high NO_2 column densities are observed, therefore this region is very important for the comparison discussed below.

7.1.I.b Validation of the Validating Instrument

The similar measurement techniques of SCIAMACHY and AMAXDOAS are big advantage for the validation as both vertical and slant column densities can be compared. On the other hand both retrievals rely on certain assumptions used for the air mass factor calculation. For serious comparison additional information is necessary to substantiate the AMF simulations.

For the 19/02/2003 ground based in situ data from the ARPA (agencia regionale per la protenzione dell' ambiente, www.arpa.emr.it) in Bologna are available (private communications via Andrea Petritoli, 25/08/2004). In addition the aerosol optical thickness from AERONET Ispra (Zibordi, 2004, http://aeronet.gsfc.nasa.gov, 17/01/2005) and the soundings from Linate and San Pietro (available at the University of Wyoming http://weather.uwyo.edu/upperair/sounding.html, 17/01/2005) were used. The mixing layer height in Linate and San Pietro can be assumed to be 160 m AGL at minimum in the morning hours, the vertical aerosol optical thickness was 0.3 and stayed constant for most of the day. This information was used to calculate the AMFs for AMAXDOAS and SCIAMACHY (chapter 4.4.III). The four ground based in situ data closest to the flight track were used to calculate the tropospheric vertical column: $TVCD = \int_0^{MLH} c(z)dz$.

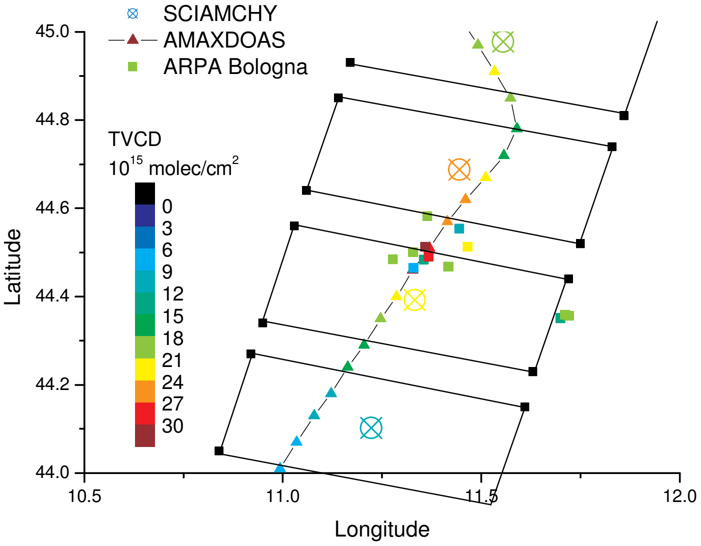

Figure 7-4: Ground based data in Bologna (squares), AMAXDOAS (triangles) and SCIAMACHY (circles) close to Bologna. For all data sets a mixing layer height of 200 m was assumed.

The situation close to Bologna is shown in Figure 7-4. For all instruments 200 m mixing layer height is assumed, here. For the separation of stratospheric and tropospheric signal the standard methods (linear interpolation and reference sector - Figure 7-7a) are used.

For the comparison with the AMAXDOAS data, the four in situ measurements situated closest to the flight track are averaged. The mixing ratio (42 ± 22 ppb) was assumed to be constant in the mixing layer, here the error is given by the standard deviation. For a mixing layer of 200 m this resulted in a tropospheric vertical column of (23 ± 12)*10^{15} molec/cm^2 and in (34 ± 18)*10^{15} molec/cm^2 for 300 m (Figure 7-5).

In Figure 7-5 the TVCDs for the ground based in situ data, AMAXDOAS and SCIAMACHY are shown. We studied different MLHs and good agreement can be found for a MLH between 200 m and 300 m above ground.

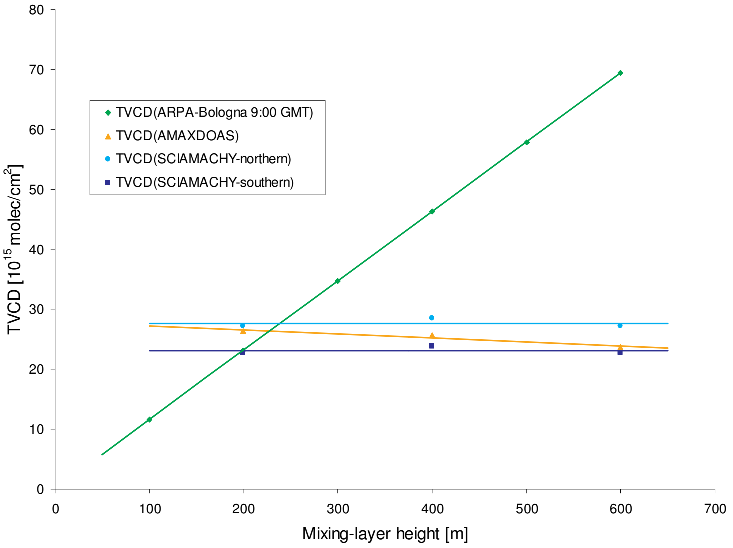

Figure 7-5: Tropospheric vertical NO2 column density derived from the in situ data of ARPA Bologna (green), AMAXDOAS (orange) and SCIAMACHY (blue). In Figure 7-4 it is shown that many of the ground based data are in the gap between two SCIAMACHY pixels, therefore the values for both pixels are shown. The southern SCIAMACHY pixel covers the first mountains of the Apennines.

7.1.I.c Comparison of the tropospheric Slant Columns

The SCIAMACHY data used for this comparison were retrieved by Andreas Richter at the IUP-Bremen. The analysis is described in detail in [Richter et al., 2004]

A general problem of the comparison to SCIAMACHY data is the different spatial resolution of AMAXDOAS, as discussed in the introduction of this chapter. During this flight (19/02/2003) two cases of strong local gradients were observed by the AMAXDOAS, they are marked in Figure 7-6: In the southern Alps (45.8° N) the Falcon crossed the Adige valley. One of the most important highways between Italy, Austria and Germany, respectively, runs through this valley. Neither from Figure 7-2 nor from the O_4 observations can we conclude whether there was smog in this valley as well. For SCIAMACHY this signal is too weak, the signal of the large pixel is mainly influenced by the clean air over the snow capped mountains. Here the high albedo of the snow leads to a large influence of the mountains compared to the dark and polluted valley.

For the tropospheric columns shown here the reference sector method and the linear fit of the minima were used. To emphasis the gradients in the viewgraph all AMAXDOAS data are shown separately. In the following we will use the AMAXDOAS data averaged across one SCIAMACHY Pixel.

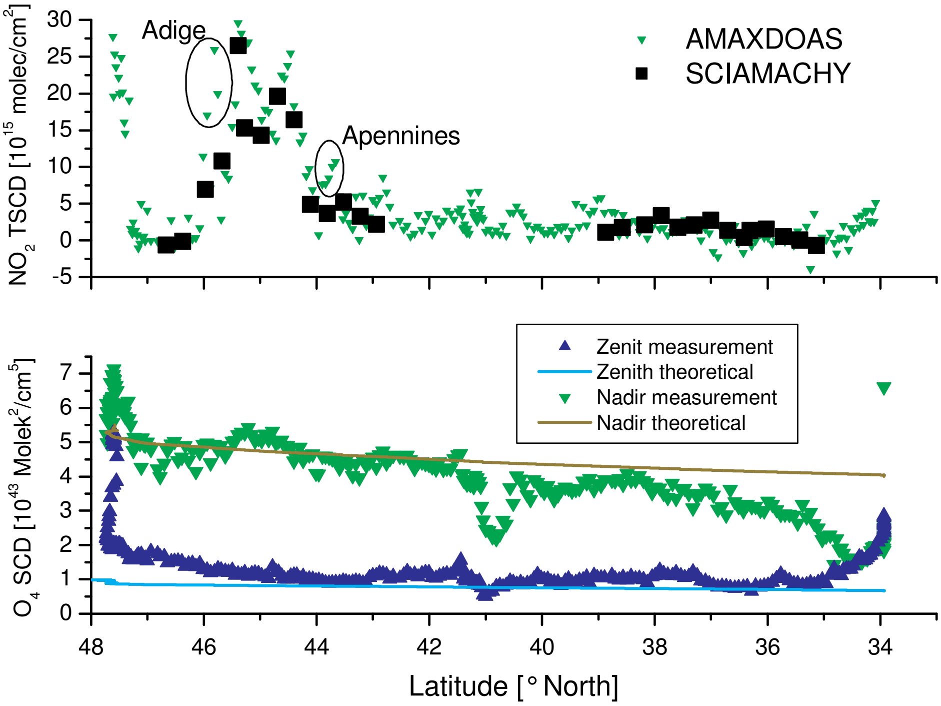

Figure 7-6: Tropospheric slant column density versus the latitude observed on 19/02/2003. Between 43.8° N and 40.2° N SCIAMACHY did not measure in nadir mode. In the Alps and Apennines higher values are observed by AMAXDOAS than by SCIAMACHY. In the Alps the peak can clearly be attributed to the Adige Valley.

Different methods for the separation of tropospheric and stratospheric columns were introduced in chapter 3.4. Here we want to investigate the influence of the separation for the correlation between SCIAMACHY and AMAXDOAS. Figure 7-7 a) to d) show correlation plots of the SCIAMACHY slant columns with the ones measured by AMAXDOAS. Four combinations of different background corrections are shown:

a) The standard combination where the linear correction for the AMAXDOAS and the reference method for SCIAMACHY is used. (e.g. Figure 7-6)
b) both AMAXDOAS and SCIAMACHY were corrected with the linear fit method,
c) the 1/cos(SZA) method was applied to AMAXDOAS data and the reference sector method to SCIAMACHY,
d) 1/cos(SZA) was used for both datasets.

The two missing combinations (linear for AMAXDOAS versus 1/cos(SZA) for SCIAMACHY and vice versa) are not shown here as they do not contain further information.

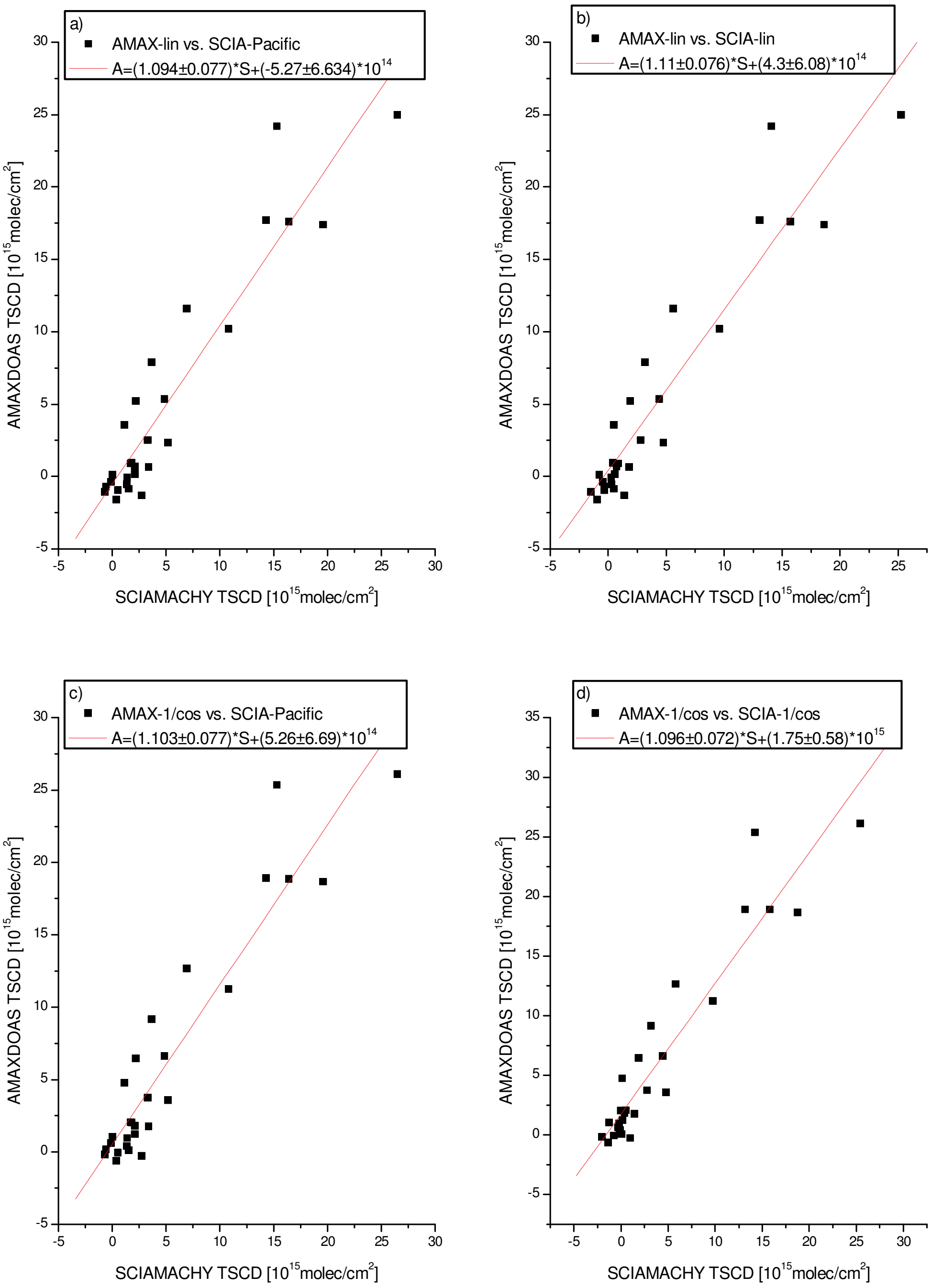

Figure 7-7: Comparison of tropospheric slant columns (19/02/2003) for different separations between tropospheric and stratospheric column densities:

a) Upper left panel: Reference for SCIAMACHY and linear fit for AMAXDOAS (Figure 7-6)

b) Upper right panel: For both instruments a linear fit was used.

c) Lower left panel: reference for SCIAMACHY and 1/cos(SZA) for AMAXDOAS.

d) Lower right panel: 1/cos(SZA) was used for both.

As can be seen the influence of different corrections on the slope of the correlation is very small, within the error, all the slopes equal 1.1. The AMF for this special situation are given in chapter 4.4.III. According to the AMF a difference in the slant column densities in the observed range can be expected. The main reason is the difference sensibility to tropospheric absorption due to different altitude of the instruments.

The intercepts of the fits are zero within the error, except for the combination d). The 1/cos(SZA)-Method seems to introduce an offset to the SCIAMACHY data of the order of -1*10^{15} molec/cm^2. A comparison to c) excludes an offset in the AMAXDOAS data here.

7.1.I.d Comparison of the Vertical Columns

For the comparison of the vertical columns the standard tropospheric slant columns i.e. linear interpolation for AMAXDOAS and reference sector method for SCIAMACHY were used.

As already mentioned, the tropospheric slant columns of AMAXDOAS are about 10% higher than those observed by SCIAMACHY. The AMF were calculated for three different heights of the mixing layer. According to the sensitivity studies discussed in chapter 4.4.III the sensitivity of both instruments increases with an increasing thickness of the mixing layer height.

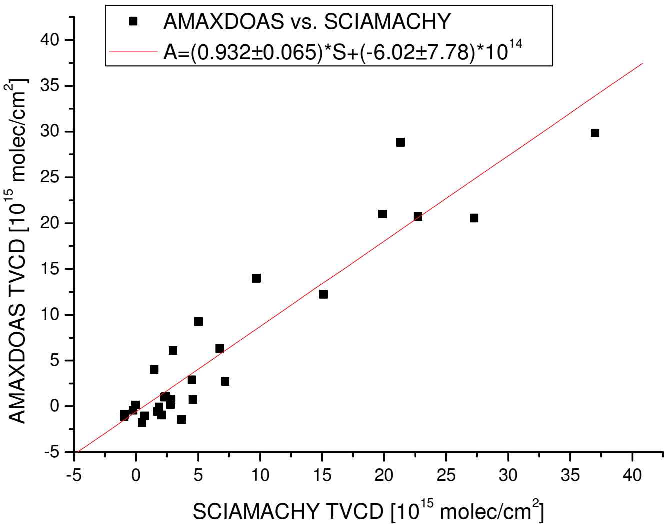

Figure 7-8: Correlation plot between SCIAMACHY and AMAXDOAS NO_2 vertical columns. For both instruments a MLH of 200 m was assumed for the calculation of the AMF.

The correlation between SCIAMACHY and AMAXDOAS tropospheric vertical columns is shown Figure 7-8. Here the AMF with a 200 m MLH was used, for both SCIAMACHY and AMAXDOAS. The correlation is quite good, the slope equals 0.93 ± 0.06 and the intercept is zero within the error. The errors given are based on the fluctuations and derivations of the data, any systematic effects are ignored. Of course the systematic effects influence the correlation as well; in the following we will discuss some of them.

The different spatial resolution is one of the main causes for different results. This effect can only be minimized to a certain degree by averaging the AMAXDOAS measurements. For the overall comparison, it only results in a scatter of the individual results compared to the regression.

The NO_2 cross sections used for the analysis were very similar but not the same, both analyses used cross sections for temperatures in the stratospheric range – 223 K for AMAXDOAS and 243 K for SCIAMACHY. The difference in the differential cross sections is below 5 % (Figure 7-9).

The error introduced by using the wrong temperature for the cross section can be up to 20% [Boersma et al., 2004]. However in our case, this effect would influence both instruments in this comparison in the same way. The correlation would be very similar except that both instruments would observe larger slant columns.

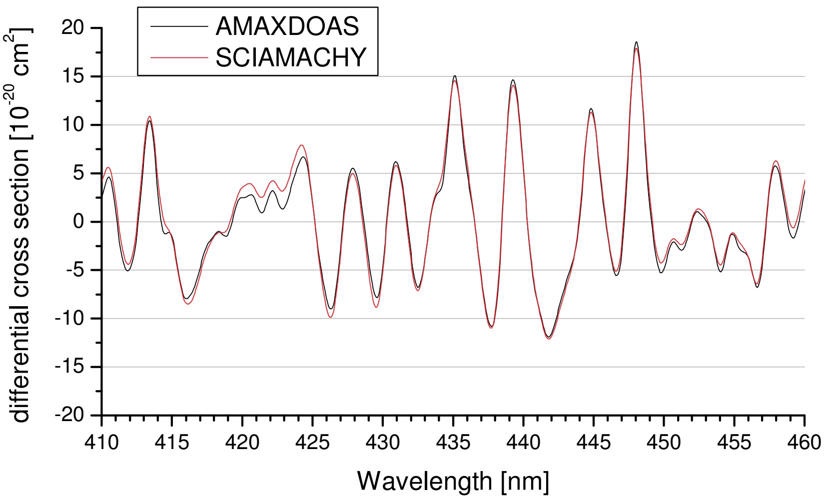

Figure 7-9: differential NO_2 cross section used in the different analysis procedures both convoluted with the AMAXDOAS instrumental function: Red line SCIAMACHY, black AMAXDOAS.

The time difference between the AMAXDOAS and the SCIAMACHY overpass, of course also influences the observed columns. AMAXDOAS crossed the Po basin between 8:40 and 8:50 GMT whereas SCIAMACHY scanned this region at 9:49 GMT. Ground based data in Bologna showed the local mixing ratio decreased from 42 ppb to 35 ppb (average of 4 points close to the flight track) between 9:00 GMT and 10:00 GMT. If the MLH increased (in the same way) the vertical column would still be the same, and according to the time of the day we would expect the latter to be the reason for the observed decrease rather than transport or photochemical NO_2 destruction. The wind speed on this day was about 3 m/sec from north-west, so the transport of the air masses can be approximated to be 10 km in the maximum and the same air mass would still be covered by the same SCIAMACHY pixel.

Also the Solar Zenith Angle changes in the time between the two observations, for AMAXDOAS the average SZA was 67.5° and for SCIAMACHY it was 61°. In chapter 4.4.III the AMFs for various mixing layer heights were discussed. The influence of the solar zenith angle especially in this range is below 5 %. According to the AMF a difference in the slant columns can be expected in the way we observed it. Other reasons like different cross sections, temporal variations or transport of air masses are unlikely but cannot be excluded.

7.1.I.e Comparison to the Near Real Time Product

Several versions exist of the SCIAMACHY tropospheric vertical columns which mainly differ in the assumptions made for the air mass factor calculations. In the last sections, the AMF was determined using external information for the time and location studied, and very good agreement was found between satellite and AMAXDOAS measurements. However, the near real time (NRT) images of tropospheric vertical NO_2 columns posted in the world wide web on http://www.doas-bremen.de (as used in Figure 7-10) use a simplified air mass factor where the NO_2 is constant in the lowest 1000 m and decreases linearly up to 2000 m and a maritime aerosol is used [Richter and Burrows, 2002]. Here we compare the AMAXDOAS measurements with the near real time products.

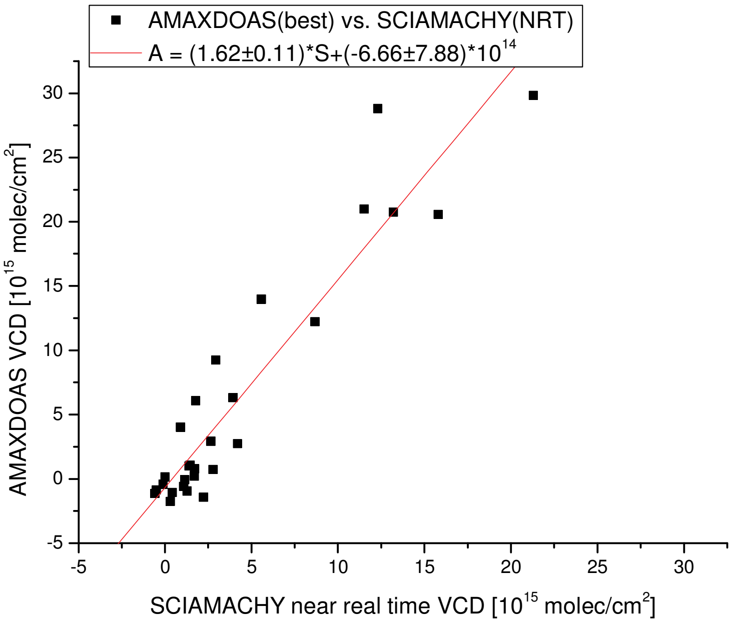

Figure 7-10: Comparison of SCIAMACHY near real time NO_2 data to AMAXDOAS measurements.

The results are shown in Figure 7-10. The linear fit now has a slope of 1.62 but the intercept is still close to zero ($(-6.66 \pm 7.88) * 10^{14}$). As discussed above the SCIAMACHY and AMAXDOAS data will agree far better than that, if the correct settings for the AMF are used. Hence the discrepancy can be explained by the difference between the two sets of AMFs. The standard SCIAMACHY AMFs are about 60% higher than those calculated here for the Po valley.

Although the error of 60% in the AMF is large, it is within the range quoted in previous papers (e.g. 50 % Heland et al., 2002). The reason is that the specific atmospheric conditions in the Po valley (high aerosol load and low mixing layer height) are very different from the assumptions made for calculating the standard AMF.

7.1.I.f Excursion: Winter Smog Event in northern Switzerland

The comparison of the SCIAMACHY data to AMAXDOAS from this flight was finished with a very good agreement. Nevertheless I want to add a discussion of the AMAXDOAS observation over northern Switzerland. This is not only done for private interest, as I lived in Konstanz (Germany) for many years, but also because this was one of the largest smog events observed in this region in recent years.

The clouds north of the Alps (Figure 7-2) belong to a smog situation that developed in this area form 19/02/2003 until the 22/02/2003 [NZZ, 07/03/2003] and references therein (www.Ostluft.ch, 21/04/2004). According to these references this was one of the strongest smog events in this area in the last decade. The time series for February 2003 of the main pollutants measured in the centre of Zürich is shown in Figure 7-11. Beginning with the 19/02/2003, the concentrations of NO_2 and SO_2 as well as the number of particles increase. In addition to the situation in the centre the ozone data from the mountain station (Bachtel) is shown, where an increase is observed as well. According to the chemistry studied in chapter 2, we can assume this station is not affected by the smog situation. The maximum mixing layer height must be below this station (1400 m ASL) as expected for winter smog conditions.

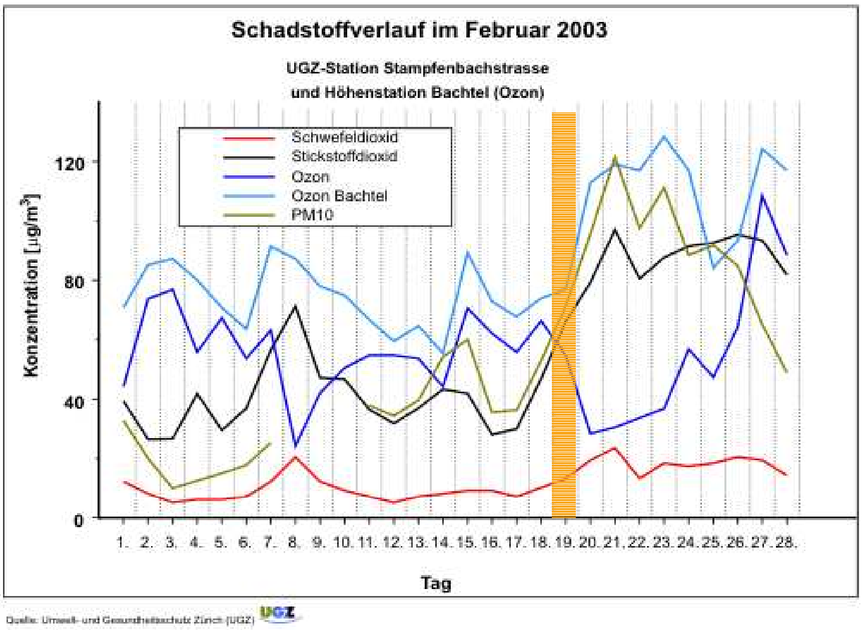

Figure 7-11: Concentration of the main pollutants in Zürich in February 2003.
The NO_2 is shown in black, the O_3 in blue. The light blue was observed in 1400 m altitude (1000 m above the city). The mixing height was lower than 1000 m, and the NO_2 was below this measurement station (www.Ostluft.ch, 21/04/2004 – Umwelt und Gesundheitsschutz Zürich).

Unfortunately there was no SCIAMACHY nadir observation over this area on this day and it is therefore not part of the previous discussions. The situation described above was observed in Zürich. As a smog event is often caused by large scale meteorological conditions (inversion), a similar situation might be observed in northern Switzerland and the German boarder including the Bodensee (Lake Constance).

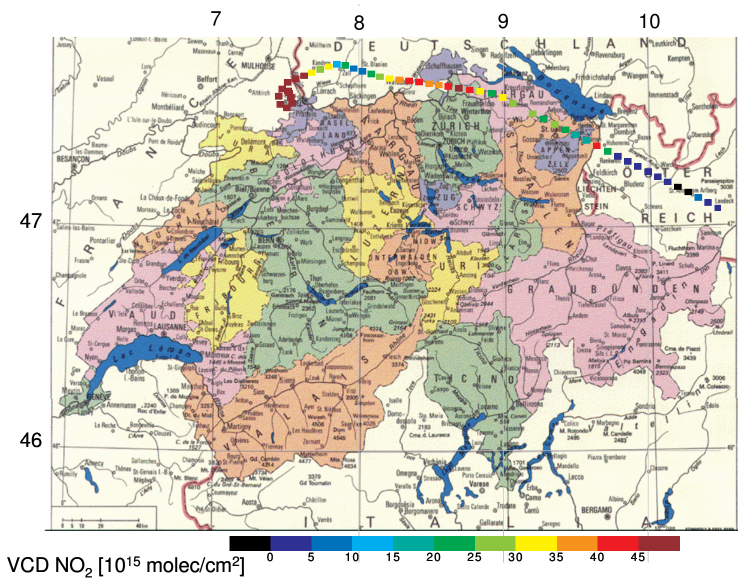

Figure 7-12: Observed tropospheric vertical NO_2 columns in northern Switzerland and southern Germany. High values are observed in the region of Schaffhausen and in the Kanton of Zürich. Further to the east towards Appenzell the values decrease.

In Figure 7-12 the VCD were overlaid to a political map of Switzerland. The observed high column densities are most probably caused by the mentioned smog event. The highest values are observed between the region of Schaffhausen and the north of the Kanton Zürich. Further to the east between St. Gallen and Appenzell lower column densities were measured. On the boarder between, Austria and Switzerland one single data point with a high column density is observed in the alpine Rhine valley. It may be caused by both the smog and the emissions of the highway, following the valley.

The exact reason for the observed difference between the east and the west is hard to find, because there are more than one important effects involved here. The observed column density is the integrated signal from the ground to the mixing layer height. In the eastern regions the ground level is higher (more than 600 m ASL compared to less than 400 m) whereas the absolute height of the mixing layer in the smog situation might be relative constant. Therefore the layer of the NO_2 is thinner but this does not mean the column density is less.

According to the Schweizer Bundesamt für Umwelt, Wald und Landschaft (BUWAL – www.umweltschutz-schweiz.ch/buwal/de, 21/03/2005) the emissions are similar in the regions, which where covered by the AMAXDOAs measurement (Figure 7-13).

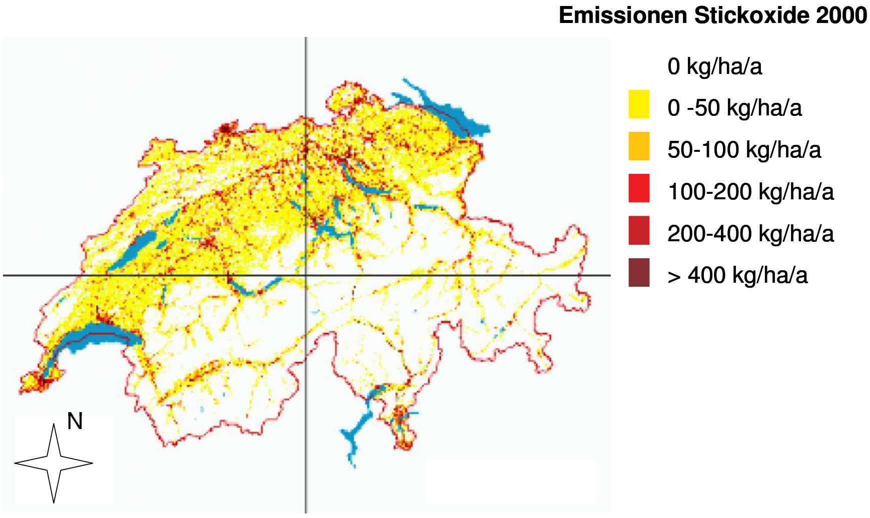

Figure 7-13: Annual averaged NO_x emission data in Switzerland, based on the Year 2000 data. In the interesting region south of the Bodensee no east-west gradient is observed (BUWAL – www.umweltschutz-schweiz.ch/buwal/de, 21/03/2005).

If the actual NO_2 is dominated by the emissions, we can expect the vertical column density to be the same. Hence the reason for the observed gradient can hardly be the local emissions although this cannot be excluded.

The local gradients in the in situ stations are very high depending mainly on local influences like traffic emissions. Therefore a comparison to these data seems to be not very useful.

A systematic influence of the measurement will be discussed in the following.

The different mixing layer height has a large influence on the observation (chapter 4.4.III). The instrument is more sensitive for tropospheric NO_2 when the mixing layer is higher. Hence, if the mixing layer height is lower in the east the instrument is less sensitive in this case and the observed columns will decrease. The effect is not strong enough to explain the observation completely because the respective AMF differ by about 20%.

During the observation the plane's flight altitude still increased from 7000 m close to Schaffhausen to 11000 m close to the alpine Rhine valley. The influence of the different flight altitudes was discussed in chapter 4.4.I and found be to small enough to be ignored here.

In chapter 3.4 two different ways of separating the tropospheric from stratospheric signal were introduced. The difference between the two methods is small for small solar zenith angle. At the time the Falcon flew over the region discussed here, the solar zenith angle was 75°. The effect of the different separations on the vertical column densities can be seen in Figure 7-14. We expected to find lower VCDs in the western part of the flight as the solar zenith angle was higher at the beginning. In total the effect is less than 15% and the observed gradient cannot be explained as the artefact caused by the simplified correction.

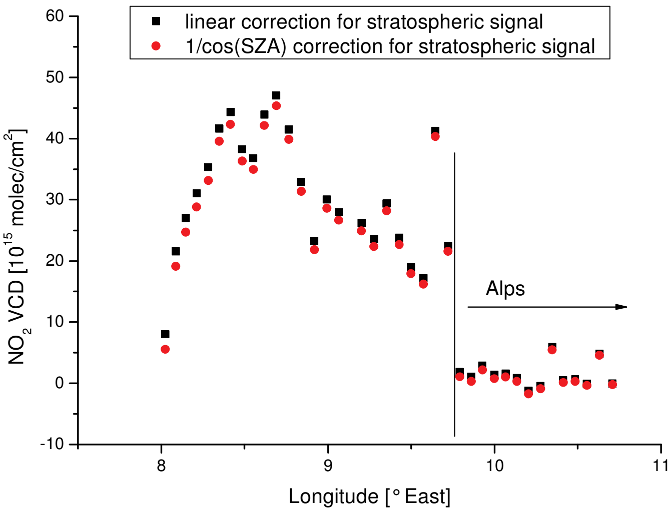

Figure 7-14: Vertical column density calculated for the two different approaches to correct for the stratospheric signal. As expected the influence is larger in the west, but the difference is o f the order of 10 % hence it cannot explain the east west gradient.

AMAXDOAS measurements are very sensitive for a change in the surface albedo. If there is snow during parts of the flight, this will strongly affect the observed column density. The higher albedo of the snow enhances SCD. Hence the observation would be explained if there was snow in the West (400 m ASL) but no snow 50 km further to the east (600 m ASL). According to our personal experiences this cannot be excluded but seems rather unlikely.

From Figure 7-2 we cannot conclude whether the observed cloud has the same optical density all along flight. If this was not the case, then the observed data would change due to the different cloud properties.

The observed gradient along the flight track might well be caused by a combination of many of the above mentioned explanation mainly the different mixing layer height, changes in the cloud properties as well as local gradients.

After this short excursion to an interesting smog event we will again concentrate on the main topic of this section: Validation of the SCIAMACHY instrument.

7.1.II 10/03/2003 from Oberpfaffenhofen to Kiruna

On the flight on 10/03/2003 from Oberpfaffenhofen to Kiruna also polluted areas and clean air regions were observed. However the weather conditions were not as good as on 19/02/03, therefore the latter flight was chosen for a more detailed comparison. The SCIAMACHY data used for the comparison in the last section were retrieved by Andreas Richter in Bremen. In this section, I will compare the AMAXDOAS to the SCIAMACHY scientific product retrieved by Steffen Beirle from our own research group here at the Institut für Umweltphysik in Heidelberg. Details about the retrieval of this scientific product are described in [Beirle, 2004].

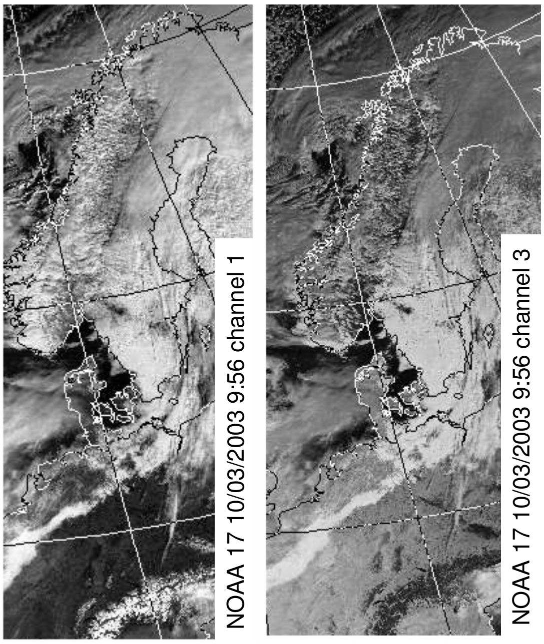

Figure 7-15: Satellite image (NOAA) showing the cloud coverage over central and northern Europe on 10/03/2003. The visible channel is shown on the left panel and the shortwave infra-red to the right. By comparison it is obvious that the Alps are cloud free and covered with snow. A large cloud can be made out (at about 50° North) close to the Ruhrgebiet, but no snow can be realized here. Also over southern Sweden dense clouds are observed, in northern Sweden there are less clouds but some snow.

In Figure 7-15 the cloud situation on 10/03/2003 is shown. Close to the Ruhrgebiet (51° N, 7° E), where the highest column densities are expected dense cloud influence the signal. The cloud coverage in this area was about 50%. In Figure 7-17 a photo of the real cloud situation is shown. More quantitative information is retrieved by the HICRU cloud algorithm direct from SCIAMACHY observations [Grzegorski et al., 2004].

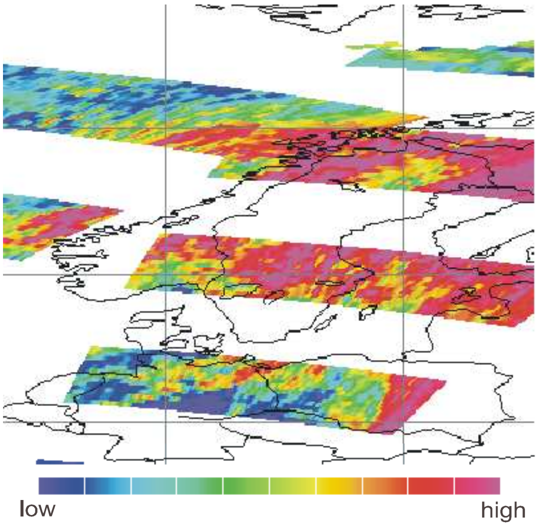

Figure 7-16: Cloud information based on the HICRU algorithm (Michael Grzegorski privat communication, March 2004)

Figure 7-17: Photo taken from inside the Falcon close to the Ruhrgebiet. The cloud coverage is less than expected from Figure 7-15.

The HICRU data are based on the PMD-measurements from SCIAMACHY which observe the same area as the SCIAMACHY NO_2 data, but have a better spatial resolution. The HICRU algorithm delivers not exactly one to one information of the cloud coverage but a combination of the information about coverage, cloud albedo and cloud top height.

Nevertheless, from Figure 7-16 we can conclude that only the southern part of the Ruhrgebiet was covered by a dense cloud of about 50% coverage. Further to the North the clouds were not that dense about 10% coverage (Figure 7-17).

A first qualitative comparison of the vertical columns is shown in Figure 7-18 – the standard products of both AMAXDOAS and SCIAMACHY were used for this illustration. High column densities are observed by both instruments for the Ruhrgebiet and a rapid decline to the north is also detected by both instruments. Nevertheless for a more quantitative comparison we will again compare the slant columns first.

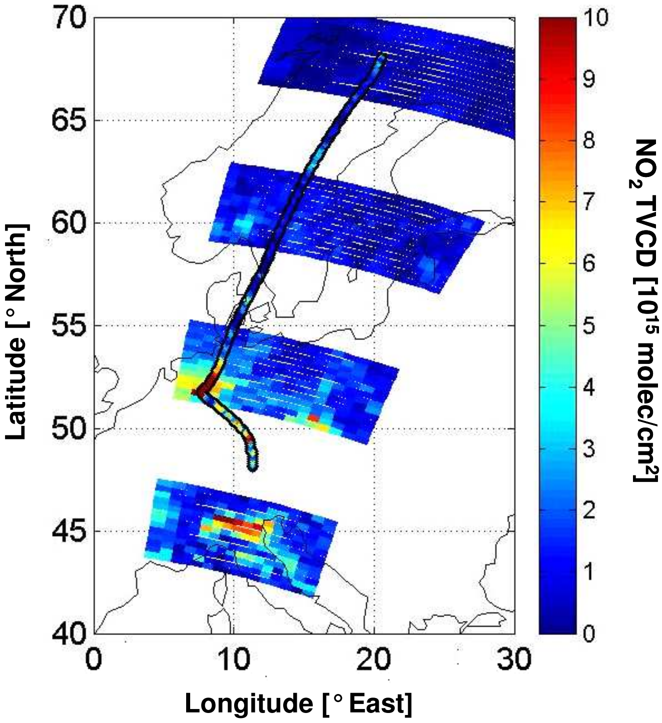

Figure 7-18: Tropospheric vertical column measured by SCIAMACHY and AMAXDOAS in 10^{15} molec/cm^2 along the flight. The highest column densities are observed close to the Ruhrgebiet.

7.1.II.a Comparison of the tropospheric Slant Columns

A comparison of the tropospheric slant columns is shown in Figure 7-19, in general they agree quite well. The high concentrations related to the Ruhrgebiet are detected by both instruments and the signal is of the same order of magnitude ($15*10^{15}$ molec/cm^2 and $17.5*10^{15}$ molec/cm^2). Over less polluted areas e.g. northern Germany and southern Sweden, a slight difference is observed.

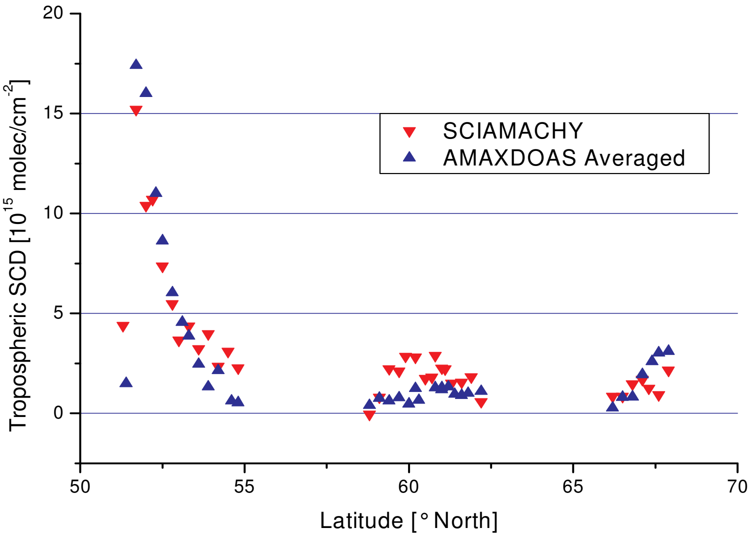

Figure 7-19: tropospheric slant column densities along for the flight (10/03/2003) as a function of latitude. The highly polluted Ruhrgebiet (51° N) is clearly observed by both instruments. Over northern Germany (54° N) and southern Sweden (60° N) SCIAMACHY observers higher SCDs than AMAXDOAS.

Following the discussion of 7.1.I.c we used the reference sector method for the SCIAMACHY data and a polynomial (2nd order) for AMAXDOAS to subtract the stratospheric signal.

A correlation plot for the tropospheric slant columns is shown in Figure 7-20. According to the higher sensitivity the TSCD from AMAXDOAS are higher. As discussed above there is a small offset in the SCIAMACHY values (southern Sweden), which leads to a negative intercept in the correlation plot.

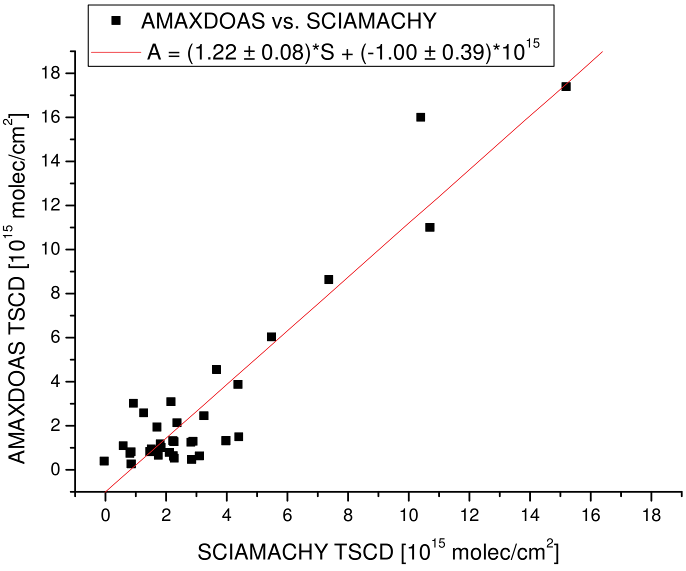

Figure 7-20: Correlation between SCIAMACHY and AMAXDOAS slant columns. As expected the AMAXDOAS values are higher.

7.1.II.b Comparison of the Vertical Columns

In section 7.1.I we underlined the importance of the correct settings for the AMF calculation. Now we try to find appropriate settings for the AMF calculations based on independent observations:

- The mixing layer height was about 1000 m (soundings in Essen, http://weather.uwyo.edu/upperair/sounding.html, 20/05/2005).
- The cloud coverage was discussed in detail above. The cloud altitude was estimated from the soundings to be about 6000 m.

Aerosol data from AERONET are not available for this day in the greater region. So we assumed a standard profile to calculate the AMF.

The influence of clouds on the AMF for both instruments SCIAMACHY and AMAXDOAS was discussed in a sensitivity study in the radiative transfer chapter 4.4.II. Both instruments AMAXDOAS and SCIAMACHY are influenced in a similar way by clouds in about 6000 m altitude, the sensitivity decreases rapidly and is very small for cloud coverage of 50 %. In the simulation the complete SCIAMACHY pixel is covered by 10 % cloud. In the real measurements this is hardly true and the observations average across the different region with different cloud coverage. The AMAXDOAS instrument is not that strongly affected by the different cloud coverage inside the field of view.

As the highest values are observed in an area with 10 % cloud coverage we suppose this to be the best setting for the calculation of the AMF. To find an appropriate choice for each observation point is not realistic and not useful[1].

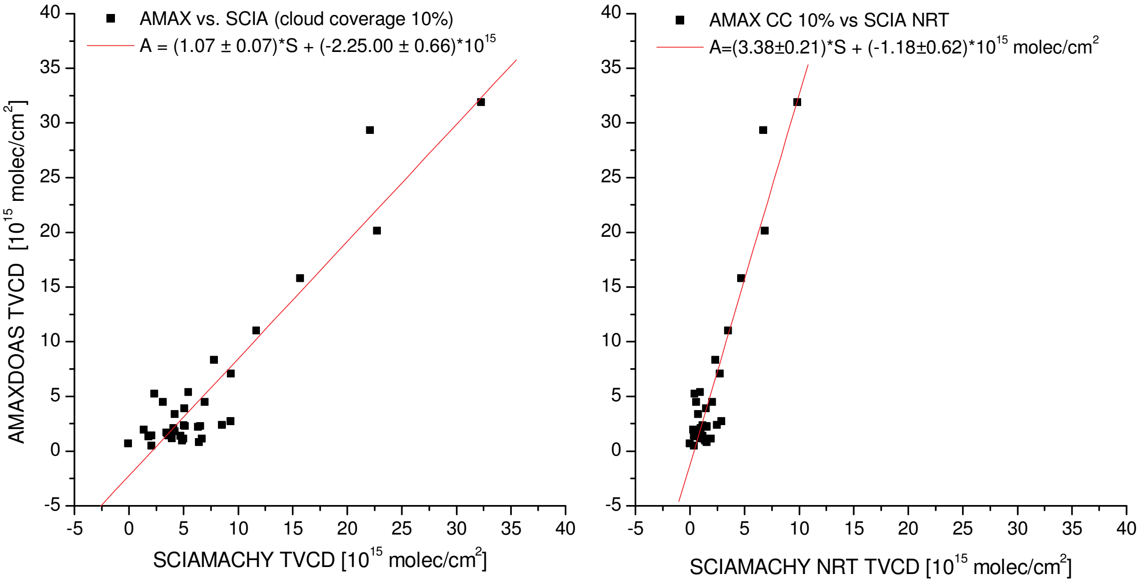

Figure 7-21: Correlation plots for AMAXDOAS versus SCIAMACHY NO_2 vertical columns:
Left panel: a cloud coverage of 10% was assumed for both instruments,
Right panel: the SCIAMACHY NRT was used, and compared to the most realistic AMAXDOAS dataset with 10% cloud coverage.

As well as for the flight on 19/02/2003 we did a direct correlation of the tropospheric vertical column. The results shown in Figure 7-21 (left panel) are based on AMF assuming 10 % cloud coverage, for the right panel the SCIAMACHY near real time product was used.

In a similar way as we did in sections 7.1.I.d and 7.1.I.e first a comparison using the most realistic settings for the AMF is given (Figure 7-21 left), afterwards, the SCIAMACHY near real time product (Figure 7-21 right) are compared to the same AMAXDOAS data.

According to the discussion above 10 % cloud coverage seems to be a realistic choice for the Ruhrgebiet where the highest column densities were observed, for the clean air regions like southern Sweden the cloud coverage is definitely under estimated (Figure 7-15 and Figure

---

[1] For an accurate description of the atmosphere as it is necessary for AMF calculation more information is needed. If all this information was available, nothing new would be gained from the satellite measurements.

7-16). The correlation (Figure 7-21 left) is quite good: the slope is close to unity (1.07 ± 0.07) but the offset is still large $(-2.25 \pm 0.66)*10^{15}$ molec/cm^2. According to the discussion of the slant columns it is mainly caused by the differences observed over the clean air regions. Over the polluted areas (higher TVCD) the agreement appears to be better. When the cloud coverage is increased the slope of the correlation increases as well, up to 1.22 when 50% are assumed. The offset gets even larger $((-8.04 \pm 2.61)*10^{15}$ molec/cm^2) in this scenario (not shown).

The scientific SCIAMACHY NO_2 near real time product is available on request per email. A comparison to this product is shown in Figure 7-21 right panel. For AMAXDOAS the data with 10% cloud coverage were used as we assume them to be most realistic. The difference between AMAXDOAS and SCIAMACHY is really large. The slope of the correlation equals more than 3, whereas the intercept is decreased to 1.18 ± 0.62. For the highly polluted regions the AMF used in the NRT product introduce a large error under the given conditions. Note the AMFs used here differ from those simulated with Tracy (chapter 4.4.II) (Steffen Beirle, privat communication, November 2004). Hence the surprisingly high difference can be explained as the AMFs used for the calculations differ by up to a factor of four.

The systematic effects discussed in the previous section will not be repeated one by one and discussed in detail. However we mention the main facts briefly. The NO_2 cross section used for AMAXDOAS was the same as in the previous section and assumed a temperature of 223 K. The difference to the cross section for SCIAMACHY can be neglected completely as the temperature was 221 K for the SCIAMACHY analysis.

SCIAMACHY measured over Germany at 9:50 UT at this time the Falcon had just taken off from Oberpfaffenhofen and headed north-west. Over the Ruhrgebiet the time difference was more than 30 min, over southern Sweden it equalled 2 hours. This also causes a difference in the solar zenith angle which is about 3° in the maximum. This difference is really small, due to the 2 hours time difference a large change in the SZA would be expected. The time of the day is the easy explanation. ENVISAT crossed Sweden at about 9:45 UT which is about 10:45 local time. The Falcon cruised over the same region about 12:45 LT the difference to the local noon is 1:15 hours for SCIAMACHY and 0:45 hours for AMAXDOAS.

The wind, which had a minor effect in the Po basin, blew with 1 to 4 m/s depending on the altitude from south-west (220°). According to the flight track of the Falcon over the east of the Ruhrgebiet the wind transported rather polluted air masses to the observation side. During the short time difference the air masses were transported 7.2 km in the maximum. So the difference is even smaller as in the Po basin.

7.2 Comparison of stratospheric Nitrogen Dioxide Columns

There are many AMAXDOAS and SCIAMACHY data available (mostly on request per email). However we will present two case studies here, one for the northern latitudes and one from the southern flights:

- 04/09/2002 local flight in Kiruna north to Spitsbergen
- 17/09/2002 From Mallorca via Djerba and Niamey to Yaoundé crossing the Sahara desert.

The airborne measurements were performed to validate SCIAMACHY observation over remote regions as well. Therefore we study these two flights over remote regions (Sahara and north polar sea) detailed here. Besides, the results are very interesting in their own, they were already presented by Heue et al., [2003].

For the retrieval of total NO_2 flights in remote areas, where the tropospheric NO_2 is negligible, are well suited, because the signals of the telescopes directed in nadir and zenith are influenced by the tropospheric absorptions as discussed in chapter 3.4.
To retrieve the total vertical column the Langley plot (chapter 4.5.I) is applied to both data sets discussed below.

7.2.I 04/09/2002 from Kiruna to Spitsbergen and back

7.2.I.a Cloud Coverage and other Parameters

The flight on 04/09/2002 began at Kiruna at 15:58 UT and 19:47 UT the plane landed again in Kiruna, at this time it was already dark in Kiruna. Throughout the whole flight it was very cloudy below the aeroplane, according to the log. This can also be confirmed by the satellite image (www.sat.dundee.ac.uk/auth.html) but is not shown here.
During the duration of the flight the solar zenith angle changed from 80° to 99°. Good AMAXDOAS measurements can be performed as long as the solar zenith angle is below 94°. If the SZA increases to higher values, it will be too dark; therefore no data are shown for this period.

7.2.I.b The observed dSCD and the VCD

The observed dSCDs as a function of time are shown in Figure 7-22. Both viewing directions observe the same signal throughout most of the flight, only a slight constant shift is observed.

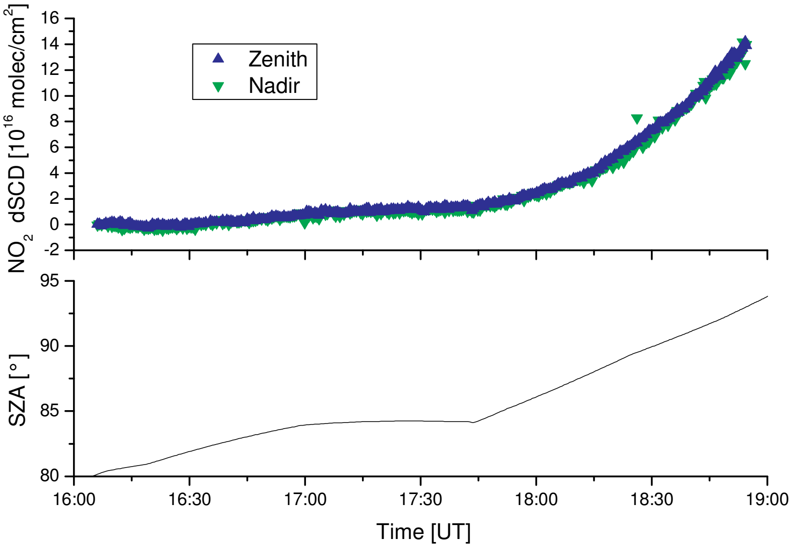

Figure 7-22: Observed dSCD as function of time (upper panel) and the solar zenith angle along the flight (lower panel). The reference of the analysis was taken at 16:37:32, when both nadir and zenith dSCD agree quite well.

The general trend of the dSCDs can be explained by the solar zenith angle and the AMF depending on it. To retrieve the total vertical column a Langley plot was made (Figure 4-22). According to the principle uncertainties of the Langley plot additional information from ground based DOAS measurements might be useful. The vertical columns as function of latitude are shown in Figure 7-23.

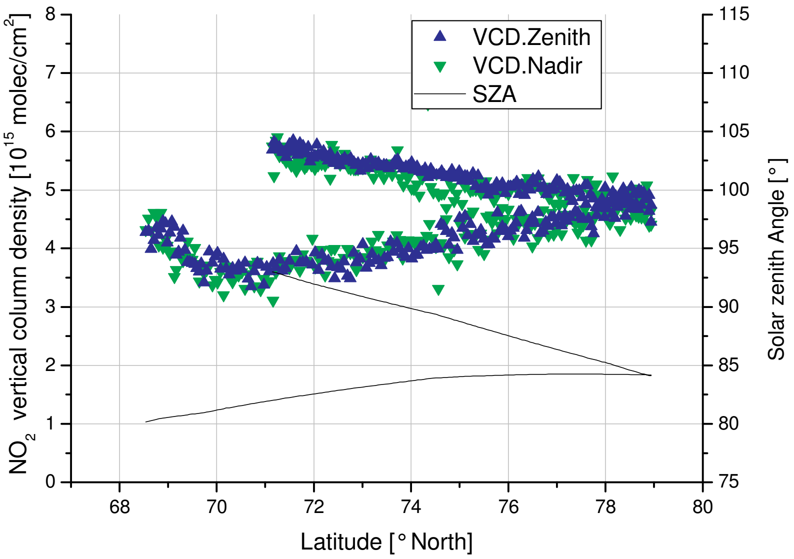

Figure 7-23: Vertical column and solar zenith angle as function of latitude. Both zenith and nadir agree well and follow the SZA.

The vertical column densities agree well for nadir and zenith. The observed trend agrees with the assumption that the NO_2 concentration is dominated by the photo stationary stead. The solar zenith angle along the flight track is therefore shown as well in Figure 7-23.

7.2.I.c Comparison to ground based DOAS Measurements

Along the flight track there are two measurement places where a comparison is possible. One is in Kiruna and the other one is in Ny-Ålesund (Spitsbergen).

The comparison with ground based DOAS measurements is useful as the retrieval of the vertical column using the Langley plot is not straight forward due to the photochemical processes taking place in the stratosphere. However we have to be aware that the retrieval of the ground based DOAS data applies the same method. The total column is calculated during sunrise and sunset when both the vertical column and the AMF change rapidly.

For Ny-Ålesund data are available (Thomas Wagner, Talk at ESA Meeting in Frascati, 2002). During sunrise $4.3*10^{15}$ molec/cm^2 were observed and in the evening $4.8*10^{15}$ molec/cm^2. The Falcon reached Spitsbergen at 17:45 UT which is about 18:30 local solar time. The solar zenith angle was 84.2°, so the evening value is expected to compare better to the AMAXDOAS measurements. The AMAXDOAS data vary between $4.4*10^{15}$ molec/cm^2 and $4.9*10^{15}$ molec/cm^2 and are therefore in good agreement to the vertical columns retrieved from the ground based data.

Due to the ascend crossing dense clouds we have no AMAXDOAS data from Kiruna, the Falcon reached a flight altitude above the clouds at 16:06 UT and 68.5° north. In Kiruna (67.8° North) there are no data available from this specific day (Barbara Dix, personal communication, 19/08/2005). So for the comparison we have to take the data from 06/09/2002 and try to interpolate for the two days period. Caused by the annual variation however the vertical column changes extremely at this time of the year. The result of the ground based measurement, as illustrated in Figure 7-24, do not allow such an interpolation due to the lack of data between 27/08/2002 and 03/09/2002.

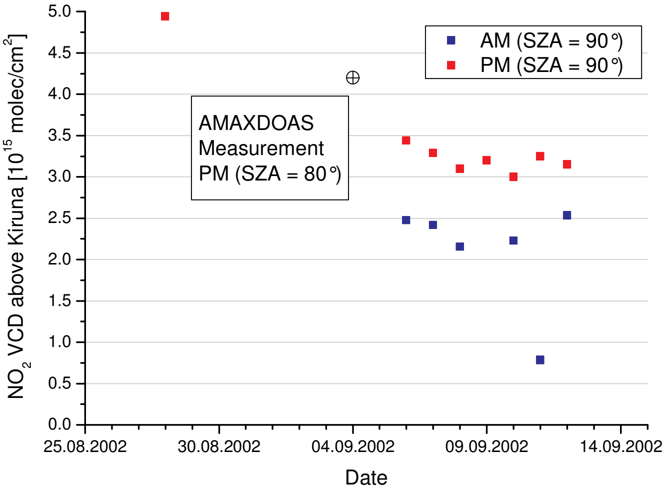

Figure 7-24: Ground based Measurements of the vertical column density in late summer 2002 in Kiruna. (Barbara Dix, private communication file date 22/08/2005) In addition the AMAXDOAS result is shown.

Nevertheless a comparison might still be useful as AMAXDOAS observed higher values over the southern part, which cannot be explained by the photochemistry (Figure 7-23). In Kiruna the vertical columns on 06/09/02 were $2.5*10^{15}$ molec/cm^2 in the morning hours and $3.5*10^{15}$ molec/cm^2 in the evening. This indicates that the diurnal variations are much larger in Kiruna than in Ny-Ålesund. The AMAXDOAS result of $4.2 \pm 0.2*10^{15}$ molec/cm^2 for the afternoon overestimates the total column slightly, although it agrees well with the GOME data.

7.2.I.d Comparison to GOME and SCIAMACHY

For the 04/09/2002 unfortunately only few SCIAMACHY total NO$_2$ columns are available. So we use GOME data for the comparison. GOME results are well established and have been validated for many years so this comparison might rather be a validation of AMAXDOAS than of GOME data.

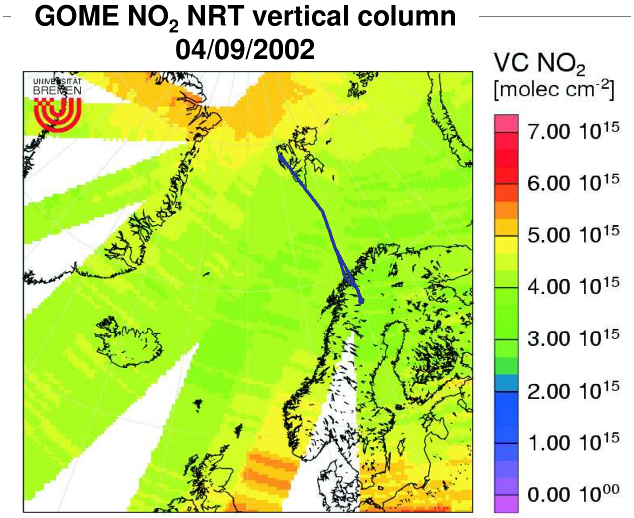

Figure 7-25: GOME NRT vertical column on 04/09/2002, in addition the flight track is shown in blue. Here no AMAXDOAS data are shown (Andreas Richter, private communication, December 2002).

After we compared AMAXDOAS to GOME we can still check for the two data points available for SCIAMACHY. For Kiruna and Ny-Ålesund SCIAMACHY total columns are available for validation purpose at the University of Bremen (www.iup.physik.uni-bremen.de/DOAS/SCIA_no2_data_acve.htm, 02/07/2003). Here all the SCIAMACHY data for a maximum distance of 200 km to the ground based measurement stations are averaged. For the stratospheric vertical column however the expected gradients are small and the averaging only causes a minor error.

As shown in Figure 7-25 the total vertical NO_2 as observed from GOME varied between $4.0*10^{15}$ molec/cm^2 in Kiruna and $4.66*10^{15}$ molec/cm^2 around Spitsbergen. Close to the Norwegian coast the total column is between $3.66*10^{15}$ molec/cm^2 and $4.0*10^{15}$ molec/cm^2 GOME crossed Kiruna at about 10:00 UT and the solar zenith angle for the GOME measurements was about 60°.

Due to the diurnal cycle of NO_2 a direct comparison is only useful for the first leg of the Falcon's flight, here a qualitative comparison can be done. In Figure 7-23 we observed that the AMAXDOAS values are lower at about 70° North. This compares well with the lower values observed by GOME. Close to the Norwegian coast both instruments observe a vertical column density around $3.5*10^{15}$ molec/cm^2. On the first part of the flight (to Spitsbergen) the total columns observed by AMAXDOAS agree well with GOME. On the way back the decreasing photolysis frequency let to an increase in the AMAXDOAS data. The increase in the total NO_2 column is not observed by GOME, as this instrument passes over the polar region in the morning hours..

The ENVISAT satellite passed Kiruna at 11:31 UT (61.2° SZA) and observed a VCD of $3.68*10^{15}$ molec/cm^2. This is in the range of the GOME data but slightly lower than the AMAXDOAS data close to Kiruna. For Spitsbergen the situation is different: Here the average SCIAMACHY data result in $4.05*10^{15}$ molec/cm^2 at about 12:30 UT (72.1° SZA). AMAXDOAS's VCD in the region of Spitsbergen are definitely higher ($4.7*10^{15}$ molec/cm^2) but were observed at 17:45 UT (84.2°SZA). The SZA range (Figure 7-23) of the AMAXDOAS measurements is too small to extrapolate to an assumed SZA of 72.1° close to Ny-Ålesund.

Considering the different measurement times a good agreement of AMAXDOAS observation with both ground based observation and both satellite instruments GOME and SCIAMACHY is found.

7.2.II 17/09/2002 from Palma de Mallorca to Yaoundé

The maximum range of the Falcon is 3700 km without the AMAXDOAS (~10 % less due to the domes) so for this flight over the Sahara desert two fuelling stops had to be made one was in Djerba (Tunisia) and the other one in Niamey (Niger). During these refuelling stops the instruments kept on measuring. However these data are not very useful due to the change in the flight altitude. The idea was to keep the instrument under stable conditions i.e. CCD cooled and spectrometer warm. For the first stop this worked fine, during the second stop however the Falcon stood on the airfield in Niamey and the sun was standing high (SZA~16°). The temperature inside the aeroplane rose to 35.5°C and the instruments got trouble with high temperatures. The spectrometer got warmer than the usual temperature of 40° C and the CDD cooling did not work properly as the air around the CCD was too warm. Therefore the data on the last leg from Niamey to Yaoundé are not of good quality. As there were many clouds reaching up to the flight altitude (11100 m), i.e. the Falcon flew through the clouds, these data cannot be used for our purpose anyway.

7.2.II.a <u>Cloud Coverage along the flight</u>

The cloud coverage (www.eumetsat.int, 30/03/2005) of northern Africa and the Mediterranean is shown in Figure 7-26. This image illustrates the situation at 12:00 UT. The aeroplane took off from Palma de Mallorca at 5:30 UT and arrived in Yaoundé at 16:00 UT. Between Mallorca and Djerba it was cloudy below the plane and mostly clear above. Over the desert it was very hazy and only a few clouds were observed at the beginning. Only in the last part when entering the tropics between Niamey (12° North) and Yaoundé (2° North) large tropical rain clouds were observed and crossed by the aeroplane. These thick clouds are not fully observed in the EUMETSAT image as they developed in the afternoon.

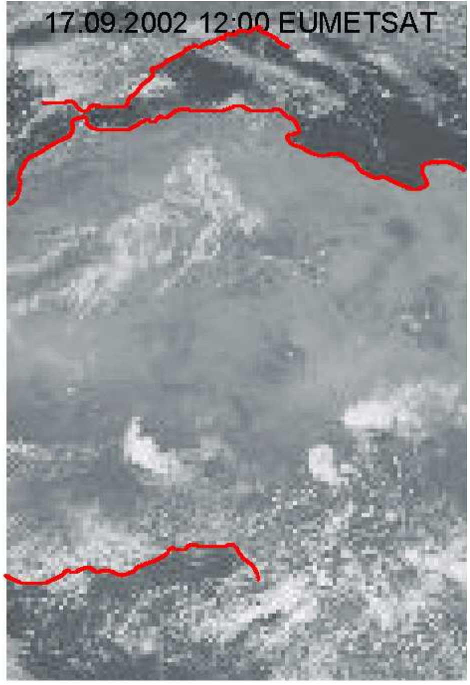

Figure 7-26: Cloud coverage over northern Africa and the Mediterranean on 17/09/2002 as observed by the Meteosat satellites (www.eumetsat.int, 30/03/2005). The approximated coast lines were marked by hand so the reader can distinguish between clouds and surface. Over the Mediterranean clouds can be made out between France and Tunisia (west of Italy). Large clouds can also be realised south of the Sahara, over the desert it was very hazy.

7.2.II.b Slant and Vertical Columns and Comparison with SCIAMACHY

In contrast to the flight discussed above, measurements were performed under a large range of solar zenith angles; they changed between 10° minimum and about 90° in the maximum. The largest change in the observed slant column density occurs during the times of sunrise and sundown. During sunrise the Falcon flew from Mallorca to Djerba.

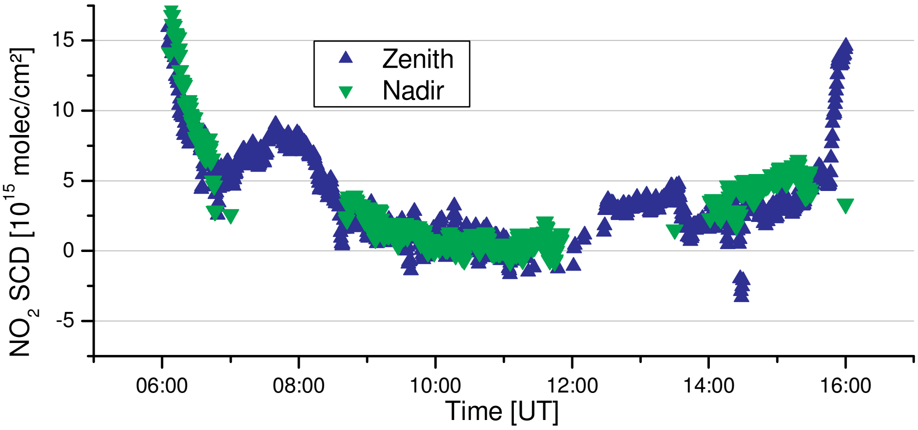

Figure 7-27: Slant column densities for the complete flight between Mallorca and Yaoundé on 17/09/2002. Spectra from 11:00:19 UT were chosen as reference to reduce the stratospheric absorption for Nadir and Zenith.
During the refuelling stops it was too dark below the aeroplane to retrieve any slant column from the nadir spectra. In the zenith data a strong increase during descends is observed. At 11:20 UT the zenith telescope was shut by the shutter to protect the instrument.
Both nadir and zenith observations decrease rapidly during the sunrise (6:00 UT).

During sunrise only those data are shown in Figure 7-27 where the aeroplane had already reached the flight altitude. These data were used to determine the slant column density of the reference spectrum with a Langley plot. The solar zenith angle changed between 82.4° at 6:00 UT and 72.1° at 6:40 UT.

For the central part of the flight crossing the Sahara desert the vertical columns observed by SCIAMACHY agree well with those observed by AMAXDOAS as shown in Figure 7-28. The first part is not covered by any SCIAMACHY pixel and during the last part a large discrepancy can be observed. This can be explained by the unstable temperature of the instrument and influence of clouds the Falcon had to cross. The clouds developed between noon and 15:30 UT. During the cloud free parts of the flight lower VCDs were observed (between 2 and $3*10^{15}$ molec/cm^2). One extreme example on the influence of a tropical cloud will be discussed in section 7.3.

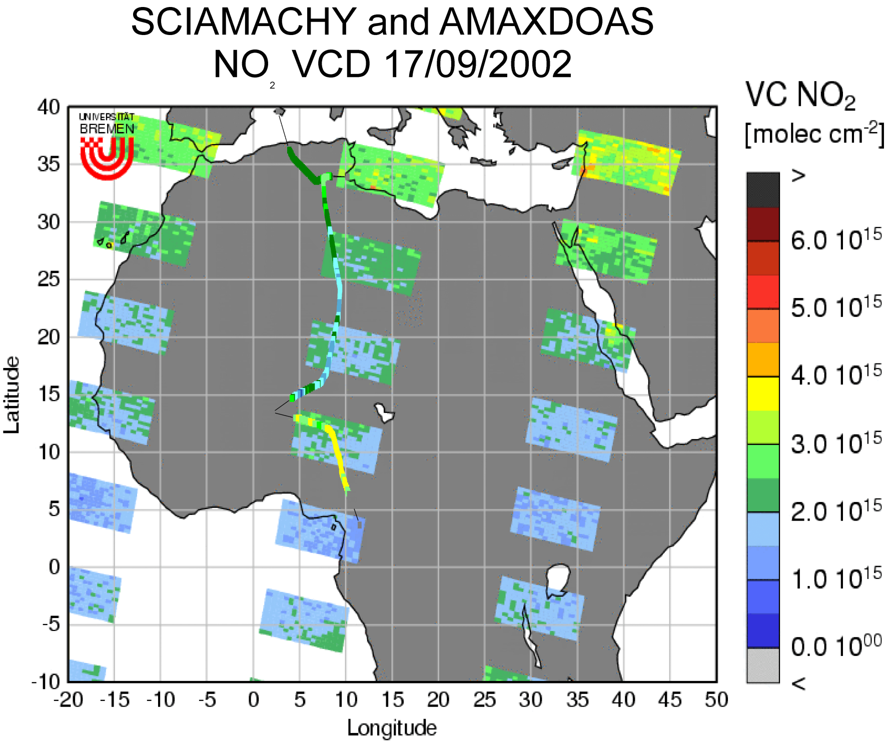

Figure 7-28: Vertical column densities from SCIAMACHY (large pixel) and AMAXDOAS (thin line) in northern Africa, here the same scale with similar colours was used. Again for AMAXDOAS only the data observed at a constant flight altitude are shown. (SCIAMACHY plot Andreas Richter, personal communication, 25/07/2003)

According to long term observations with GOME on ERS2 the burning season in the northern tropical rainforest is rather in January/February than in September. However before excluding this possibility it can be checked with data from fire observing satellites like Modis (available at the University of Maryland http://maps.geog.umd.edu, April 2005). As there are no fires mentioned here we assume the NO_2 is not emitted from biomass burning.

The comparison between SCIAMACHY and AMAXDOAS has to concentrate on flight across the Sahara desert. Both instruments observe higher values in the north (30° – 25° North) compared to the lower vertical columns in the south (20° North). Besides the general trend the observed vertical columns are in the same range varying around $2.5*10^{15}$ molec/cm^2 in the northern and $2*10^{15}$ molec/cm^2 in the southern pixel. In both data sets a high variability is observed, as expected it is higher for the AMAXDOAS, due to the smaller pixel size. A correlation plot as in 7.1.I.d is less useful here. The results of both instruments vary only slightly between 1.5 and $2.5*10^{15}$ molec/cm^2, the noise of both data sets is in the order of $0.2*10^{15}$ molec/cm^2.

7.3 Nitrogen Dioxide and Ozone inside a tropical Cloud

Inside a large cloud different effects cause an enhanced dSCD: Due to multiple scattering the light path is increased (chapter 4.5.II), for NO_2 often the concentration inside the cloud is enhanced due to updraft or local production by lightning. Such an enhanced NO_2 column density was observed on 25/09/2002 on the Flight from Yaoundé to Nairobi. The dSCD as a function of the position is shown in Figure 7-29, here it is overlaid to a satellite image of MODIS terra. The red circle indicates the position (1° 15' 46''N, 22° 38' E) where the Falcon crossed the cloud.

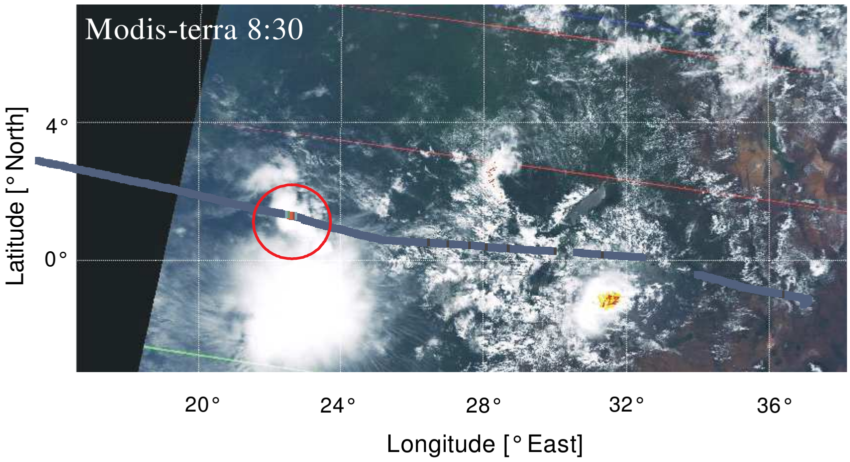

Figure 7-29: Satellite image (MODIS Terra) of eastern central Africa. The Falcon passed by a big storm in the east and in the west she crossed a dense cloud field (red circle) (satellite image: http://modis-atmos.gsfc.nasa.gov/images/index.html, March 2005).

7.3.I Measurement Results

The enhanced slant column densities of O_4 and H_2O are used to estimate the light path enhancement inside the cloud in chapter 4.5.II. In the following we concentrate on the NO_2 and O_3 results. For all trace gases an increase in the dSCDs is observed at same moment when the Falcon crossed the cloud. In Figure 7-30 (upper panel) the observed NO_2 data for all lines of sight are shown. For comparison the O_4 and H_2O data for the zenith are shown again in the lower panel (Figure 4-25).

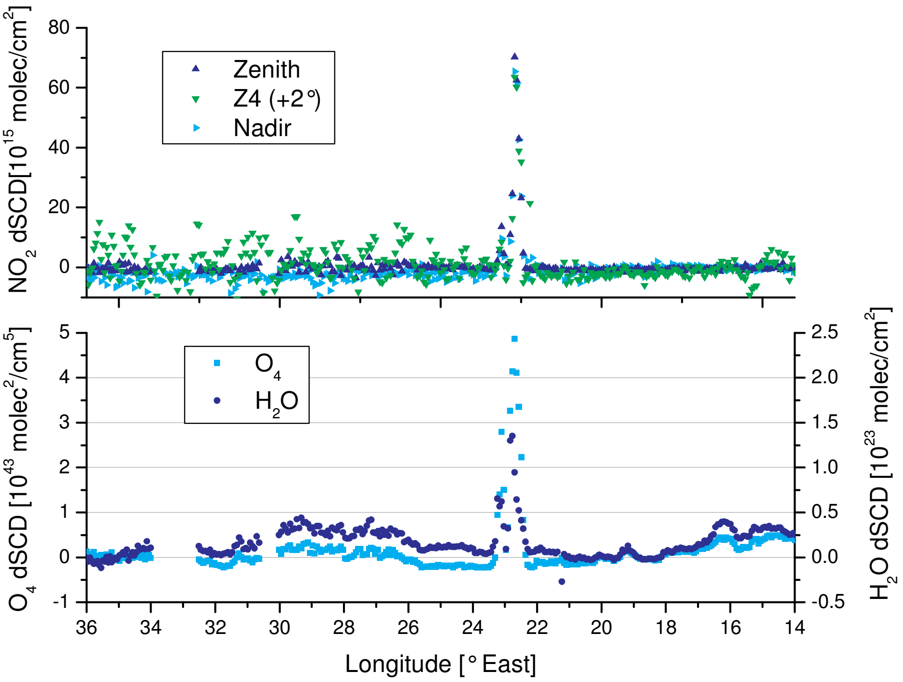

Figure 7-30: Upper panel: NO_2 dSCD during the flight for all active telescopes. An extreme peak is observed in all lines of sight at 22.6° East. Dark blue triangle upwards for zenith, light blue triangle side wards for 2° forward and for the nadir telescope a green triangle orientated downwards is used. Lower panel: O_4 (light blue and left scale) and H_2O (dark blue and right scale) dSCDs from the Zenith viewing telescope. At the same time as the NO_2 enhancements are observed a similar effect can be made out in the O_4 and the H_2O.

In Figure 7-31 the NO_2 and O_3 retrieved from the UV-data are shown, they were supported by Ping Wang in private communication on 06/05/2005. The peak observed in the visible data can be observed here as well. Compared to the vis-data the NO_2 SCD is slightly enhanced, which cannot be explained up to now as a longer light path inside the cloud is rather unlikely.

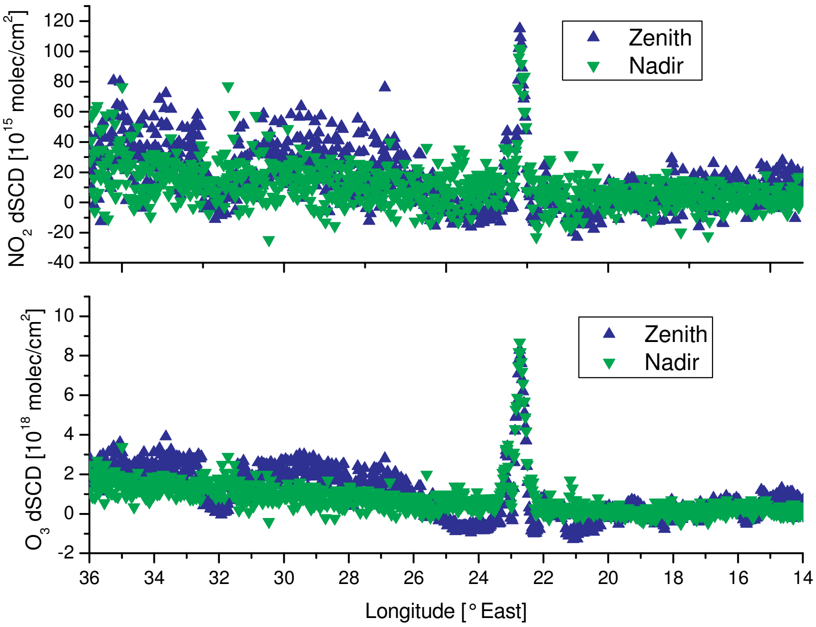

Figure 7-31: The differential slant column densities for O_3 (lower panel) and NO_2 (upper panel) observed by the UV-instrument. For both trace gases the same peak is observed as well. As usual the Zenith data is shown in blue and the nadir in green.

An overview of the differences in the SCD caused by the cloud is given in the following table:

	NO_2 [10^{16}]	**O_3 [10^{18}]**	**H_2O [10^{23}]**	**O_4 [10^{43}]**
Zenith	7.00 ± 0.05		1.31 ± 0.1	5.04 ± 0.1
Zenith (UV)	11.5 ± 1.2	8.70 ± 0.4		
Nadir	6.30 ± 0.1		1.31 ± 0.1	4.4 ± 0.2
Nadir (UV)	9.40 ± 3	8.00 ± 0.8		
Z4 (+2°)	6.20 ± 0.2		1.39 ± 0.1	4.7 ± 0.1

Table 7-A: Overview on the differential slant columns caused by light path enhancement. The data are in molec/cm^2 except O_4 which is in molec^2/cm^5.

7.3.II Nitrogen Dioxide inside the Cloud

In chapter 4.5.II the light path enhancement inside the cloud is approximated to 180 km with a cloud bottom altitude of 7.2 km and 16 km cloud top height. To derive the average NO_2 concentration inside cloud this information is essential. The dSCD of NO_2 are shown in Figure 7-30, in average they increased by $6.5*10^{16}$ molec/cm^2. As we did for O_4 we can ignore the light path before and after the cloud. So the observed dSCD equals:

$$dS(NO_2) = \int_L c(l) \cdot dl$$

where c(l) stands for the NO_2 concentration in the cloud and L is the light path as calculated above. Following the discussion above we assume again a uniform distributed light path inside the cloud and calculate the NO_2 by assuming a constant mixing ratio (m) in the cloud:

$$dS = L \cdot < c > = L \cdot \frac{1}{(T-B)} \int_B^T m \cdot n(z) \cdot dz$$

$$m = \frac{dS}{L} \cdot \frac{T-B}{\int_B^T n(z) \cdot dz}$$

where L stands for the average light path, n(z) is the air number density at the given altitude and B and T represent the cloud base and cloud top height respectively.

We retrieve a NO_2 mixing ratio of 0.49 ppb for a cloud base height of 7.2 km a cloud top height of 16 km and a total light path of 178 km inside the cloud. Usually the mixing ratio at this altitude is around 0.02 ppb, so we try to find out about the origin of the enhanced NO_2 value.

Other measurements of lightning produced NO_x resulted in 2 to 5 ppb [Höller et al., 1999] inside the cloud. The tropospheric updraft they assumed over Europe was of the order of 1 ppb NO_x. Inside the cloud the NO/NO_x-ratio (NR) is about 0.4 to 0.6, depending on the distance to the cloud edge mainly. At the cloud edge multiple scattering enhances the actinic flux, hence the NR increases up to 0.9. Therefore the local NO_2 mixing ratio varies between 0.1 and 0.6 ppb depending on the position inside the cloud. Similar but slightly lower values were observed by Huntrieser et al. [2002]: 0.5±0.2 ppb NO_x or 0.3 ppb NO_2.

Due to different anthropogenic emissions, the NO_x concentration can be expected to be lower in the Congo basin than in Europe. If we assume the emission to be lower by a factor of 2, the updraft over Congo basin will be 0.1 to 0.3 ppb NO_2, which seems to be rather low, compared to our result. For the exact quantification of the updraft NO_2 in the above quoted publications, tracers like CO or CO_2 are used, combined with profile measurements of the according tracers. The other way is, to take measurements in similar but electric inactive clouds as background. However both methods cannot be used to quantify the updraft NO_2 in our case. None of the instruments on board the Falcon measured CO or CO_2. The Lightning Imaging Sensor (LIS) (available at: http://thunder.nsstc.nasa.gov/data, 05/10/2005) observed the same area 3 h 15 min later, hence the lightning activity of the special cloud cannot be estimated by these data. Nevertheless the available data are shown in Figure 7-32, the size of the triangles indicates the number of the observed flashes. Although no flashes were registered in this region, lightning cannot be excluded as additional NO_2 source.

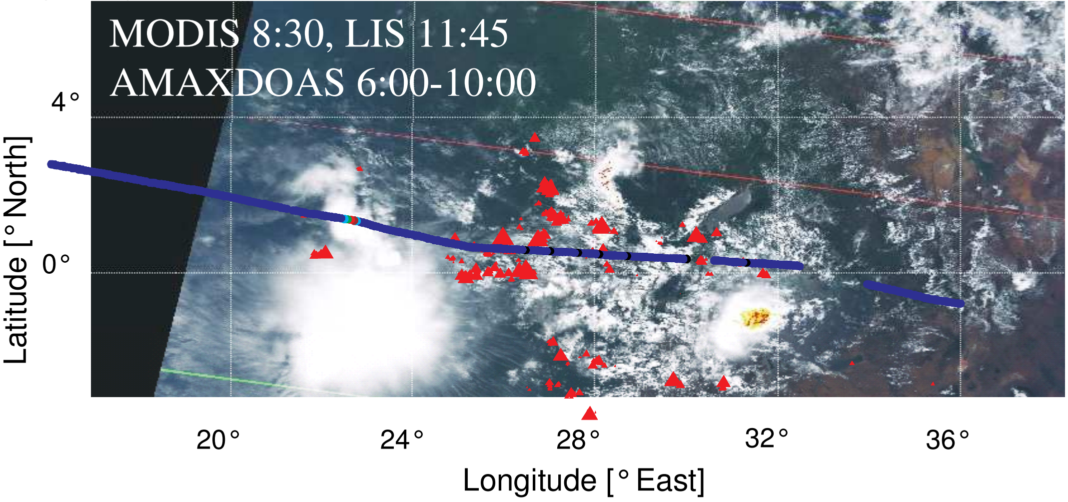

Figure 7-32: Lightning Imaging Sensor data (http://thunder.nsstc.nasa.gov/data, 05/10/2005) and the Falcon flight track (25/09/2002) overlaid to the MODIS image (Figure 7-29). The size of the triangles indicates the number of the observed flashes.

Biomass burning leads to enhanced NO_x concentration in the boundary layer and hence increases the updraft NO_2. Usually the burning season in this part of the tropical rain forest is rather in January or February than in September, hence we would not expect biomass burning to be the source of the observed NO_2. Nevertheless this possibility has to be checked before it can be excluded. Fires counts are retrieved from the MODIS satellite images. These data are shown in Figure 7-33. In the most interesting region close to the observed cloud no large fires were detected by the satellite. Therefore an enhanced tropospheric NO_2 is rather unlikely.

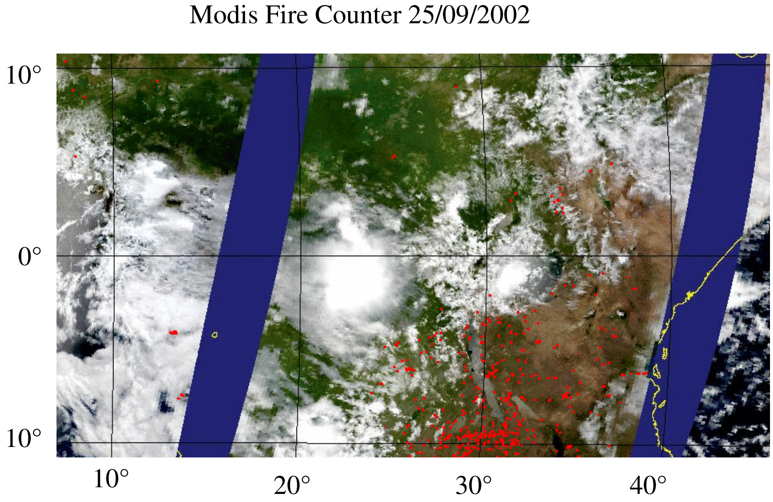

Figure 7-33: MODIS Terra Fire counter for 25/09/2002. Many Fires were observed at about 10° S, 30° E. In the central Congo basin (thick cloud in the centre) only few fires were observed. In the central Congo basin (thick cloud in the centre - Figure 7-32) only no fires were observed.

The observed NO_2 concentration (~0.5 ppb) seems too high to be caused by tropospheric updraft only, especially when enhanced NO_2 due to biomass burning can be excluded. Therefore lightning is most probable the origin of the observed NO_2. In other studies CO, CO_2 or O_3 are used as tracers to distinguish between tropospheric updraft and lightning produced NO_x. The importance of O_3 however is ambiguous, Höller et al. [1999] wrote: “Boundary layer air can clearly be recognised by its low CO_2 and high O_3 content”, the same group [Huntrieser et al, 2002] wrote 3 years later: “A small decrease (in the ozone concentration) is visible between 9 and 10 km, which may be caused by convective transport”. An overview on the literature concerning ozone production, destruction and transport in thunderstorm clouds is given by [Winterrath et al., 1999].

Nevertheless the O_3 data or the average mixing ratio is interesting in itself. The observed ozone data are shown in Figure 7-31, together with the NO_2 dSCDs. The peak observed in the data from the visible instrument, can be made out in the O_3 as well.

In the same way as the NO_2 mixing ratio is retrieved, the O_3 mixing ratio can be calculated to 60 ppb. The average ozone mixing ratio of the tropical standard profile equals 70 ppb for the interesting altitude interval. Measurements over the tropical South Atlantic [Mauzerall et al., 1998] observed around 60 ppb in the clean air background between 7 and 12 km altitude. This agrees very well with our result.

The error due to the retrieval procedure and the uncertainty in the dSCD is quite high. The latter can be estimated by up to 10% for each SCD. In our retrieval the SCD of O_4, H_2O and NO_2, O_3 respectively, were used. This leads to an error only caused by the SCD up to 15% in the minimum. The error of the light path retrieval cannot be estimated as the retrieval depends on too many assumptions e.g. standard O_2 and temperature profile.

The enhanced NO_2 values were partly caused by updraft. However, lightning as additional source has to be considered although additional measurements (LIS) can neither prove this assumption right nor wrong.

7.4 OClO Observation during the EUPLEX Campaign

Besides NO_2 and O_3 also OClO was observed with the AMAXDOAS instrument. The retrieval was done in the UV and the data presented were gratefully supported by my former Bremian colleague Ping Wang (private email, 16.03.2005). Parts of the results were already published in [Wang et al., 2003] another publication concerning the interpretation is in progress [Wang et al., 2005 c]. The AMAXDOAS project has been a cooperation right from the beginning, therefore I can also present some of her results here as well. Besides, it can be regarded as a demonstration of the capabilities of the AMAXDOAS instrument. In the visible wavelength region the OClO absorption was too weak for a reasonable analysis.

7.4.I The Flight Track and Measurement Conditions

The EUPLEX campaign (chapter 6.2) focused on PSC and the related chemistry. The AMAXDOAS took part as a hitchhiker during the end of January 2003. On 26/01/2003 the Falcon flew form Kiruna to the north, taking off during sunrise (8:49 UT, 89.8° SZA). After take-off the Falcon headed north towards the polar night until she turned back east of Spitsbergen, where the solar zenith angle was 99.3°. At 12:54 UT the Falcon arrived at Kiruna during sunset (SZA = 89.8°). Reasonable measurements are only possible if the solar zenith angle is below 94°. So results can be expected form 9:12 UT (when the Falcon reached flight altitude) to 10:00 UT (when the sun reached 94° SZA). On the way back from the north the time interval expands from 11:36 UT until 12:30 UT.

In Kiruna there was snow fall when the Falcon took off and it was still cloudy when she arrived back. The clouds are not that important for the rest of the flight, as we can expect the OClO to be situated above the clouds and close to the flight altitude (11000 m).

7.4.II Data Analysis

The fitting procedure as used for the vis camera are described in chapter 3.3. In the UV some parameters for the retrieval are different. The fitting window was between 345 and 380 nm, besides OClO [Wahner et al., 1987] also BrO [Wahner et al., 1988], NO_2 [Burrows et al. 1998], O_4 and two O_3 [Burrows et al., 1999] cross sections (273 K and 221 K) were included as well as a Ring spectrum [Vountas et al., 1998]. The reference spectrum was taken from a different flight in the tropics (24/02/2003) close to Nairobi, the SZA was about 8°. Hence we can expect there are no OClO absorptions in the reference. Also the absorptions of NO_2 and O_3 are low in the reference spectrum due to the small solar zenith angle and possible interferences in the fit are minimized.

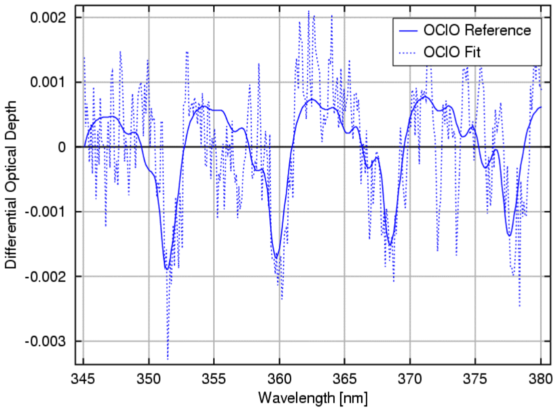

Figure 7-34: OClO fit (72.71° N, 22,28° E, 91.94° SZA) retrieved from a spectrum which was observed with +2° telescope. The solid line is the fitted OClO cross section, the dotted line shows the spectrum plus the fit residual [Wang et al., 2003].

An example fit is shown in Figure 7-34. The residual structure is of the order of 1 ‰. The OClO cross section can clearly be made out in the fits, beside the spectra observed during night.

7.4.III Slant Column Densities

In the nadir viewing direction no OClO was detected, since the signal was too low for the necessary signal to noise ratio. The time series of the slant column densities of the other three telescopes are shown in Figure 7-35. In the same figure the solar zenith angle is shown as well, for angles higher than 94° no measurements were possible, which in indicated by the straight lines in the centre of the plot.

It seems that the two telescope directed in flight direction observe higher OClO column when flying north into the vortex as when flying south out of the vortex. The position of the polar vortex is shown in Figure 7-36. Inside the vortex GOME observations show enhanced column densities of OClO. Between Kiruna and Spitsbergen there seems to be a strong gradient in the OClO. This can be expected as Kiruna was just outside the vortex. However only the slant column densities are shown in Figure 7-35, and the increase can be attributed to both a change in the OClO concentration or a longer light path due to different solar zenith angles.

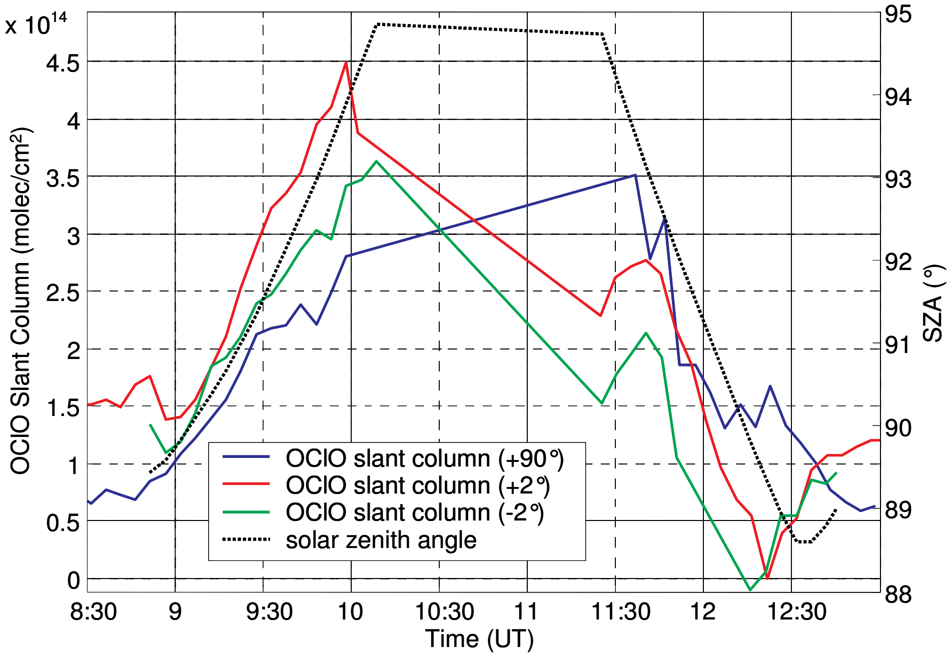

Figure 7-35: Time series of the OClO slant column density (left ordiante) and solar zenith angle (right ordinate). The grid lines refer to the left ordinate. In nadir no OClO was detected. The other three lines of sight are shown and indicated by different colours [Wang et al., 2003].

Also the relative azimuth angle is important for the interpretation of the AMAXDOAS results. On the first part of the flight the telescopes were directed to the north and the relative azimuth angle was more than 90°. On the second part one telescope (-2°) was closed by the shutter to avoid direct sunlight (chapter 5.1), the relative azimuth angle was close to zero. Together with the observed O_4 column densities this effect is used to retrieve some aerosol information [Wang et al., 2005].

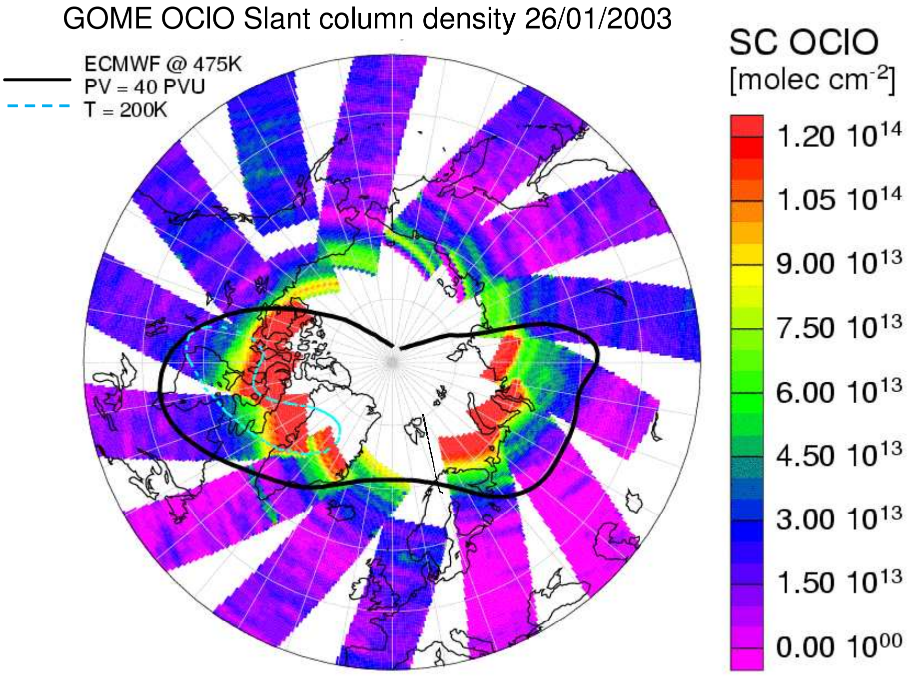

Figure 7-36: OClO columns derived from GOME observation, the bold black line indicates the polar vortex (40 PVU) at the 475K level, the dashed light blue line is the 200 K temperature isoline. The thin black line shows the flight track between Kiruna and Spitsbergen crossing the edge of the polar vortex [Wang et al., 2005 c].

In this study Ping Wang used a photochemical radiative transfer model, it accounts for both the change in the profile due to photochemistry and the change in the AMF caused by changes in the solar angles. The measurement can be explained by both a gradient in the OClO concentration between Spitsbergen and Kiruna and by the change in the relative solar azimuth angle. When flying north the telescopes are directed into the polar vortex, where higher concentrations are found, whereas on the way back they are directed to the lower concentrations.

7.5 Conclusions AMAXDOAS on the Falcon

In this chapter several examples of AMAXDOAS results gained from flights on board the Falcon are shown. The strength of the AMAXDOAS for the validation of satellite tropospheric NO_2 columns is demonstrated. The agreement between the slant columns is in the expected range, the systematic disagreement can be attributed to the different sensibilities of the two instruments.

The tropospheric vertical column densities of both instruments, SCIAMACHY and AMAXDOAS, strongly depend on the correct settings for the AMF calculation. If the correct setting is used the agreement is very good, if a standard AMF is used the differences to the best settings are of the order of 50 to 100 %. The comparisons highlight the importance of appropriate AMFs in the retrieval – only with reasonable assumptions good agreement with independent measurements can be achieved. For global data sets, such information is often not available, and model predicted profiles for NO_2 and sometimes also aerosol loading have to be used.

Due to the viewing geometry AMAXDOAS is unable to retrieve total slant columns. The comparison between AMAXDOAS and SCIAMACHY total vertical columns depends on the correct AMFs but also on the temporal variation in the observed stratospheric column. The observed agreement for the two examples was quite good.

Inside a large cloud observed over the Congo basin a strong light path enhancement was observed (chapter 4.5.II). The length of the light path was estimated to 178 km and an average NO_2 mixing ratio of 0.5 ppb was retrieved. Compared to the standard atmosphere it is enhanced by a factor of 25. The ozone mixing ratio is rather similar to the outside air. If we assume the updraft NO_x in the Congo Basin to be about half of the updraft in Europe, then additional sources like lightning will have to contribute to the observed NO_2.

For the measurement of stratospheric OClO the AMAXDOAS is well suited, a chemical radiative transfer model developed in Bremen seems to be a powerful tool to retrieve OClO vertical columns from the observed dSCDs.

8 Results of the FORMAT Campaigns

Two measurement campaigns were organized in the context of the FORMAT project. The first took place in August 2002, the second in September 2003. The campaigns and how AMAXDOAS instrument was used are described in the chapters 5.11.II and III and in chapter 6.3. and 6.4. In total 20 flights were performed in the area of Milano and the Po basin.

For both campaigns an entire set of the observed slant column density along the flights is shown in the attachments. Displayed are the dSCDs for the viewing directions -16° and -7° backwards for the first and the second campaign respectively. These lines of sight were chosen as the sensitivity to boundary layer trace gases is higher compared to nadir. The other downward looking telescopes show similar results. In general higher values of both trace gases were observed north of Milano and in most cases a spatial agreement is observed. Only when passing by a point source of NO_x, e.g. power plants or cement plants, high NO_x values appear which are not correlated with any other enhancement. The ozone variations cannot be detected with the AMAXDOAS as the signal to noise ratio is too low.

Two flights will be discussed in detail in this chapter. The first section (8.1) concentrates on the distribution of formaldehyde around the city of Milano, based on measurements from 16/08/2002. In the second study (section 8.2) the NO_x emission from a power plant will be discussed in detail, based on the measurements performed on 26/09/2003.

8.1 16/08/2002 Formaldehyde around Milano

In this section we concentrate on the 16/08/2002 as the flight track was ideal to observe the distribution of HCHO and NO_2 around Milano. The formaldehyde concentrations were relative high and the plume of the city was well observed in the measurement results. The results presented here are in preparation for publication [Pundt et al., 2005 c].

8.1.I Flight Pattern and Weather Conditions along the Flight

In the FORMAT I campaign the aeroplane was based in Lugano (CH) 50 km north-west of the border to Italy (chapter 6.3.II). On the 16/08/2002 it took off at 12:56 GMT and returned to the airport at 15:37 GMT. The flight track is shown in Figure 8-1. The aeroplane first flew a quadrangle around Milano (anticlockwise) and a triangle crossing the inner city afterwards. This pattern was repeated before the plane headed north to the base in Lugano again. The flight track was specially designed to estimate the emission of formaldehyde originating from the town. The four locations at the corners were used in chapter 4.5.III, to deduce the aerosol profile. The flight track between Lugano and Como is not important here and is therefore not shown. The hatched area in the centre of the figure is a rough approximation of Milano and the smaller suburbs[1] situated at the edge. The other towns and suburbs between Milano and the Alps are not shown here. South of the town the area is mostly agriculturally used (chapter 6.3.I).

---

[1] In Italian they are called Milanini – small Milanos.

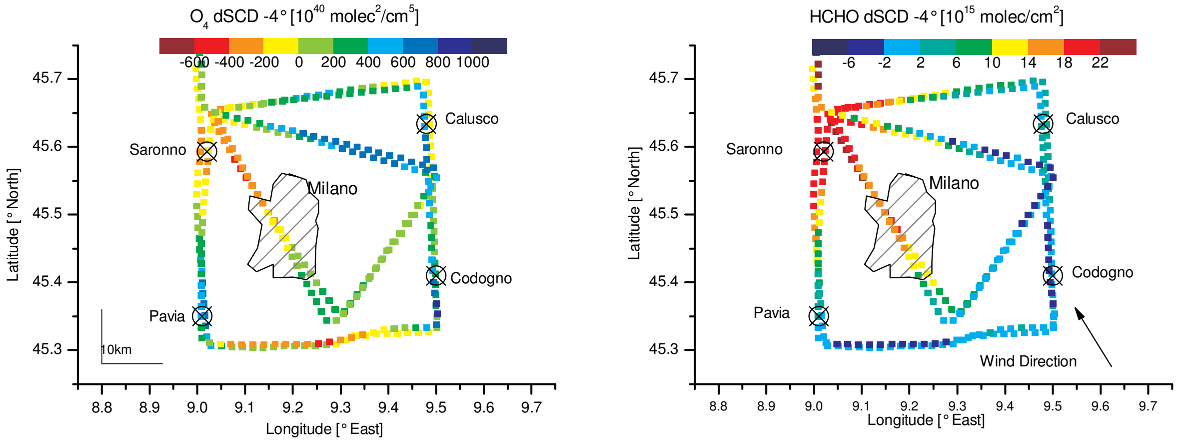

Figure 8-1: The flight track around the city of Milano (indicated by the hatched area) and the four locations used for the detailed analyses. In the left panel the O_4 dSCD is shown, in the right one you can see the observed HCHO dSCD. The reference was taken south-west of Milano close to Pavia.

The observed dSCDs of O_4 and HCHO are shown in Figure 8-1: North-west of Milano an enhancement in the HCHO data is observed, in the same region the O_4 data decrease, indicating a higher aerosol load.

The wind was low on this day. According to the sounding in Linate (available at the University of Wyoming http://weather.uwyo.edu/upperair/sounding.html, checked 29/06/05) the wind blew from south east (135°) with 1.5 m/s. Other wind data available from ground based measurements in Alzate and Bresso confirm the wind speed (± 0.5 m/s), the wind direction however is very variable (± 30°).

The aerosol extinction for eight different measurement points was retrieved as described in chapter 4.5.III. High aerosol extinctions (~ 1.5 km^{-1}) were found in the north west of Milano and in luff of the town lower values around 0.4 km^{-1} were deduced.

8.1.II Measurement Results

Although the observed O_4 dSCDs are discussed in detail in chapter 4.5.III, the observed slant columns are shown in Figure 8-2. Here we will concentrate on formaldehyde and nitrogen dioxide.

The strong NO_2 peaks observed close next to the cement works in Calusco are not discussed in this section as we want to focus on HCHO mainly[2]. In section 8.2 the emission flux of a power plant will be discussed in detail.

For Formaldehyde four enhancements were observed in the north western region of flight pattern. It is visible in the data of all telescopes, upward and downward, in the zenith (+82°) the signal is significantly lower than in the other lines of sight. All the others telescopes observe an enhancement of the same order of magnitude. In nadir (-84°) higher fluctuations are observed which is caused by the low signal (intensity) and the resulting higher noise. For the retrieval of the mixing ratio below the aeroplane it is therefore neglected.

---

[2] A similar point source of HCHO was not observed in the first FORMAT campaign, in the second campaign agricultural fires were the only point source observed.

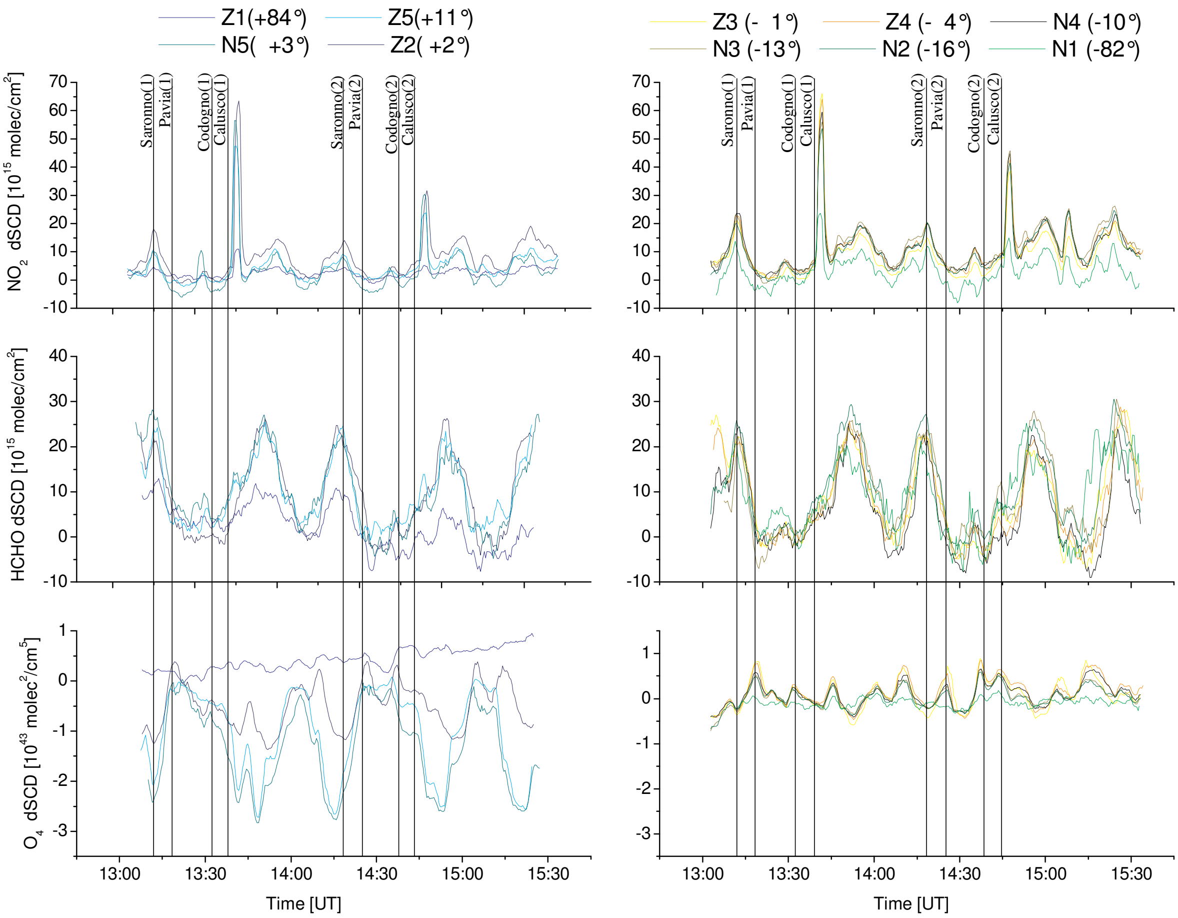

Figure 8-2: Time series of the observed trace gases NO_2, HCHO and O_4. In the left panel the data of the upward directed telescopes are shown, and in the right panel the "downward data" are illustrated. In the NO_2 data strong peaks caused by the cement plant in Calusco can be realised (~13:40 and 14:30). Beside these point source emissions, a good temporal coincidence between the HCHO and NO_2 is obvious: The four peaks observed here were observed in the northern western regions (Figure 8-1).

8.1.III Retrieval of the HCHO AMFs

The aerosol extinction profile was retrieved for eight different positions along the way. To retrieve the HCHO AMF at these positions the Box Air Mass Factors (Box AMF) are very helpful. As explained in chapter 4.1 the Box AMF describes the sensitivity of one line of sight i for a concentration c_j in a certain layer j. The observed slant column density can be calculated:

$$S_i = \sum_j A_{Box,i,j} \cdot c_j \cdot \Delta z_j \tag{8.1}$$

where Δz_j represents the vertical extinction of the layer.

Based on the lower visibility in the northern regions we expect the Box AMF to be smaller there as in the southern part. Due to the high aerosol load the light path is short because the light is scattered in higher altitudes and partly shielded from the surface. Therefore the absorption caused by the same concentration is low (Figure 8-3).

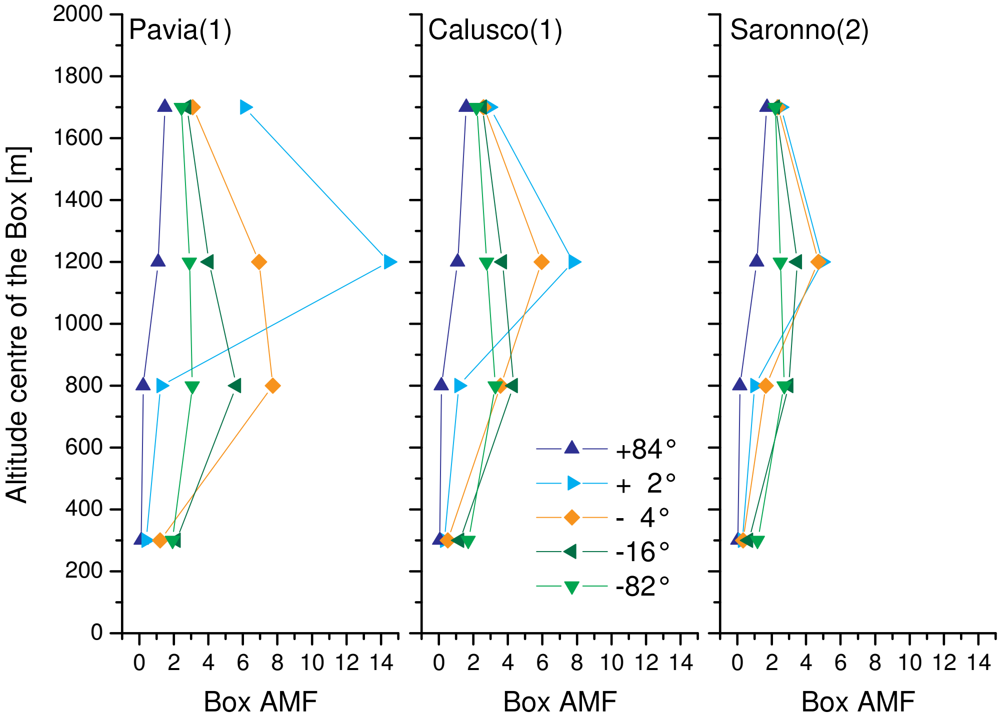

Figure 8-3: Box AMFs for specific lines of sight for Pavia(1), Calusco(1) and Saronno(2). The flight altitude was at 1100 m (not shown).

Besides the expected findings that the AMAXDOAS is less sensitive when flying through higher aerosol load, there is another interesting result. The left panel of Figure 8-3 shows, that in the low aerosol case the telescope directed in -4° (below the horizon) is more sensitive in the layer between 600 m and 1000 m than in the flight altitude (1100 m). This is in agreement to our expectation. The light path through the upper box (1000-1400 m) is short, due to the position of the detector 100 m above the edge. In the next box the same light path crosses most of the box until it is scattered. However, comparing this to the high aerosol case (right panel), the Box AMF for 800 m is even lower than the one in the flight altitude box. Even in the moderate aerosol load in Calusco the same finding can be observed. This can be explained as more light is scattered in higher altitudes and contributes to the signal, whereas the contribution of the lower altitude is rather small.

The sensitivity of the other telescopes is as expected. The telescope directed to the zenith (86°) is insensitive to the lowest layer. The upward looking telescope (+2°) is most sensitive in the flight altitude, here the sensitivity decreases to less than 50 % in the high aerosol load. If looking to Nadir, almost no difference is caused by the different aerosol loads; the Box AMF in the boxes below the aeroplane equals 2 (± 0.2). The Box AMFs can be used to retrieve the AMF for a specific line of sight if the concentration profile c(j) is known:

$$A_i = \frac{S_i}{V} = \frac{\sum_j A_{Box,i,j} \cdot c_j \cdot \Delta z_j}{\sum_j c_j \cdot \Delta z_j} \tag{8.2}$$

In principal it is possible to derive the concentration profile from measurements with different elevation angles. Several approaches to retrieve the concentration profiles were used: Matrix inversion using SIRT (chapter 3.5.II) or a Monte-Carlo approach [Friedeburg, 2003] but no clear profile could be retrieved (attachment B).

Hence one relative profile was assumed for the entire flight. Based on the independent other observation we assumed the HCHO mixing ratio to be constant in the mixing layer and decrease rapidly with height afterwards (Wolfgang Junkermann, presentation at the FORMAT meeting in Garmisch-Partenkirchen on 22-24/01/03). The assumed profile is shown in Figure 8-4 the mixing ratio is constant for the mixing layer (below 1000 m). In the box above the mixing layer (1000 – 1400 m) we assumed it to be 70 % of this value. Above 1400 m the HCHO profile was set to zero.

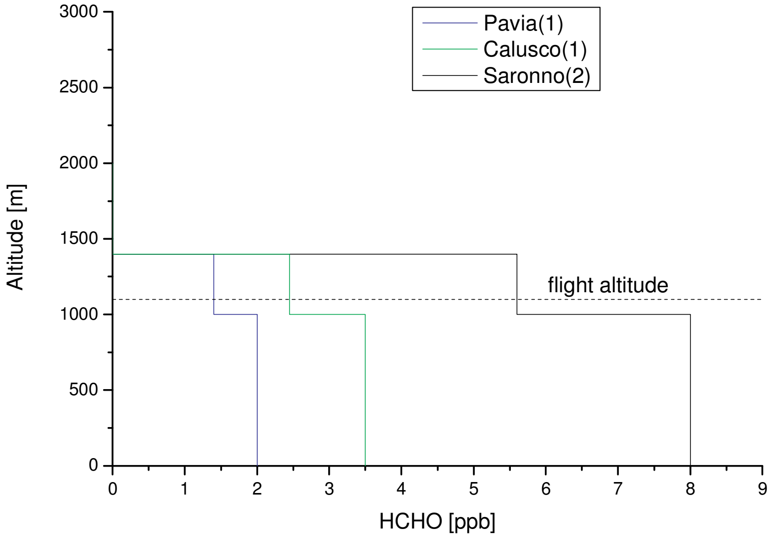

Figure 8-4: Assumed profiles for three measurement points. In the reference site in Pavia we assumed a mixing ratio of 2 ppb. The other values are chosen to achieve an agreement between the observed and the assumed slant column densities.

As the concentration profile is independent of the location the AMF only depends on the Box AMF and hence on the aerosol load (equation 8.2 assume a constant profile $c_j \equiv c$).

The reference site was assumed to be clean with 2 ppb HCHO. As we cannot retrieve the information directly from our measurements, an assumption has to be made. From the same day no in situ measurement were performed in the southern background. Therefore we used the observations on 15/08/2003 by Wolfgang Junkermann. He observed about 2 ppb in the region of our reference on the day before (private communication, file date: 24/09/2004).

In section 8.1.IV the influence of this assumption on the vertical columns and the total flux is discussed in detail. For the polluted regions it is of the order of 20%.

If the concentration profile is known, the vertical column density is given by the integration across the altitude range. For the eight measurement points the respective mixing ratios and the vertical column densities are given in Table 8-A.

	Saronno 1	**Pavia 1**	**Codogno 1**	**Calusco 1**	**Saronno 2**	**Pavia 2**	**Codogno 2**	**Calusco 2**
MR [ppb]	9	2	2.2	3.5	8	2.5	2.2	3
VCD [10^{15}]	26.1	5.8	6.4	10.1	23.2	7.2	6.4	8.7

Table 8-A: Retrieved Mixing ratios and vertical column densities for the individual measurement locations.

8.1.III.a Interpolation along the Flight Track

The next step will be some kind of interpolation between the measurement points to get the vertical column density for the entire flight. According to the definitions (chapter 3.2.III) the relation between the differential slant column and the vertical column is given by:

$$V = \frac{dS + S_{ref}}{A} \tag{8.3}$$

While the dS is measured, the slant column density of the reference (S_{ref}) was estimated in the last section. The air mass factor depends on many parameters, some of them are known (e.g., SZA, SAA or flight altitude) some are unknown. The aerosol extinction was retrieved in chapter 4.5.III for eight selected position, between these positions it is not known exactly known. The aerosol load obviously changes along the flight (chapter 4.5.III), hence the sensitivity changes accordingly. The observed O_4 column is a well established tool to estimate the visibility and the aerosol load. In the following it will be used to estimate the sensitivity to HCHO as well. A correlation between the modelled AMF for HCHO and O_4 is observed for the downward looking telescopes as can be seen in Figure 8-5. This will be used to calculate the HCHO-AMFs for the complete flight.

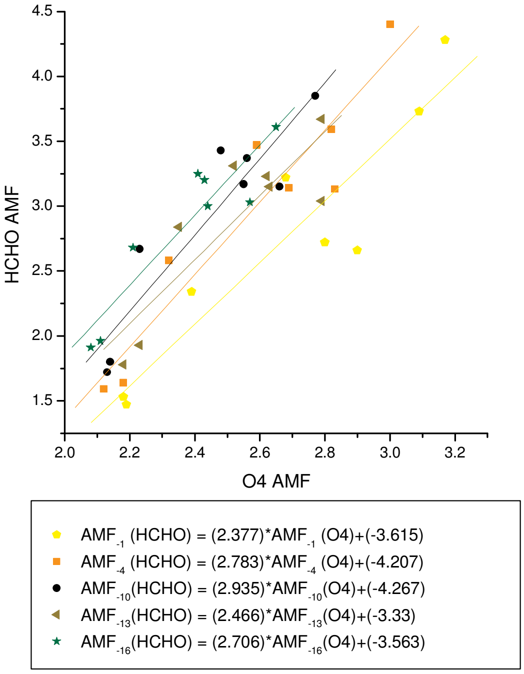

Figure 8-5: A correlation between the O_4- and the HCHO-AMF is observed for the downward directed telescopes.

Before applying the new result, we should stop for a short time to ask for the reason of the finding.

The observed relation is mainly caused by two data points where low O_4-AMF and low HCHO-AMF are observed. The two important points belong to the observation in Saronno. Here the aerosol load was high compared to the other stations. The high aerosol extinction causes a low Box AMF (Figure 8-3) and a low sensitivity for both O_4 and HCHO. So both AMF are low in this region. A third data point which might be important to the observed relation belongs to the first overpass over Calusco, where a moderate aerosol extinction was assumed and hence the calculated AMF for O_4 and HCHO are lower compared to the rest but higher than in Saronno. The main reason for the observed relation is the different aerosol load along the flight track, resulting in different sensibilities. The absolute concentrations of formaldehyde are of no influence for the AMFs.

Now we will again concentrate on the original problem: To retrieve the vertical column density along the flight track. For any time t the vertical column can be calculated:

$$V(t,HCHO) = \frac{S(t,HCHO)}{A(t,HCHO)} \tag{8.4}$$

The relation discussed above provides us with the AMF for HCHO as soon as we know the O_4-AMF. Based on our simulation we know the O_4-AMF for the complete flight:

$$A_i(t,O_4) = \frac{dS_i(t,O_4)}{V(O_4)} + A_{ref,i}(O_4) \tag{8.5}$$

In a similar way the formaldehyde slant column density can be retrieved, just add the simulated SCD for the reference point we discussed above. The retrieved vertical columns of five downward directed telescopes (-1°, -4°, -10°, -13° and -16°) are shown in Figure 8-6 as a function of time, for the final result they were averaged. The nadir telescope is not included as the noise is very high. The general pattern looks very similar: High vertical column densities are observed during four time intervals. They can be attributed to the plane crossing the north-west of the town. The vertical column density here varies between 27 and 37*10^{15} molec/cm^2. In the southern parts the vertical column densities are much lower: around 4 to 10*10^{15} molec/cm^2. In those regions where less HCHO is observed the differences between the various lines of sight are up to 5 10^{15} molec/cm^2. Relative to the mean value the maximum error is about 40 % and the average deviation is of the order of 20 %.

In Figure 8-7 the averaged vertical column along the flight track is shown. The results will be discussed in detail in the next section and we continue with the description of the analysis here.

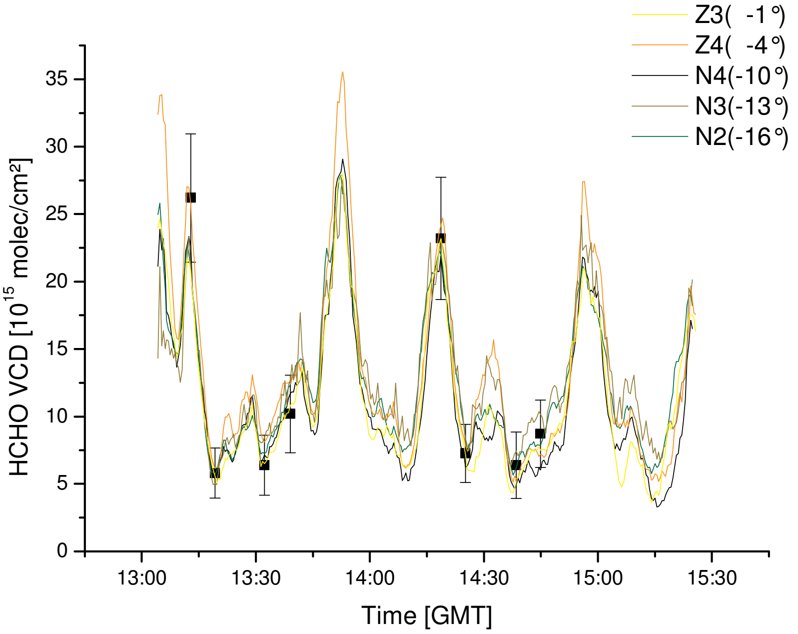

Figure 8-6: The vertical column density calculated for five different lines of sight. The agreement in general is very good. Only for some places the telescope Z4 (-4°) overestimates the vertical column compared to the other telescopes In addition the vertical profile retrieved for the individual measurement points are given. In the highly polluted areas, the vertical columns based on the interpolation method are little lower than the one retrieved by the direct estimation (Table 8-A).

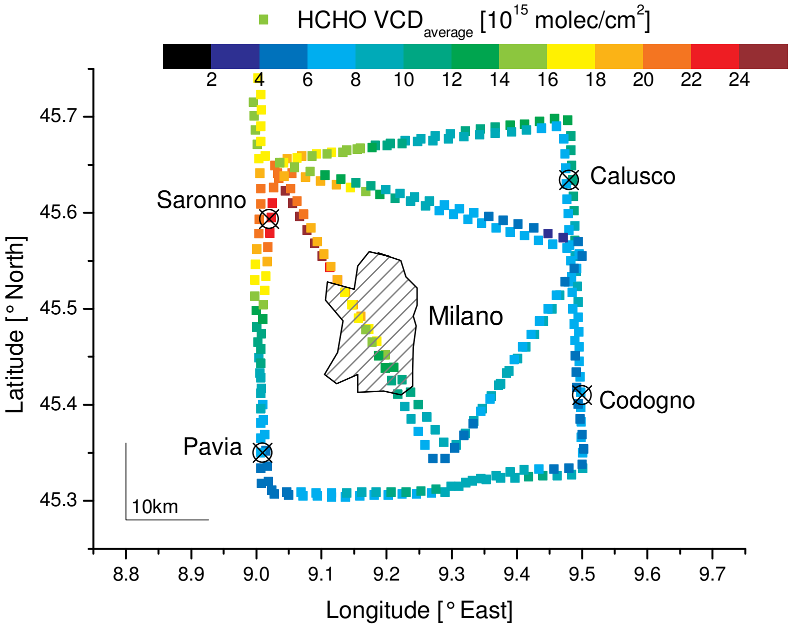

Figure 8-7: Vertical column densities along the flight track, average of five downward directed telescopes. Due to the high noise the nadir telescope was ignored here.

If the relative concentration profile is the same for the entire flight (as we assumed it to be) the average mixing ratio can be retrieved very easily from the vertical columns: Just divide the vertical column by the mixing layer height. The relation between mixing ratio and concentration has to be taken into account as well as the lower mixing ratio between 1000 m and 1400 m. Hence the factor for the conversion equals 1 ppb/($2.9*10^{15}$ molec/cm^2). This relation is used to map the VCDs to mixing ratios. The averaged mixing ratio as a function of the flight track is shown in Figure 8-8. Due to the used relation between vertical column and mixing ratio the horizontal distribution obviously is the same as for the vertical column.

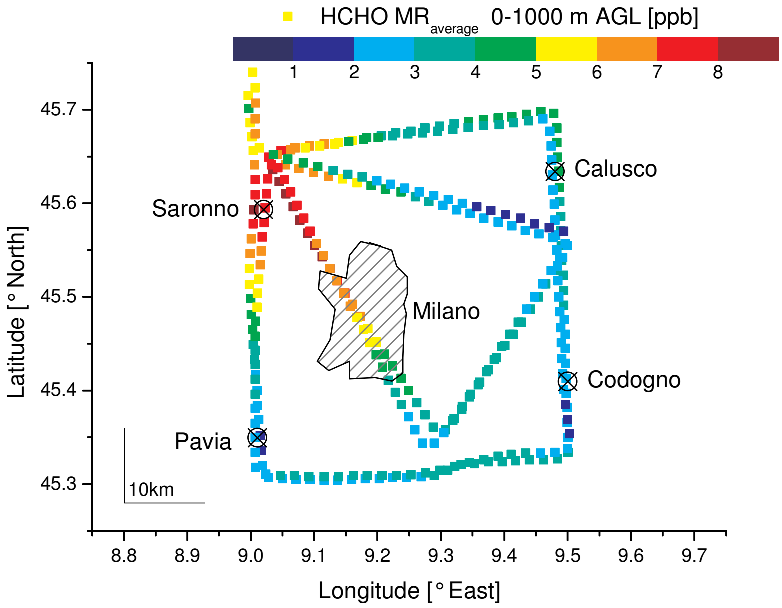

Figure 8-8: Average volume mixing ratio in the lowest 1000 m along the flight track.

North-west of Milano the highest values were observed (about 6 – 8 ppb). This agrees well with the mixing ratios in Bresso (6 ppb) and Alzate (5.5 ppb) on this day (Claudia Hak, personal communications, April 2005). The background mixing ratio in the south and east of the town is about 2 ppb based on our background estimation. In the north-east close to Calusco in the first overpass enhanced values (3 – 4 ppb) were observed.

Due to the different flight tracks and the different times of the flight a direct comparison with the formaldehyde measurement form Wolfgang Junkermann is difficult. Nevertheless both datasets are shown in Figure 8-9. The relative low values he observes in the northern part of the flight can be explained by the different flight altitude. North of Alzate in the Alpine crest the flight altitude is not limited to 2000 ft (ASL) as it is in the south. In this region the profile flights were performed. In the southern region the flight altitude is limited to 600 m, and the in situ measurements were performed in this altitude. The AMAXDOAS had the exceptional permission to fly in higher altitudes. Due to DOAS method our measurement is an average value of the lowest 1000 m above ground.

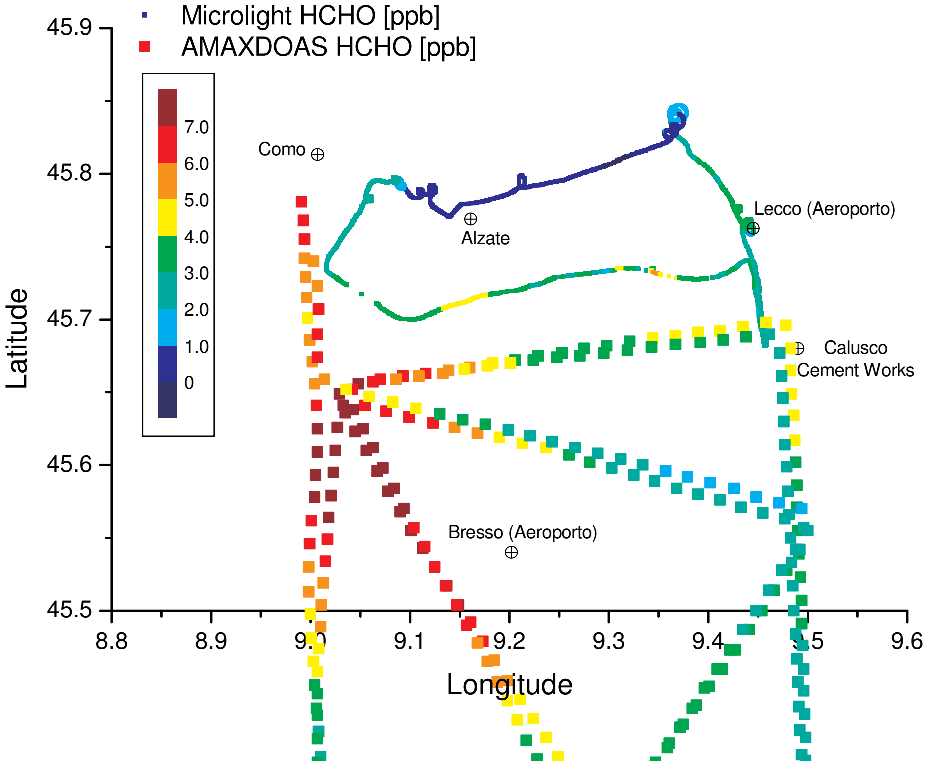

Figure 8-9: Formaldehyde mixing ratios observed by both aeroplanes participating in the FORMAT I campaign. In the North East of Milano both planes observed about 3 – 4 ppb with only half an hour time difference. The absolute values observed north of the town agree quite well. Only in the north west some discrepancies were observed.

North of Milano both measurements agree quite well. In the east local maximum values about 5 ppb were observed. A large discrepancy is observed in the west. Here the AMAXDOAS measurements result in a minimum of 5 ppb whereas the instruments onboard the microlight observed about 2.5 – 3 ppb constantly. Along the flight track of the AMAXDOAS observed strong gradients of 1 – 2 ppb within several kilometres, hence the observed gradient is relative strong but not unrealistic.

8.1.III.b Estimation of the Formaldehyde Flux

Based on the calculated vertical columns the net formaldehyde emissions of greater Milano can be retrieved. For the moment we concentrate on one section of the flight e.g. Saronno-Pavia. The wind blew from south-east; the angle between flight direction and wind direction equaled 45°. The flux Φ through an assumed vertical plane defined by the flight direction reaching from ground to the top of the HCHO profile (1400 m) is given by the integrated concentration in the plane multiplied by the wind speed and the sine of the relative wind direction α:

$$\begin{aligned}\Phi &= \iint c(h,s)\cdot v_{wind}(h,s)\cdot \sin(\alpha(h,s))\cdot dh\cdot ds\\ &= \int v_{wind}(s)\cdot \sin(\alpha(s))\cdot \left(\int c(h,s)\cdot dh\right)\cdot ds\\ &= \int v_{wind}(t)\cdot \sin(\alpha(t))\cdot V(t)\cdot v_{aeroplane}(t)\cdot dt\end{aligned} \tag{8.6}$$

In the first equation two assumptions are made: The wind speed and the wind direction are independent of the altitude. Both assumptions are not exactly true. Nevertheless as along as the concentration is constant with altitude an average wind speed and wind direction can be assumed. In the last equation we used the definition of the vertical column density is inserted. In our example the flux is calculated by:

$$\Phi = \int_{T_{Saronno}}^{T_{Pavia}} v_{aeroplane}(t)\cdot v_{wind}(t)\cdot \sin(\alpha(t))\cdot V(t)\cdot dt$$

If the heading angle of the aeroplane (relative to north) is larger than 135° (south-east) than α(t) is defined as positive otherwise it is negative. This results in positive or negative flux respectively. Due to the flight track anticlockwise around the town and the wind direction, the fluxes out of the rectangle are positive and those into it are negative.

On 16/08/2002 the wind speed was 1.5 m/s as mentioned in the introduction of this section 8.1.I. The flux was calculated separately for each part of the flight. In the corners the viewing geometry is completely unknown as the slope parameters varied very quickly – they even changed within one measurement. Hence the AMFs in these areas might be wrong, although no systematic effect in either the HCHO or the O_4 columns is observed. Three data points in each corner are omitted for calculating the flux. For the different flight legs of the rectangle the flux is given in Table 8-B.

Flight Track	Saronno-Pavia	Pavia-Codogno	Codogno-Calusco	Calusco-Saronno
1st round	5.370	-3.947	-3.866	5.893
2nd round	6.401	-4.586	-2.673	4.403

Table 8-B: Formaldehyde flux in 10^{24} molec/s. The negative flux indicates the flux into the rectangle, the positive values stand for the outflow of the area.

The HCHO flux originating from the city of Milano is the sum of the first and the fourth part of the flight and equals $11*10^{24}$ molec/s. In the same period HCHO flux of $7.5*10^{24}$ molec/sec into the city is observed. The total flux is then calculated for both rounds in average to $3.5*10^{24}$ molec/s (0.63 tons/h). The partial fluxes for the first and the second round are similar to each other; hence we can assume this flux to be constant at least for the measurement time (about 2 h).

8.1.IV Discussion of the Results Part I – Error and Analysis

In the last paragraph the analysis was described. Before we discuss the results from the chemical point of view, we want to check our analysis. Whether the results are consistent or not can be checked by comparing the results (VCD or MR) from different lines of sight. However the analysis of all lines of sight is based on the same assumptions concerning the reference slant column, the profile for the calculation of the AMF and the interpolation of the AMF. Hence an agreement between the different lines of sight can be expected but cannot be used as an indicator sufficient for a correct result. If on the other hand five different lines of sight resulted in five different vertical columns, this would demonstrate very well, that part of the analysis is not performed correctly. The result of the five downward directed telescopes are shown in Figure 8-6, here no significant discrepancy is observed.

Estimating the error of the complete retrieval is very difficult or impossible as it relies on assumptions we can hardly substantiate by independent data, besides those already mentioned. At the beginning we calculated the O_4 AMFs to retrieve the aerosol extinction for eight points of the flight. The measured data equal the difference between two simulated sets of AMFs. If the aerosol load in the reference is completely wrong, the other points are wrong as well but the difference might still be correct. Due to the numerous sets of extinction profiles and the good agreement between the measurements and the simulations, we assume the data are correct.

For the analysis of the following error we assume the aerosol extinction to be correct, and concentrate on the errors we can quantify. To estimate the error of the vertical column densities three errors have to be quantified:

- The uncertainty of the reference slant column,
- the error of the AMF,
- the measurement error in the differential slant column.

As soon as these errors are estimated we can calculate the total error of the vertical column. In the following we will discuss them one by one and calculate their influence on the VCDs of the five telescopes used above for the calculation of the average VCD.

The slant column density of the reference was calculated with the assumption that the mixing ratio in Pavia equals 2 ppb. If we assume the background concentration to be wrong by less than 50 %, and the Box AMF to vary by about 0.1, then the error of the reference SCD will be given by:

$$\Delta S = \sqrt{\sum_j (\Delta A_{Box,j} \cdot c_j \cdot z_j)^2 + (A_{Box,j} \cdot \Delta c_j \cdot z_j)^2} \approx 33\% \cdot S$$

Here an average value for the downward looking telescopes is given. For the different lines of sight the error varies in the range of 31 % to 36 %. The variations will be considered in the further analysis. The error of the reference slant column density contributes to the error of the vertical column density. If all the other error were 0, the error in the VCD would be 15 % to 33 % depending on the location. In the regions with high slant columns (Saronno) the influence of the assumed background is small. Whereas in those regions where no differential slant column is observed (Pavia) no information is gained directly from the measurements. Therefore the error is given by the error in the assumed reference slant column.

The AMF used to derive the vertical column was based on the correlation between O_4-AMF and HCHO-AMF. Hence the uncertainties of the fitted HCHO-AMF as well as the uncertainty of the linear fit have to be considered. The AMFs are based on the assumed profile. Studying all kinds of possible profiles might lead to an estimation of the error. However as we cannot retrieve the profile information from the data, this approach is not very useful here. Instead we study two extreme cases of the profile, first all the observed HCHO is situated in the lowest layer and second the other extreme it is concentrated around the flight altitude. In both cases the total AMF equal the box AMF for respective box, from ground to 600 or close the flight altitude box (1000 m – 1400 m).

As expected from Figure 8-3 the -1° line of sight is almost insensitive in this case, the AMF is close to 0.5 in this case. But also for all the other lines of sight the respective AMF decreases, and is below 2 for all lines of sights. If the HCHO is situated close to the flight altitude, largest influence will be observed for the telescope elevated by -1°. While the total AMF equalled 4.5 we retrieved previously in the extreme case it increases up to 13. The influence on the -16° AMF is rather small it is increased by about 13%. As the simulated slant column densities do not agree with the observation these AMF cannot be used to estimate a realistic error in the simulated AMFs themselves and assume the error is small compared to the error of the linear fit. To estimate the error of the fit the difference between the fitted curve and the simulated data is used.

$$\Delta A_i(HCHO) = \sqrt{\frac{\sum_{l=1}^{8}(A_{loc,i}^{fit} - A_{loc,i}^{sim})^2}{7}}$$

here i again stands for the line of sight and loc numbers the eight points used for this study. Depending on the line of sight the absolute error varies between 0.35 and 0.25.

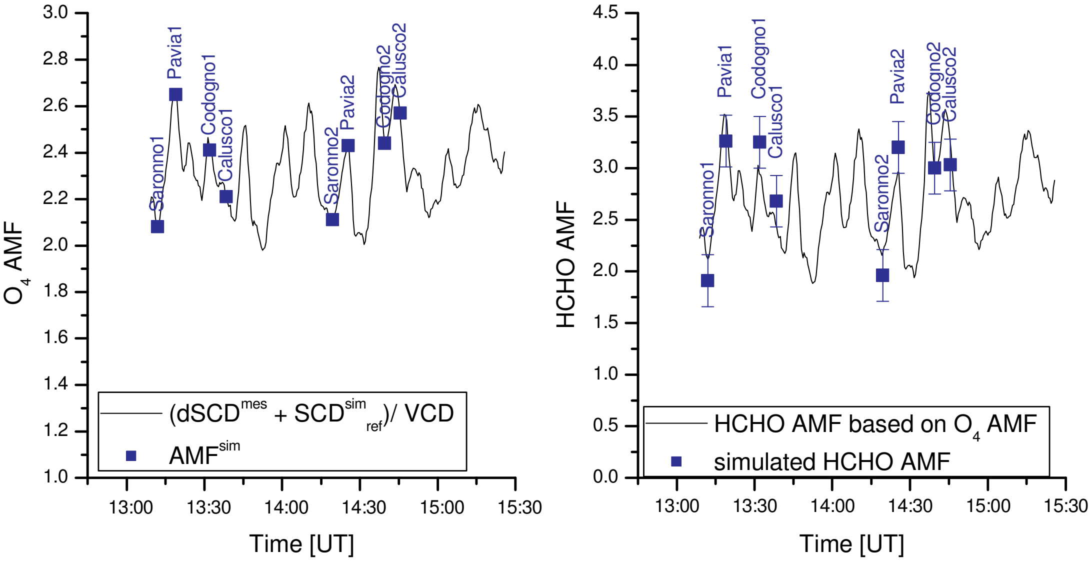

Figure 8-10: The simulated AMFs for both O_4 (left) and HCHO (right) for the telescope directed to -16°. In addition to the interpolated data (black line) the simulated data are shown in blue. For the HCHO-AMF the error (0.25) as discussed above is shown as well.

The interpolated HCHO-AMF for the complete flight is shown in Figure 8-10. If the error is estimated as described above, the simulated values agree well with the interpolation within the error. The assumed error in the AMF leads to an error in the vertical column density of 8 % to 18 %. This time the dependency on the location is the other way round as before. The high HCHO slant columns correlate with the high aerosol load and the small AMFs. Here the error introduced by the wrong AMF is high (18%). Whereas in the clean regions the AMFS are high hence the same absolute error in the AMF results in lower errors in the VCD (8 % to 10 %).

The error in the differential slant column density was discussed in chapter 3.3, the average error in the slant column density equals $3.5*10^{15}$ molec/cm^2. The effect of the DOAS error is of the order of 10 % (7 % - 15 %), hence it is of the same order magnitude as the effect of the AMFs or the assumed reference.

An overview of the individual sources of the error is given below:

	Background [%]	**Box-AMF**	**AMF-interpolation**	**DOAS – fit [molec/cm²]**
Uncertainty	50	0.1	0.3	$3.5*10^{15}$
relative Error of the VCD [%]	16-30	1-2	8-18	7-15

Table 8-C: Individual sources of error and their influence on the total VCD.

For the five most relevant downward looking telescopes (-1° to -16°) the total error is of the order of 20 % to 40 %. The average error in the eight measurement points is 32 %. One reason for the error is the uncertainty in the assumed reference column. If we knew the concentration in Pavia to be correct by 20 % instead of 50 %, this would reduce the total error to 20 %.

If the vertical column has an error of 32 % or more, how large is the error in the flux? The flux's estimation was based on the average of five vertical column densities, each of them has an error of 32 %. Hence the average has an error of 30 %, as we have to assume the error in the background reference and the AMF to be systematically whereas the influence of the DOAS fit error is reduced by averaging several lines of sight.

Besides the vertical column the wind speed, the relative direction of the wind and the speed of the aeroplane are used for the flux estimation. According to wind data from Linate on 16/08/2002 the wind speed was 1.5 m/s with an uncertainty of 0.5 m/s, the wind direction was 135° (± 30°). The speed over ground of the plane was 272 km/h ± 10 km/h. This uncertainty here is small compared to the others and will not be taken into account.

Again we will study the influence of the three possible error sources separately. For the calculation we first concentrate on the flight part between Saronno and Pavia, where the flux equals $5.37*10^{24}$ molec/s. After we discussed the error in this part of the flight, we will expand the discussion on the complete box around Milano. The influence of the wind speed and the vertical column is the same for all parts of the flight. A change in the wind direction however influences the local fluxes completely different. In our example we assume the aeroplane headed south from Saronno to Pavia. Hence the influence of the wind direction would be large if the wind blew rather from the south than from south-east. In the next part of the flight the plane headed east from Pavia to Codogno. In total the error caused by the wind direction is reduced when the complete flight is taken into account.

The relative error of the wind speed is 33 % and therefore the relative error of the flux caused by the wind speed is 33 %. For the vertical column we assume a constant uncertainty along the flight of 30 %, which causes the same error in the flux.

The wind direction is certain only by 30°, this has a large influence on the estimated flux. If the relative angle was 105° instead of 135°, then the flux is the first section would be higher by a factor of $\sin(105°)/\sin(135°) \approx 1.36$. On the other hand if the wind direction was 165° the relative angle would be 15° and the flux would decrease to $1.97*10^{24}$ molec/s. Hence our estimation would dramatically overestimate the real situation. Caused only by the uncertainties of the wind direction the relative error is +36 %, -63 %.

Based on these three possible sources of the uncertainties the total error equals +57,89 %, to -77.66 %[3].

To estimate the influence of the wind direction the flux for the minimum and maximum wind direction was calculated for this part of the flight. The same method is applied to all parts of the flight taking into account for the flux estimation. An overview of the individual fluxes for the extreme values of the wind direction is shown in Table 8-D.

---

[3] Including the uncertainty of the aeroplane's speed the error is: 77.76 %.

Flight track (wind direction)	**Saronno-Pavia**	**Pavia-Codogno**	**Codogno-Calusco**	**Calusco-Saronno**
1st round (105°)	7.30	-1.46	-5.26	2.89
2nd round (105°)	8.71	-1.70	-3.64	2.16
1st round (165°)	1.99	-5.37	-1.43	7.31
2nd round (165°)	2.37	-6.24	-9.89	5.46

Table 8-D: Depending on the wind direction the total flux changes, here for the two extreme values of the uncertainty range the partial fluxes are shown, again in 10^{24} molec/s (compare Table 8-B).
105° = 135° - 30° in the upper part of the Table,
165° = 135° + 30° in the lower part.

For the two extreme wind directions the total flux can be calculated:
Flux(105°) = $4.50*10^{24}$ molec/s
Flux(165°) = $1.55*10^{24}$ molec/s
Compared to the value of $3.5*10^{24}$ molec/s the deviation equals +28 % to -55 %, this error is only caused by the uncertainty in the wind direction. The other errors and uncertainties are ignored during this calculation.
For the total flux originating from the area inside of the square around Milano all errors have to be considered. The photochemical production and direct emission of formaldehyde sum up to $3.5*10^{24}$ molec/s (+53 %, -71 %).

8.1.V Discussion of the Results Part II – other Trace Gases and Chemistry

To study the chemistry of formaldehyde and the photo oxidation was the main aspect of the FORMAT campaigns. In the following section this aspect will be discussed for the actual flight. The chemistry of formaldehyde, nitrogen oxides and ozone was introduced in chapter 2.1. Hence before discussing the chemical aspects, the results of O_3 and NO_2 are presented briefly.

8.1.V.a Tropospheric Ozone

The observed ozone is mainly influenced by the stratospheric ozone layer. The absorption caused by the stratospheric ozone is proportional to $A \approx 1/\cos(\vartheta)$. The solar zenith angle varied between 35.9° and 60.6° during the flight, so it was low enough to use approximation.

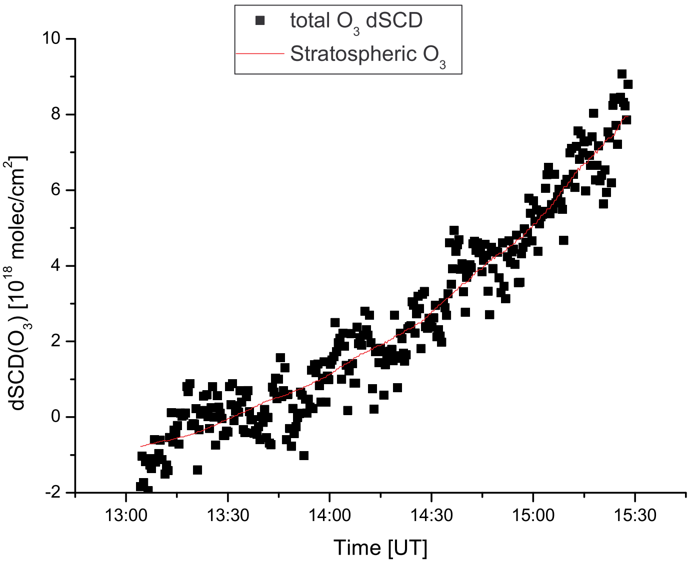

Figure 8-11: observed O_3 dSCD for the -4° telescope. In addition to the observed data the stratospheric signal is shown in red.

In Figure 8-11 the total O_3 dSCDs of the entire flight are shown. A Langley plot (chapter 7.2.I.b) was used to estimate the stratospheric signal, which is indicated in the figure as well (red line). To subtract the stratospheric signal from the total dSCD as discussed in the case of NO_2 in chapter 3.4 is of no use here. The resulting O_3 tropospheric slant column density (TSCD) contains no significant information about the tropospheric ozone distribution around Milano.

We calculate an expected ozone signal. The background concentration of ozone is about 50 ppb and we assume a local increase by 50 ppb. If the local maximum extends over an altitude range of 1400 m, the difference in the vertical column equals $1.6*10^{17}$ molec/cm^2. According to Figure 8-10 the HCHO-AMF is about 4, if we assume the same AMF for O_3 the expected differential slant column equals $6.4*10^{17}$ molec/cm^2. The noise observed in the data can be estimated from Figure 8-11. It is approximately $1*10^{18}$ molec/cm^2 and is therefore higher than the expected tropospheric signal.

This result is not really surprising, similar effects have been observed in the ground based measurements already (Thomas Wagner, private communication 17/03/2005).

On board of the microlight an ozone measure system was installed as well. In the north-westen region where we observed the plume only few measurements are available as the instrument failed. The few existing values indicate a slight increase compared to the central region.

8.1.V.b Tropospheric Nitrogen Dioxide

In contrast to stratospheric ozone absorptions, the influence of the stratospheric nitrogen dioxide is small for the observed SZA range. In Figure 8-2 no general trend in the NO_2 dSCD is observed – compared to Figure 8-11. Therefore we completely ignore any stratospheric influence, the observed differential slant columns can be seen as tropospheric differential columns.

Despite the strong emission peak close to the Calusco cement work, the NO_2 dSCD almost show the same pattern as the HCHO data. To retrieve vertical NO_2 columns the same method as described above can be applied. We assume background level of 3 ppb in the lowest 1000 m and use the AMF we calculated for formaldehyde. Again the time series for the vertical columns are shown (Figure 8-12) The differences between Z4(-4°) and the average are less than 30 %.

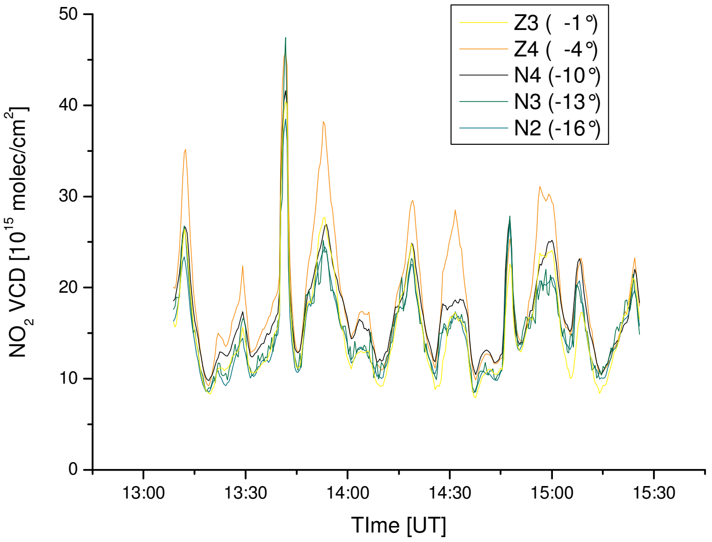

Figure 8-12: Time series of the NO_2 VCD for the five downward directed telescope. The general agreement between the different lines of sight is quite good.

In Figure 8-13 the distribution of the vertical NO_2 column density is shown. The similar distribution of NO_2 and HCHO is obvious (Figure 8-7 and Figure 8-13). In a more detailed comparison it seems the NO_2 maximum is above the town, whereas the maximum of HCHO is shifted a little to the north-west. Although a decrease in NO_2 and a parallel increase in HCHO might be explained by the chemical reaction discussed in chapter 2.1, however, the uncertainties in this region are rather high.

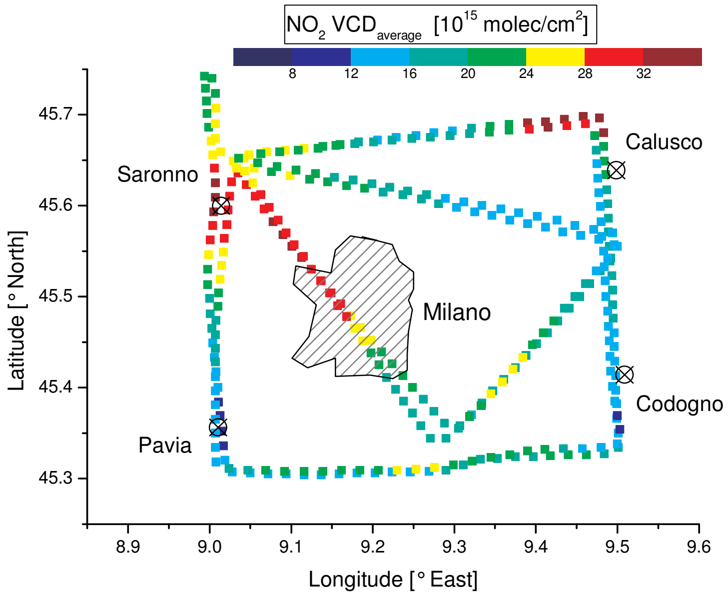

Figure 8-13: NO_2 vertical column densities as function of geographical position, average of the five downward looking telescopes. The scale was chosen to concentrate on the north-western corner of the flight track, the high concentration caused by the local emissions in Calusco are out of range (in the smoothed data the maximum is $53*10^{15}$ molec/cm^2).

To estimate the NO_2 flux originating from the town is rather difficult as the emission of the cement works in Calusco interfere with the town's emissions. The plume of Calusco Cement plant was not crossed completely and the turn was flown inside the plume, hence it is not suitable for to estimate the emission. The town's emission can be estimated rather roughly by integrating across the enhanced concentration in the north-west from north to south. This leads to $4.7*10^{24}$ molec/s or $5.3*10^{24}$ molec/s (1.4 and 1.57 t/h) depending on the flight track.

The enhanced NO_2 values north-west of the town might as well be locally emitted as they might be caused by the town's plume. The higher formaldehyde levels in the same region indicate that the observed pollution might rather be the town's plume then a local effect. Inside the plume the VOCs react with oxidation species and formaldehyde is produced (chapter 2.1.III). Hence it can be used as a tracer for the photo oxidation. Both species HCHO and NO_2 are known to be precursors of O_3. We would therefore expect to observe an enhance ozone level in the plume as well. However, the ozone concentration in the plume depends on the plumes age, i.e. the time between the emissions or photochemical production of the precursors and the measurement. Because of that, only a slight enhancement if at all is expected. The ozone observations of the AMAXDOAS instrument are dominated by a bad signal to noise ratio, hence they cannot be used to substantiate our expectation.

8.2 26/09/2003 Nitrogen Oxides Emissions

During the second FORMAT campaign in September 2003 we did not only concentrate on formaldehyde around Milano, in addition emissions from local point sources were studied a bit more in detail. Along the Po-river there are several power plants (e.g. Chivasso (Piemont), Piacenza, Ostiglia and Sermide (Lombardia) and Porto Tolle (Venezia)) to supply northern Italy with electrical power. However many of them are too faraway (e.g. Porto Tolle[4], or Chivasso) for a detailed investigation of the emissions, the others situated in areas with very restricted flight rules (e.g. Piacenza close to the US – airbase). We decided to concentrate on Sermide, although it was running with half the capacity. Next to Sermide there is a second power plant in Ostiglia, which was in reconstruction as well and only some test were performed in September 2003 (the operator told us).

The power station in Sermide consists of four units. It is driven by natural gas and combustion oil. In total it provided an electrical power of about 1300 MW. During summer 2003 two of the four units were rebuilt and the remaining two had a capacity of 640 MW.

Due to private communication with Gianni Sogari (capo sezione manutenzione mechanica e civile, chief of the maintenance) on the specific day a test of the third unit was performed producing another 250 MW. The total NO_x emissions in the time between 13:00 and 14:00 GMT were 880 kg for all three blocks.

8.2.I Flight Track

The aeroplane started at 8:50 UT heading south to Pavia, then east to Cremona, Mantova and all the way to the Adriatic coast, where we surrounded the power plant of Porto Tolle and flew west again to the airport in Reggio nell' Emilia for refuelling. After a stop of about 1 hour the plane started again at 12:40 UT. We circled around the power plants of Sermide and Ostiglia, crossing the plume downwind of Sermide three times and one time downwind of Ostiglia, to check for small emission of a possible test. The wind speed and wind direction were calculated online by the pilot based on the true air speed and the speed over ground. After the plume flights an "upward dive" through the mixing layer was performed, here a comparison with the microlight (D-MIFU) was planned but the HCHO-measurements on board the microlight failed. Than the aeroplane flew back to the base and finally arrived at 15:00 UT.

---

[4] Porto Tolle is about 1h 30 min flight from Milano Bresso. It is just in the range of the Partenavia but for the flight back a refuelling stop has to be made. The closest airport is in Reggio nell' Emilia, which is perfectly situated along the flight leg back to Milano.

The AMAXDOAS measurements worked fine right from the start in the UV. In the visible the computer crashed on the first part between Milano and Mantova and was restarted close to Mantova. An overview over the flight track and the observed NO_2 dSCDs is shown in Figure 8-14.

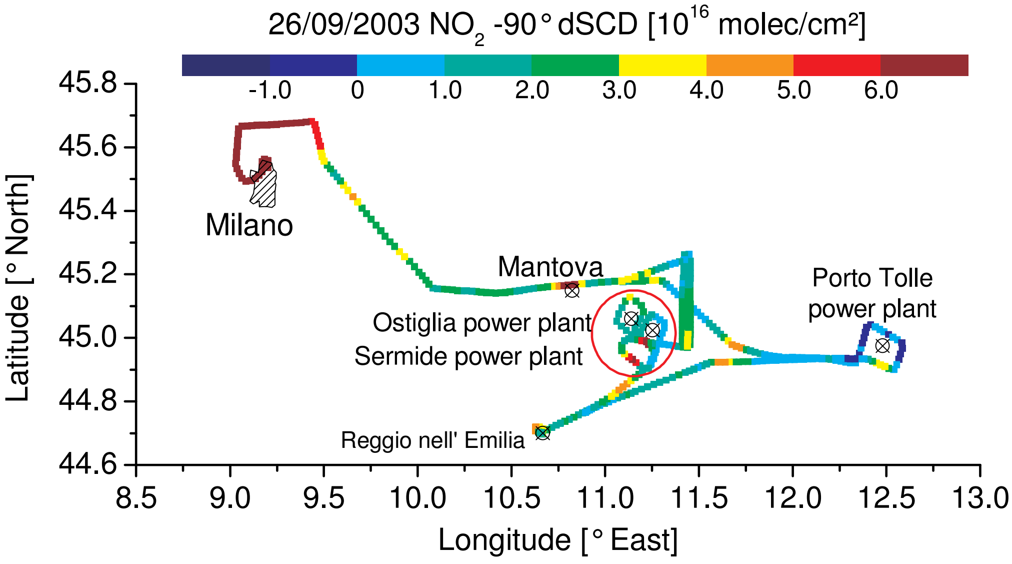

Figure 8-14: Differential SCD observed by the nadir line of sight along the flight. Downwind of the power plants in Sermide and Porto Tolle higher SCD are observed. Besides the very high values north of Milano can be made out as well as the low values close to the coast.

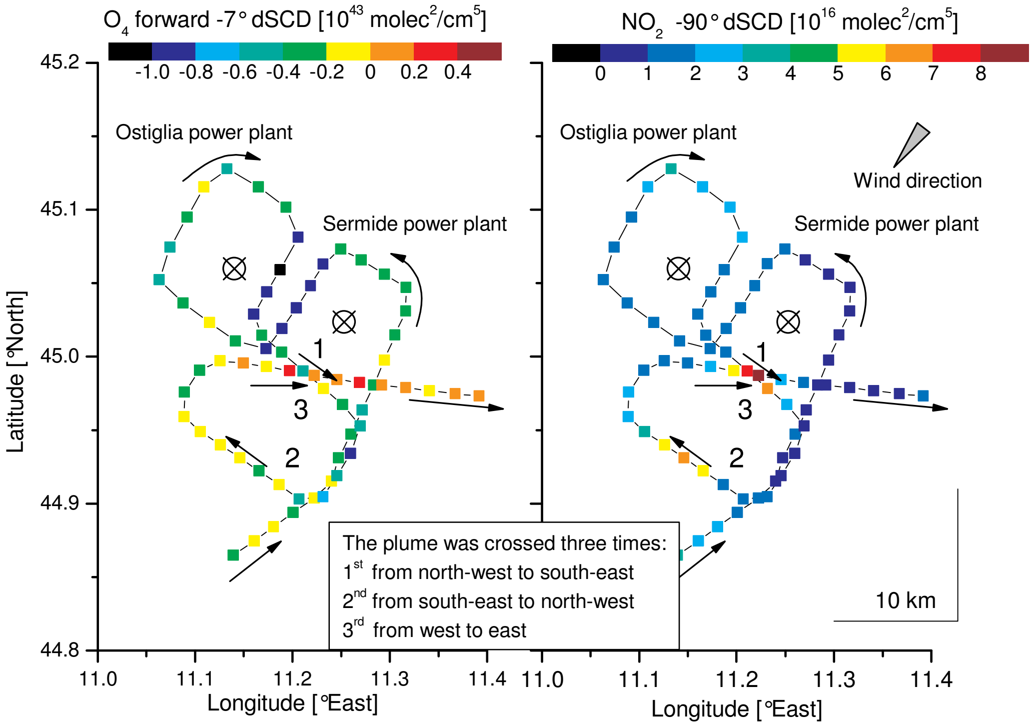

Figure 8-15: Details on the flight track around Sermide and Ostiglia. The arrows indicate the flight directions around the power plants.
Left panel: The O_4 data for one forward directed telescope, the O_4 decreases as the plane flies towards the sun. During the overpasses of the plume no change in the O_4 is observed.
Right panel: NO_2 observed by the nadir telescope, compare Figure 8-14.
Here values for two different telescopes are shown, as the O_4 observations in the nadir do not change with the flight direction, hence this effect could not be explained. On the other hand nadir is used to illustrate how the wind direction can be calculated by the observed dSCDs.

Besides the large sources like Milano and Mantova the high column densities are observed downwind of the power plants in Sermide and Porto Tolle but not in Ostiglia. A slight east west gradient can be observed as well, while the dSCD is negative close to the coast, values around $2*10^{16}$ molec/cm^2 are observed just east of Milano. The reference was taken upwind of Porto Tolle at the Adriatic coast.

A detailed picture of the flight track around Sermide is shown in Figure 8-15, as can be seen the plume was crossed three times. The first and the third time the plume was crossed close to the power plant at a distance of 5 km the second overpass was flown at 13.4 km distance.

8.2.II Conditions along the Flight

As mentioned in chapter 6.4.I the weather conditions were excellent in the period between the 23/09/2003 and 27/09/2003. On the 26/09/2003 only very few small clouds were observed, mostly close to the Adriatic coast. The visibility in Milano was as bad as usual, whereas it was much better in the central and eastern Po basin.

For the calculation of the AMFs a visibility of 23 km was assumed, which is in agreement with the personal impressions and the photos taken during the flight (Figure 8-16). After the case study flight around Sermide an upward dive through the mixing layer was performed. Based upon the report in the log we can assume the mixing layer height to be 1700 m, above the mixing layer the visibility was much better (follows by the definition of the mixing layer). Both the Alps and the Apennines were visible from the centre of the Po basin (Figure 8-17).

For the albedo we assumed 4 % for the stubble fields. In the campaign description the harvest season was mentioned and the local tradition to burn the straw on the fields. For an emission study of a point source such additional sources have to excluded as good as possible. Although the ground distance between the aeroplane and the power plant cannot be seen completely in Figure 8-16, no additional sources like that can be realised. In the log normally each observed fire was mentioned. As there is no fire mentioned here, we can conclude that no field was burned in this area.

Figure 8-16: Photo of Sermide power plant taken during the second plume flight. As can be seen the visibility is far better than 13 km, which is the distance to the plant during this time. The photo was taken with zooming modus of the camera.

Figure 8-17: Photo taken during the profile flight above the boundary layer, in the background the mountains of the Apennines can be made out.

According to the onboard observations the wind speed was 1.5 m/s blowing form 16° north. The soundings in Linate and San Pietro also observed low winds of up to 3 m/s in the mixing layer with very variable wind directions (50° ± 50°). The colleagues on board the Dimona measured the wind all along the flight. They observed 2.1 m/s ± 1.8 m/s west of Mantova. In total we conclude the wind speed was about 1.5 m/s ± 0.5 m/s. The positions of the observed NO_2 peaks are used to calculate the local wind direction. If the wind direction is locally constant in time then both peaks and the chimney will line up along the wind direction, this results in a wind direction of 39° ± 10° (north-east).

8.2.III Observed Slant Columns in lee of Sermide

The slant columns in the nadir line of sight along the flight track are shown in Figure 8-14. In the following we will concentrate on the section close to Sermide (Figure 8-15). This section of the flight took about 40 min (12:50 UT to 13:30 UT), including the flight in the luff of the plant and the box around Ostiglia. The time series of the observed NO_2 dSCDs for the three overpasses is shown in Figure 8-18. As usual not all ten lines of sight are shown here to keep the viewgraph clear.

In the time series of the three overpasses some of the important information is clearly visible. The observed slant column densities in the directions -7° forward and backward are much higher than those in the nadir and zenith. Due to the longer light path these elevation angles are more sensitive as discussed in chapter 4.4.VII. A slight enhancement is observed in the zenith LOS as well, so parts of the plume might be above the flight altitude (~ 600 m AGL). Although the zenith telescope is not completely insensitive to enhanced concentrations below the aeroplane, this possibility is rather likely. Comparing the forward (black) and backward (red) directed telescope a time difference of about 1 minute is observed, whereas the peaks in nadir and zenith were measured simultaneously. A time difference can be expected, caused by the lines of sight. The forward directed telescope is the first to observe the plume whereas the backward is still directed into clean background air.

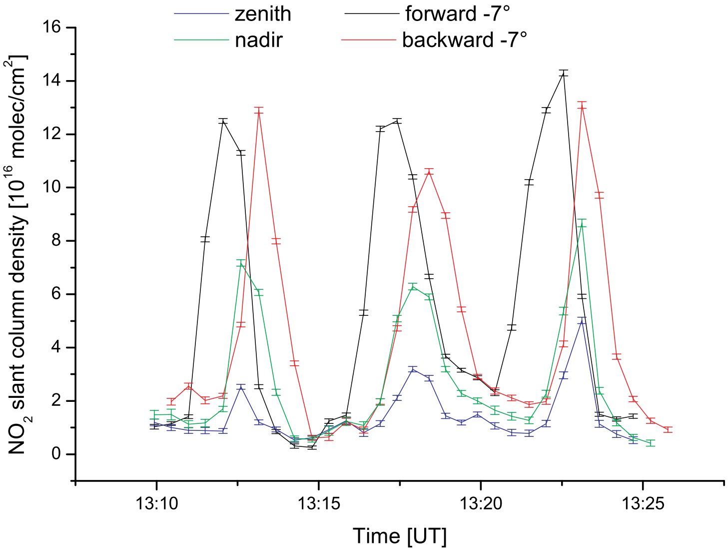

Figure 8-18: Time series of differential slant column densities observed by four telescopes during the overpasses. Here only four of ten telescopes are shown to simplify the viewgraph. The strongest absorptions are detected by the telescopes directed to -7°. The enhancements in nadir and zenith are much smaller. The slight signal in the zenith indicates that parts of the plume are above the aeroplane.

8.2.IV Tomographic Inversion

In the tomographic inversion the fact that the same air mass is observed by different lines of sight at different times is used to reconstruct the 2-dimensional concentration distribution. Details about the theory of DOAS tomography were described in chapter 3.5.

For the inversion 2-dimensional Box-AMF are crucial. In chapter 4.4.VII.b we explained how the Box-AMFs are calculated based on the single scattering approximation. The comparison between single scattering AMF and multi scattering simulation with Tracy showed a reasonable agreement. Hence the single scattering approximation can be used for the inversion.

A sensitivity study performed with single scattering AMF and realistic settings for the reconstruction of the Sermide plume showed that vertical resolution should be 125 m rather than 100 m (Bing Chao Song, private communication, July 2005). 2 km grid size was used for the horizontal resolution along the flight track. The total area of interest had an altitude of 2 km and a length of 20 km.

The mathematical problem to be solved for the 2-dimensional reconstruction is:

$$S_i = \sum_j A_{ij} \cdot c_j \tag{8.7}$$

where A is the linear forward model as described in the chapters 3.5.I and 4.4.VII. The index i includes all measurements from all lines of sight and all positions along one cross section. The latter can be done as the duration of the overpasses is short and the atmospheric conditions can be assumed to be slowly varying.

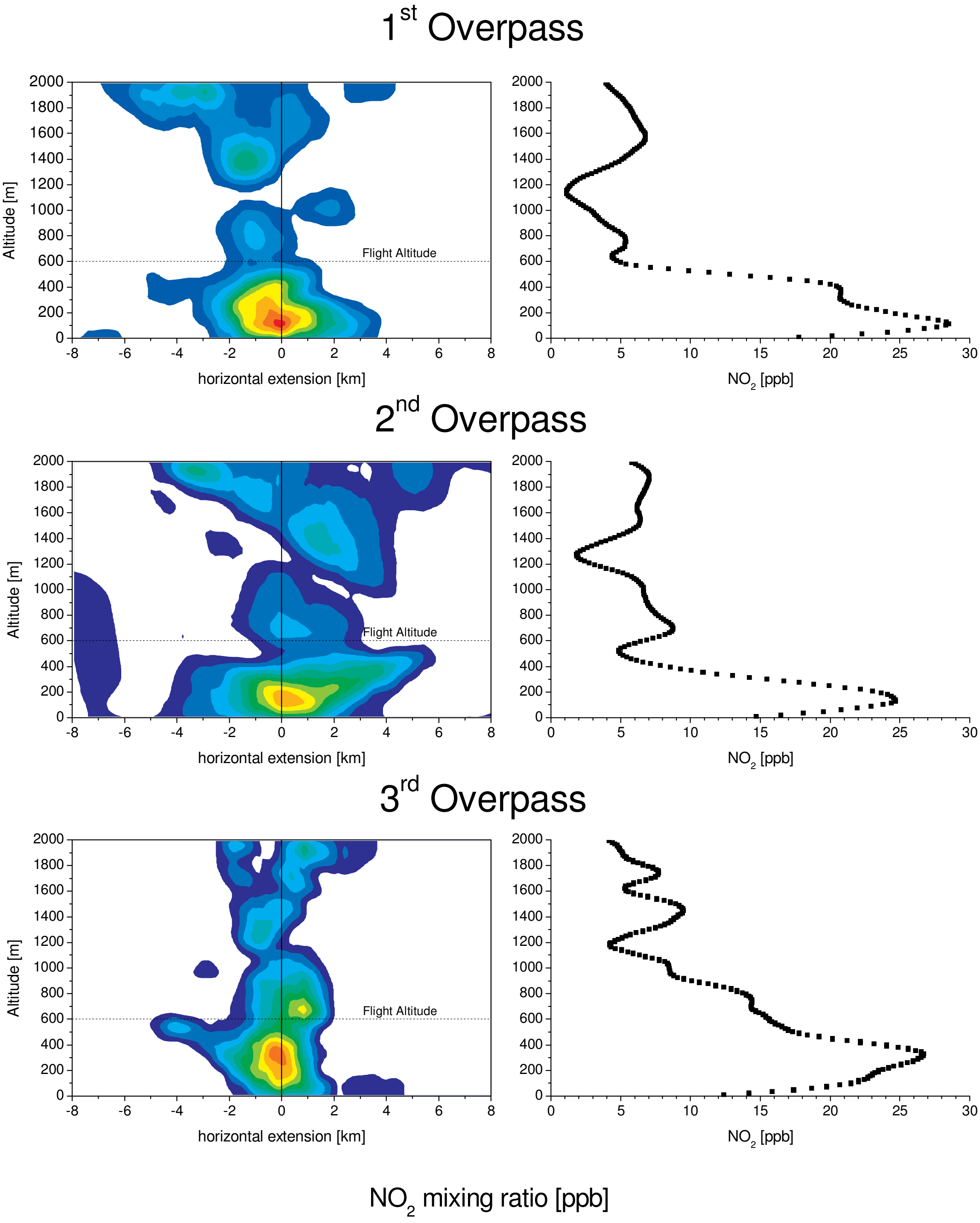
1st Overpass

2nd Overpass

3rd Overpass

Figure 8-19: Reconstructed plume for the first, the second and the third overpass. The 2-dimensional plot is shown in the left panels and the profile in the plume centre in the right panels [Pundt et al., 2005 b].

The grid shifting (chapter 3.5.II) was applied as well with a shift of 1/10 in both dimensions so 100 reconstructions were performed for each overpass. The final reconstruction is shown in Figure 8-19. In the left panels the 2-dimensional distributions perpendicular to the wind direction are shown and in the right panels the profiles in the plumes centres are shown. The maximum concentration reaches 29 ppb, 25 pbb and 27 ppb for the first, the second and the third overpass respectively. The altitude of the maximum varies between 110 m and 330 m, for comparison the stack is 220 m high (Gianni Sogari, private email. 25/08/04). The distribution reconstructed for the first and the third overpass are similar with respect to the maximum concentration and the width of the plume. The second overpass was flown in larger distance to the power plant, the maximum concentration is a little lower and the plume seems to be wider. The integrated concentration for second overpass however is higher; hence the decrease in the maximum is most probable caused by the turbulent mixing with clean air and not by the chemical lifetime of NO_x.

While the position and the shape of the plume seems to be reconstructed quite well, in the background some artefacts are introduced. Most of the reconstructed concentration above 1200 m altitude might be artificially introduced by the reconstruction as well as the smaller peaks such as in the 2nd overpass at -7 km distance from the plume centre.

The statistical DOAS error of 10 % only leads to a total error of about 1 %. A sensitivity study based on an assumed plume and calculated SCDs was performed (Bing Chao Song private communication). After the SCDs were calculated a statistical noise of the order of the measurement error was added and the profile was reconstructed. 200 noise studies were performed and compared to a reconstruction without noise, the difference in the reconstructed plume was 1 % compared to the noiseless data.

8.2.V Flux Estimations

In the following we will calculate the NO_2 flux originating from the Sermide power plant. Here two different methods are applied and compared to each other and to emission data of the power plant. The first approach uses the traditional method where the vertical column is calculated using one AMF per line of sight for the whole overpass. This well established estimation method will be compared to an estimation based on the DOAS tomography, which allows a detailed reconstruction of the plume shape and hence the estimation of the flux.

8.2.V.a Based on Traditional Methods

Based on the observed dSCD the emissions of the plant can be estimated. The method presented here is straight forward and was already used for similar studies [Melamed et al., 2003] based on a simplified viewing geometry.

First the total flux through the plane defined by the flight direction and the vertical can be calculated. For each individual line of sight (i), this flux is given by equation (8.6).

Here the difference in the tropospheric vertical column between lee and luff side of the plant is used (ΔVCD) multiplied by the speed of the aeroplane, the wind speed and the sine of the relative angle α of the wind to the flight direction. During the short time interval of 3 minutes we can assume the wind speed and the speed of the aeroplane to be constant:

$$\Phi_i = v_{aeroplane} \cdot v_{wind} \cdot \sin(\alpha) \cdot \int_{T_1}^{T_2} \Delta V_i(t) \cdot dt$$

In the O_4 dSCD no effects of the plume are observed, therefore the aerosol load does not change between the plume and the surrounding clean air. As the AMF for the individual lines of sight are independent of the time as well the formula can be written as:

$$\Phi_i = v_{aeroplane} \cdot v_{wind} \cdot \sin(\alpha) \cdot \frac{1}{A_i} \cdot \int_{T_1}^{T_2} \Delta S_i(t) \cdot dt$$

Integrating across three or four data points is relative uncertain as the integral strongly depends on the interpolation. For the integral a Gaussian was fitted to the data points and integrated. In Figure 8-20 one example of the fit is shown.

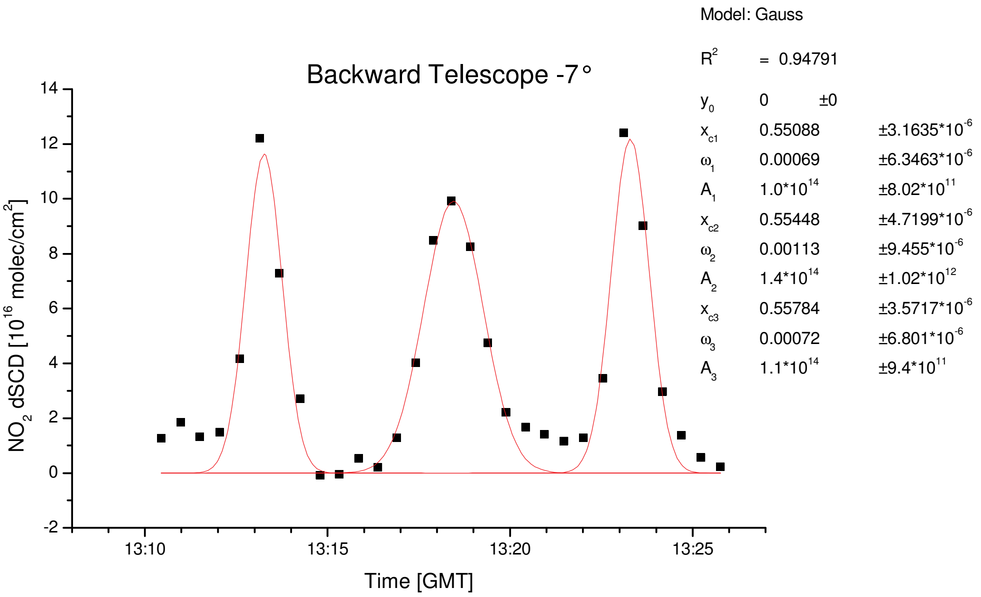

Figure 8-20: Example of the Gaussian fit to the observed dSCD of the telescope directed backward (-7°).

The next step is to find the correct settings for the AMF simulations. It is obvious that the vertical column should be the same for all lines of sight. A visibility of 23 km was used to calculate the aerosol extinction. Based on the performed upward dive the mixing layer height is known to be 1700 m. The aerosol extinction used in the simulations was constant in the mixing layer.

The NO_2 profile has a strong influence on the AMF. Due to the relative short distance to the source we can assume the NO_2 is not well mixed. Instead of assuming a profile and calculate the AMFs for each individual line of sight we simulated the Box AMFs as described in chapter 3.4.VII and attachment A. Using the Box AMF the AMF can be calculated with equation 8.2. The concentration profile used here was adapted from the tomographic inversion.

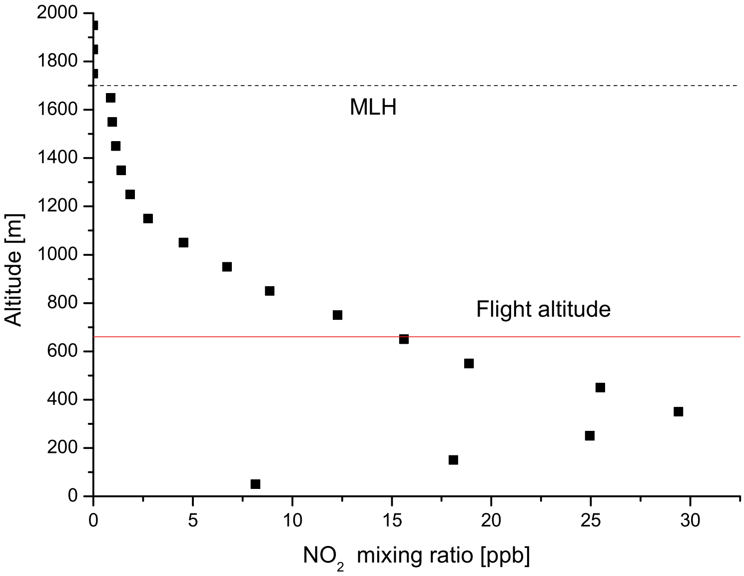

Figure 8-21: NO_2 profile assumed for the calculation of the AMF.

The maximum of the assumed profile was situated between 300 m and 400 m altitude (Figure 8-21). As expected parts of the profile have to be assumed to be above the flight altitude.

The flux for all lines of sight and overpasses was calculated using the method and the profile described above. In Figure 8-22 for the second overpass the flux of all lines of sight are shown, the agreement between the ten lines of sight is reasonable but not perfect. The most probable reason is that the assumed profile does not exactly fit the real situation, besides the horizontal variations in the NO_2 distribution are completely ignored.

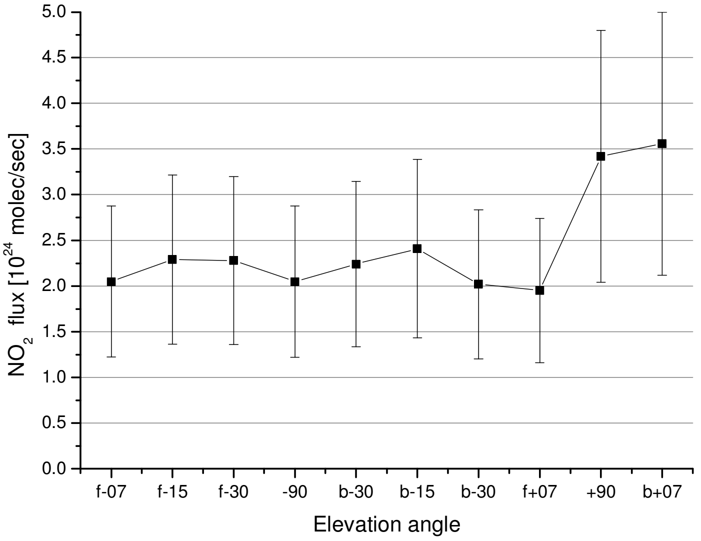

Figure 8-22: The calculated NO_2 flux for the 2nd overpass for all lines of sight. The letters on the abscise indicate whether the telescope is directed backward (b) or forward (f), the numbers equal the elevation angle relative to the horizon, negative number stand downward looking telescopes.

The average of all lines of sight results in 1.50, 2.43 and $1.88*10^{24}$ molec/s for the first, the second and the third overpass. The comparison with official emission data of the power plant will be given after the flux is calculated using the 2-dimensional tomographic reconstruction.
The errors of the calculated flux were discussed in detail in the last section 8.1.IV hence there is no need to repeat the discussion and only the main numbers are given.
As mentioned the wind was very low, the error in the wind speed was 30 %, other errors are of course the DOAS fit (20 %), the NO_2 cross section (3.5 %, neglected), the Gaussian fit to the observed dSCD (included in the 20 % DOAS error) and the AMF (10 %) based on the Box AMF and the assumed profile. A change in the wind direction by 10° leads to an error of 4 % and if the speed of the plane is wrong by 10 km/h the error in the emission estimation will be 5 %. The total error of the emissions based on this analysis is 40 %.

8.2.V.b Based on the Tomographic Inversion

If the 2-dimensional distribution perpendicular to the wind direction is known, the flux can be calculated by integrating across the plume:

$$\Phi_i = v_{wind} \cdot \int_{X_1}^{X_2} \int_{Z=0}^{Z} c(x,z) \cdot dx \cdot dz$$

like in the last section v_{wind} stands for the wind velocity to the and c for the concentration.
For the three overpasses a total flux of 4.4, 5.5 and $3.7*10^{24}$ molec/s is derived. The flux is based on the integration of the complete reconstructed concentration distribution.
The artefacts discussed above were ignored in a second calculation of the flux, integrating across the plume only. The flux was reduced by about 50 % and resulted in 2.05, 2.55 and $2.53*10^{24}$ for the first, second and third overpass.
A similar effect was observed in an experiment with long path DOAS tomography [Mettendorf et al, submitted 2005]. In this study a well defined NO_2 concentration was measured and reconstructed using the DOAS tomography. They found out that the

concentration can in principle be reconstructed well. The position of the maximum and the local concentration is reconstructed correctly. On the other hand the integrated concentration is overestimated depending on the assumed error in the data up to 50 %. The error is given is not only given by the DOAS retrieval but also by the diameter of the light beam. The latter becomes more and more important when the plumes diameter is small. When the plume's diameter is about a factor of ten larger than the diameter of the light beam it cannot be ignored. In the case of the airborne measurements, the light beam is not well defined, but we can assume this effect to be important here as the horizontal resolution of the measurement was about 2 km and the width of the plume (Figure 8-19) is about 6 – 8 km.

If the artefacts were ignored, the total flux would reduce by 50% therefore the error in the flux would be about 50% in the minimum. Besides this systematic overestimation there are some statistical errors. In principle the error is mainly given by the same sources as discussed in the last section, i.e. the wind direction and velocity, the DOAS fit error, the AMF and the NO_2 cross section. The effect caused by the uncertainty of the wind speed is similar and causes an uncertainty in the flux of 30 %. The error in the DOAS fit results in an uncertainty of the reconstructed concentration of 1%. Another difference is the AMF. While we assumed an error of 10 % in the total AMF, there is no total AMF in this case. However for the Box AMF the single scattering approximation was used, based on the comparison in chapter 4.4.VII.b, we assume an error of 20 %. In total the flux varies by ±46 %. For the three overpasses a local NO_2-flux is estimated:

1st overpass: 2.05 (±0.93)*10^{24} molec/cm^2 (5 km distance),
2nd overpass: 2.55 (±1.2)*10^{24} molec/cm^2 (13.4 km distance),
3rd overpass: 2.53 (±1.2)*10^{24} molec/cm^2 (5 km distance).

8.2.V.c Based on the official Emission Data

Edipower provided the emission data of the plant for the specific day and time. In total 880 kg of NO_x were emitted in the time between 13:00 and 14:00 GMT. To compare this data to the observed NO_2 flux in 5 km distance to the plant, the chemistry of NO_x and O_3 has to be considered, as well as the fraction of NO of the total emitted NO_x. Typical fractions of emitted NO_2 are below 10 %. We assume it varies between 5 % and 10 %, the NO_x emissions of 880 kg/h can therefore be estimated to be around 4.12 and 4.22*10^{24}molec/sec.

The chemical reactions are explained in detail in chapter 2.1.I and will not be repeated here. The main aspect is that a photochemical state exists, dominating the concentration of NO, NO_2 and O_3. The distance between the chimney and the measurement point was 5 km (13.4 km), the wind speed was 1.5 m/s, this means the NO_x was emitted about 1 hour (2 h 30 min) before it was detected. During this period the photostationary state is established, it is given by the Leighton ratio. Ozone measurements north of Sermide performed by our colleague Wolfgang Junkermann observed 55 ppb (personal communication, file date 01/10/2004). Hence we assumed an ozone mixing ratio of 55 ppb outside the plume and around 30 ppb inside. The ratio of NO_2 to total NO_x varies between 65 % and 77 % depending on the assumed O_3 mixing ratio.

So a lower and upper limit for the NO_2 flux at the measurement place is estimated: 2.74*10^{24} molec/s in the minimum and 3.26*10^{24} molec/s in the maximum.

8.2.V.d Comparison of the Nitrogen Dioxide Fluxes

According to the two different interpretation of the measurement data there are two different estimations of the NO_2 fluxes, as shown in Table 8-E.

	tomography	**tomography, plume only**	**traditional**	**operator**
1st overpass	4.40	2.05	1.50	2.74 - 3.26
2nd overpass	5.50	2.55	2.43	
3rd overpass	3.70	2.25	1.88	

Table 8-E: NO_2 fluxes at the measurement side in 10^{24} molec/s for the different retrieval techniques.

Based on the traditional straight forward calculation the result was $(1.9 \pm 0.7)*10^{24}$ molec/s, based upon the tomographic inversions the average flux equals $(2.3 \pm 1.2)*10^{24}$ molec/s. Compared to one another the tomographic inversion leads to slightly higher emission values than the traditional technique. The emission data of the operator led to a flux estimation varying between 2.74 and $3.26*10^{24}$ molec/s(~0.89 t/h). Within the errors the data agree well with flux estimation of the DOAS Tomography. However the maximum error for both the traditional flux estimation and the emission data have to be considered but the agreement is still not perfect. In the traditional approach horizontal variations in the concentration profile are ignored, this causes an error in the estimated flux. The DOAS Tomography was invented to overcome this principle uncertainty. In the mathematical inversion some artefacts are introduced, increasing the uncertainties of the flux estimations. If these are neglected the flux will be estimated very well. The problem which concentration is real and which is artefact is still not solved completely.

8.2.VI Ostiglia 26/09/2003 and 27/09/2003

The plant Ostiglia, we were told, is under construction and might do some small tests but will not produce any power (emissions) in summer 2003 (private communication between Werner Maneschg, an Italian co-worker and the operators, June 2003).

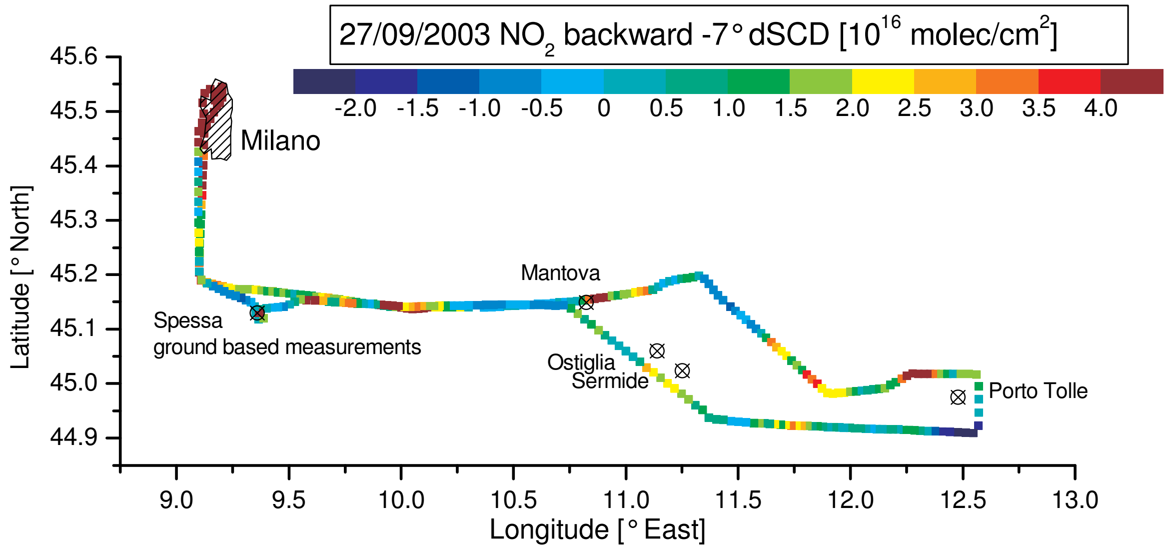

Figure 8-23: Differential slant column density as a function of the position for 27/09/2003. South of Sermide and Ostiglia clearly two peaks can be made out.

In Figure 8-15 it is obvious, that on 26/09/2003 no emission were observed in the lee of the power plant in Ostiglia. On the following day we measured along the complete Po basin from Milano to the Adriatic coast and back in one flight[5]. In Figure 8-23 the differential slant

---

[5] This flight was only possible as the plane took the direct way and as the lightest operator (former colleague Wei-Der) controlled the measurements.

column density is shown for the complete flight. South of Sermide and Ostiglia two small peaks are observed. On a second request the operators of Ostiglia told us, the plant was running in a test mode on this specific day (letter from 12/11/2004 Nicola Cinnella, Capo centrale (head of the plant)).

8.3 Conclusions AMAXDOAS during FORMAT

The AMAXDOAS was successfully operated during the two FORMAT Campaigns, in total 20 flights were performed.

The formaldehyde vertical column distribution was calculated around the city of Milano for one flight. In this calculation we considered the high variation of the aerosol distribution. Although the aerosol extinction in the background is unknown, it can be retrieved by comparison of simulated O_4 AMF with the observation. For this purpose four special positions around the flight track were chosen, each of them was over flown twice.

The Box AMFs for the respective aerosol profile were used to retrieve the total AMF for HCHO. Between the specially selected measurements the AMF were interpolated. The vertical column densities of HCHO varied between $30*10^{15}$ molec/cm² inside the plume to $5*10^{15}$ molec/cm² over the remote area. The plume of the city was estimated to be around 20 km wide and the total flux out of Milano was $11*10^{24}$ moles/s. In the same period the flux into the observed area equalled $7.5*10^{24}$ molec/s. No point source of Formaldehyde can be realized in the data. The same method as for the formaldehyde can be applied to the tropospheric nitrogen dioxide distribution around the town.

Based on measurements in the lee and the luff side of the Sermide power plant we estimated the NO_2 flux originating from the power plant.

First the traditional approach using one AMF per line of side neglecting the time resolution of the measurements was used. The flux was estimated to 1.50, 2.43 and $1.88*10^{24}$ molec/s (± 40 %) for the three overpasses. In a second analysis of the same dataset the 2D-NO_2 distribution inside the plume could be reconstructed by DOAS tomography. The reconstructed distribution was used to estimate the plant's NO_2 flux to 4.4, 5.5 and $3.7 * 10^{24}$ molec/s. If we concentrate the flux calculation on the plume the flux will be reduced to 2.05, 2.55, $2.53 * 10^{24}$ molec/cm^2 (± 40 %). The official NO_x emission data of the plant can be used to calculate the NO_2 flux at the measurement side, approximately the flux is between 2.74 and $3.26*10^{24}$ molec/s.

Although the uncertainties are relative high the agreement is quite good, main uncertainties are given by the low wind speed and the variation in the wind speed and direction.

The data observed on 26/09/2003 were used to estimate the SO_2 emission of the power plant in Porto Tolle and the refinery in Mantova [Wang et al., 2005 b].

From the power plant in Ostiglia to our surprise an emission was detected which turned out to be caused by a test of the renovated unit.

9 Conclusion and Outlook

Within this thesis a novel remote sensing instrument, the Airborne Multi AXis DOAS, was constructed and operated during 4 measurements campaigns. In total 49 flights were performed. Depending on different purposes it was installed on two different aeroplanes. The AMAXDOAS has unprecedented properties: For the first time 2-dimensional trace gas distribution can be measured from UV/vis remote sensing on an aeroplane. The novel viewing geometry requires new and sophisticated inversion techniques. These were developed, tested and successfully applied to the AMAXDOAS observations. However further interesting results might be obtained from the observations. A new radiative transfer program might be combined with the DOAS tomography reconstruction methods to obtain even better reconstruction of the NO_2 concentration inside the plume.

9.1 *AMAXDOAS for SCIAMACHY Validation*

The AMAXDOAS was flown on board the Falcon at about 35000 ft altitude close to the tropopause height. The tropospheric NO_2 can be well separated from the stratospheric signal. As also the signal in the zenith directed telescope is affected by tropospheric pollution it is less useful to subtract the zenith signal for the separation. Two different approaches for the separation of tropospheric and stratospheric signal based on a differential method were investigated, the difference between both was found to be small. For the simulation of the NO_2 AMF additional information from independent observation about the meteorological conditions is used.

The comparison of SCIAMACHY tropospheric slant columns resulted in a good agreement. Also the tropospheric vertical column observed by the two instruments agreed well. However, the agreement strongly depends on the atmospheric conditions assumed for the AMF simulations. The validation of SCIAMACHY using the AMAXDOAS instrument highlights the importance of using the correct description of the atmosphere for the AMFs and the potential of SCIAMACHY to retrieve excellent tropospheric vertical columns.

The retrieval of stratospheric VCDs from AMAXDOAS measurements also strongly depends on the meteorological conditions and the solar zenith angle. Over remote regions like the Sahara desert or the polar sea a good agreement of the total vertical column with the satellite instrument GOME and SCIAMACHY is achieved. The observed differences can well be explained by the temporal differences between the two observations, influencing either the stratospheric concentration or the measurement conditions (e.g. clouds).

During the flight on 25/09/2002 over the Congo basin the Falcon crossed a dense cloud. In all trace gases an increase in the dSCDs is registered during this time period. The observed O_4 dSCDs are used to calculate the ratio between cloud thickness and light path for different pairs of cloud bottom and cloud top altitude. The most realistic values of this ratio are assumed to be around 20. In addition the light path inside the cloud is independent of the trace gas. Based on the O_4 and H_2O dSCDs an average light path was retrieved from several pairs of cloud bottom and cloud top height. Only in small range of possible solution the light paths differ by less than 10 %. The altitude of the cloud bottom is about 7.2 km and for the cloud top it is approximately 16 km. The O_4 and H_2O observations result in an average light path of 180 km inside the cloud. The light path enhancement is used to deduce the average NO_2 mixing ratio of 0.5 ppb, inside the cloud, which is definitely enhanced, compared to ambient air conditions. The updraft NO_2 over the Congo basin is approximated by half the value typically quoted for Europe. Additional NO_2 sources like lightning have to be considered as cause of the observed values. Although lightning cannot be proved by any independent information.

9.2 AMAXDOAS for tomographic Measurements

During the FORMAT campaigns, the AMAXDOAS also performed measurements in low altitudes close to the top of the mixing layer, which is ideal to study local pollution caused by anthropogenic emissions. The project concentrated on the distribution of ozone precursors like formaldehyde and nitrogen dioxide.

To retrieve the HCHO distribution from one selected flight around Milano, the aerosol distribution has to be approximated first. The O_4 measurements from different lines of sight and different locations are used to approximate the aerosol extinction for this flight. Although the differential columns are measured the total O_4 columns are retrieved by comparing different sets of simulated AMFs with the observed data.

Using the retrieved aerosol extinction, the respective Box AMFs are calculated and used to derive total HCHO-AMFs. To interpolate the retrieved HCHO vertical columns along the flight track, a relation between the O_4-AMFs and the HCHO-AMFs is used as well as an assumed background concentration. The deduced formaldehyde mixing ratios compare quite well with in situ measurements. The plume of Milano was about 20 km wide and a net HCHO flux from the entire city of 0.6 t/h (+53 %, -71 %) was observed during a two hours flight.

During the second FORMAT campaign one special flight for a detailed study of NO_x emissions was performed. In lee of a power plant the plume was crossed three times in two different distances from the plant. Based on the tomographic inversion technique the 2-dimensional concentration distribution inside the plume is retrieved. Here the fact that different lines of sight observed the maximum at different times and with different sensitivities is used. The local conditions close to the plume are reconstructed well, despite some small additional artefacts, which result in an overestimation of the retrieved flux ($5.5*10^{24}$ molec/s). The traditional method using one AMF per line of sight and ignoring the horizontal gradients yields lower results (~ $1.9*10^{24}$ molec/s) but the problem that only one profile is assumed is not solved and the horizontal resolution is ignored.

Compared to the official NO_x emission data ($2.7 – 3.2*10^{24}$ molec/s), the best result can be retrieved by ignoring the artefacts ($2.3*10^{24}$ molec/s). But the question whether a concentration maximum is real or not cannot always be decided. Nevertheless the first results of the 2-dimensional plume cross sections are very promising and the instrument is well suited for further studies. With an improved measurement technique (see below) and better radiative transfer simulations the airborne tomographic inversion technique might be further improved.

9.3 Outlook

The instrument was well suited for the tasks summarised above. However some smaller changes might be useful for the future. An up-to-date computer for the AMAXDOAS will increase the horizontal resolution and the tomographic inversion will benefit from additional data points.

A scanning viewing geometry allows a direct comparison of nadir, zenith and elevated lines of sight. A similar improved setup was recently invented for ground based MAX-DOAS instruments and is very successful. However, for the airborne measurements a scanning system will reduce the horizontal resolution, hence it is only suited for high flight altitudes and low gradients.

The expansion of the wavelength range is currently under discussion. An additional spectral window in the near infra-red might deliver important additional information. Especially the range between 1560 nm and 1590 nm might be interesting for the detection of CO_2. In the context of the Kyoto protocol an instrument like this might be used to estimate the carbon dioxide emissions of single point sources like power plants, but also natural sources like volcanoes are of great scientific interest. As CO_2 is quasi inert it will be very useful for the interpretation of plume studies like those presented in chapter 8.2. Inside the plume both chemical processes and turbulent mixing are important for the local concentration of any trace gas. Here, CO_2 is a good tracer to separate these two aspects.

With the current instrument only measurements parallel to the flight direction can be performed. If an imaging DOAS instrument is installed on the aeroplane, additional information perpendicular to the flight direction will be obtained. This is of great scientific interest for different tasks, e.g. plume studies, here one single flight along the plume can deliver important information about the chemical evolution and the turbulent mixing inside the plume.

A Tracy Bug Report

The radiative transfer model Tracy simulated most AMFs quite well as demonstrated in this work. The program was developed recently at the Institut für Umweltphysik (Friedeburg, 2004) in Heidelberg. Normally a newly developed program suffers some bugs, which are observed in the every day use. In this section I will explain the bugs, observed during this work. I do not intent to discredit Christoph von Friedeburg's work, but I want other Tracy users to be aware of the following problems. Besides it might be helpful to find an appropriate bug test for any future radiative transfer simulation program.

A.1 Solar Azimuth Bug

The AMF of many tropospheric trace gases depends on the relative solar azimuth angle – which is the angle between detector and the sun. Tracy settings allow the independent choice of both parameters azimuth angle of the detector and solar azimuth angle. For the 1-dimensional case this is not necessary. The 2-dimenional AMF shown in chapter 4.4.VII will only simulate the real situation, if both parameters can be used independently, as the discretisation grid is fixed to the standard longitude and latitude grid.

In the 1-dimensional study we expect the AMFs to depend on the relative azimuth angel. The absolute solar azimuth angle should be completely unimportant. In the simulation, however, a strong dependency of the absolute solar azimuth angle is observed. The study concentrates on realistic conditions for the flight around Milano on 16/08/2002 close to Calusco. The flight altitude is 1100 m and one telescope is elevated by 3°, the solar zenith angle is 42°. To retrieve the aerosol profile we simulated the AMF for 360 nm at different positions. The O_4-AMFs for two different absolute solar azimuth angles are presented in Figure 1. The solar azimuth angle of 232° corresponds to the real situation, 180° is chosen for comparison. The ordinate gives the relative azimuth angle of the telescope, this means the absolute angle of sun is subtracted. Hence a symmetric plot with a minimum O_4-AMF at 0° relative azimuth angle is expected for both scenarios.

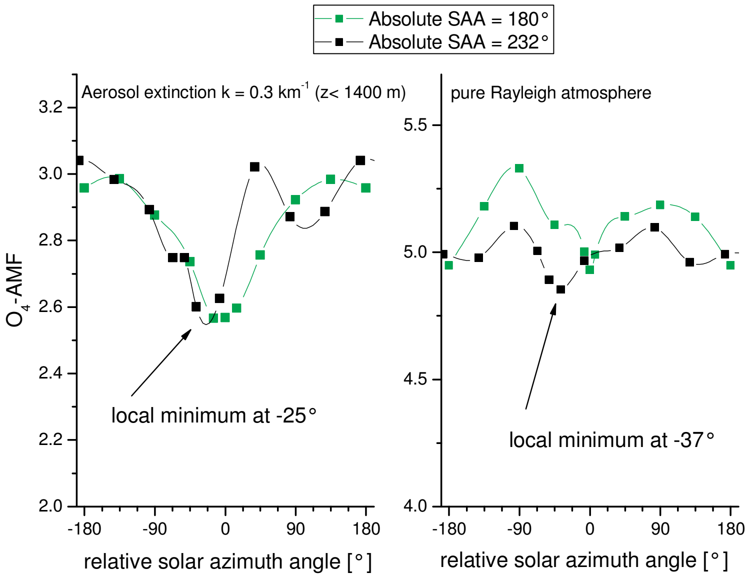

Figure 1: O_4-AMF simulated with different absolute solar azimuth angle (128° black line and 180° green line). Two different scenarios are shown: With aerosol (left) and a pure Rayleigh atmosphere (right). For this study we concentrate on a telescope elevated by 3°. The other settings were chosen according to flight conditions around Milano on 16/08/2002.

Independent of the aerosol load the excepted behaviour will not be observed, if the absolute solar azimuth angle is set to 232°. Further investigation for different wavelength regions (440 nm and 1066 nm) and additional absolute solar azimuth angle showed that only four absolute solar azimuth angles (0°, 90°, 180°, 270°) can reproduce our expectations. Hence these angles are recommended for any Tracy simulation. The detailed reason for the observed error is not yet fully understood.

A.2 Box Air Mass Factors and Air Mass Factors

With Tracy two independent possibilities to simulate 1-dimensional Box AMFs are given:

1. For a certain layer a box like profile is assumed and the AMF is simulated for the Box profile.
2. The Box AMFs are directly simulated by Tracy.

As indicated in Chapter 4.4.VII the results based on theses two methods do not agree.

In a simple test a profile consisting of two layers is used. The detector is situated just above the second layer (Figure 2). The wavelength of 360 nm is used as well as the viewing geometry of the first FORMAT campaign the same position as in the previous section. The Solar Azimuth error is considered.

The total AMF, the Box AMF and the AMF for the Box profiles are calculated simultaneously. Tracy is not run twice and the observed discrepancy is not given by the variance in various simulations.

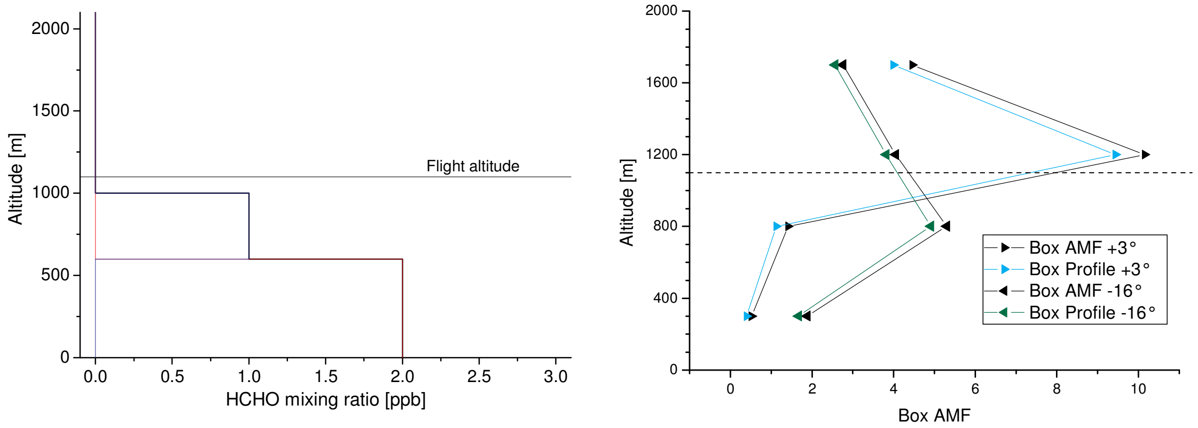

Figure 2: left: The formaldehyde profile consists of two box like profiles, reaching from ground level to 600 m (red line) and from 600 m to 1000 m (blue line). Right: BoxAMFs for two lines of sight simulated with the moderate aerosol extinction.

The AMFs calculated for the individual layers are expected to agree with the Box AMF. As they do not agree (Figure 2 right) one of them must be wrong (or both?). The total AMF might give a criterion to distinguish right from wrong. Based on the Box AMF and the given profile the complete AMF is calculated by:

$$AMF = \frac{\sum_{j=1}^{2} BAMF_j \cdot c_j \cdot \Delta z_j}{\sum_{j=1}^{2} c_j \cdot \Delta z_j}$$

We assume those Box AMFs to be correct, which result in the same AMFs as calculated directly.

Figure 3 illustrates the comparison for a pure Rayleigh atmosphere and for a moderate aerosol load. If no aerosols are included in the simulation, all AMFs will agree perfectly well. Differences will be observed, if the aerosol is included: The AMFs based on the Box profiles agree well with the directly simulated AMFs, but those based on the Box AMFs differ by about 20 %. Hence for future calculations Box profiles instead of the standard Box AMFs are recommended.

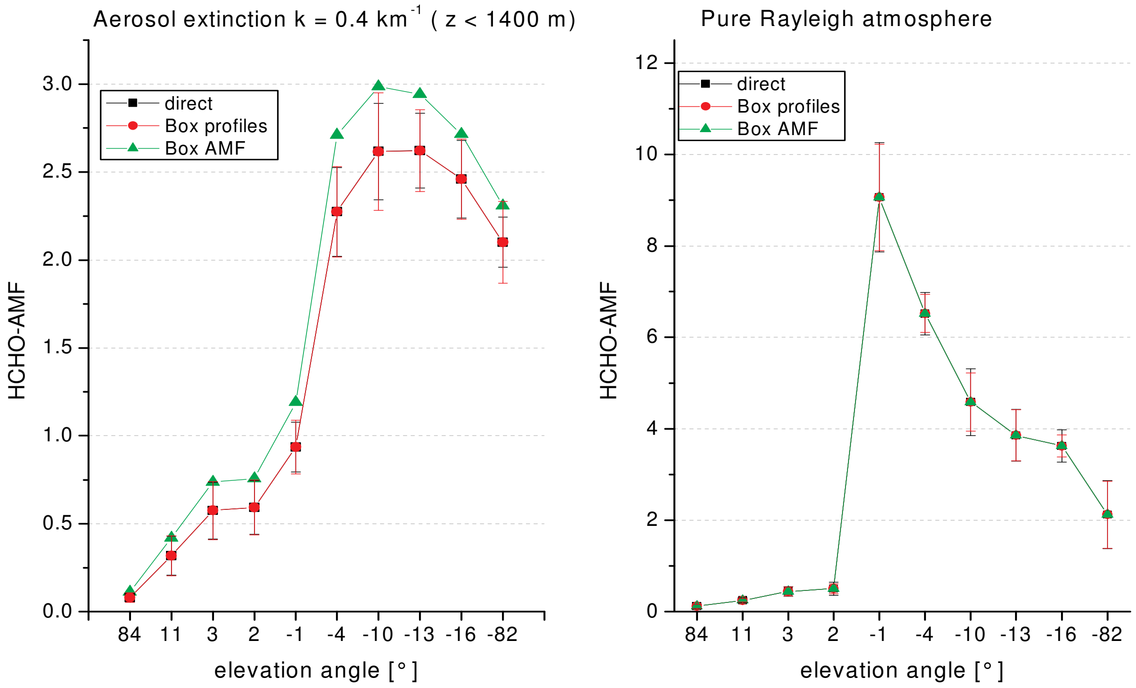

Figure 3: Total AMFs based on the three different approaches. Two different cases were included in the study without aerosol (right) and with aerosol (left). While all AMFs agree perfectly well in the case of a pure Rayleigh atmosphere, the one based on the Box AMFs differ by about 20 %, if the aerosol is included.

According to private communication with Christoph von Friedeburg, the incorrect Box AMFs result from an approximation used for the calculation:

$$BAMF = \frac{SCD(box)}{VCD(box)} \approx \frac{l(box)}{\Delta z(box)}$$

here l equals the light path inside the box.

A.3 Force Mode in Limb Geometry

The description of the program given in chapter 4.3 explained that a photon is launched from the detector. Afterwards it is scattered in the atmosphere according to the local extinction and if it leaves the top of the atmosphere, the last scattering event will be used to force the photon towards the sun. This works quite fine (except for the bugs mentioned here) as long as the photon is scattered. For some special viewing geometries scattering events are rather improbable like for a zenith directed telescope observing longer wavelengths. A special mode of forcing is implemented to overcome this problem. In this mode (forcemode 1) the probability p_{scat} a photon is scattered is calculated in advance and all photons are forced to be scattered during their path through the atmosphere. The intensity of the individual photons is afterwards weighted with the probability p_{scat}.

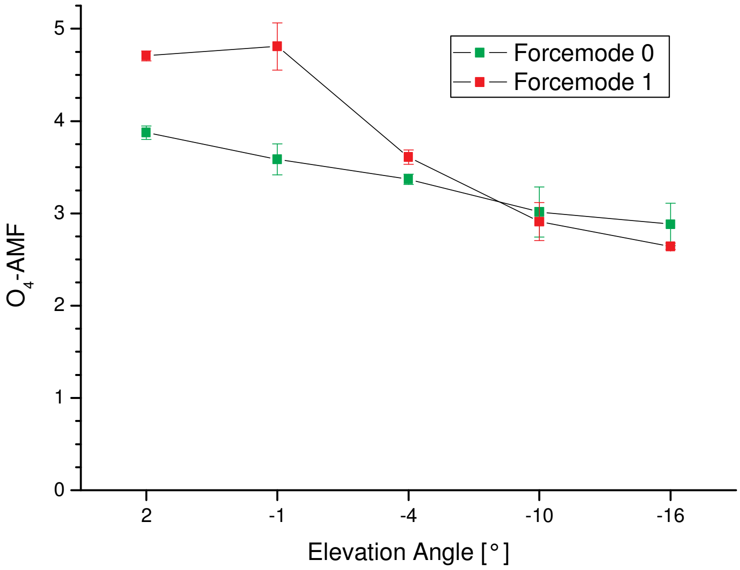

Figure 4: O_4-AMFs simulated with the two different force modes for five different elevation angles. In this simulation no aerosols were included. A large discrepancy is observed for the -1° line of sight, for the lines of sight -4° to -16° the difference is rather small.

For limb geometry, like most of the AMAXDOAS lines of sight in low altitude, forcemode 0 is recommended. Forcemode 1 leads to high deviations in this case as illustrated in Figure 4.

A.4 Detector Position

The above mentioned bugs were discovered or documented by myself, the last important one, however, was discovered and investigated in detailed by Frank Weidner who also used Tracy for his PhD-thesis. According to his studies the detector must not be placed close to the edge of one voxel, especially not when doing limb observation.

According to private communications with Christoph von Friedeburg (August 2004) this bug is related to the one discussed previously. The problem occurs due to an incorrect approximation of the intersection between the line of sight and the voxel's edge for small intersection angles.

B Profile Retrieval for Format I

In section 8.1.III we discussed the AMF along the flight with varying aerosol extinction in different region around Milano: In this section we used a discretisation according to four boxes between 0 and 2000 m: 0 – 600 m, 600 – 1000 m, 1000 – 1400 m and 1400 – 2000 m. The AMF however is calculated assuming the mixing ratio is the same in the two lower boxes and is 70 % of this value in the third box and above 1400 m we assumed it to be zero. To assume a standard HCHO profile after the aerosol extinction profile was retrieve relative exactly is inconsistent. The reader may ask why we did not retrieve an HCHO profile as we did for the aerosol extinction. The answer is as simple as it is disappointing: We tried to and failed. In the following attachment the several approaches to retrieve an HCHO profile are documented.

Based on the aerosol extinction we calculated the Box AMF and according to section 4.1 the local slant columns can be calculated as:

$$SCD_{loc,i} = \sum_j BAMF_{loc,i,j} \cdot c_{loc,j} \cdot v_j$$

where loc stands for the measurement place and i represents the elevation angle. The sum is calculated across the four layers. Considering the complete measurement including all lines of sight, the equation may be written as matrix equation:

$$\mathbf{SCD}_{loc} = \mathbf{AMF}_{loc} \cdot \mathbf{Cv}_{loc}$$

The vector $\mathbf{Cv_{loc}}$ is the product of the concentration multiplied by the layer thickness, i.e. it is the partial vertical column.

The observed differential slant column is given by the difference between a measurement point loc and the reference place ref:

$$\begin{aligned}\Delta\mathbf{SCD_{loc}} &= \mathbf{AMF_{loc}} \cdot \mathbf{Cv_{loc}} - \mathbf{AMF_{ref}} \cdot \mathbf{Cv_{ref}} \\ &= \left(\mathbf{AMF_{loc}}, -\mathbf{AMF_{ref}}\right) \cdot \begin{pmatrix} \mathbf{Cv_{loc}} \\ \mathbf{Cv_{ref}} \end{pmatrix}\end{aligned}$$

In the last step we combined the two **AMF** matrixes to one and also the two vectors **Cv** are written as one vector.

This is a standard linear equation system and can be solve with the same mathematical methods as usually used in the tomographic inversion (Chapter 3.5.II).

In the analysis we concentrate on the measurements observed during the second overpass over Saronno, because the observed differential columns are large and the differences in the Box AMF are high as well. To solve the equation the respective routine from the TOMO-Lab [Laepple et al., 2004] inversion program was used.

For the row acting methods a priori profile is essential. Hence a first check is the dependency on the used a priori profile. In this test an extreme and a moderate case are studied, e.g. a constant profile of zero or some realistic profiles are given as a priori. If the profile can be retrieved from the measurements, the different a priori profiles will result in the same profile.

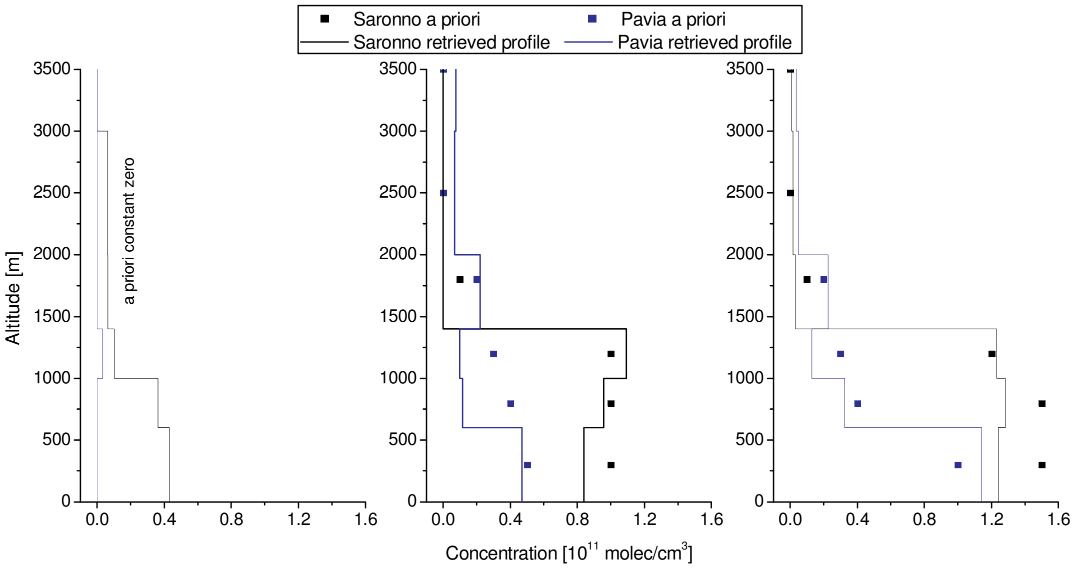

Figure B-1: Different profiles retrieved for Saronno (2nd overpass) using the matrix inversion. The profile depends on the assumed a priori profile.

The results for three different a priori profiles are shown in Figure B-1. Comparing the panels of the figure the dependency on the a priori is obvious. Not only the absolute concentrations are different, but also the relative distribution is different. Due to the differential measurement the absolute concentration cannot be determined. So the differences in the concentrations can be called systematic and we would not expect to retrieve this correctly.

To retrieve at least some profile information a combination of the matrix inversion as described above and a most realistic a priori profile was applied. The a priori was based on the expectation that the mixing ratio is constant in the mixing layer and decreases rapidly in higher altitudes. These expectations are confirmed by in situ measurements performed by the other two aeroplanes participating in the FORMAT project. However the results differ only slightly from the assumed a priori, hence the slight variations are ignored.

The same air masses are observed by different telescopes using different elevations angles, the differences in the observed slant columns as well as the different Box AMFs were used to retrieve the profiles. Figure B-1 demonstrates that the observed differences are not large enough to retrieve a reasonable profile based on these observations.

The problem might also be caused by the retrieval algorithm. Hence the Monte-Carlo algorithm was used as well to retrieve the profile. In this method pairs of random profiles are used to calculate dSCDs. If the one pair agrees with the measurement within a certain error, then these two profiles will be saved as one possible solution. The final result is given by the average of the possible solutions and the standard deviation describes the errors. To speed up the algorithm some a priori can be given to the algorithm and the random profiles vary around this a priori.

Compared to the algebraic approach the Monte-Carlo based retrieval contains more information about the uncertainty of the profile. If the standard deviation of the retrieved profile contained the two possible solutions shown in Figure B-1, a “general” profile would still be retrieved within large errors. This profile cannot be used to retrieve the AMFs but it might contain information about the profile height.

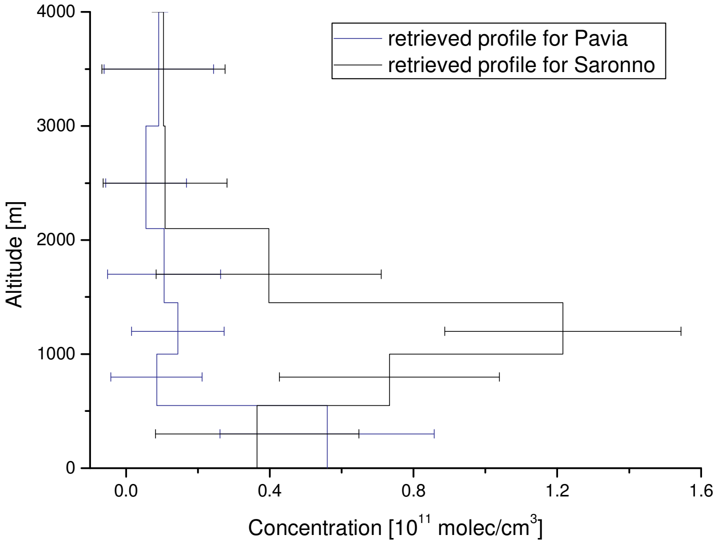

Figure B-2: Profiles retrieved with the Monte-Carlo based algorithm. The profiles are averaged over 1700 possible solutions.

The results of the Monte-Carlo based algorithm are shown in Figure B-2. The absolute values agree well with the profiles shown in Figure B-1. However this is caused by the a priori information used in the retrieval. The errors of the retrieved data are of the order of $0.4*10^{11}$ molec/cm^3 compared to the absolute values it is about 40 %, which seems to be a reasonable error. The retrieved profile however is not useful for any further calculation of HCHO-AMFs.

C Overview of the total NO_2 VCDs SCIAVALUE I

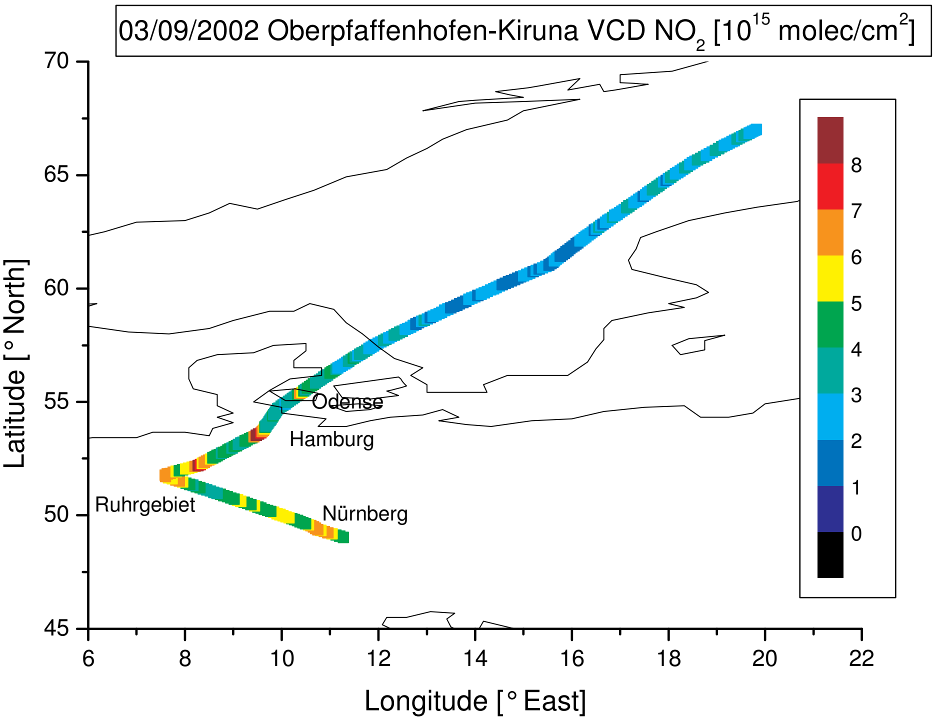

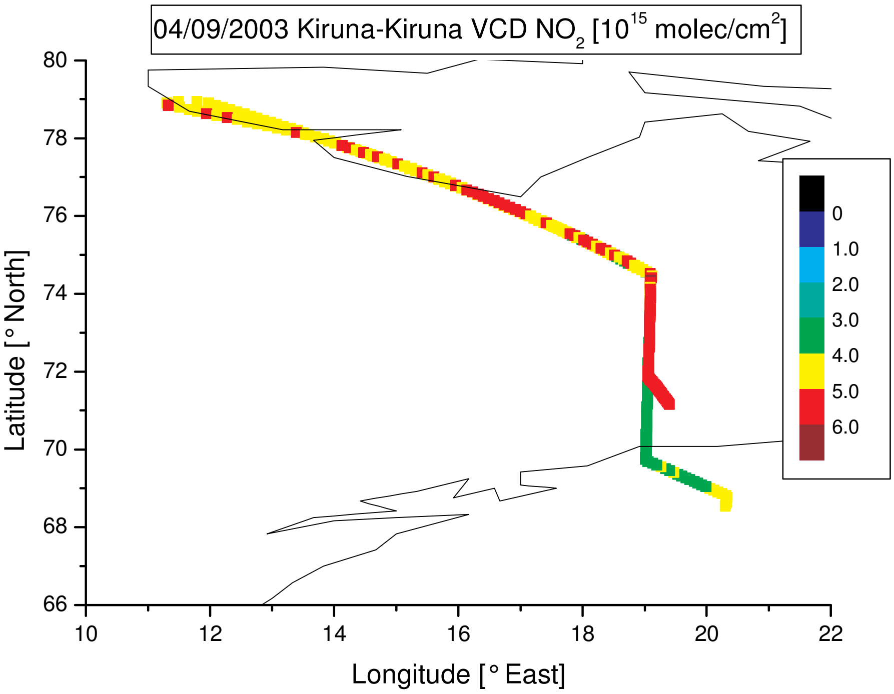

04/09/2002 Kiruna local flight via Spitzbergen is discussed in chapter 7.2.I

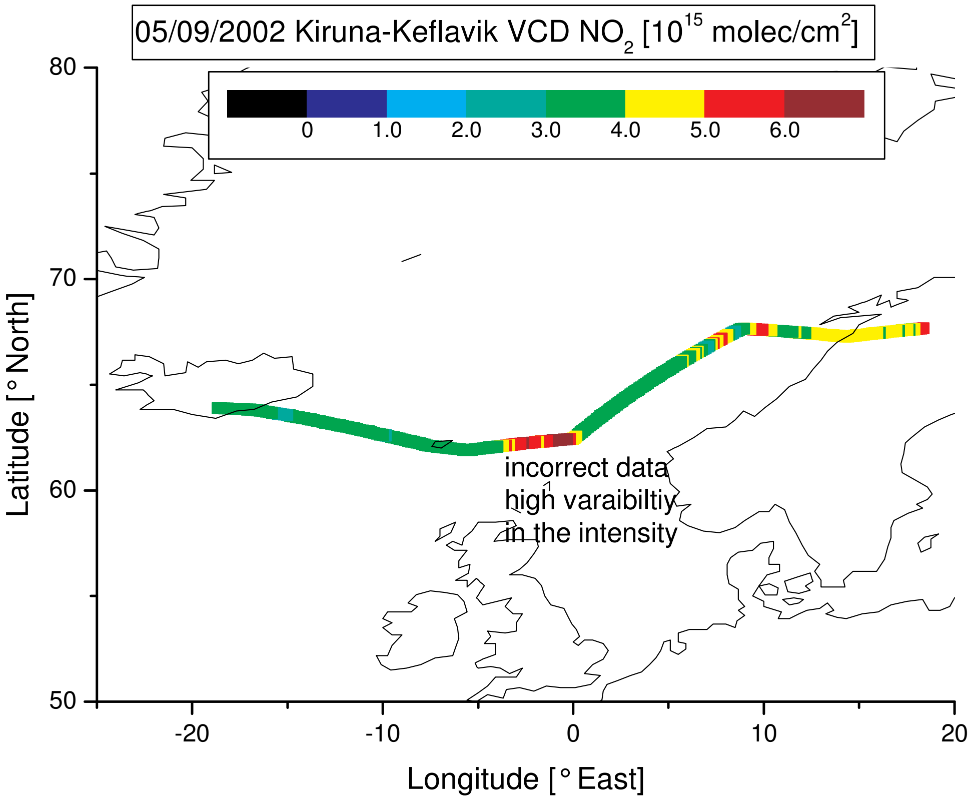
05/09/2002 Kiruna-Keflavik VCD NO$_2$ [10^{15} molec/cm^2]
0
1.0
2.0
3.0
4.0
5.0
6.0
incorrect data
high varaibiltiy
in the intensity
80
70
60
50
Latitude [° North]
-20
-10
0
10
20
Longitude [° East]

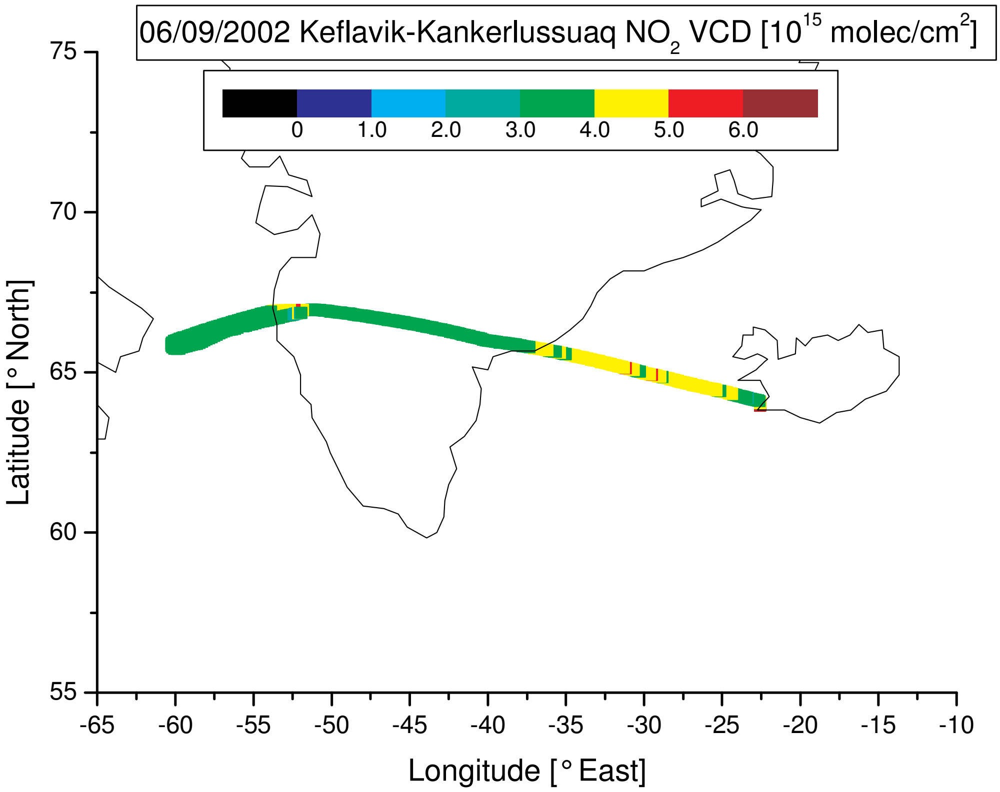
06/09/2002 Keflavik-Kankerlussuaq NO$_2$ VCD [10^{15} molec/cm^2]
0
1.0
2.0
3.0
4.0
5.0
6.0
75
70
65
60
55
Latitude [° North]
-65
-60
-55
-50
-45
-40
-35
-30
-25
-20
-15
-10
Longitude [° East]

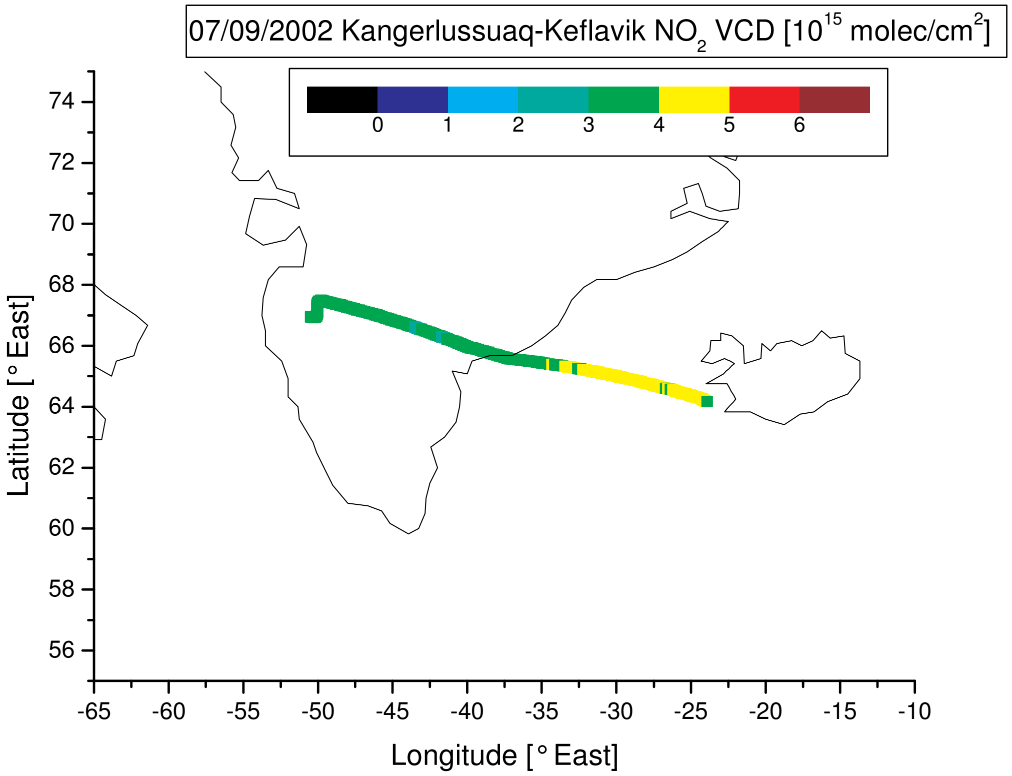
07/09/2002 Kangerlussuaq-Keflavik NO$_2$ VCD [10^{15} molec/cm^2]
0
1
2
3
4
5
6
Latitude [° East]
74
72
70
68
66
64
62
60
58
56
-65
-60
-55
-50
-45
-40
-35
-30
-25
-20
-15
-10
Longitude [° East]

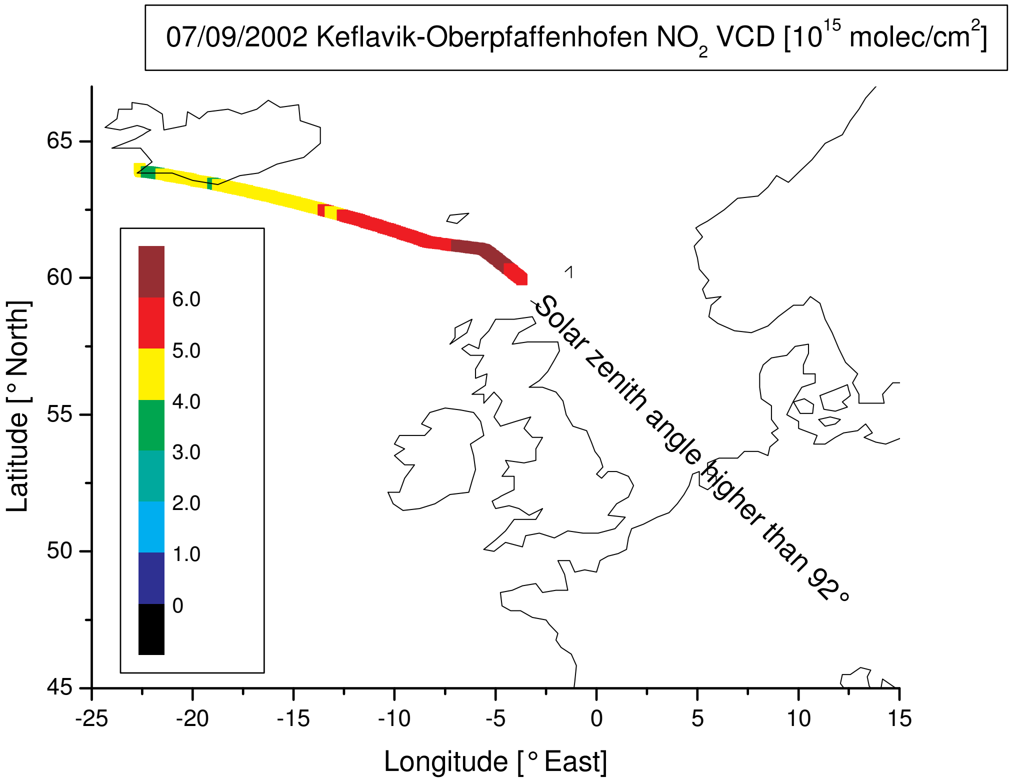
07/09/2002 Keflavik-Oberpfaffenhofen NO$_2$ VCD [10^{15} molec/cm^2]
6.0
5.0
4.0
3.0
2.0
1.0
0
Solar zenith angle higher than 92°
Latitude [° North]
65
60
55
50
45
-25
-20
-15
-10
-5
0
5
10
15
Longitude [° East]

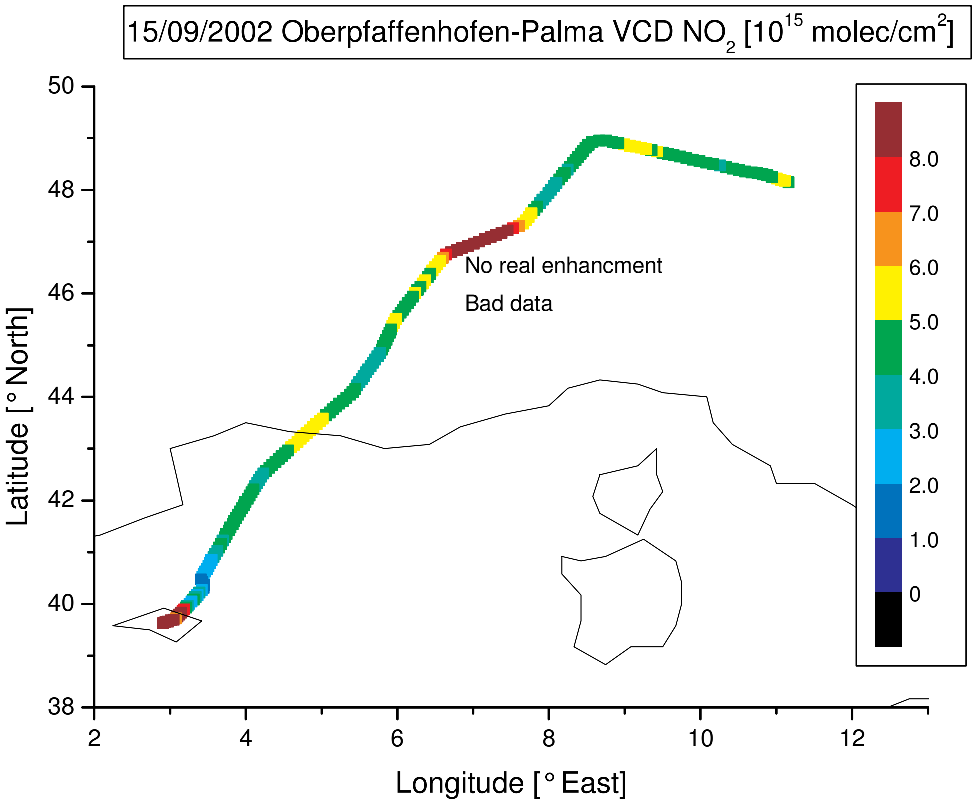

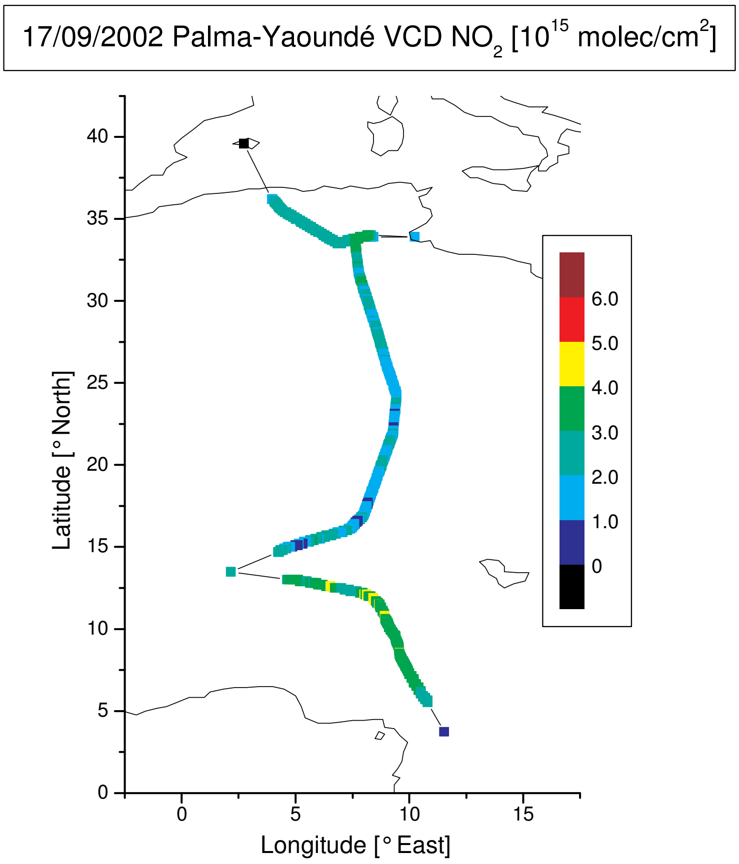

17/09/2002 from Palma de Mallorca to Yaoundé is discussed in chapter 7.2.II

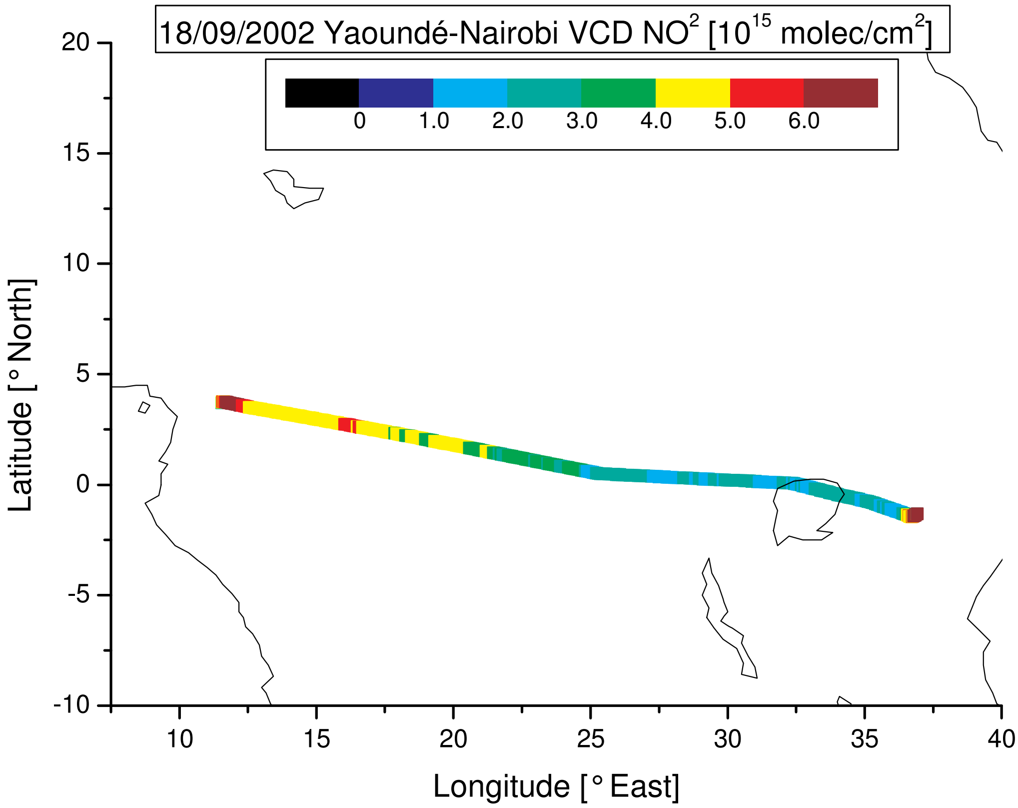
18/09/2002 Yaoundé-Nairobi VCD NO^2 [10^{15} molec/cm^2]
0
1.0
2.0
3.0
4.0
5.0
6.0
20
15
10
5
0
-5
-10
Latitude [° North]
10
15
20
25
30
35
40
Longitude [° East]

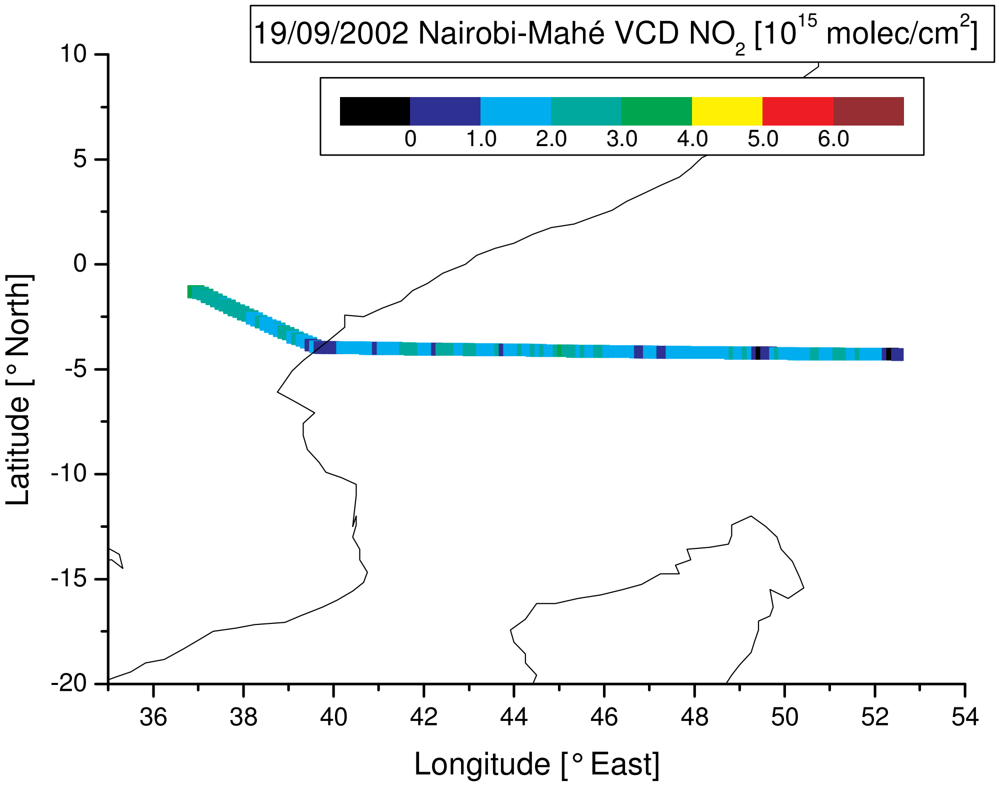
19/09/2002 Nairobi-Mahé VCD NO_2 [10^{15} molec/cm^2]
0
1.0
2.0
3.0
4.0
5.0
6.0
10
5
0
-5
-10
-15
-20
Latitude [° North]
36
38
40
42
44
46
48
50
52
54
Longitude [° East]

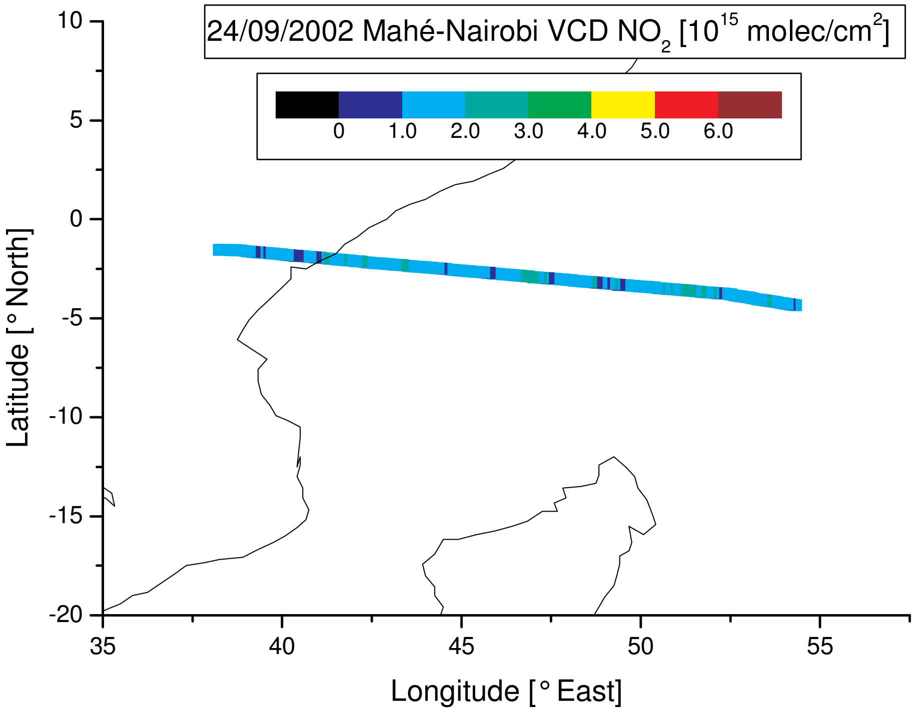

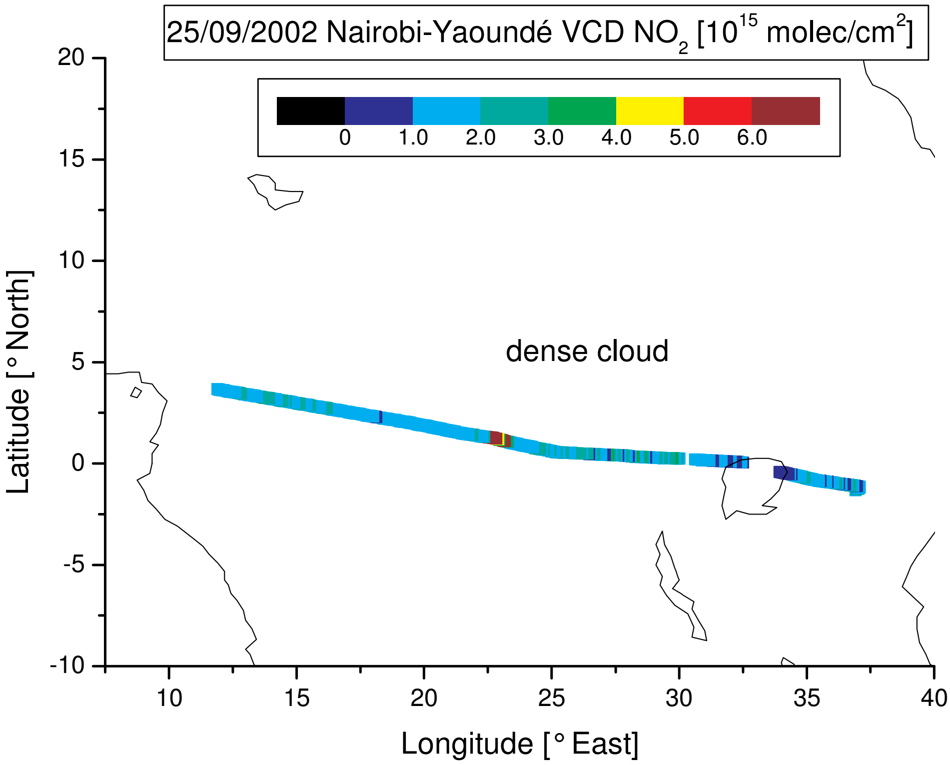

The light path enhancement and the NO_2 concentration inside the cloud is discussed in the chapters 4.5.II and 7.3 respectively

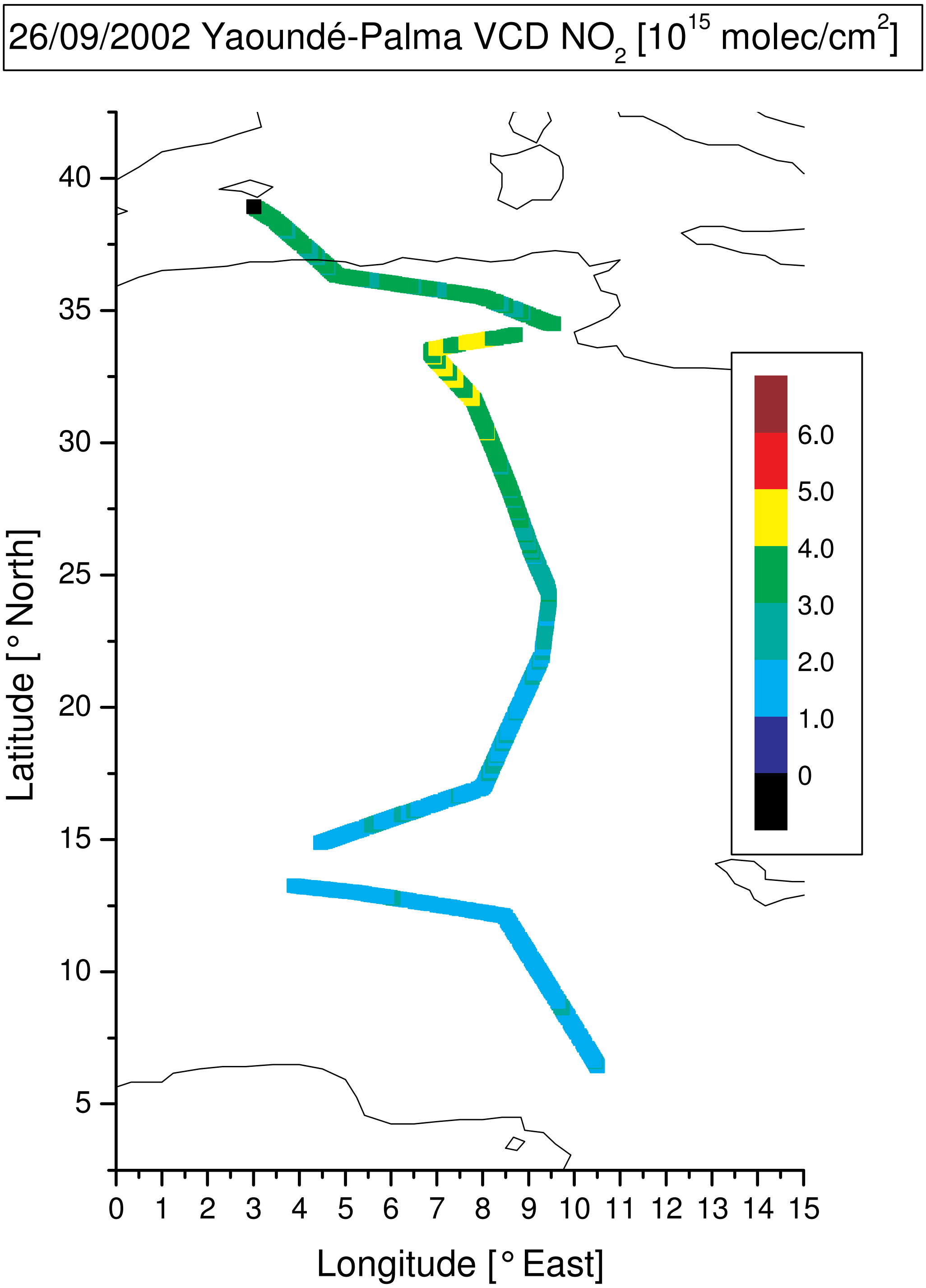
26/09/2002 Yaoundé-Palma VCD NO_2 [10^{15} molec/cm^2]
Latitude [° North]
Longitude [° East]
40
35
30
25
20
15
10
5
0
1
2
3
4
5
6
7
8
9
10
11
12
13
14
15
6.0
5.0
4.0
3.0
2.0
1.0
0

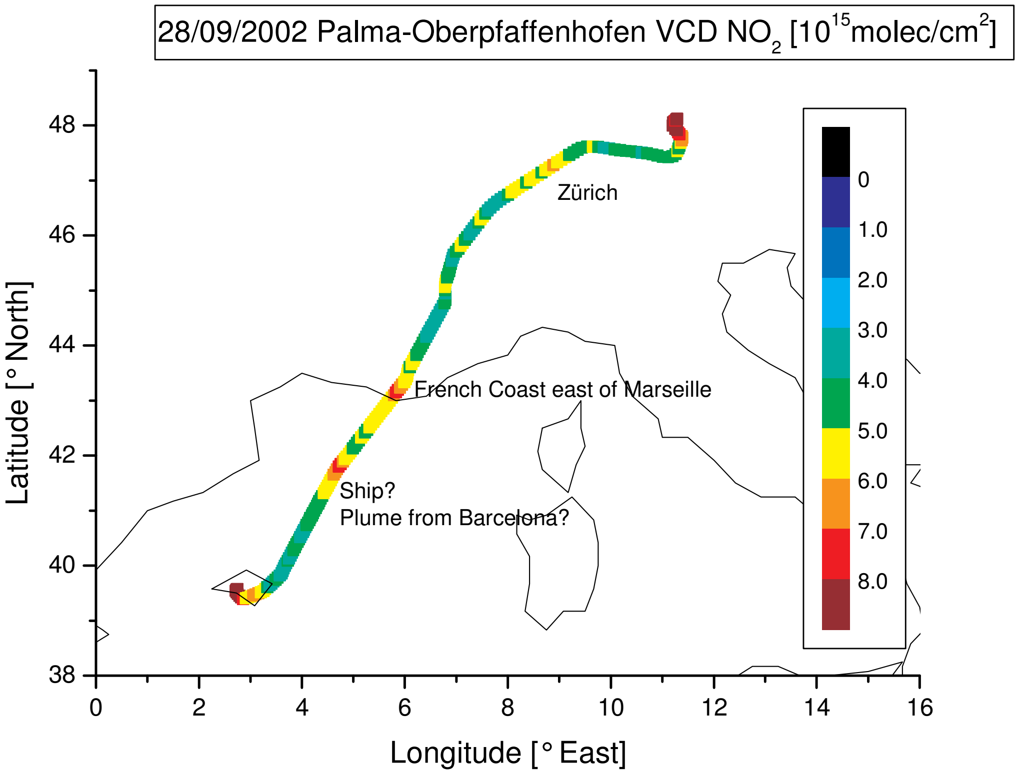
28/09/2002 Palma-Oberpfaffenhofen VCD NO$_2$ [10^{15}molec/cm^2]
Zürich
French Coast east of Marseille
Ship?
Plume from Barcelona?
Latitude [° North]
Longitude [° East]
38
40
42
44
46
48
0
2
4
6
8
10
12
14
16
0
1.0
2.0
3.0
4.0
5.0
6.0
7.0
8.0

D Overview of the total NO_2 VCDs SCIAVALUE II

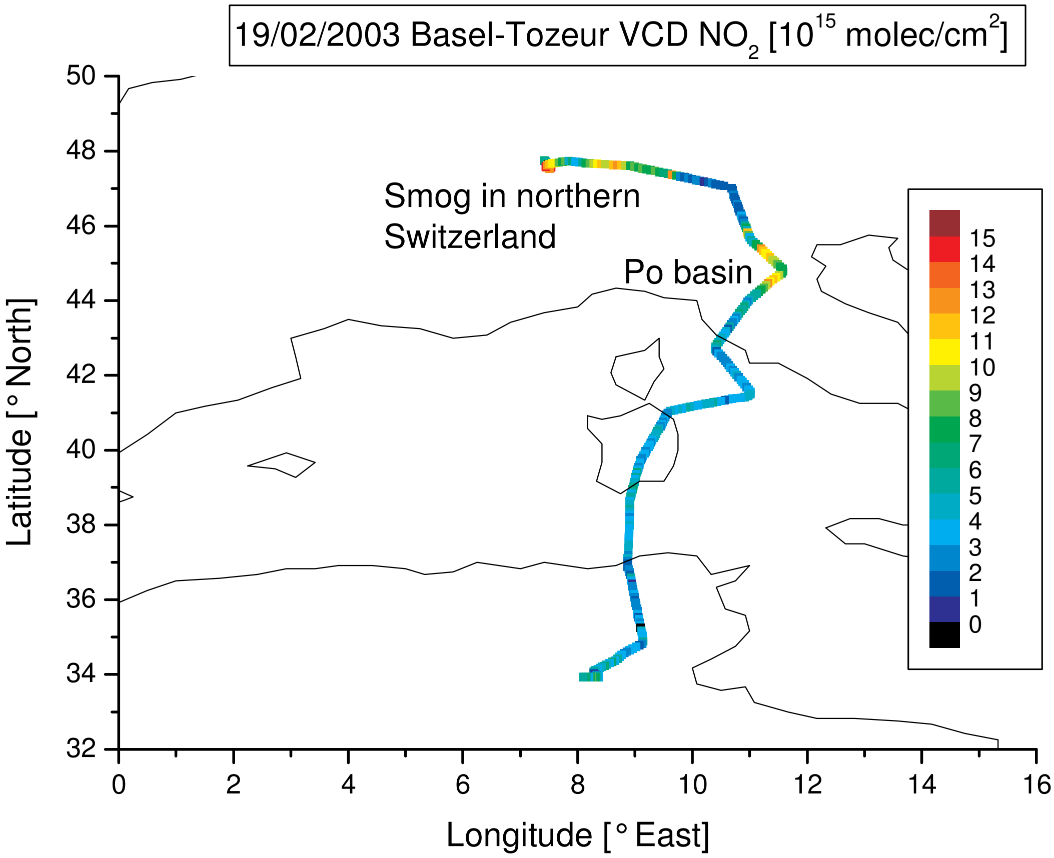

19/02/2003 Oberpfaffenhofen-Basel-Tozeur for details refer to chapter 7.1.I

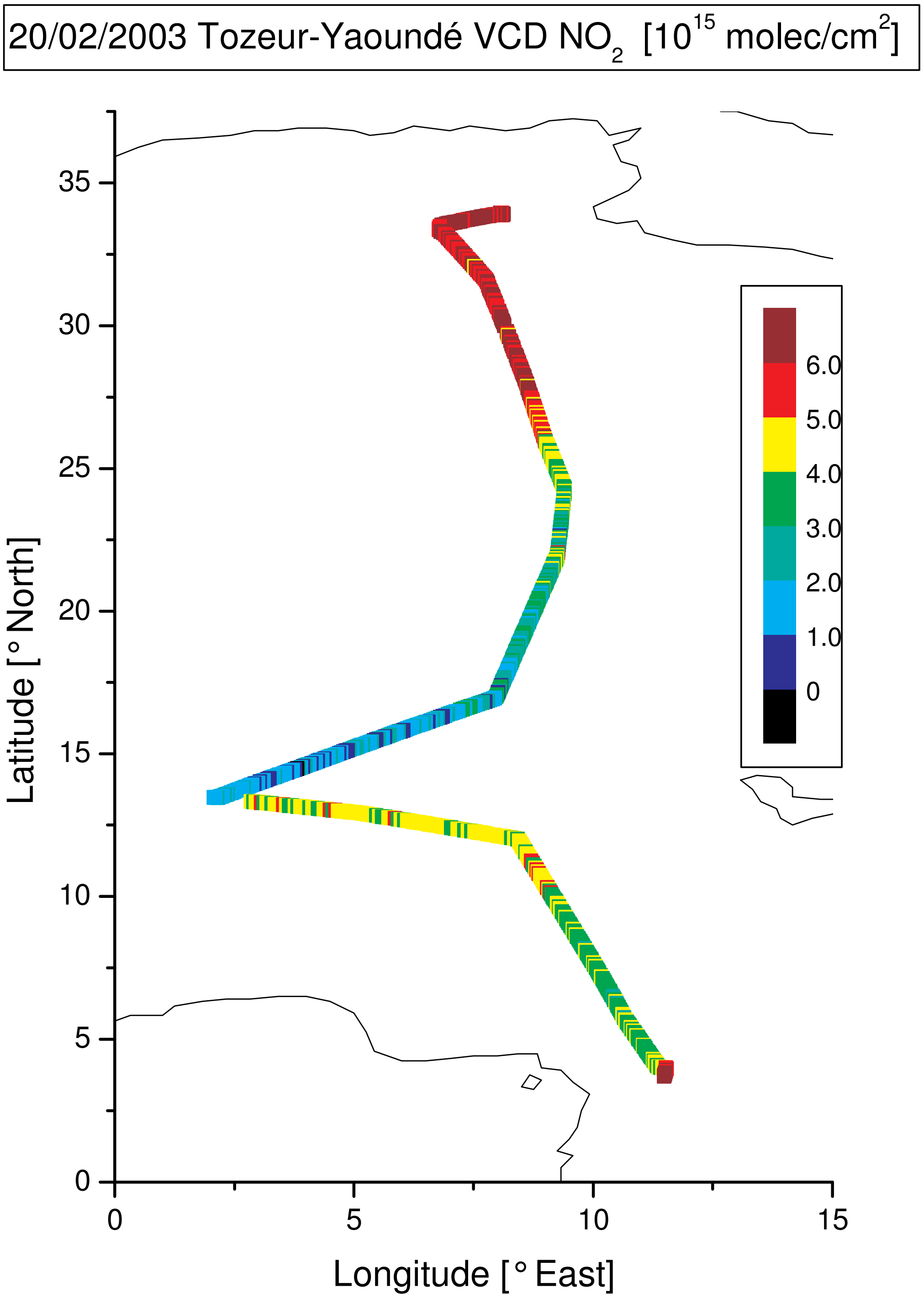
20/02/2003 Tozeur-Yaoundé VCD NO_2 [10^{15} molec/cm^2]
Latitude [° North]
Longitude [° East]
0
5
10
15
20
25
30
35
0
5
10
15
6.0
5.0
4.0
3.0
2.0
1.0
0

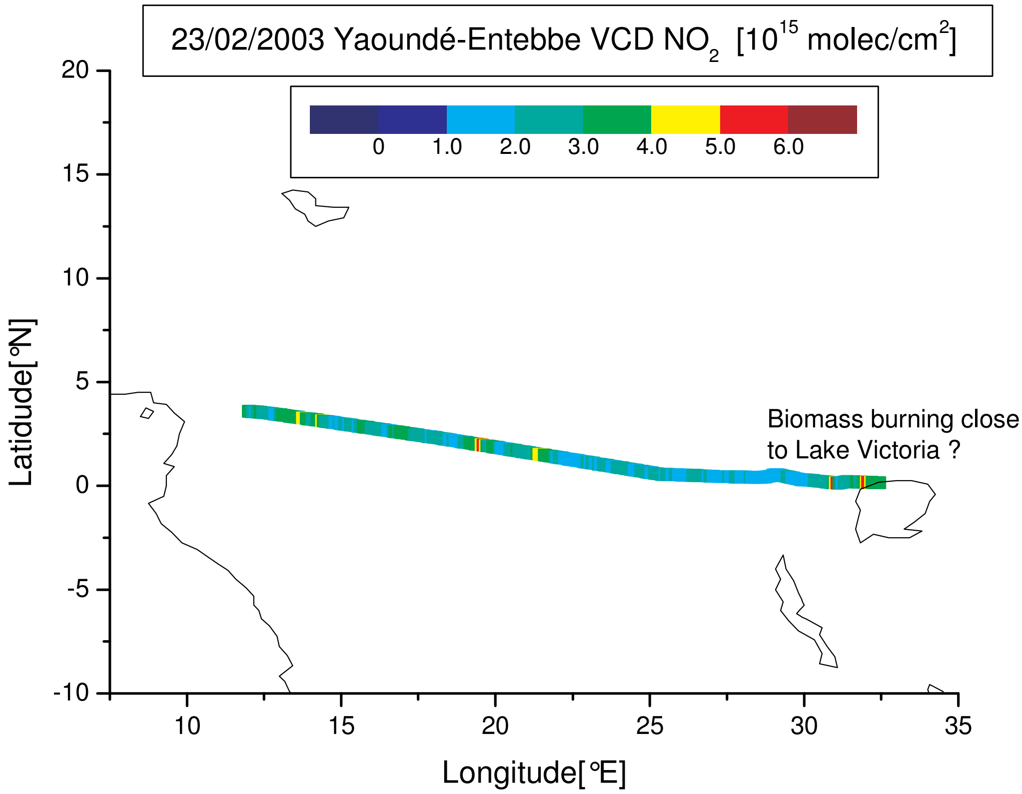

23/02/2003 Entebbe-Nairobi (30 min) no measurement were performed.
24/03/2003 Nairobi-Mahé Emergency landing in Mombasa, problems with the hydraulics "test flight" at the beginning

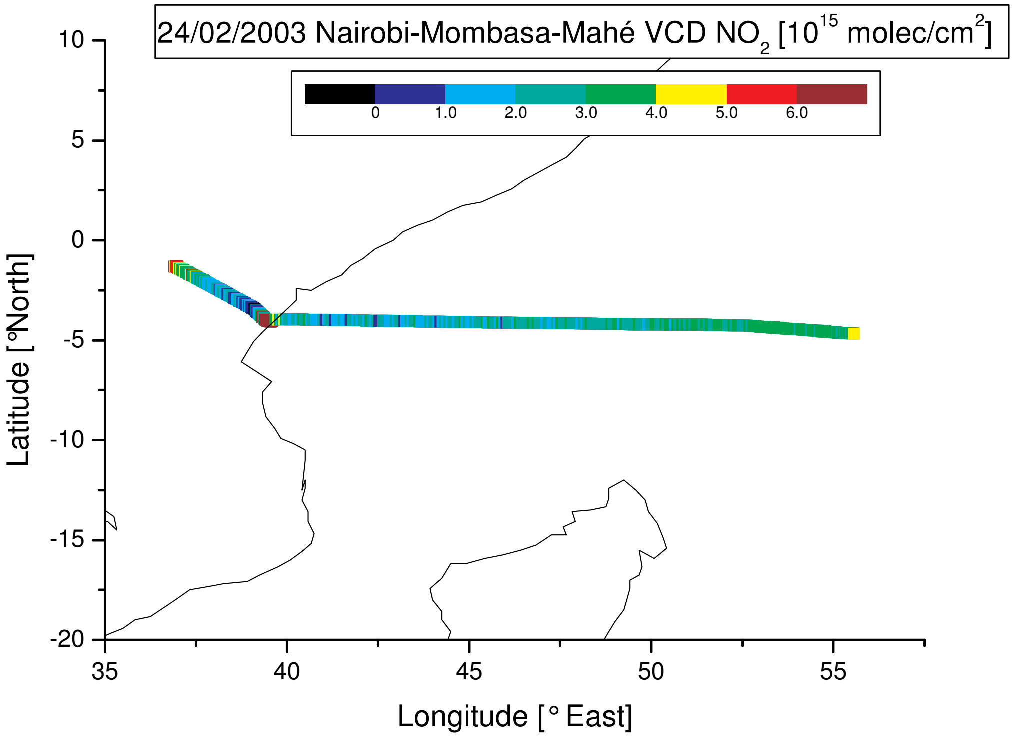

27/2/2003 Mahé-Nairobi no measurements, computer failed soon after take-off

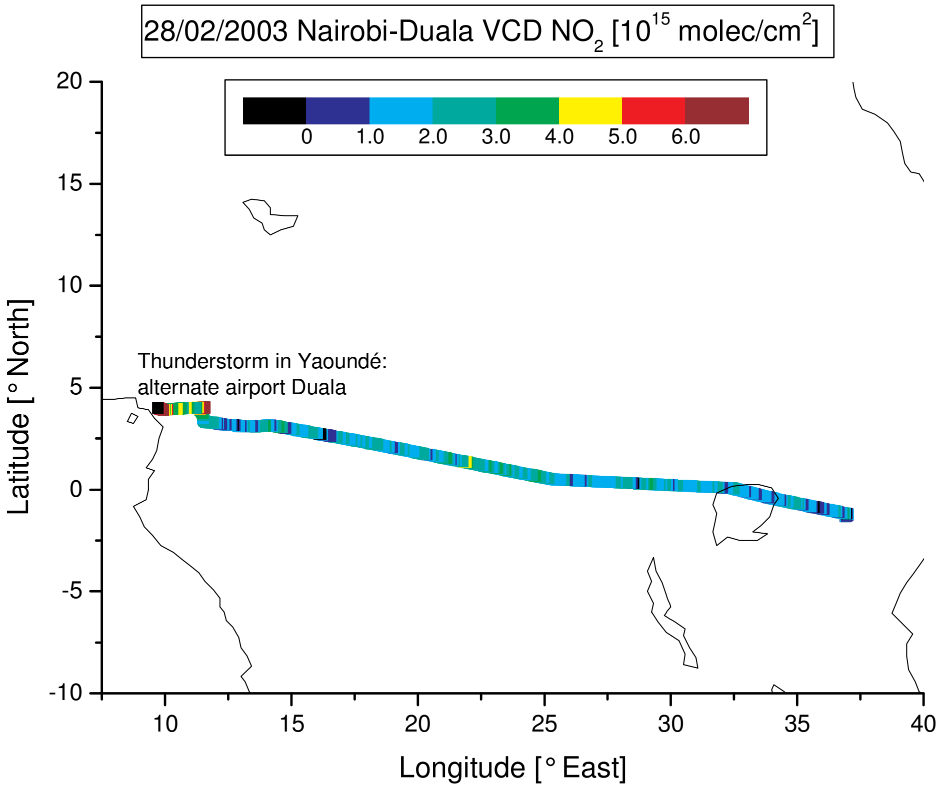

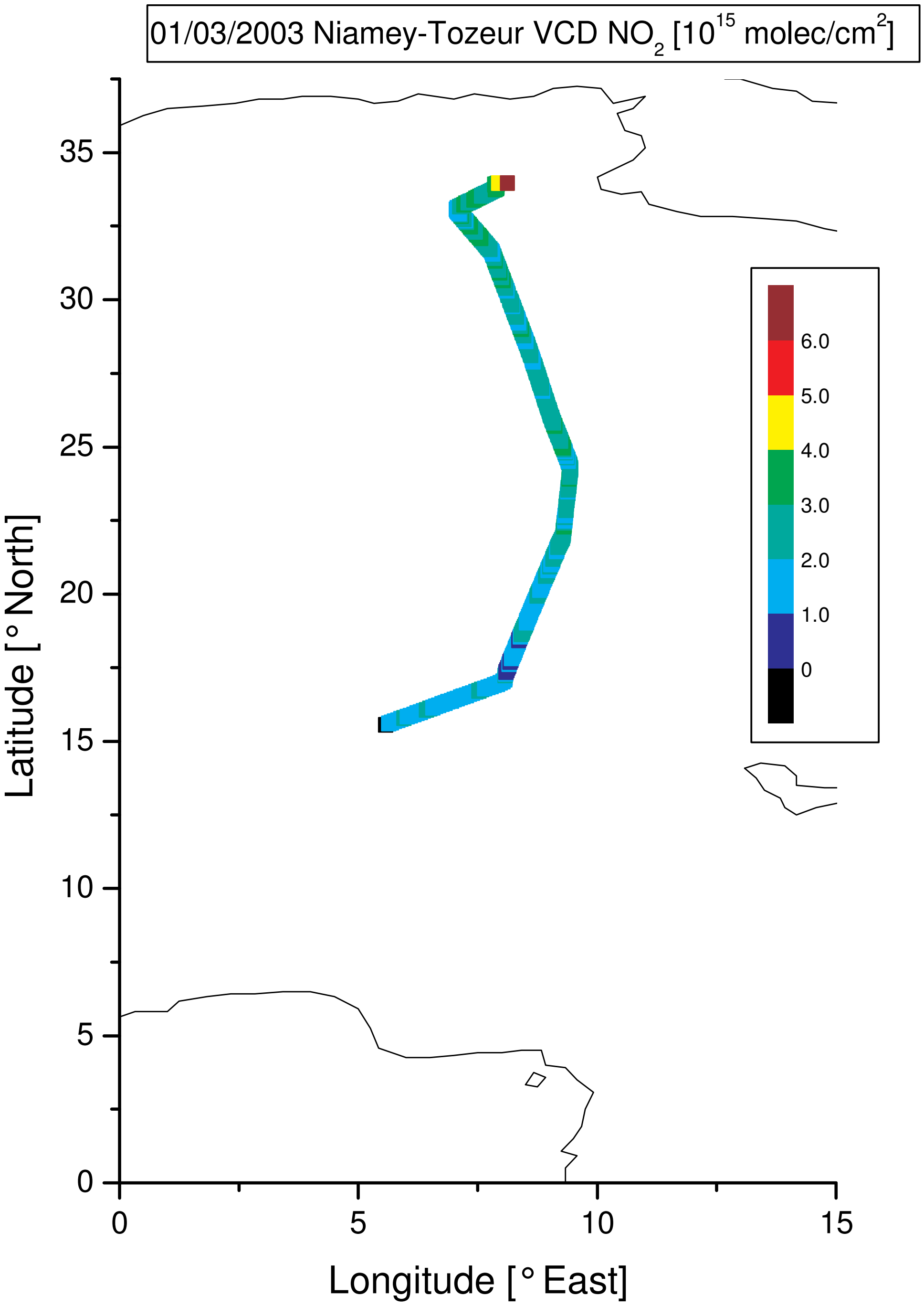

01/03/03 No data between Duala and Niamey – accidentally deleted in Niamey?

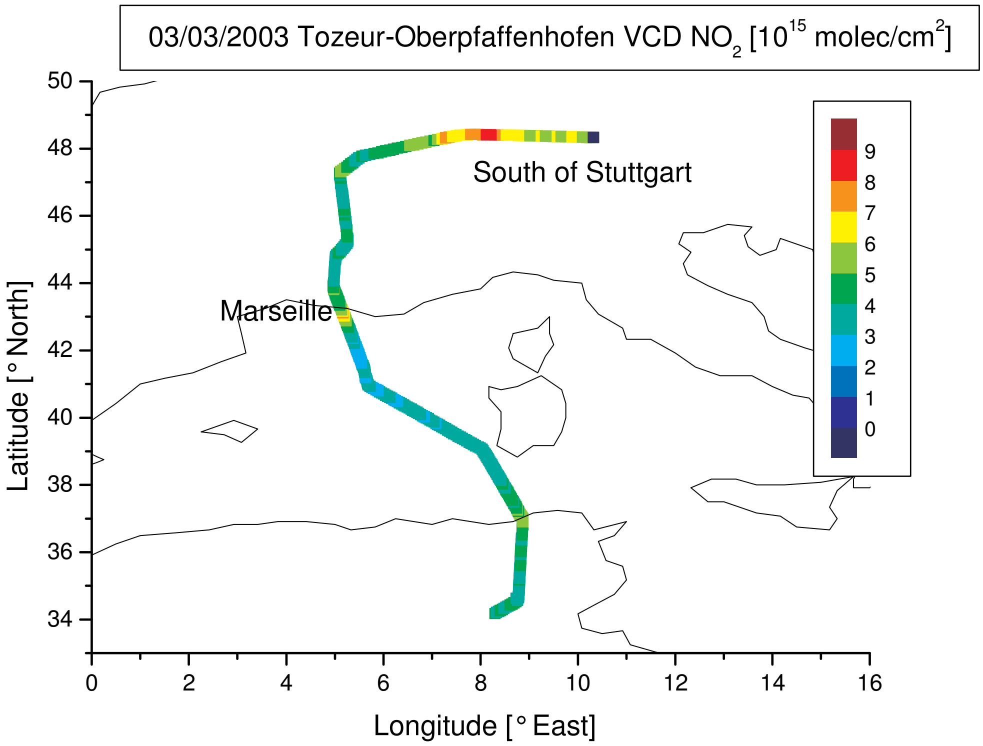

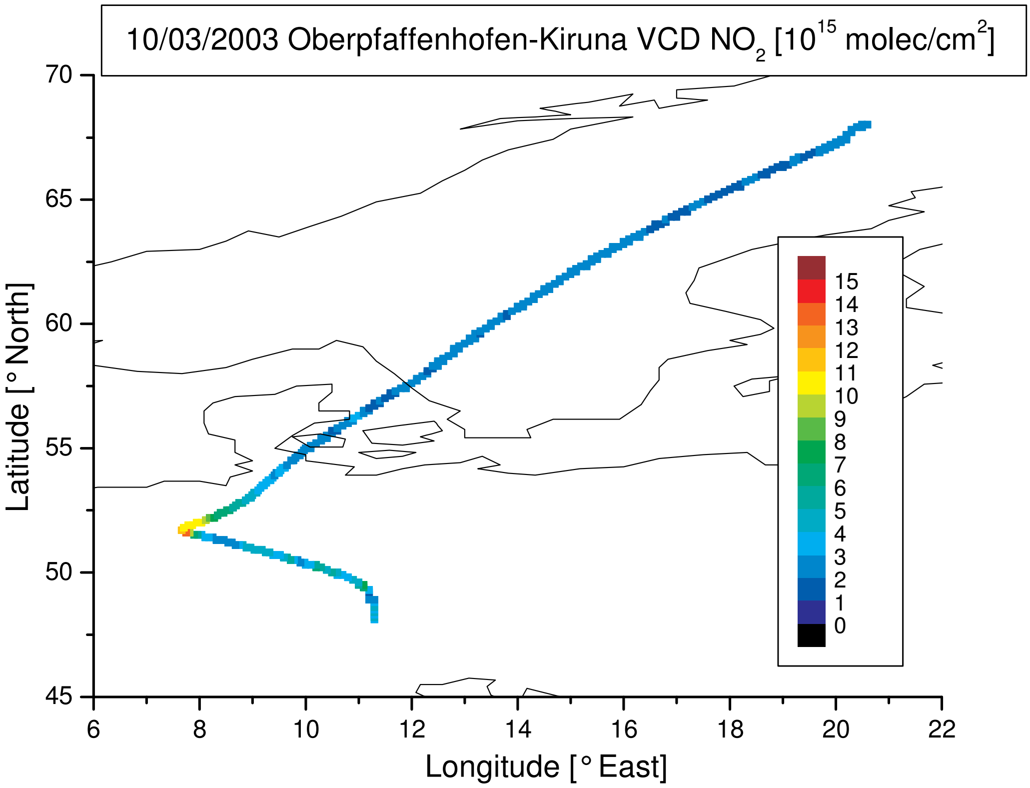

10/03/2003 Oberpfaffenhofen-Kiruna is discussed in detail in chapter 7.1.II

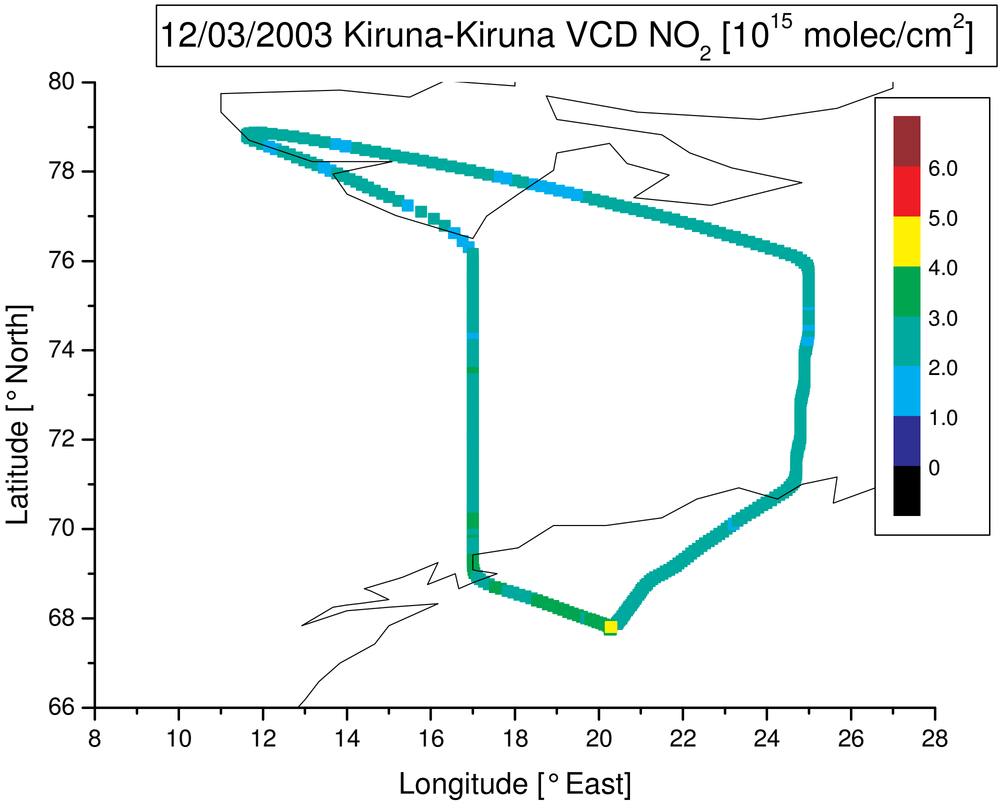
12/03/2003 Kiruna-Kiruna VCD NO$_2$ [10^{15} molec/cm^2]
Latitude [° North]
80
78
76
74
72
70
68
66
Longitude [° East]
8
10
12
14
16
18
20
22
24
26
28
6.0
5.0
4.0
3.0
2.0
1.0
0

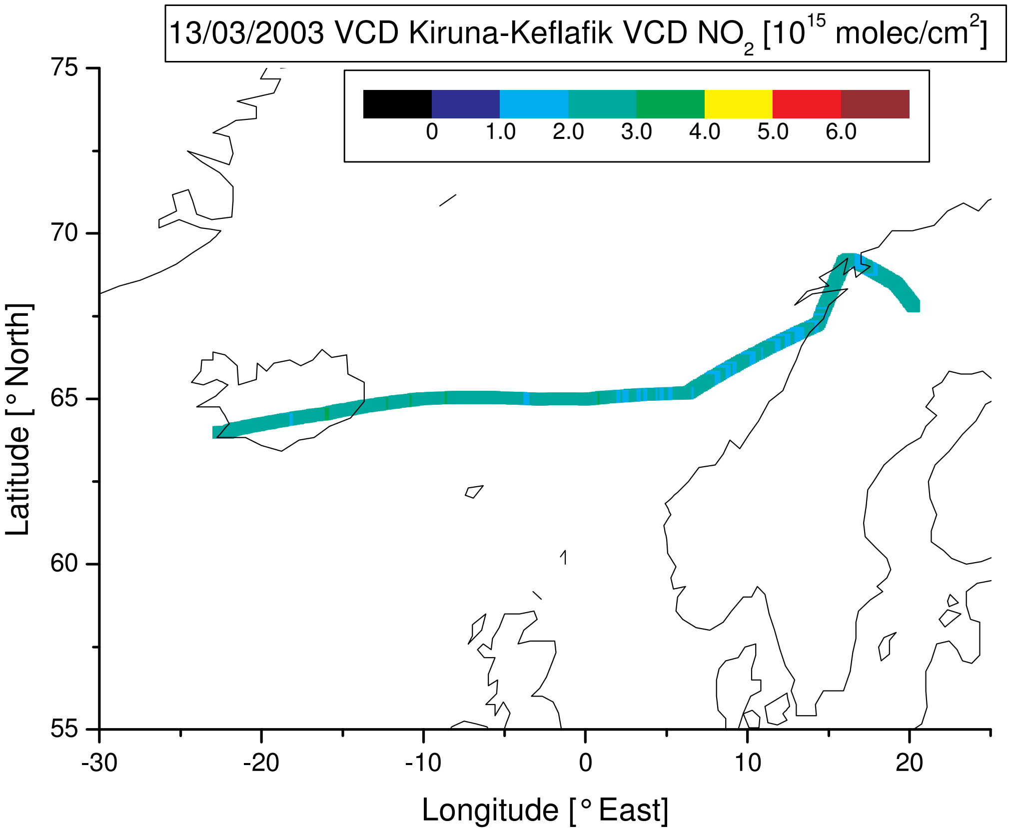
13/03/2003 VCD Kiruna-Keflafik VCD NO$_2$ [10^{15} molec/cm^2]
0
1.0
2.0
3.0
4.0
5.0
6.0
Latitude [° North]
75
70
65
60
55
Longitude [° East]
-30
-20
-10
0
10
20

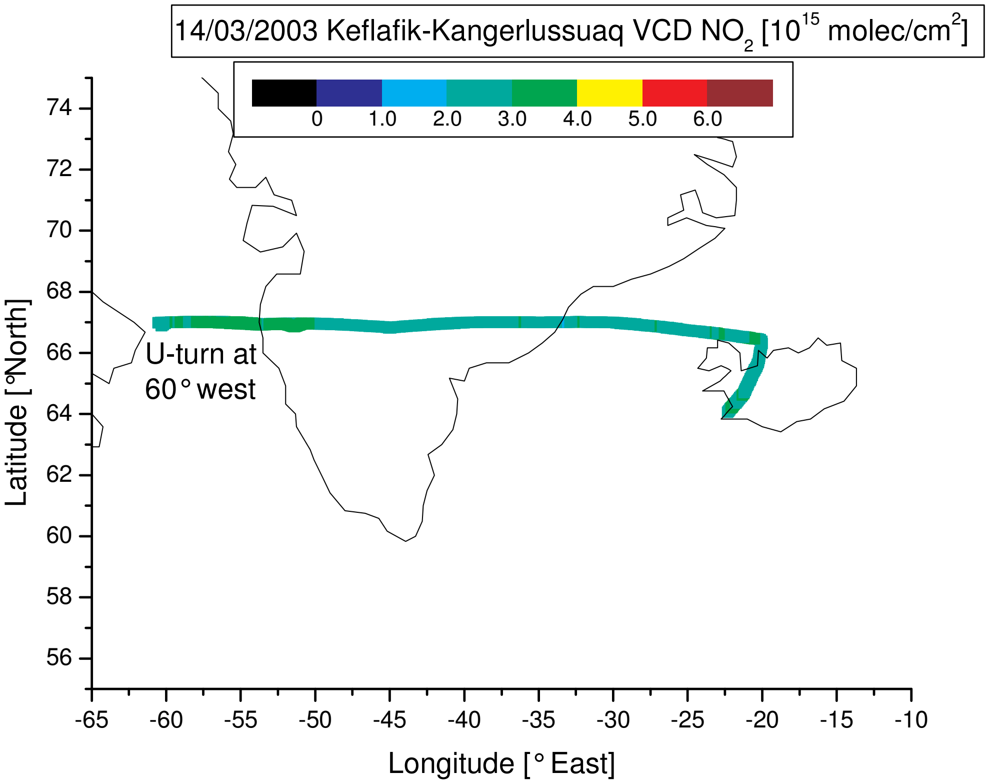
14/03/2003 Keflafik-Kangerlussuaq VCD NO_2 [10^{15} molec/cm^2]
0
1.0
2.0
3.0
4.0
5.0
6.0
U-turn at
60° west
Latitude [°North]
74
72
70
68
66
64
62
60
58
56
-65
-60
-55
-50
-45
-40
-35
-30
-25
-20
-15
-10
Longitude [° East]

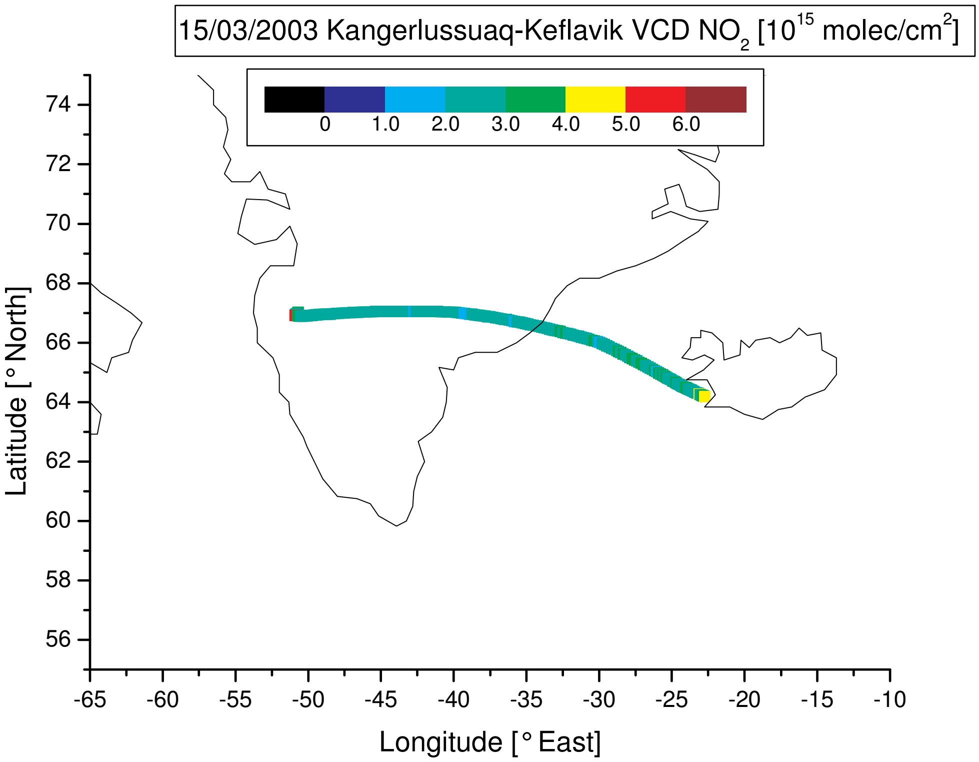
15/03/2003 Kangerlussuaq-Keflavik VCD NO_2 [10^{15} molec/cm^2]
0
1.0
2.0
3.0
4.0
5.0
6.0
Latitude [° North]
74
72
70
68
66
64
62
60
58
56
-65
-60
-55
-50
-45
-40
-35
-30
-25
-20
-15
-10
Longitude [° East]

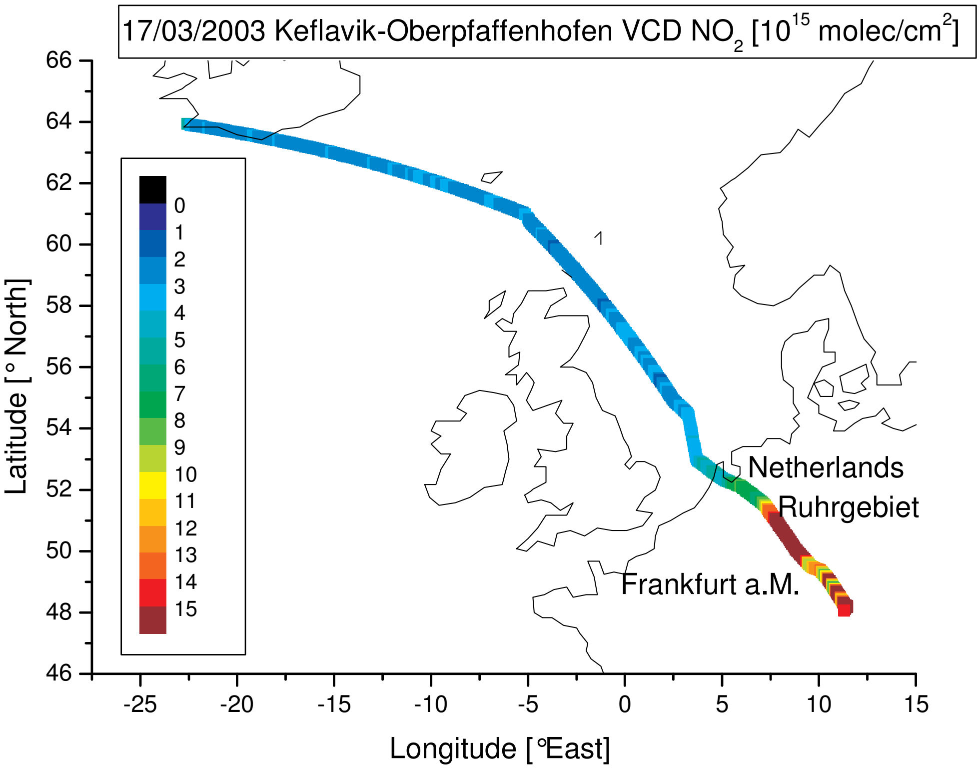

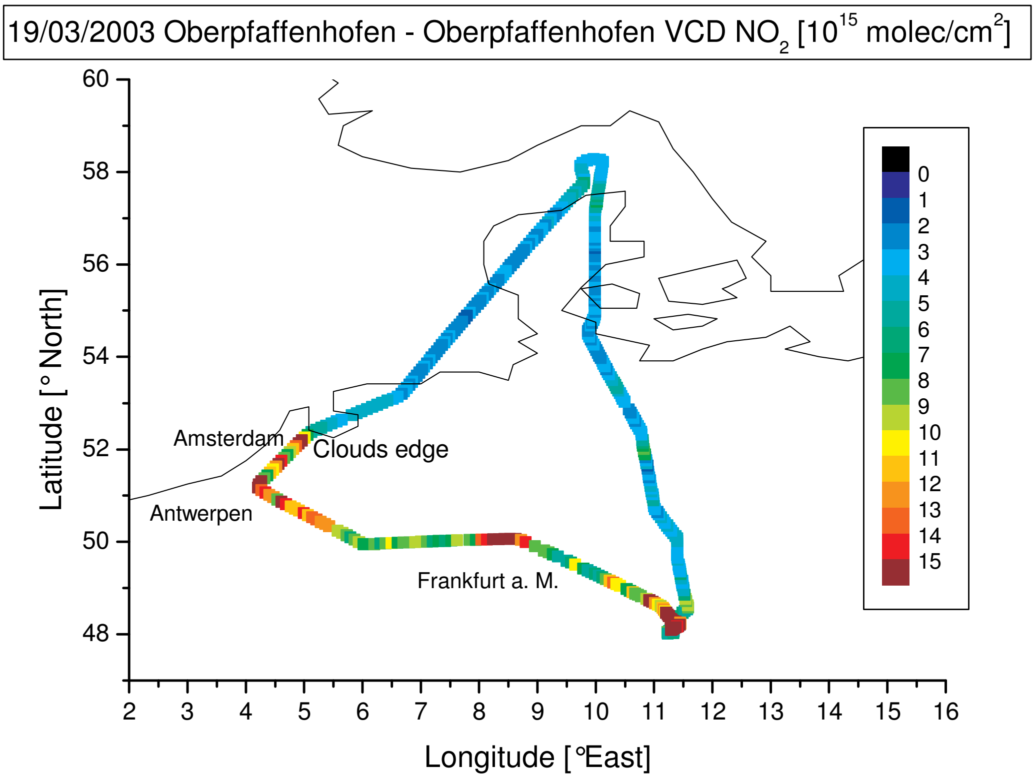

a detailed discussion of the AMAXDOAS data from 19/03/2003 Oberpfaffenhofen local flight – via Denmark and Holland – is given by Wang et al., [2005].

E Overview of the SCDs FORMAT I

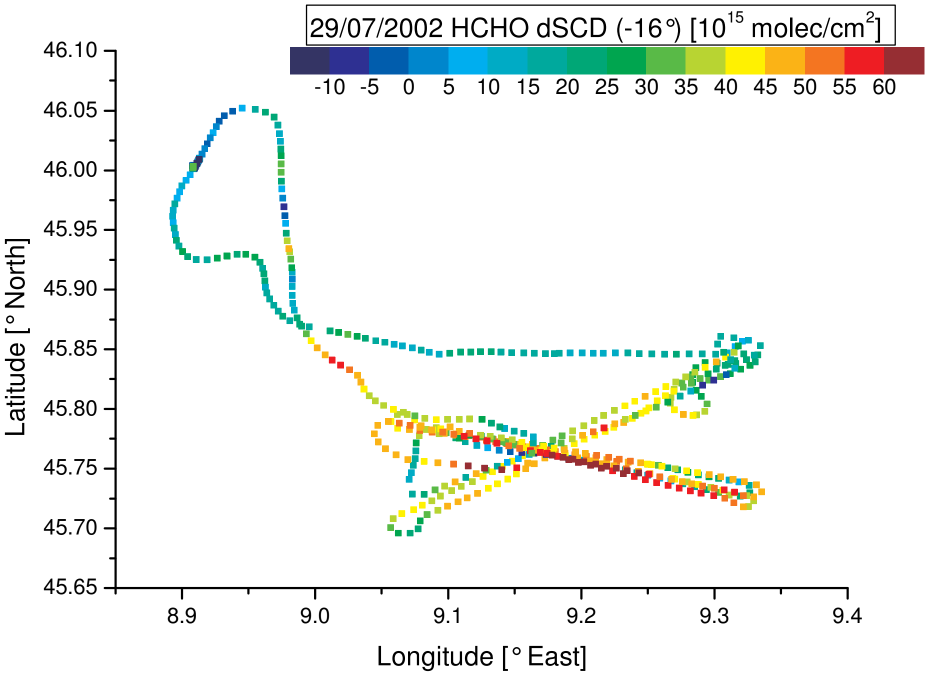

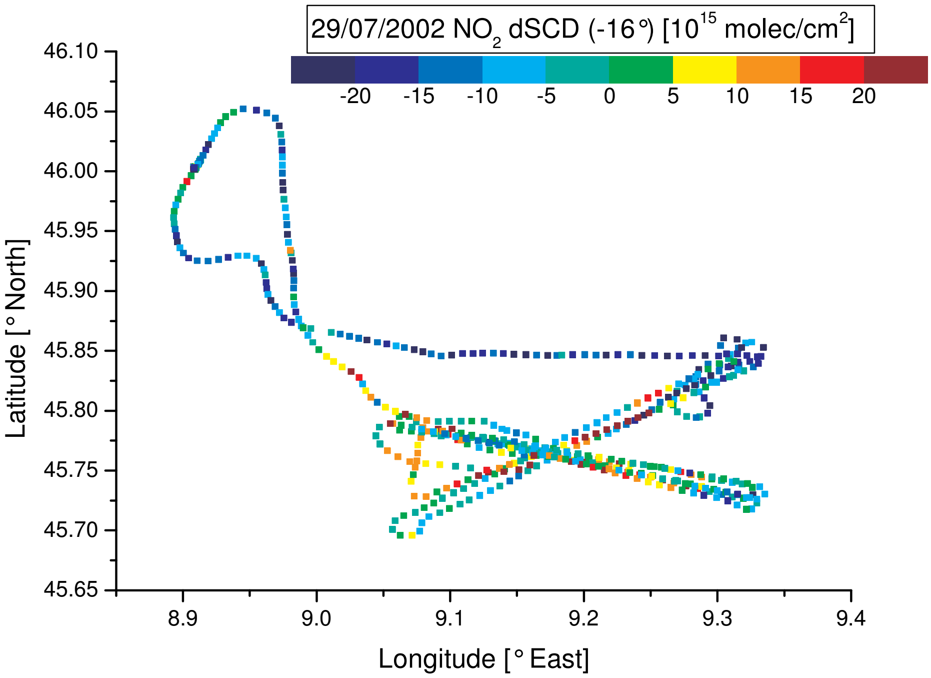

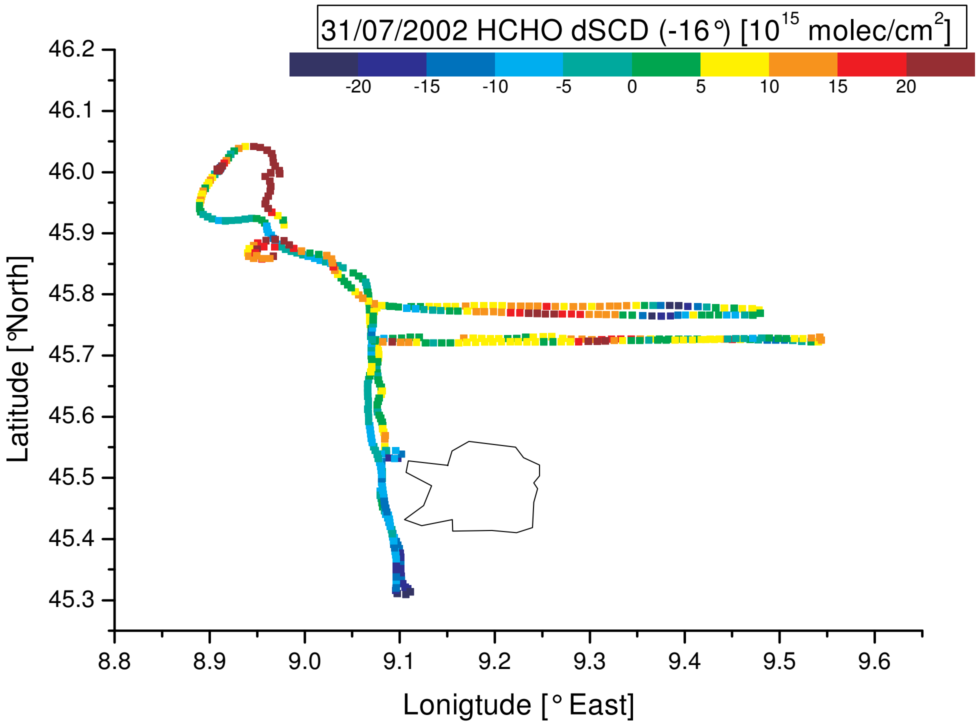
31/07/2002 HCHO dSCD (-16°) [10^{15} molec/cm^2]
-20
-15
-10
-5
0
5
10
15
20
46.2
46.1
46.0
45.9
45.8
45.7
45.6
45.5
45.4
45.3
Latitude [°North]
8.8
8.9
9.0
9.1
9.2
9.3
9.4
9.5
9.6
Lonigtude [° East]

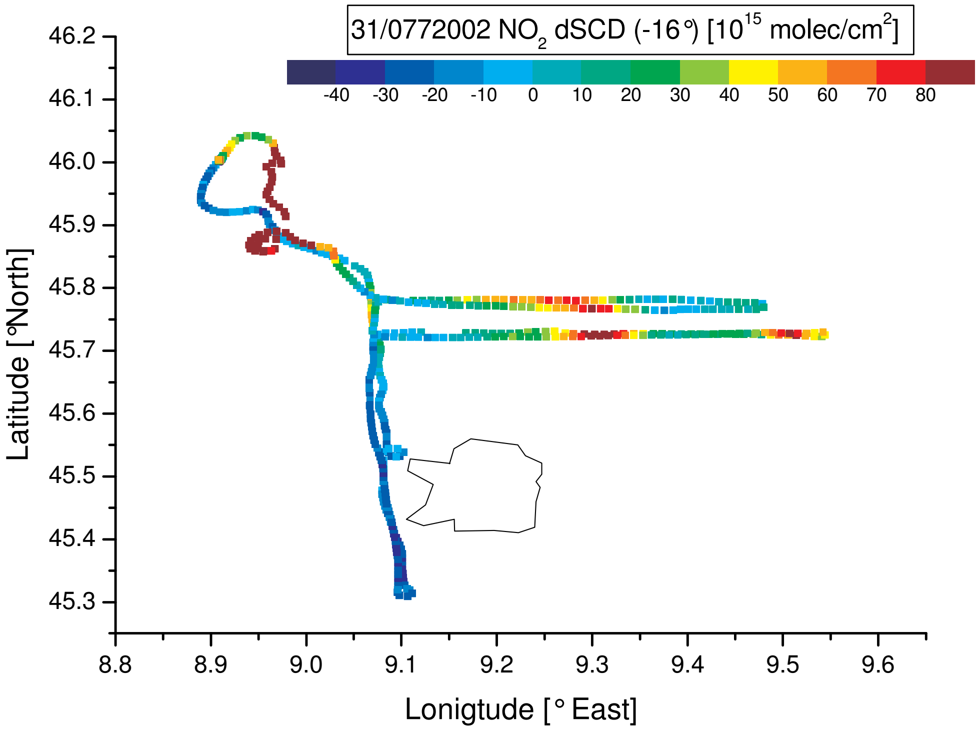
31/0772002 NO$_2$ dSCD (-16°) [10^{15} molec/cm^2]
-40
-30
-20
-10
0
10
20
30
40
50
60
70
80
46.2
46.1
46.0
45.9
45.8
45.7
45.6
45.5
45.4
45.3
Latitude [°North]
8.8
8.9
9.0
9.1
9.2
9.3
9.4
9.5
9.6
Lonigtude [° East]

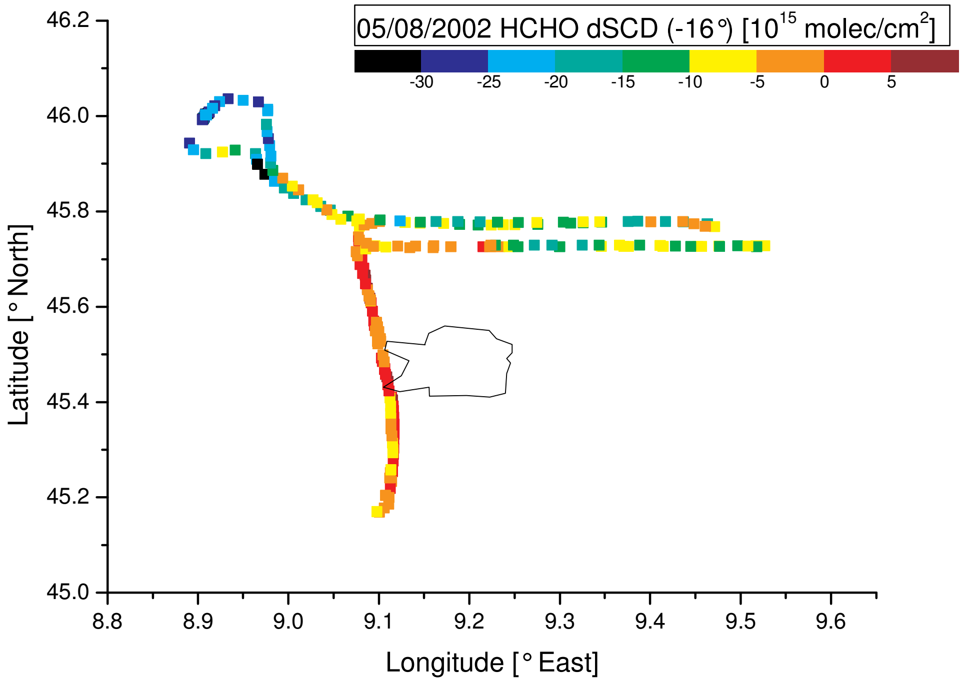
05/08/2002 HCHO dSCD (-16°) [10^15 molec/cm^2]
-30
-25
-20
-15
-10
-5
0
5
46.2
46.0
45.8
45.6
45.4
45.2
45.0
Latitude [° North]
8.8
8.9
9.0
9.1
9.2
9.3
9.4
9.5
9.6
Longitude [° East]

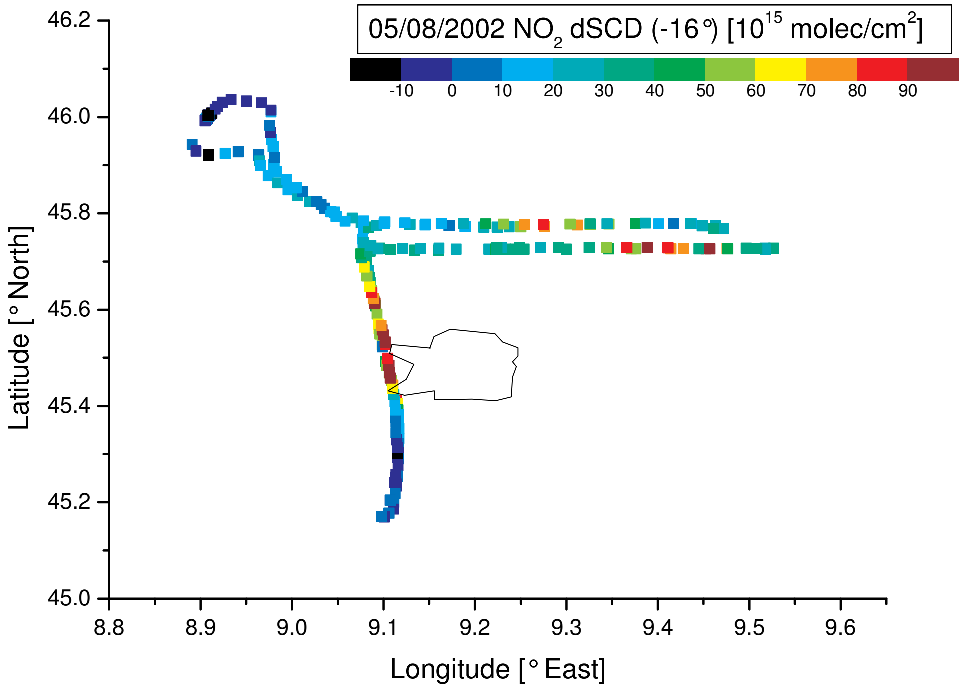
05/08/2002 NO2 dSCD (-16°) [10^15 molec/cm^2]
-10
0
10
20
30
40
50
60
70
80
90
46.2
46.0
45.8
45.6
45.4
45.2
45.0
Latitude [° North]
8.8
8.9
9.0
9.1
9.2
9.3
9.4
9.5
9.6
Longitude [° East]

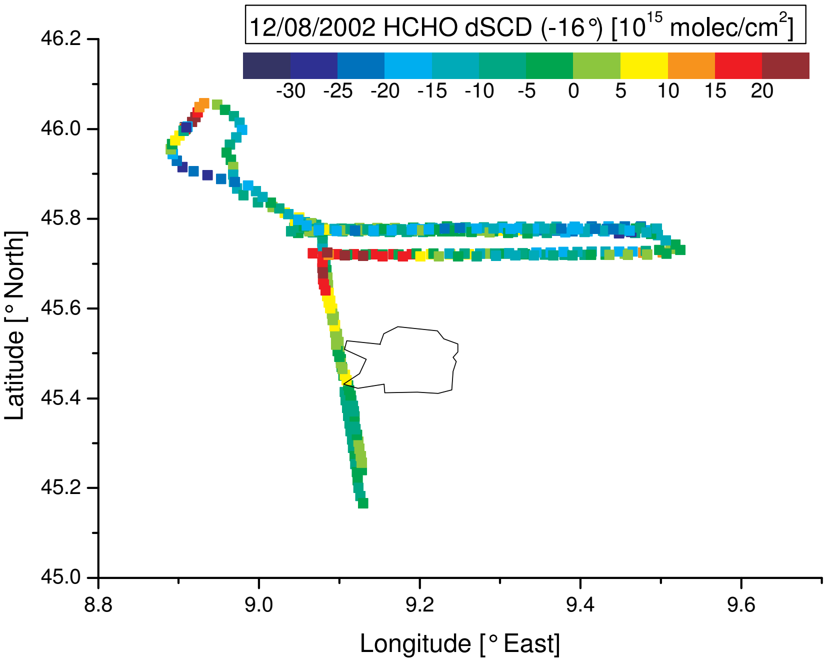
12/08/2002 HCHO dSCD (-16°) [10^15 molec/cm^2]
-30
-25
-20
-15
-10
-5
0
5
10
15
20
Latitude [° North]
46.2
46.0
45.8
45.6
45.4
45.2
45.0
8.8
9.0
9.2
9.4
9.6
Longitude [° East]

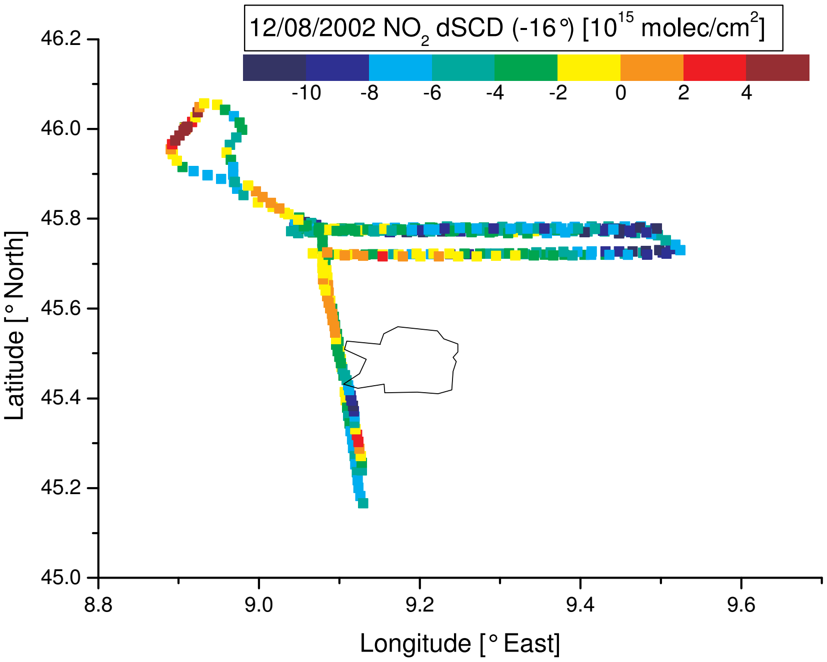
12/08/2002 NO2 dSCD (-16°) [10^15 molec/cm^2]
-10
-8
-6
-4
-2
0
2
4
Latitude [° North]
46.2
46.0
45.8
45.6
45.4
45.2
45.0
8.8
9.0
9.2
9.4
9.6
Longitude [° East]

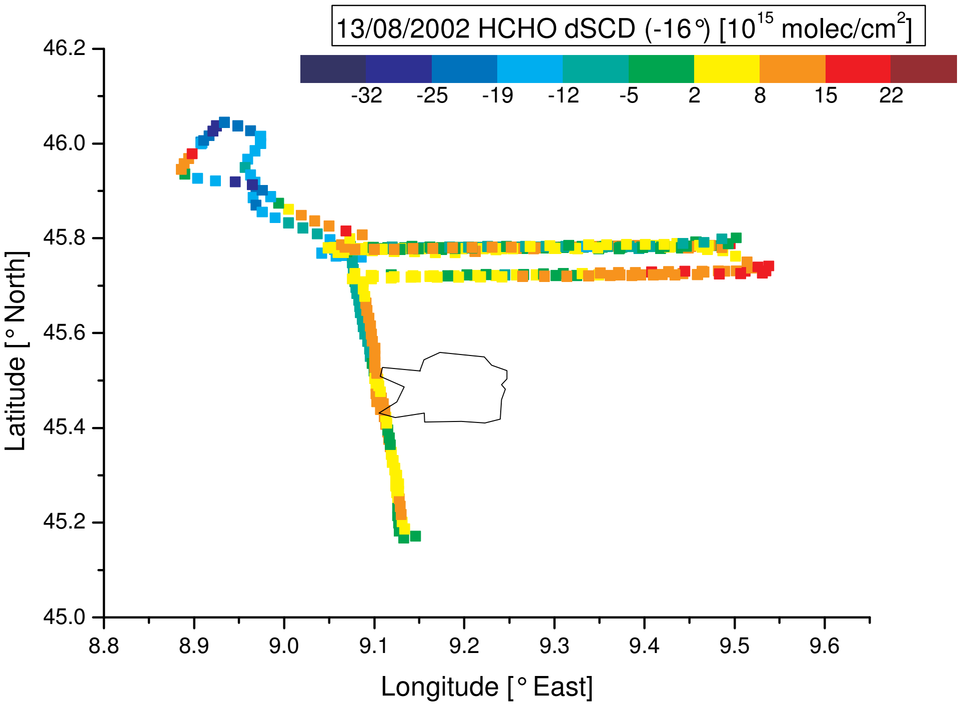
13/08/2002 HCHO dSCD (-16°) [10^{15} molec/cm^2]
-32
-25
-19
-12
-5
2
8
15
22
46.2
46.0
45.8
45.6
45.4
45.2
45.0
Latitude [° North]
8.8
8.9
9.0
9.1
9.2
9.3
9.4
9.5
9.6
Longitude [° East]

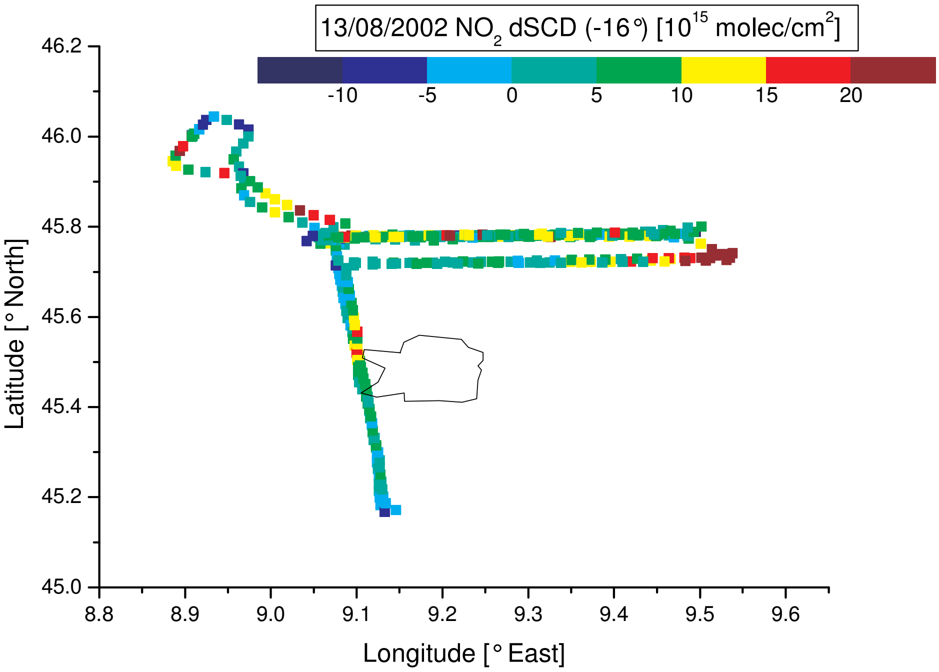
13/08/2002 NO_2 dSCD (-16°) [10^{15} molec/cm^2]
-10
-5
0
5
10
15
20
46.2
46.0
45.8
45.6
45.4
45.2
45.0
Latitude [° North]
8.8
8.9
9.0
9.1
9.2
9.3
9.4
9.5
9.6
Longitude [° East]

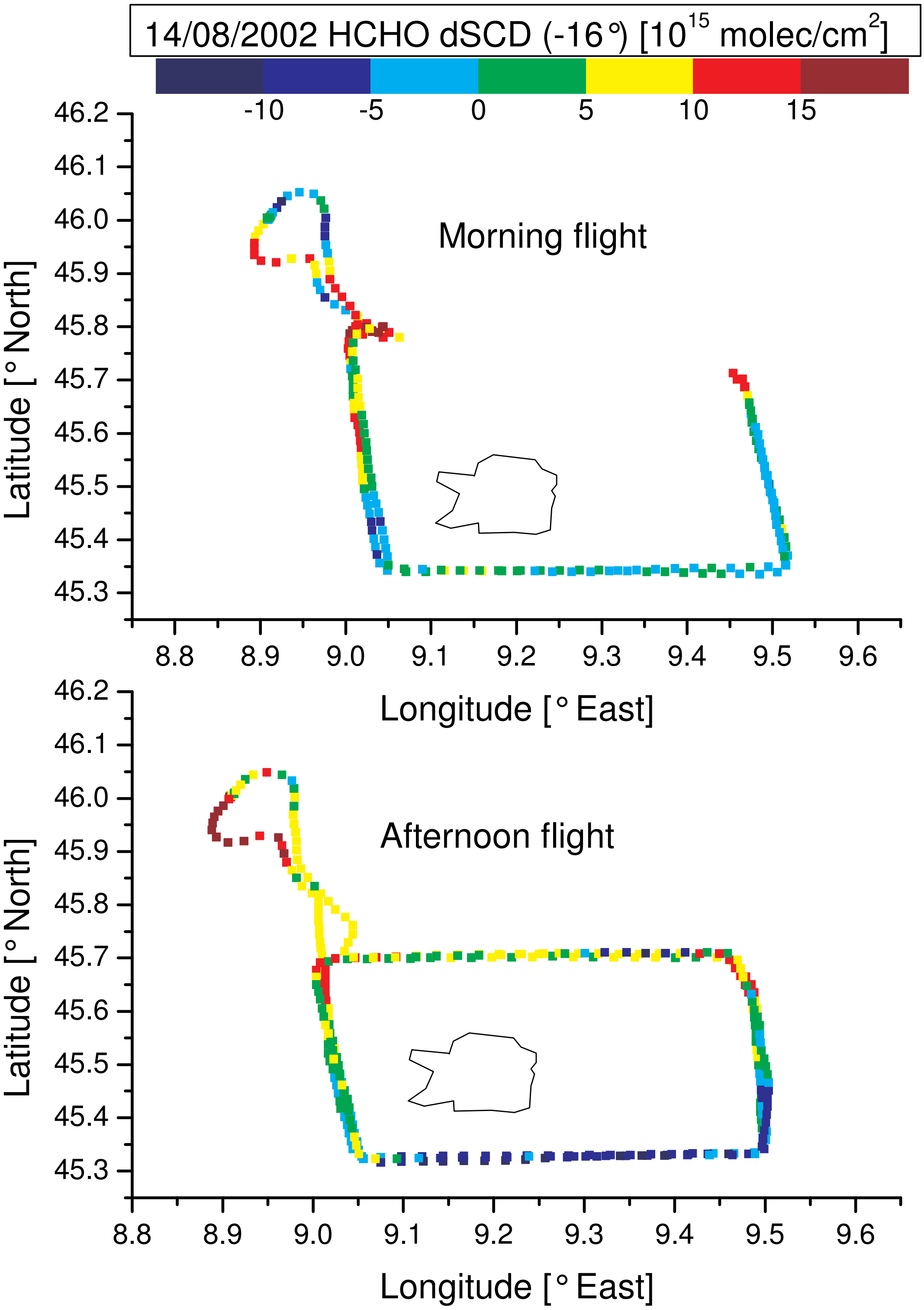
14/08/2002 HCHO dSCD (-16°) [10^15 molec/cm^2]
-10
-5
0
5
10
15
Morning flight
Afternoon flight
Latitude [° North]
Longitude [° East]
46.2
46.1
46.0
45.9
45.8
45.7
45.6
45.5
45.4
45.3
8.8
8.9
9.0
9.1
9.2
9.3
9.4
9.5
9.6

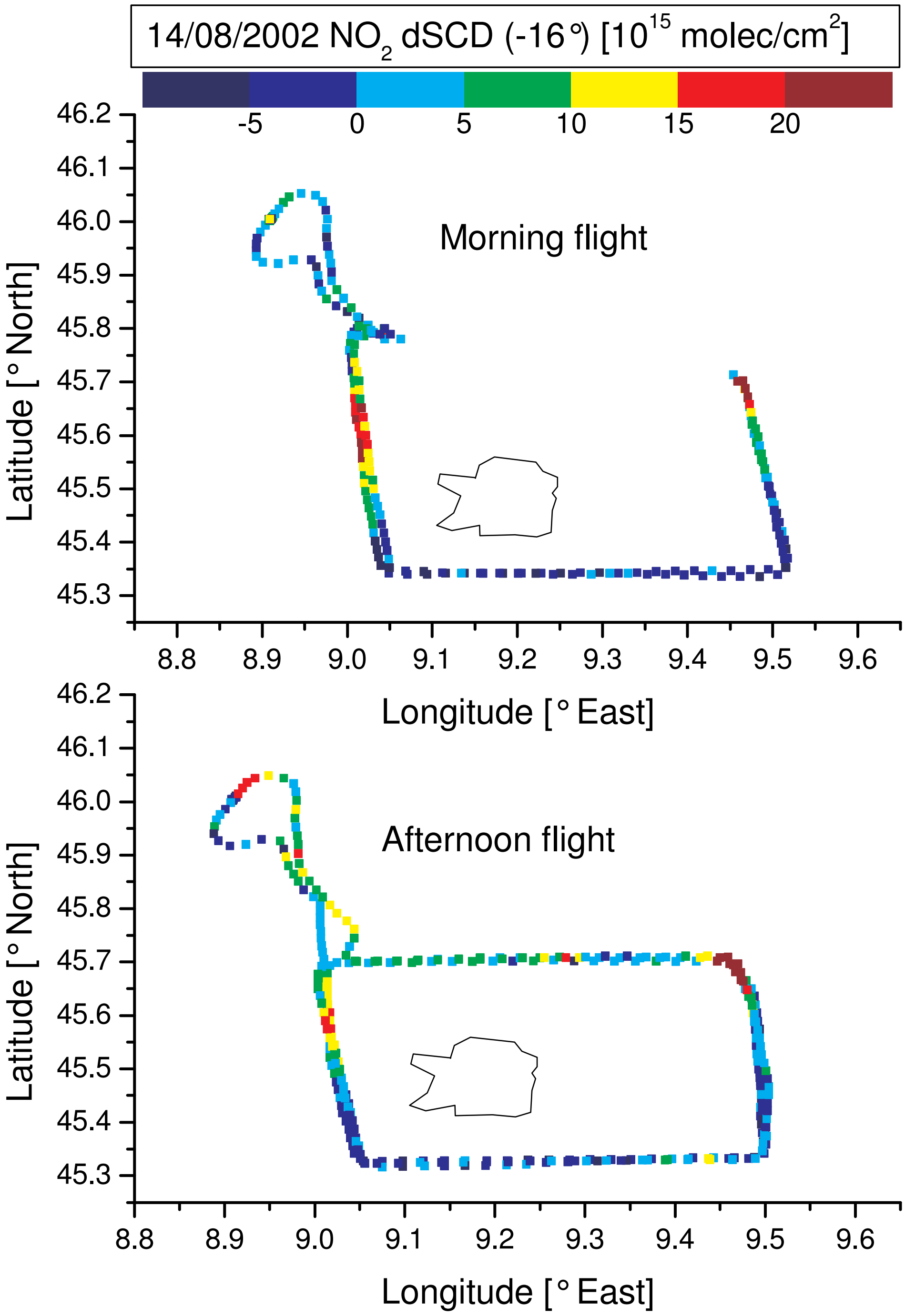
14/08/2002 NO$_2$ dSCD (-16°) [10^{15} molec/cm^2]
-5
0
5
10
15
20
46.2
46.1
46.0
45.9
45.8
45.7
45.6
45.5
45.4
45.3
Latitude [° North]
Morning flight
8.8
8.9
9.0
9.1
9.2
9.3
9.4
9.5
9.6
Longitude [° East]
Afternoon flight

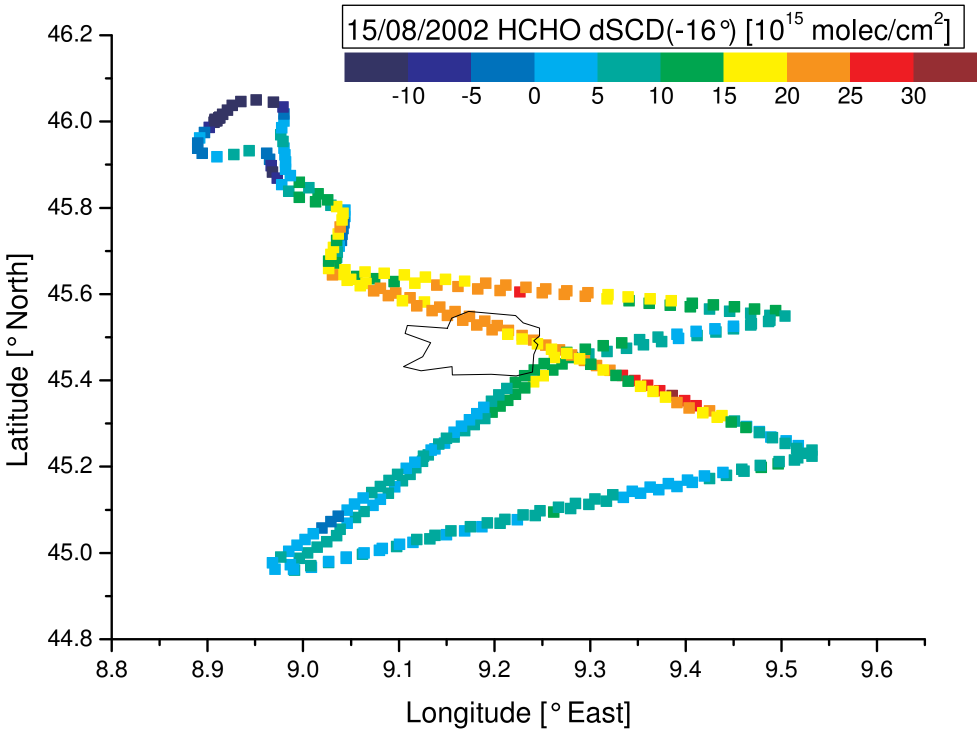
15/08/2002 HCHO dSCD(-16°) [10^{15} molec/cm^2]
-10
-5
0
5
10
15
20
25
30
Latitude [° North]
46.2
46.0
45.8
45.6
45.4
45.2
45.0
44.8
Longitude [° East]
8.8
8.9
9.0
9.1
9.2
9.3
9.4
9.5
9.6

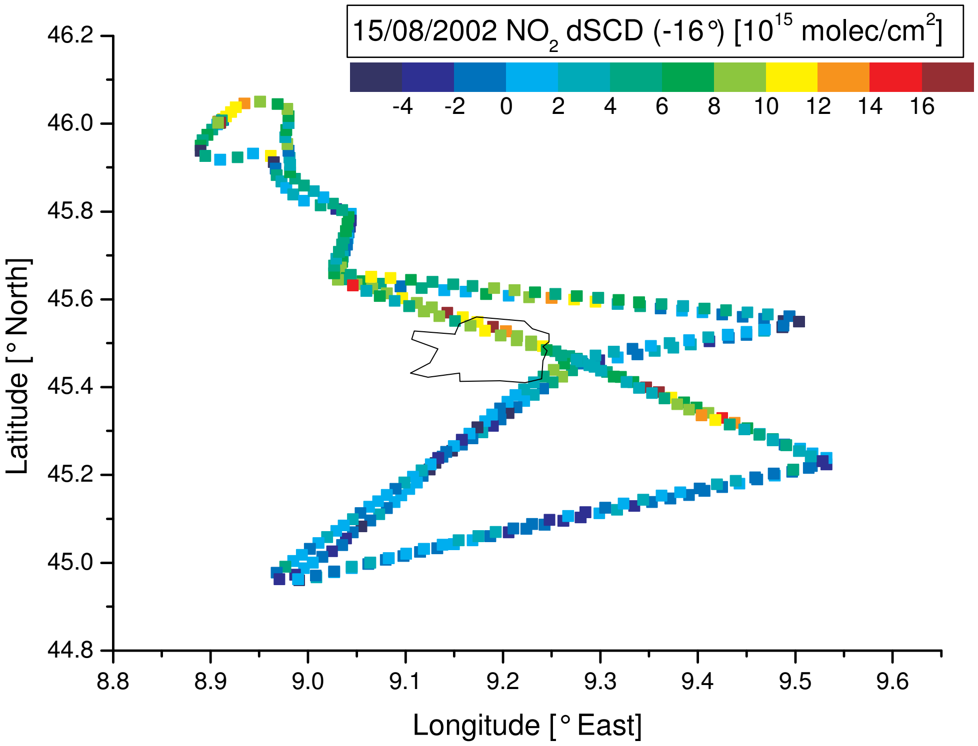
15/08/2002 NO_2 dSCD (-16°) [10^{15} molec/cm^2]
-4
-2
0
2
4
6
8
10
12
14
16
Latitude [° North]
46.2
46.0
45.8
45.6
45.4
45.2
45.0
44.8
Longitude [° East]
8.8
8.9
9.0
9.1
9.2
9.3
9.4
9.5
9.6

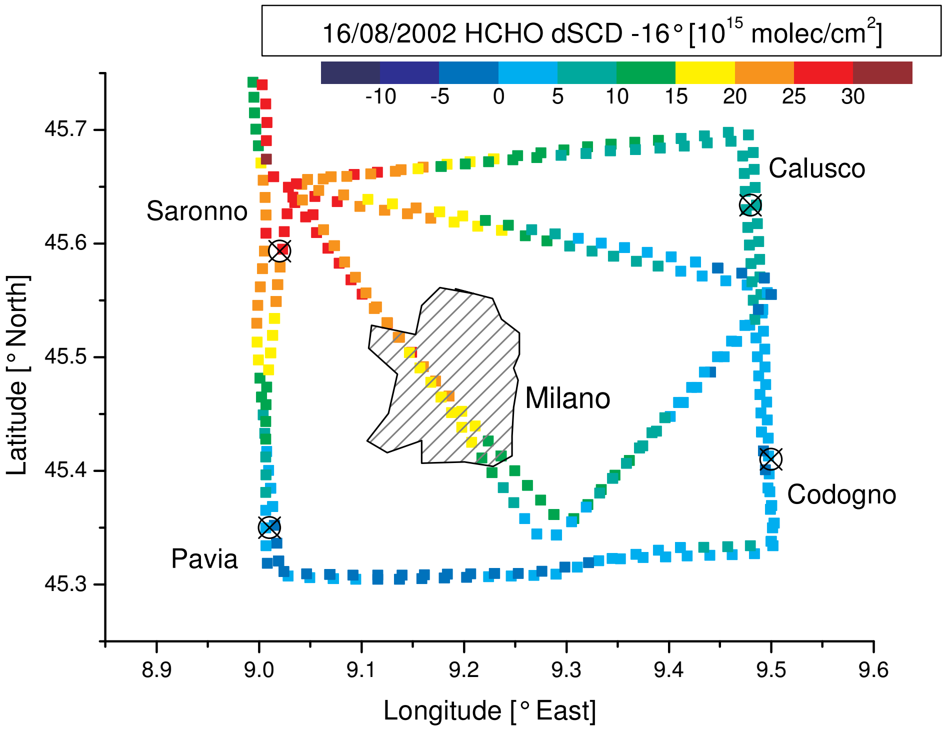

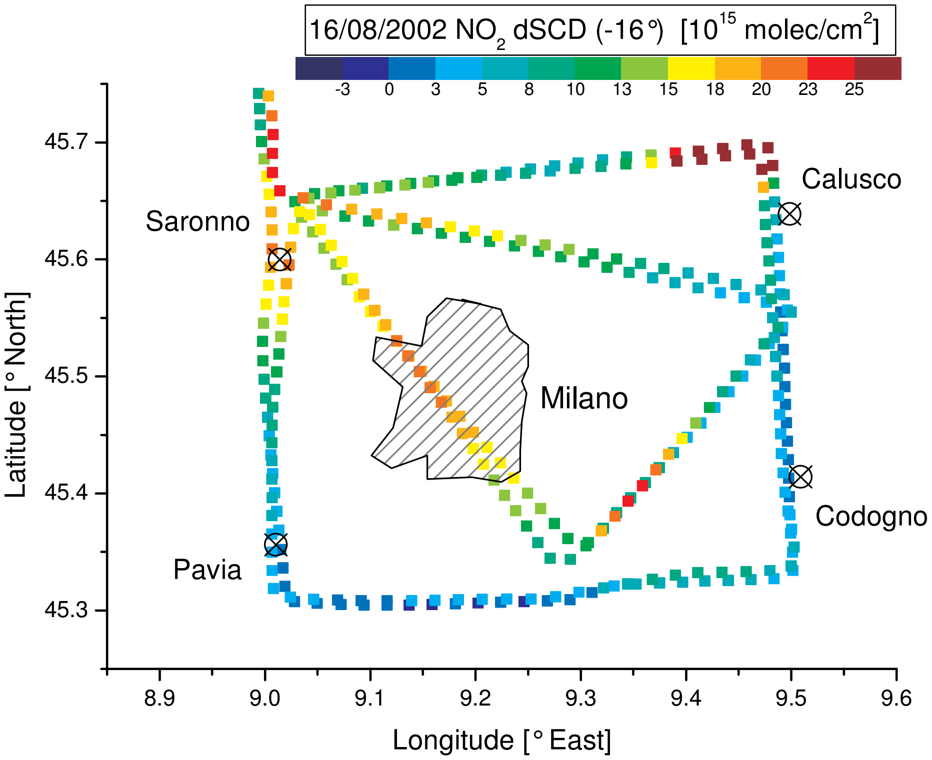

16/08/2002 this flight is discussed in detail in chapter 8.1

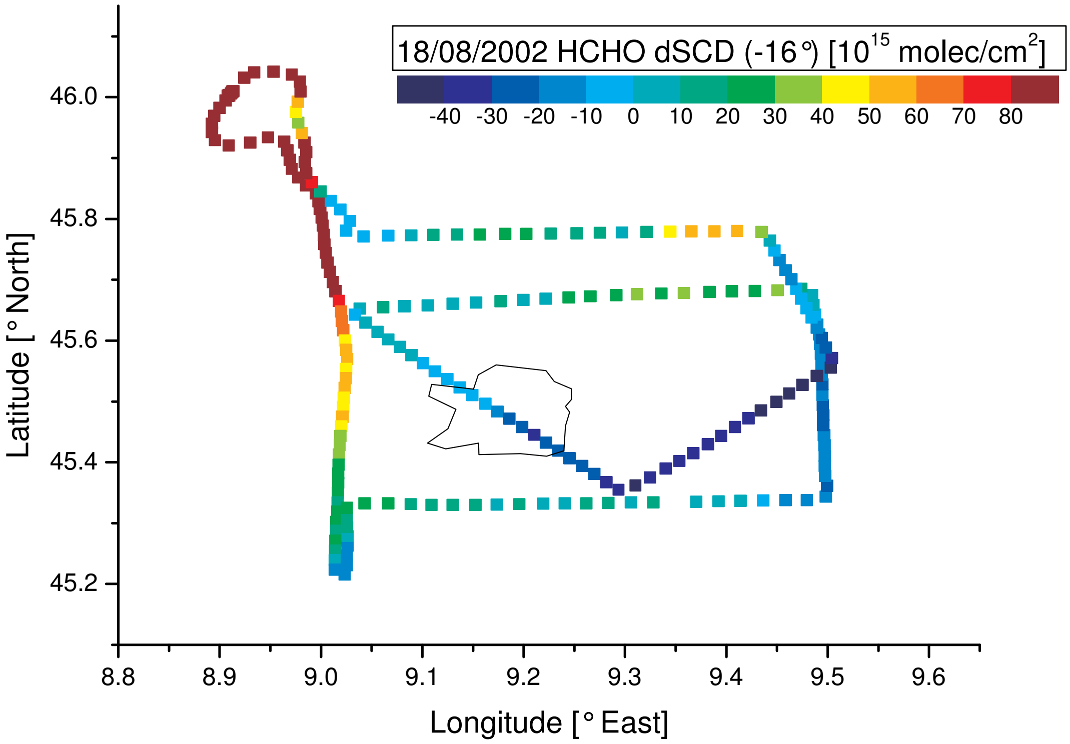

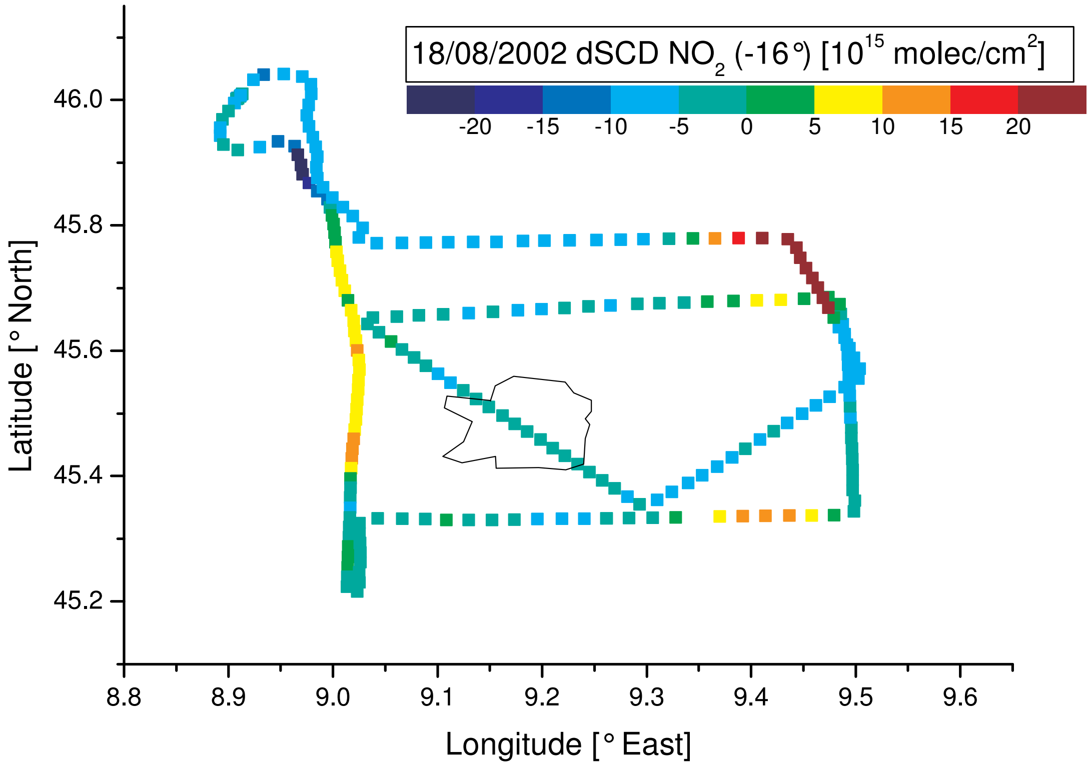

Cooling failed – inexperienced operator

F Overview of the SCDs FORMA II

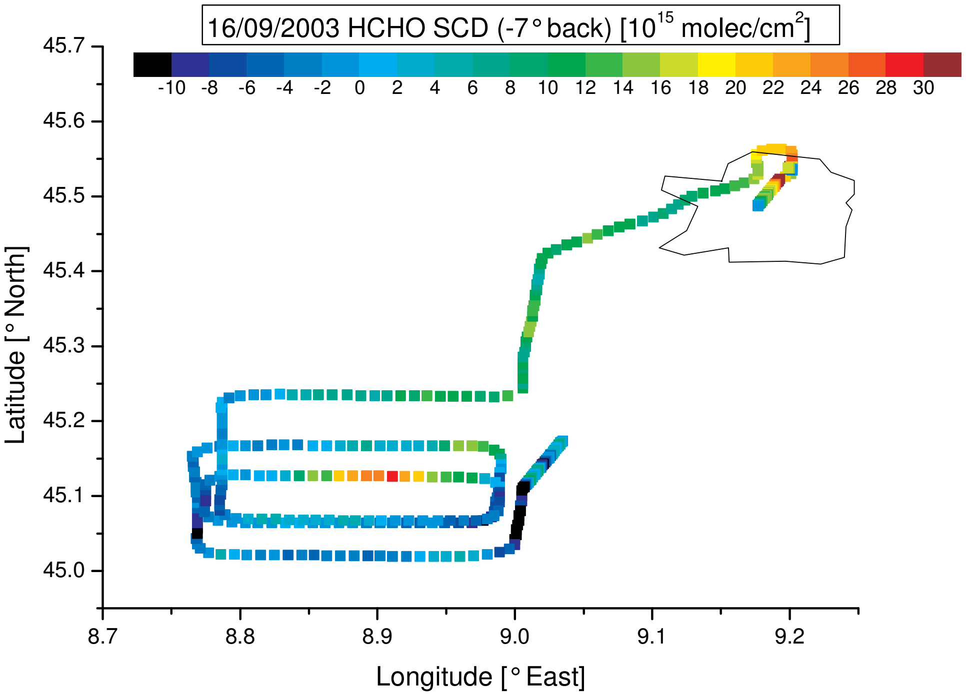

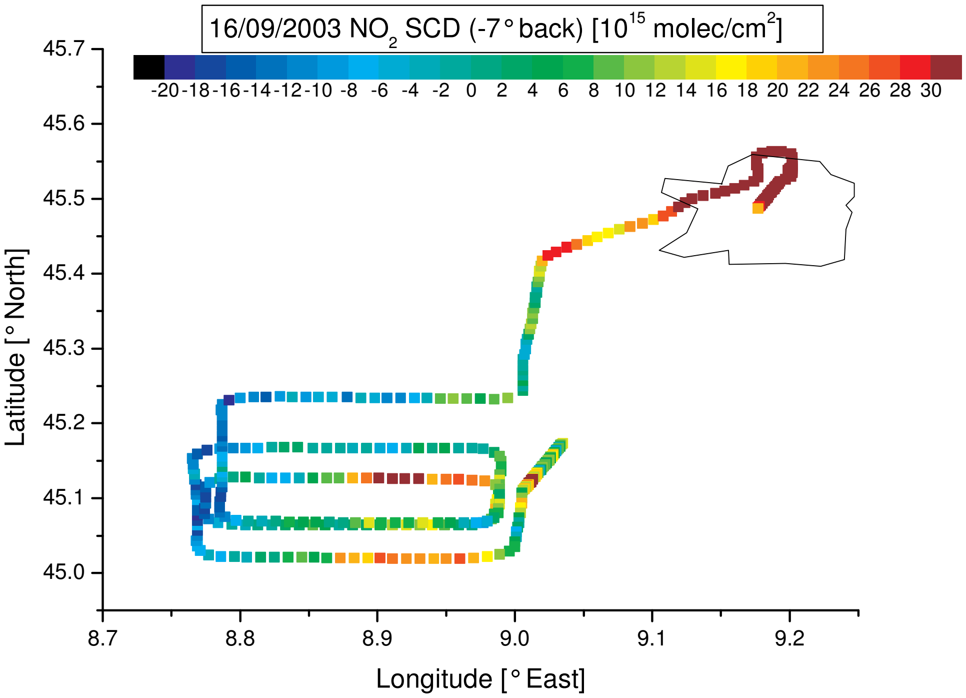

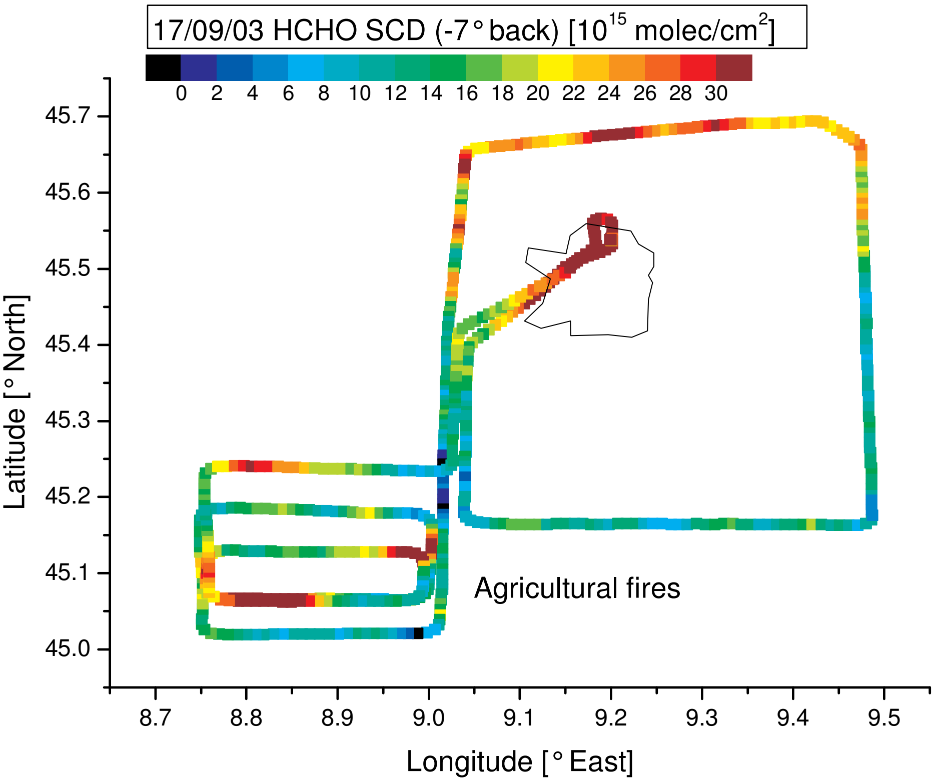
17/09/03 HCHO SCD (-7° back) [10^{15} molec/cm^2]
0 2 4 6 8 10 12 14 16 18 20 22 24 26 28 30
Latitude [° North]
45.0
45.1
45.2
45.3
45.4
45.5
45.6
45.7
Longitude [° East]
8.7
8.8
8.9
9.0
9.1
9.2
9.3
9.4
9.5
Agricultural fires

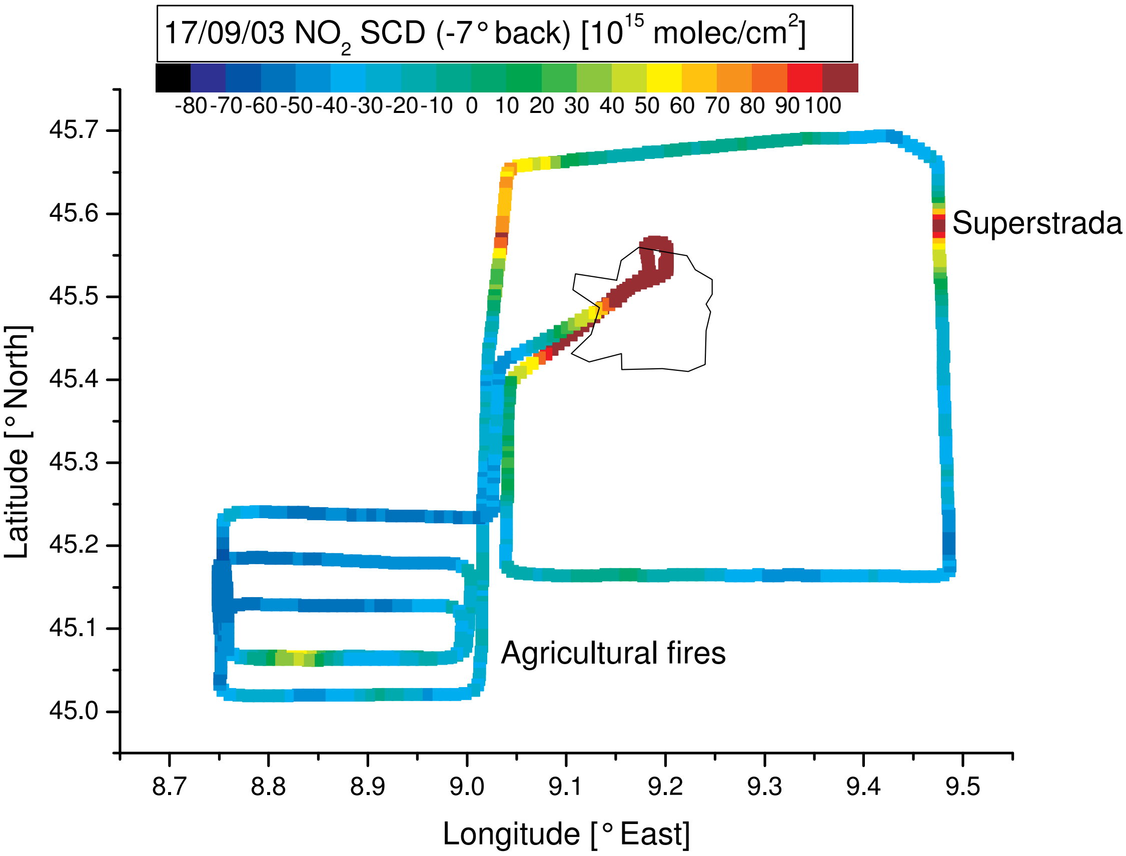
17/09/03 NO$_2$ SCD (-7° back) [10^{15} molec/cm^2]
-80 -70 -60 -50 -40 -30 -20 -10 0 10 20 30 40 50 60 70 80 90 100
Latitude [° North]
45.0
45.1
45.2
45.3
45.4
45.5
45.6
45.7
Longitude [° East]
8.7
8.8
8.9
9.0
9.1
9.2
9.3
9.4
9.5
Superstrada
Agricultural fires

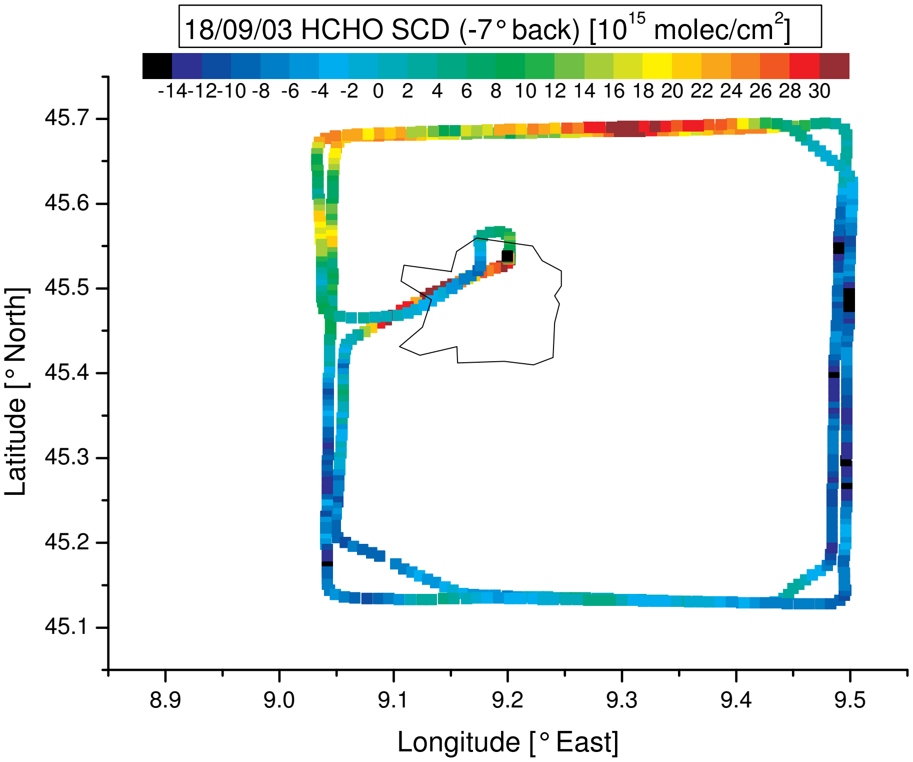
18/09/03 HCHO SCD (-7° back) [10^{15} molec/cm^2]
-14 -12 -10 -8 -6 -4 -2 0 2 4 6 8 10 12 14 16 18 20 22 24 26 28 30
45.7
45.6
45.5
45.4
45.3
45.2
45.1
Latitude [° North]
8.9
9.0
9.1
9.2
9.3
9.4
9.5
Longitude [° East]

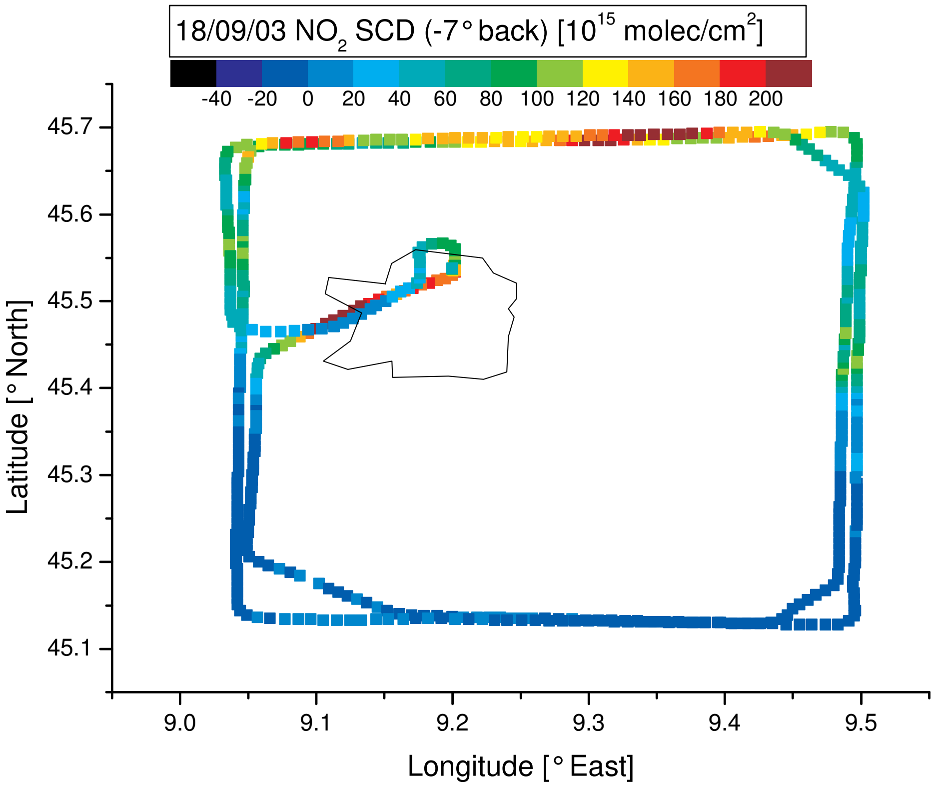
18/09/03 NO_2 SCD (-7° back) [10^{15} molec/cm^2]
-40 -20 0 20 40 60 80 100 120 140 160 180 200
45.7
45.6
45.5
45.4
45.3
45.2
45.1
Latitude [° North]
9.0
9.1
9.2
9.3
9.4
9.5
Longitude [° East]

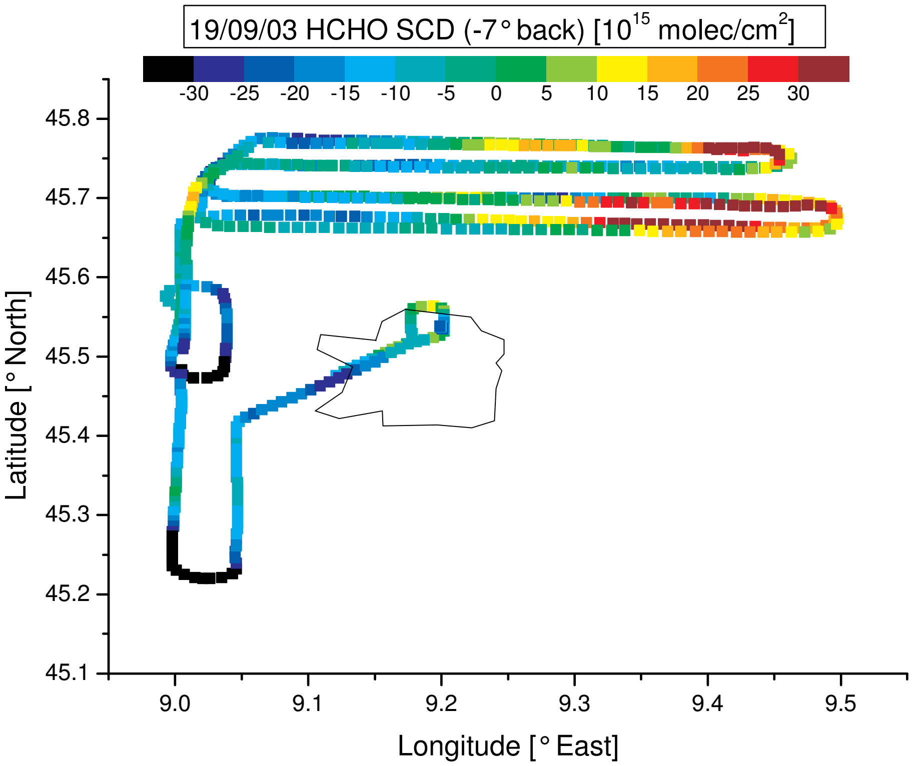
19/09/03 HCHO SCD (-7° back) [10^{15} molec/cm^2]
-30
-25
-20
-15
-10
-5
0
5
10
15
20
25
30
45.8
45.7
45.6
45.5
45.4
45.3
45.2
45.1
Latitude [° North]
9.0
9.1
9.2
9.3
9.4
9.5
Longitude [° East]

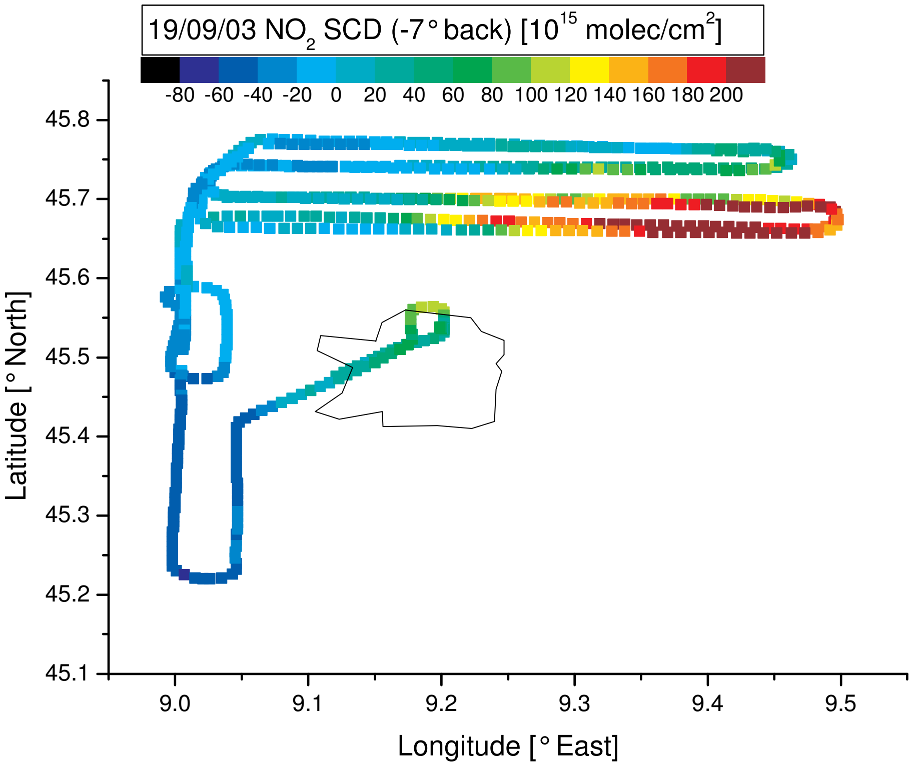
19/09/03 NO_2 SCD (-7° back) [10^{15} molec/cm^2]
-80
-60
-40
-20
0
20
40
60
80
100
120
140
160
180
200
45.8
45.7
45.6
45.5
45.4
45.3
45.2
45.1
Latitude [° North]
9.0
9.1
9.2
9.3
9.4
9.5
Longitude [° East]

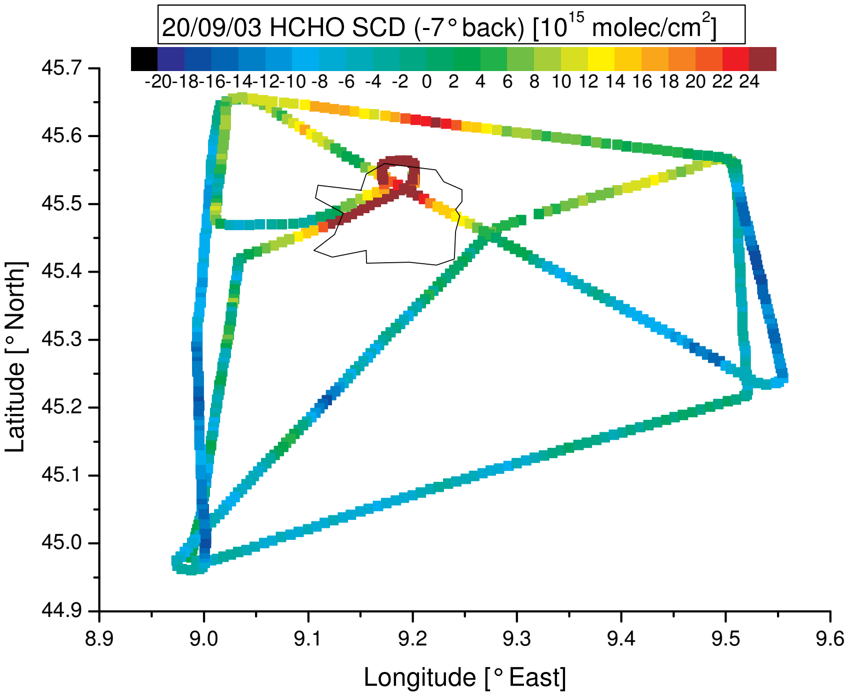
20/09/03 HCHO SCD (-7° back) [10^{15} molec/cm^2]
-20 -18 -16 -14 -12 -10 -8 -6 -4 -2 0 2 4 6 8 10 12 14 16 18 20 22 24
Latitude [° North]
45.7
45.6
45.5
45.4
45.3
45.2
45.1
45.0
44.9
8.9
9.0
9.1
9.2
9.3
9.4
9.5
9.6
Longitude [° East]

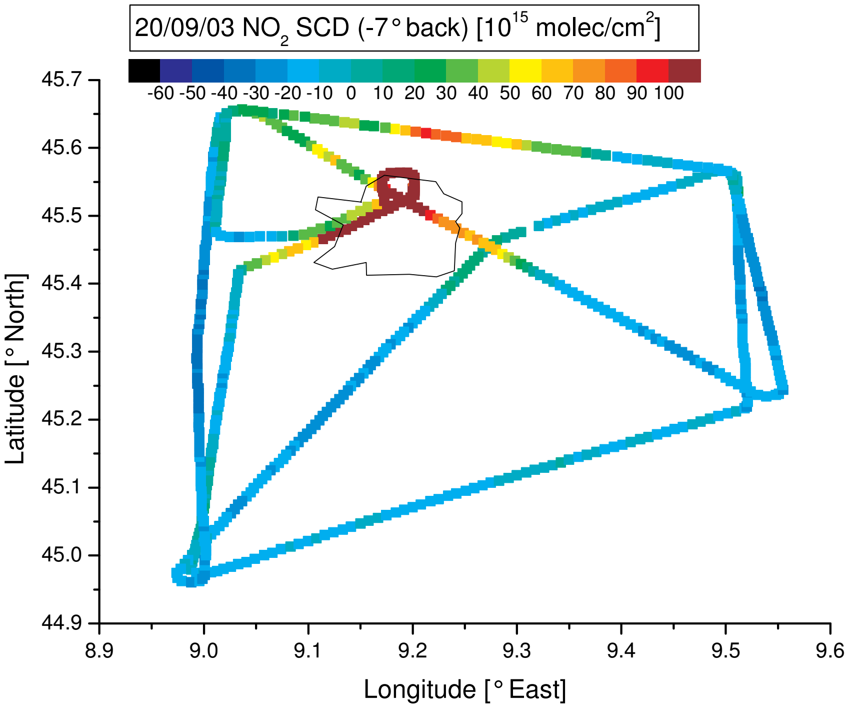
20/09/03 NO_2 SCD (-7° back) [10^{15} molec/cm^2]
-60 -50 -40 -30 -20 -10 0 10 20 30 40 50 60 70 80 90 100
Latitude [° North]
45.7
45.6
45.5
45.4
45.3
45.2
45.1
45.0
44.9
8.9
9.0
9.1
9.2
9.3
9.4
9.5
9.6
Longitude [° East]

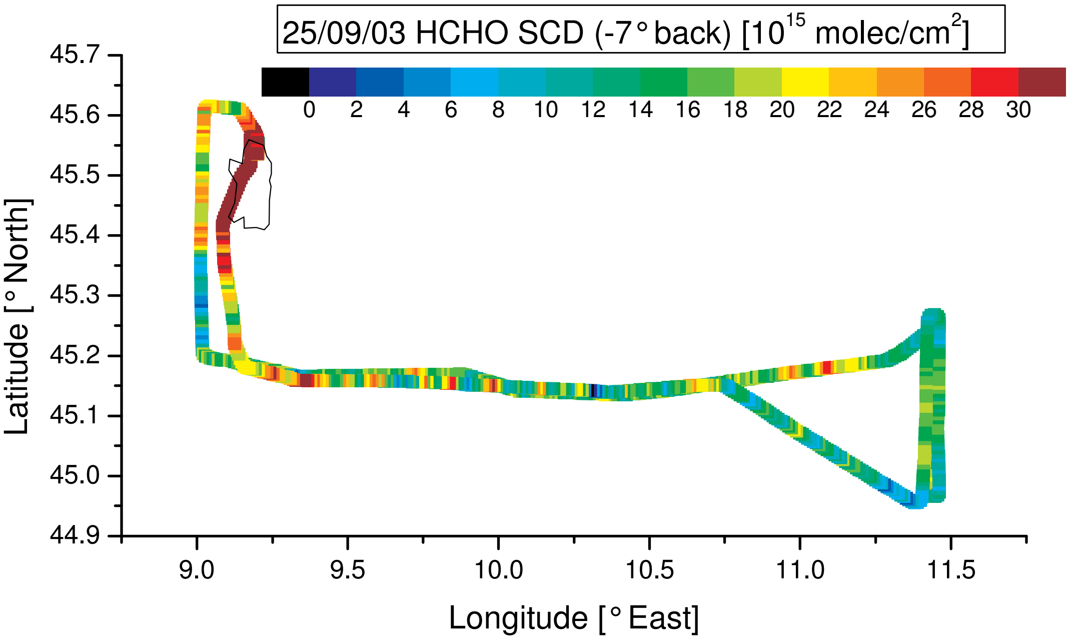
25/09/03 HCHO SCD (-7° back) [10^{15} molec/cm^2]
0
2
4
6
8
10
12
14
16
18
20
22
24
26
28
30
Latitude [° North]
45.7
45.6
45.5
45.4
45.3
45.2
45.1
45.0
44.9
Longitude [° East]
9.0
9.5
10.0
10.5
11.0
11.5

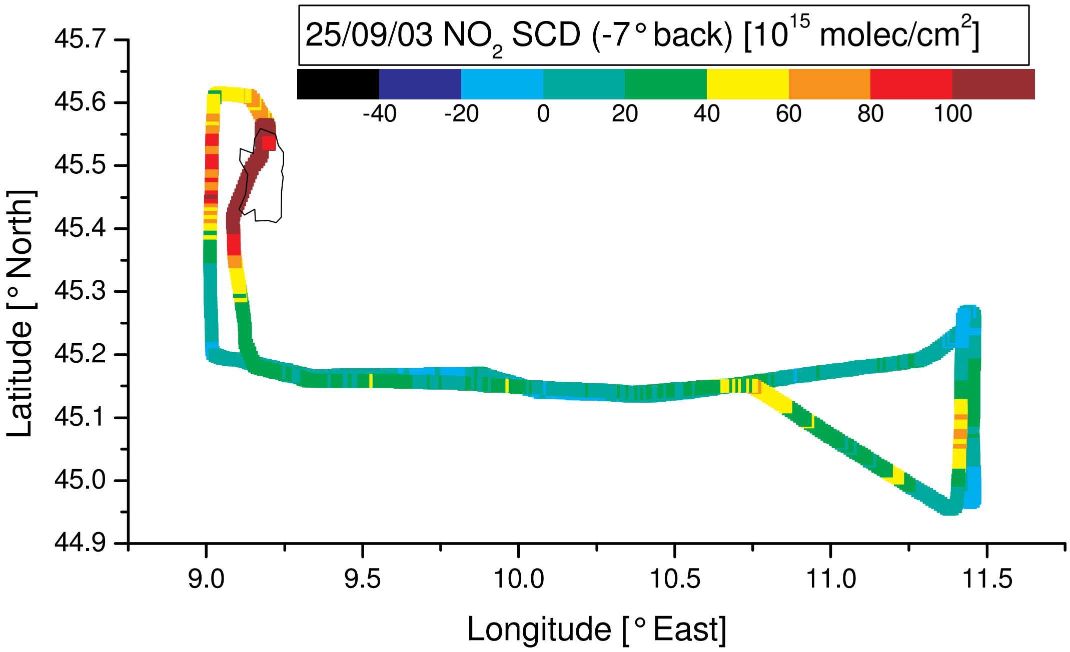
25/09/03 NO$_2$ SCD (-7° back) [10^{15} molec/cm^2]
-40
-20
0
20
40
60
80
100
Latitude [° North]
45.7
45.6
45.5
45.4
45.3
45.2
45.1
45.0
44.9
Longitude [° East]
9.0
9.5
10.0
10.5
11.0
11.5

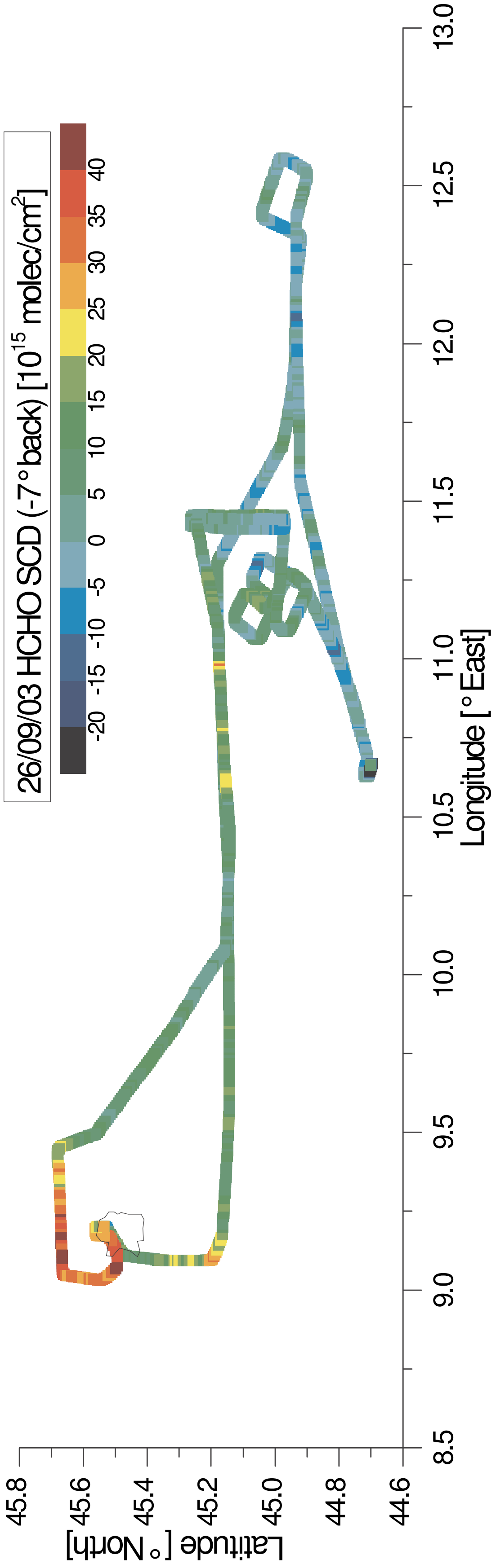
26/09/03 HCHO SCD (-7° back) [10^{15} molec/cm^2]
-20
-15
-10
-5
0
5
10
15
20
25
30
35
40
Longitude [° East]
8.5
9.0
9.5
10.0
10.5
11.0
11.5
12.0
12.5
13.0
Latitude [° North]
44.6
44.8
45.0
45.2
45.4
45.6
45.8

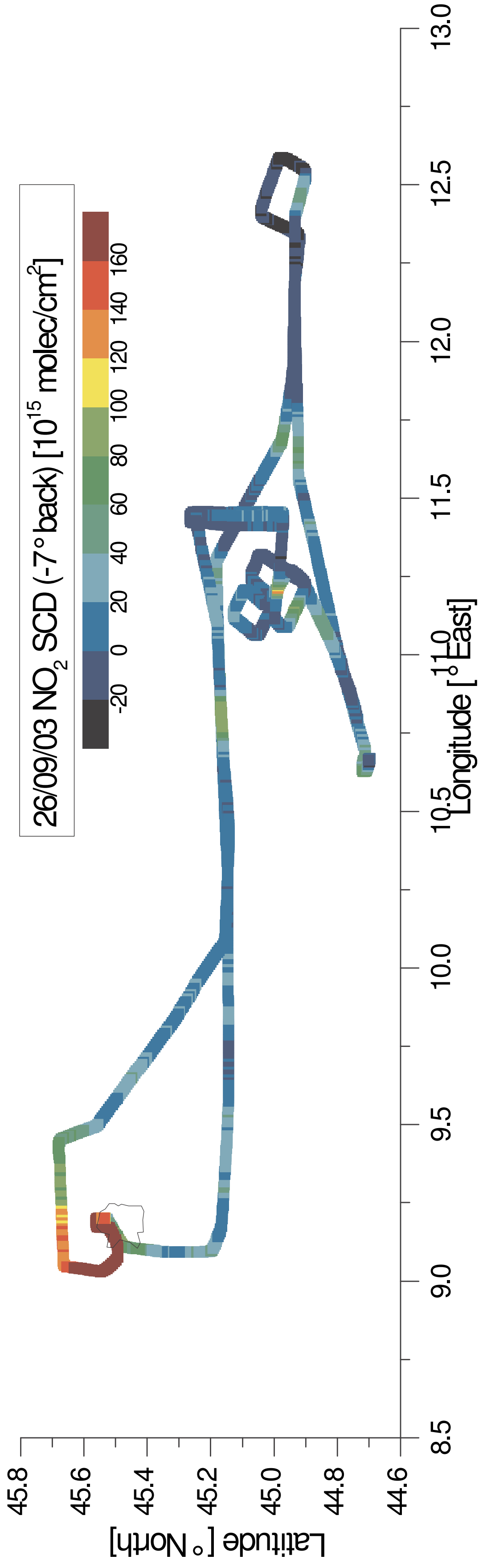
26/09/03 NO$_2$ SCD (-7° back) [10^{15} molec/cm^2]
-20
0
20
40
60
80
100
120
140
160
Longitude [° East]
8.5
9.0
9.5
10.0
10.5
11.0
11.5
12.0
12.5
13.0
Latitude [° North]
44.6
44.8
45.0
45.2
45.4
45.6
45.8

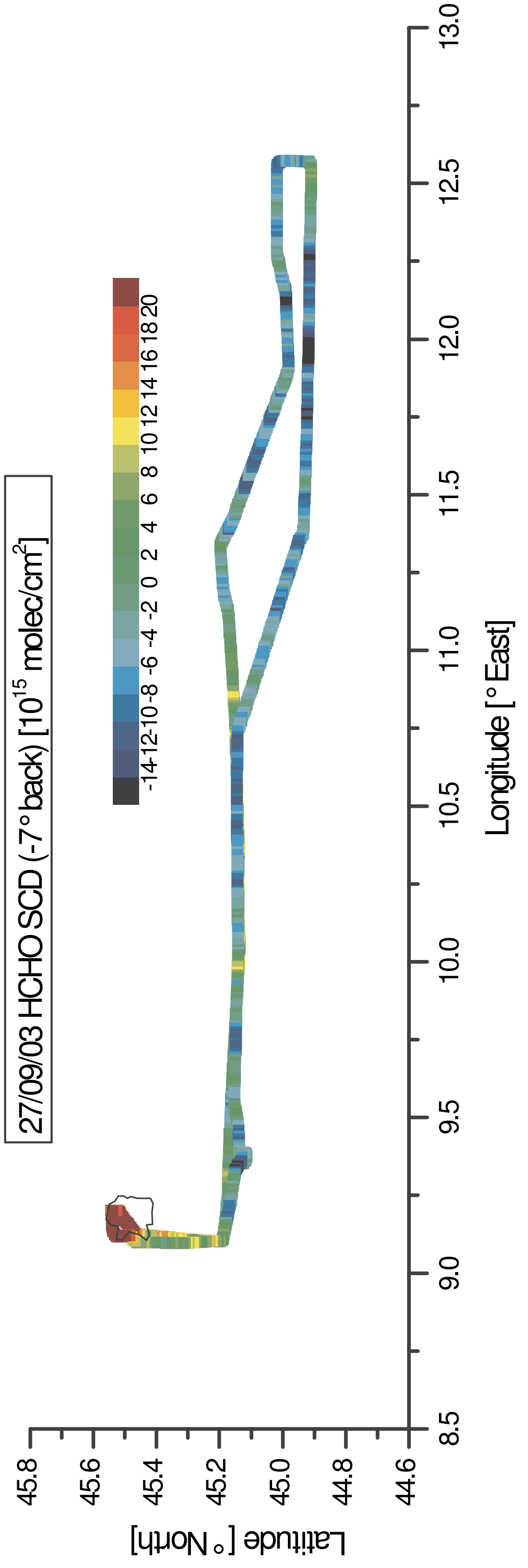
27/09/03 HCHO SCD (-7° back) [10^15 molec/cm^2]
-14 -12 -10 -8 -6 -4 -2 0 2 4 6 8 10 12 14 16 18 20
Latitude [° North]
45.8
45.6
45.4
45.2
45.0
44.8
44.6
Longitude [° East]
8.5
9.0
9.5
10.0
10.5
11.0
11.5
12.0
12.5
13.0

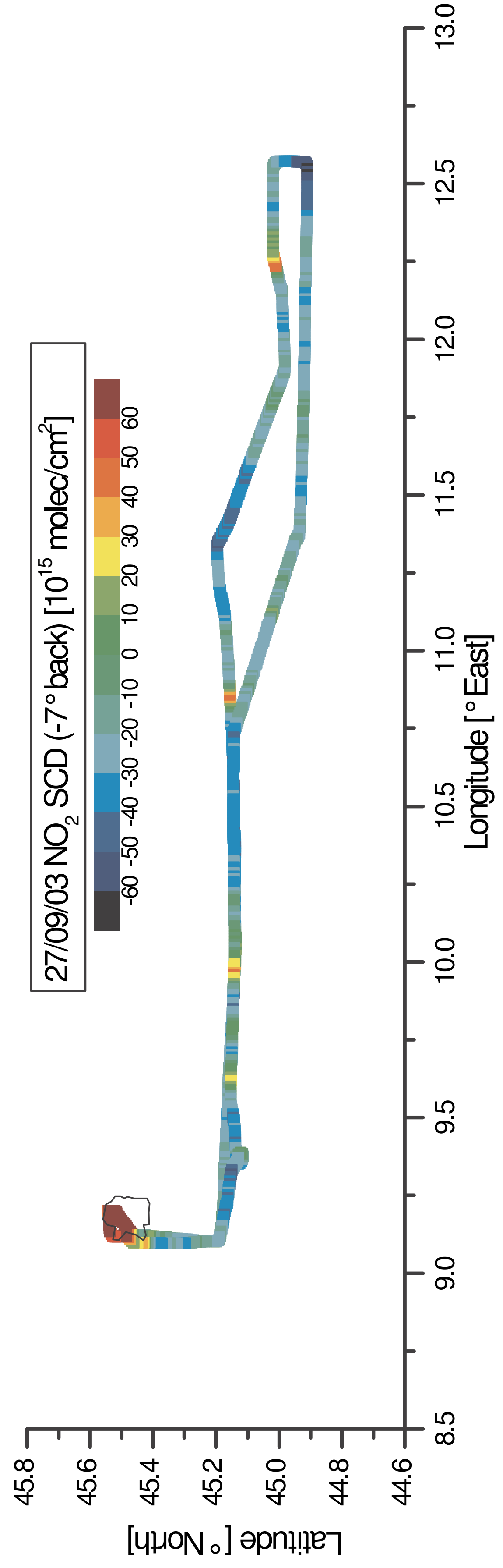
27/09/03 NO2 SCD (-7° back) [10^15 molec/cm^2]
-60 -50 -40 -30 -20 -10 0 10 20 30 40 50 60
Latitude [° North]
45.8
45.6
45.4
45.2
45.0
44.8
44.6
Longitude [° East]
8.5
9.0
9.5
10.0
10.5
11.0
11.5
12.0
12.5
13.0

References

Atkinson, R., Baulch, D. L., Cox, R. A., Crowley, J. N., Hampson, R. F., Hynes, R. G., Jenkin, M. E., Rossi, M. J. and Troe, J., Evaluated kinetic and photochemical data for O_x, HO_x, NO_x, and SO_x, *Atmos. Chem. Phys.*, 4, 1461-1738, **2004**.

Beirle, S., Estimating source strength and lifetime of Nitrogen Oxides from satellite data, *Dissertation,* Institut für Umweltphysik Universität, Heidelberg, **2004**.

Bland, V. V., Guarco, J. P. and Elderedge, T. V., Observations of NO_2 formation in two large natural gas fired boilers, *Proceedings of the 2000 International Joint Power generation conference*, Miami Beach, Florida, July 23-26, **2000**. (http://asme.pinetec.com, January 2005)

Boersma, K. F., Eskes, H. J. and Brinksma, E. J., Error analysis for tropospheric NO_2-retrieval from space, *J. Geophys. Res.,* 109, D04311, 1-20, **2004**.

Bösch, H., Camy-Peyret, C., Chipperfield, M. P., Fitzenberger, R., Harder, H., Schiller, C., Schneider, M., Trautmann, T. and Pfeilsticker, K., Intercomparison of measured and modeled stratospheric UV/vis actinic fluxes at large solar zenith angles, *Geophys. Res. Lett.*, 28, 1179-1182, **2001**.

Boßmeyer, J., Ship-Based Multi-Axis Differential Optical Spectroscopy Measurements of Tropospheric Trace Gases over the Atlantic Ocean, *Diplomarbeit*, Institut für Umweltphysik, Univerität Heidelberg, **2002**.

Bovensmann, H., Burrows, J. P., Buchwitz, M., Frerick, J., Noël, S., Rozanov, V. V., Chance, K. V. and Goede, A. P. H., SCIAMACHY: Mission Objectives and Measurement Modes, *J. Atmos. Sci.*, 56(2), 127-150, **1999**.

Brinkmann, R. T., Rotational Raman scattering in planetary atmospheres, *Astrophys. J.*, 154, 1087-1093, **1968**.

Bruns, M., NO_2 Profile Retrieval using Airborne Multiaxis Differential Optical Absorption Spectrometer (AMAXDOAS) data, *Dissertation*, Institut für Umweltphysik, Universität Bremen, **2004**.

Bruns, M., Buehler, S. A., Burrows, J. P., Heue, K.-P., Platt, U., Pundt, I., Richter, A., Rozanov, A., Wagner, T. and Wang, P., Retrieval of Profile Information from Airborne Multi Axis UV/visible Skylight Absorption Measurements, *Appl. Opt.* 43, 22, 4415-4426, **2004**.

Burrows, J. P. and Platt, U., Scanning the earth atmosphere in three dimensions for SCIAMACHY Validation, *Atmos. Chem. Phys*., special issue, **2004**.

Burrows, J. P., Dehn, A., Deters, B., Himmelmann, S., Richter, A., Voigt, S. and Orphal, J., Atmospheric remote-sensing reference data from GOME: Part 1. Temperature-dependent absorption cross-sections of NO_2 in the 231-794 nm range, *J. Quant. Spectrosc. Rad. Transfer*, 60, 1025-1031, **1998**.

Burrows, J. P., Richter, A., Dehn, A., Deters, B., Himmelmann, S., Voigt, S. and Orphal, J., Atmospheric remote-sensing reference data from GOME: Part 2. Temperature-dependent absorption cross-sections of O_3 in the 231-794 nm range, *J. Quant. Sepctrosc. Rad. Transfer*, 61, 509-517, **1999**.

Czerny, M. und Turner, A. F., Über den Astigmatismus bei Spiegelspektrometern, *Zeitschrift für Physik,* 61, 792-797, **1930**.

Dubovik, O., Holben, B., Eck, T. F., Smirnov, A., Kaufman, Y., King, M., Tandré, D. and Slutsker, I., Variability of Absorption and Properties of Key Aerosols Types observed in Worldwide Locations, *J. Atmos. Sci.*, 59, 590-608, **2002**.

Erle, F., Pfeilsticker, K. and Platt, U., On the influence of tropospheric clouds on zenith scattered light measurements of stratospheric species, *Geophys. Res. Lett.*, 22, 2725-2728, **1995**.

Fayt, C. and van Roozendael, M., WinDOAS 2.1 *software user manual*, IASB/BIRA, Uccle, Belgium, **2001**.

Feister, U. and Grewe, R., Spectral Albedo measurements in the UV and visible region over different types of surfaces, *Photochemistry and Photobiology*, 62, 736-744, **1995**.

Finlayson-Pitts, B. J. and Pitts, J. N. Jr., Chemistry of the Upper and Lower Atmosphere, Theory, Experiments and Applications, Academic Press San Diego, **2000**.

Fix, A., Ehret, G., Flentje, H., Poberaj, G., Gottwlad, M., Finkenzeller, H., Bremer, H., Bruns, M., Burrows, J. P., Kleinbühl, A., Küllmann, H., Kuttippurath, J., Richter, A., Wang, P., Heue, K.-P., Platt, U., Pundt, I. and Wagner, T., SCIAMACHY validation by aircraft remote measurements: design, execution and first results of the SCIA-VALUE mission, *Atmos. Chem. Phys.*, 5, 1273-2289, **2005**.

Frankenberg, C., Meinik, J. F., van Weele, M., Platt, U. and Wagner, T., Assessing Methane Emission from Global Space-Borne observations, *Science*, 308, 1010-1014, **2005**.

Friedeburg, C. v., Derivation of Trace Gas Information combining Differential Optical Absorption Spectroscopy with Radiative Transfer Modelling, *Dissertation*, Institut für Umweltphysik, Universität Heidelberg, **2003**.

Frieß U., Spektroskopische Messungen Stratosphärischer Spurenstoffe auf der Neumayer-Station (Antarktis) in den Jahren 1994/95, *Diplomarbeit,* Institut für Umweltphysik, Universität Heidelberg, **1997**.

Funk, O., Photon Pathlengths Distributions for Cloudy Skies – Oxygen A-Band Measurements and Radiative Transfer Model Calculations, *Dissertation*, Institut für Umweltphysik, Universität Heidelberg, **2000**.

Grainger, J. and Ring, J., Anomalous Fraunhofer line profiles, *Nature*, 193, 762, **1962**.

Greenblatt, G. D., Orlando, J. J., Burkholder, J. B. and Ravishankara, A. R., Absorption measurements of oxygen between 330 and 1140 nm, *J. Geophys. Res.*, 95, 18577-18582, **1990**.

Grzegorski, M., Frankenberg, Ch., Platt, U., Wenig, M., Fournier, N., Stammes, P. and Wagner, T., Determination of cloud parameters from SCIAMACHY data for the correction of tropospheric trace gases, *Proceedings of the ENVISAT and ERS symposium,* Salzburg, Austria, 6-10 September 2004,ESA publication SP-572 (CD-Rom), **2004**.

Hagelabwehr, Verein zur Erforschung der Wirksamkeit der Hagelbekämpfung, *Informationsbroschüre*, Landratsamt Rosenheim, 2. Auflage, **1996**.

Hak, C., Pundt, I., Trick, S., Kern, C., Platt, U., Dommen, J., Ordóñez, C., Prévôt, A. S. H., Junkermann, W., Astorga-Lloréns, C., Larsen, B. R., Mellqvist, J., Strandberg, A., Yu, Y., Galle, B., Kleffmann, J., Lörzer, J. C., Braathen, G. O. and Volkamer R., Intercomparison of four different in-situ techniques for ambient formaldehyde measurements in urban air, *Atmos. Chem. Phys.*, 5, 2881-2900, **2005**.

Hartl, A., Song, B. C. and Pundt, I., 2D Reconstruction of Atmospheric Concentration Peaks from horizontal Long Path DOAS Tomographic measurements: Parametrisation and Geometry within a discrete approach, submitted to Atmos. Chem. Phys. Disc.,**2005**.

Haug, H., Raman-Streuung von Sonnenlicht in der Erdatmosphäre, *Diplomarbeit*, Institut für Umweltphysik, Universität Heidelberg, **1996**.

Heckel, A., Richter, A., Tarsu, T., Wittrock, F., Hak, C., Pundt, I., Junkermann, W. and Burrows, J. P., MAX-DOAS measurements of Formaldehyde in the Po-Valley, *Atmos. Chem. Phys.*, 5, 909-918, **2005**.

Heland, J., Schlager, H., Richter, A. and Burrows, J. P., First comparison of tropospheric NO_2 column densities retrieved from GOME measurements and in situ aircraft profile measurements, *Geophys. Res. Lett.*, 29, 44-1-44-4, **2002**.

Hermans, C., Vandaele, A. C., Carleer, M., Fally, S., Colin, R., Jenouvrier, A., Coquart, B. and Mérienne, M. F., Absorption-cross sections of atmospheric constituents: NO_2, O_2 and H_2O, *Environ. Sci. and Pollut. Res.*, 6(3), 151-158, **1999**.

Heue, K.-P., Platt, U., Pundt, I., Wagner, T., Burrows, J. P., Loewe, A., Richter, A. and Wittrock, F., Shift-Probleme bei der Andor Kamera DU440-BU, *internal report* about the problems for the dealer LOT-Darmstadt, **2002**.

Heue, K.-P., Bruns, M., Burrows, J. P., Lee, W.-D., Platt, U., Pundt, I., Richter, A., Wagner, T. and Wang, P., NO2 over the tropics and the Arcic measured by AMAXDOAS in September 2002, *Proceedings of the 16th ESA symposium on rocket and balloon program and related research,* St. Gallen, Switzerland, 02-05 June 2003, ESA publications SP-530, August **2003**.

Heue, K.-P., Beirle, S., Bruns, M., Burrows, J. P., Platt, U., Pundt, I., Richter, A., Wagner, T. and Wang P., SCIAMACHY validation using the AMAXDOAS instrument, *Proceedings of the ENVISAT and ERS symposium*, Salzburg, Austria, 6-10 September 2004, ESA publication SP-572, (CD-Rom) **2004**.

Heue, K.-P., Richter, A., Bruns, M., Burrows, J. P., Friedeburg, C. v., Platt, U., Pundt, I., Wang, P. and Wagner, T., Validation of SCIAMACHY tropospheric NO_2-columns with AMAXDOAS measurements, *Atmos. Chem. Phys.*, 5, 1039-1051, **2005**.

Höller, H., Finke, U., Huntrieser, H., Hagen, M. and Fiegl, M., Lightning-produced NO_x (LINOX): experimental design and case study results, *J. Geophys. Res.*, 104, D11, 13911-13922, **1999**.

Hollwedel, J., Observation of tropospheric Bromine Monoxide from Satellite, Analysis of satellite data retrieved from GOME for 1996 to 2001, *Dissertation*, Institut für Umweltphysik, Universität Heidelberg, **2005**.

Hönninger, G., Friedeburg, C. v. and Platt, U., Multi AXis Differential Optical Absorption Spectroscopy, *Atmos. Chem. Phys.*, 4, 231-254, **2004**.

Huntrieser, H., Feigl, C., Schlager, H., Schröder, F., Gerbig, C., van Velthoven, P., Flatoy, F., Théry, C., Petzold, A., Höller, H. and Schumann, U., Airborne measurements of NO_x, tracer species, and small particles during the European Lightning Nitrogen Oxides Experiment, *J. Geophys. Res.*, 107, D11, ACH 5, 1-27, **2002**.

Junkermann, W., The actinic UV-radiation budget during the ESCOMPTE campaign 2001: Results of airborne measurements with the microlight research aircraft D-MIFU, *Atmos. Res.*, doi:10.1016/j.atmosres.2004.06.009, in press, January **2005**.

Kak, A. and Slanley, M., Principles of Computerized Tomographic Imaging, *IEEE Press*, **1988**.

Kern, C., Applicability of light-emitting diodes as light sources for active long path DOAS measurements, *Diplomarbeit*, Institut für Umweltphysik, Universität Heidelberg, **2004**.

Kühl, S., Quantifiying Stratospheric chlorine Chemistry by the Satellite Spectroemters GOME and SCIAMACHY, *Dissertation*, Institut für Umweltphysik, Universität Heidelberg, **2005**.

Kurucz, R. L., Furenlid, I., Brault, J. and Testerman, L., Solar Flux Atlas from 296 to 1300 nm, *Technical report*, National Solar Observatory, **1984**.

Laepple, T., Knab, V., Mettendorf, K. U. and Pundt, I., Longpath DOAS tomography on a motorway exhaust plume: Numerical studies and application to data from the BAB II campaign, *Atmos. Chem. Phys.*, 4, 1323–1342, **2004**.

Lohberger, F. Hönninger, G. and Platt, U., Ground-based imaging differential optical absorption spectroscopy of atmospheric gases*, Appl. Opt.,* 43 (24) 4711-4717, **2004**.

Louban, I., Zweidimensionale Spektroskopische Aufnahmen von Spurenstoff-Verteilungen, *Diplomarbeit*, Institut für Umweltphysik, Universität Heidelberg, **2005**.

Martin, V. R., Fiore, M. A. and van Donkelaar, A., Space –based diagnostics of surface ozone sensitivity to anthropogenic emissions, *Geophys. Res. Lett.*, 31, L06120, **2004**.

Mauzerall, D. L., Logan, J. A., Jacob, D. J., Anderson, B. E., Blake, D. R., Bradshaw, J. D., Heikes, B., Sachse, G. W., Singh, H. and Talbot, B., Photochemistry in biomass burning plumes and implications for the tropospheric ozone over the tropical South Atlantic, *J. Geophy. Res*., 103, D7, 8401-8423, **1998**.

McElroy, C. T., McLinden, C. A. and McConnell, J. C., Evidence for bromine monoxide in the free troposphere during the Arctic polar sunrise, *Letters to Nature*, 397, 338-341, **1999**.

Melamed, M. L., Solomon, S., Daniel, J. S., Langford, A. O., Portmann, R. W., Ryerson, T. B., Nicks Jr., D. K. and McKeen, S. A., Measuring reactive nitrogen emissions from point sources using visible spectroscopy from aircraft, *J. Environ. Monit*., 5, 29-34, **2003**.

Meller, R. and Moortgat, G., K., Temperature dependence of the absorption cross sections of formaldehyde between 223 and 323 K in the wavelength range 225-375 nm, *J. Geophys. Res.*, 201, D6, 7089-7101, **2000**.

Mettendorf, K. U., Aufbau und Einsatz eines Multibeam Instrumentes zur DOAS-tomographischen Messung zweidimensionaler Konzentrationsverteilungen, *Dissertation*, Institut für Umweltphysik, Universität Heidelberg, **2005**.

Mettendorf, K. U., Hartl, A. and Pundt, I., An indoor test Campaign of the Tomography Long Path Differential Optical Absorption Spectroskopy (DOAS) Technique, submitted to *J. Environ. Monit*., **2005**.

Noxon, J. F., Whipple, E. C. and Hyde, R. S., Stratospheric NO2. 1. Observational method and behaviour at midlatitudes, *J. Geophys. Res,* 84, 5047-5076, **1979**.

NZZ *Neue Züricher Zeitung*, Monatswetter, **07/03/2003**.

Petritoli, A., Ravegnani, F., Giovanelli, G., Bortoli, D., Bonaf, U., Kostadinov, I. and Oulanovsky, A., Off-Axis Measurements of Atmospheric Trace Gases by Use of an Airborne Ultraviolet-Visible Spectrometer, *Appl. Opt.*, 27, 5593-5599, **2002**.

Petritoli, A., Bonasoni, P., Giovanelli, G., Ravegnani, F., Kostadinov, I., Bortoli, D., Weiss, A., Schaub, D., Richter, A. and Fortezza, F., First comparison between ground based and satellite-borne measurements of tropospheric nitrogen dioxide in the Po basin, *J. Geophys. Res.,* 109, D150307, **2004**.

Pfeilsticker, K. and Platt, U., Airborne measurements during Arctic stratospheric experiment: Observations of O_3 and NO_2, *Geophys. Res. Lett.*, 21, 1375-1378, **1994**.

Platt, U., Perner, D. and Pätz, H., simultaneous measurements of atmospheric CH_2O, O_3 and NO_2 by differential optical absorptions, *J. Geophys. Res.*, 84, 6329-6335, **1979**.

Platt, U., Differential Optical Absorbtion Spectroscopy (DOAS), In Sigrist, M, W (Ed), *Monitorting by spectroscopic techniques*, New York: John Wiley & Sons, Inc, **1994**.

Pundt, I., DOAS Tomography: High quality 3D monitoring of tropospheric trace gases, project description, **1999**.

Pundt, I., Mapping of trace gas distribution from the ground and aircraft by UV-Vis spectroscopy, *AFO 2000 Newsletter*, BMBF, **2003**.

Pundt, I. and Mettendorf, K. U., Multibeam long-path differential optical absorption spectroscopy instrument: a device for simultaneous measurements along multiple light paths, *Appl. Opt.*, 44, 23, 4985-4994, **2005.**

Pundt, I., Mettendorf, K. U., Laepple, T., Knab, V., Xie, P., Lösch, J., Friedeburg, C. v., Platt, U. and Wagner, T., Measurements of trace gas distributions using Long-path DOAS-Tomography during the motorway campaign BABII: expermeintal setup and result for NO_2, *Atmos. Environ.*, 39, 967-975, **2005 a**.

Pundt, I., Heue, K.-P., Song, B. C., Platt, U., Wagner, T., Bruns, M., Burrows, J. P., Richter, A. and Wang, P., Two dimensional concentration distribution of a NO_2 emission plume from a point source derived by Airborne DOAS Tomography, submitted to *J. Geophys. Res.*, **2005 b**.

Pundt, I., Heue, K.-P., Wang P., Richter, A., Bruns, M., Song, B. C., Friedeburg, C. v., Laepple, T., Platt, U., Burrows, J. P. and Wagner, T., Airborne Multi Axis-DOAS measurements of formaldehyde in the plume of Milan, Italy, in preparation, **2005 c**.

Richter, A. and Burrows, J. P., Retrieval of Tropospheric NO_2 from GOME Measurements, *Adv. Space Res.*, 29(11), 1673-1683, **2002**.

Richter, A., Eyring, V., Burrows, J. P., Bovensmann, H., Lauer, A., Sierk, B. and Crutzen, P. J., Satellite measurements of NO_2 from international Shipping emissions, *Geophys. Res. Lett.*, 31, L23110, **2004**.

Roedel, W., Physik unserer Umwelt – Die Atmosphäre, Springer Verlag, Heidelberg, **1991**.

Rothman, L. S., The HITRAN molecular spectroscopic database and HAWKS (HITRAN Atmospheric Workstation): 1996 edition, Journal of Quantitative Spectroscopy and Radiative Transfer, 60(5), 665-710, **1998**.

Rozanov A., Rozanov, V. and Burrows, J. P., A numerical radiative transfer model for a spherical planetary atmosphere: combined differential integral approach involving the Picard iterative approximation, *J. Quant. Spectrosc. Rad. Transfer*, 69, 491-512, **2001**.

Sanghavi, S., An efficient Mie theory implementation to investigate the influence of aerosols on radiative transfer, *Diplomarbeit*, Institut für Umweltphysik, Universität Heidelberg, **2003**.

Sillman, S., Logan, J. A. and Wofsy, S. C., The Sensitivity of Ozone to Nitrogen Oxides and Hydrocarbons in Regional Ozone Episodes, *J. Geophys. Res.*, 95, D2, 1837-1851, **1990**.

Sinreich, R., Höhenprofilmessungen von NO_2 mit Multi-Axis-DOAS in Heidelberg, *Diplomarbeit*, Institut für Umweltphysik, Universität Heidelberg, **2003**.

Sinreich, R., Frieß, U., Wagner, T. and Platt, U., Multi Axis differential optical absorption Spectroscopy (MAX-DOAS) of gas and aerosol distributions, *Faraday Discuss.*, 130,1-12, **2005**.

Solomon, S., Schmeltekopf, A. L., and Sanders, R. W., On the interpretation of zenith sky absorption measurements, *J. Geophys. Res*, 92, D7, 8311-8319, **1987**.

Solomon, S., Miller, H. L., Smith, J. P., Sanders, R. W., Mount, G. H., Schmeltekopf, A. L. and Noxon, J. F., Atmospheric NO_3 1. Measurement technique and the annual cycle at 40° N, *J. Geophys. Res.*, 94, D8, 11041-11048, **1989**.

Stutz, J., Messungen der Konzentration troposphärischer Spurenstoffe mittels Differentieller-Optischer-Absorptionsspektroskopie, *Dissertation*, Institut für Umweltphysik, Universität Heidelberg, **1996**.

Stutz, J. and Platt, U., Numerical analysis and estimations of statistical errors of differential optical absorption spectroscopy measurements with a least-squares methods, *Appl. Opt.*, 35, 30, 6041-6053, **1996**.

Thomas, G. E. and Stammes, K., Radiative Transfer in the Atmosphere and Ocean, Cambridge University Press, Cambridge, **1999**.

van de Hulst, H. C., Light Scattering by Small Patricles, Dover Publications, **1957**.

Verkruysse, W. and Todd, L. A., Improved method “grid translation” for mapping environmental pollutants using a two-dimensional CAT scanning system, *J. Atmos. Environ.*, 38, 1801-1809, **2004**.

Voigt, S., Orphal, J., Bogumil, K. and Burrows, J. P., The temperature dependence (203-293 K) of the absorption cross sections of O_3 in the 230-850 nm region measured by Fourier-transform spectroscopy, *J. Photochem and Photobiol.*, A, 143, 1-9, **2001**.

Voigt, S., Orphal, J. and Burrows, J. P., The temperature- and pressure-dependence of the absorption cross-sections of NO_2 in the 250-800 nm region measured by Fourier-transform spectroscopy, *J. Photochem. and Photobiol.*, A, 149, 1-7, **2002**.

Vountas, M., Rozanov, V. V. and Burrows, J. P., Ring effect: Impact of rotational Raman scattering on radiative transfer in earth’s atmosphere, *J. Quant. Spectrosc. Rad. Transfer*, 60, 943-961, **1998**.

Wagner, T., Bruns, M., Burrows, J. P., Fietkau, S., Finocchi, F., Heue, K.-P., Hönninger G., Platt, U., Pundt, I., Richter, A., Rollenbeck, R. T., Friedeburg, C. v., Wittrock, F. and Xie, P., The AMAXDOAS-Instrument and its application for SCIAMACHY validation, *Proccedings of the 15th ESA symposium on rocket and balloon program and related research*, Biarritz, France, 28-31 May 2001, ESA publications SP-472, **2001 a**.

Wagner, T., Chance, K., Frieß, U., Gil, M., Goutail, F., Hönninger, G., Johnston, P. V., Karlsen-Tørnkvist, K., Kostadinov, I., Leser, H., Pertitoli, A., Richter, A., van

Roezendael, M. and Platt, U., Correction of the Ring effect and I_0-effect for DOAS observations of scattered sunlight, *Proceedings of the first DOAS workshop*, Heidelberg, Germany, 13, 14 September, **2001 b**.

Wagner, T., Friedeburg, C. v., Wenig, M., Otten, C., Platt, U., UV-visible observations of atmospheric O_4 absorptions using direct moon light and zenith scattered sunlight for clear-sky and cloudy conditions, *J. Geophys. Res.*, 107, D20, 4424, **2002**.

Wagner, T., Dix, B., Friedeburg, C. v., Frieß, U., Sanghavi, S., Sinreich, R., and Platt, U., MAX-DOAS O_4 measurements: A new technique to derive information on atmospheric aerosols – Principles and information content, *J. Geophys. Res.*, 109, D22205, **2004**.

Wahner, A., Tyndall, G. S. and Ravishankara, A. R., Absorption cross sections for OClO as a function of temperature in the wavelength range 240-480nm, *J. Phys. Chem.*, 91, 2734-2738, **1987**.

Wahner, A., Ravishankara, A. R., Sander, S. P. and Friedl, R. R., Absorption cross section of BrO between 312 and 385 nm at 298K and 223K, *Chem. Phys. Lett.*, 152:597-521, **1988**.

Wang, P., Richter, A., Bruns, M., Burrows, J. P., Heue, K.-P., Pundt, I., Wagner, T. and Platt, U., AMAXDOAS measurements and first results for the EUPLEX campaign, *Proceedings of the 16th ESA symposium on rocket and balloon program and related research*, St. Gallen, 02-05 June 2003, ESA SP-530, August **2003**.

Wang, P., Richter, A., Bruns, M., Rozanov, V. V., Burrows, J. P., Heue, K.-P., Pundt, I., Wagner, T. and Platt, U., Measurements of tropospheric NO_2 with an airborne multi axis DOAS instrument, *Atmos. Chem. Phys.*, 5, 337-343, **2005 a**.

Wang, P., Richter, A., Bruns, M., Burrows, J. P., Junkermann, W., Heue, K.-P., Wagner, T., Platt, U. and Pundt, I., Airborne multi-axis DOAS measurements of tropospheric SO_2 plumes in the Po-valley, Italy, *Atmos. Chem. Phys. Discuss.*, 5, 2017-2045, **2005 b**.

Wang, P., Richter, A., Bruns, M., Rozanov, A. V., Burrows, J. P., Heue, K.-P., Wagner, T., Pundt, I. and Platt, U., OClO vertical columns retrieval – a case study from Airborne multi axis DOAS measurements, *in preparation for Atmos. Chem. Phys. Disc.*, **2005 c**.

Weidner, F., Development and Application of a Versatile Balloon-Borne DOAS Instrument for Skylight Radiance and Atmospheric Trace Gas Measurements, *Dissertation*, Institut für Umweltphysik, Universität Heidelberg, **2005**.

Wenig, M., Jähne, B. and Platt, U., Operator Represenation as a new differential opitcal absorption spectroscopy formalism, *Appl. Opt.,* 44 (16), 3246-3253, **2005**.

Winterrath, T., Kurosu, T. P., Richter, A. and Burrows, J. P., Enhanced O_3 and NO_2 in Thunderstorm Clouds: Convection or Production?, *Geophys. Res. Lett.*, 26, 1291-1294, **1999**.

List of Figures

Tropospheric Chemistry

Differential Optical Absorption Spectroscopy

Radiative Transfer

Description of the Instrument

Description of the Measurement Campaigns

Results of the SCIAVALUE campaigns

Results of the FORMAT Campaigns

List of Abbreviations

AMF, A	Air Mass Factor
AGL	Above ground level
ASL	Above sea level
DLR	Deutsches Zentrum für Luft und Raumfahrt (German Aerospace Centre)
F/#	F-number defines the aperture of an optical instrument. $N.A. \approx \frac{1}{2 \cdot F/\#}$
ft	Feet: 1 ft = 0.3048 m, approximation: Altitude in feet*0.3 = Altitude in meters
FORMAT	FORMaldehyde As a Tracer for photo oxidation in the Troposphere
GMT	Greenwich mean time = UT
IFR	Instrumental Flight Rules, mostly used in high flight altitudes and above clouds
LOS	Line of sight, often used in the meaning of elevation angle
LT	Local time
ML	Mixing layer
MLH	Mixing layer height
N.A.	Numerical aperture see F/#
NRT	Near real time
ppb	parts per billion (1 in 10^9)
SAA,	Solar Azimuth Angle, angle between position of the sun and north
SCD, S	Slant Column Density
SCIAMACHY	Instrument on board the ENVISAT satellite
SCIAVALUE	SCIAMACHY VALidation and Utilization Experiment
SZA, ϑ	Solar Zenith Angle, angle between position of the sun and the zenith
TAS	True Air Speed
UT	Universal time = GMT
VCD, VC, V	Vertical Column Density
VFR	Visual Flight Rules, used in low altitudes, good viewing conditions $l_{vis} > 5$ km

Definition of Aviation Terms

The position of an aeroplane relative to the horizon is defined by two angles: pitch and roll. Simply spoken, the pitch will be positive, if the nose of the plane is directed upward.

If the aeroplane turns left, the right wing (marked green) will be higher than the left one and the pitch angle is positive.

The third possible angle between course over ground and the actual flight direction is called yaw. It is influenced by the wind speed perpendicular to the course. Together with the knowledge of the true air speed (TAS) and the ground speed it can be used to approximate the wind direction.

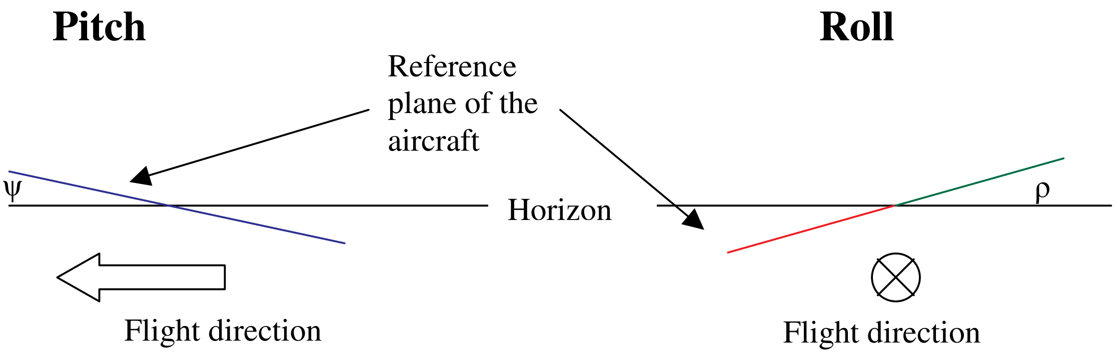

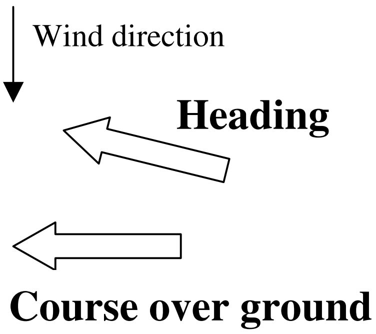

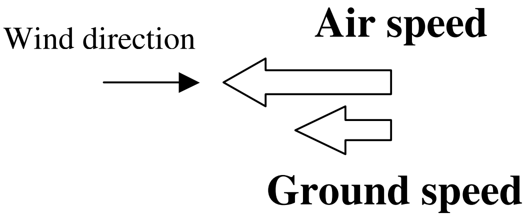

The typically of "our aeroplanes" the pitch angle varies between –10° and +10°

With the used planes, roll angles in a range between –30° and + 30° were typical.

Danksagung

Nun möchte ich mich noch bei allen bedanken, die mich während meiner Arbeit hier am Institut für Umweltphysik tatkräftig unterstützt haben:

- Professor Ulrich Platt danke ich für die interessante Aufgabenstellung.
- Da dieses Projekt in enger Kooperation mit dem IUP Bremen entstanden ist, gebührt ein entsprechender Dank auch Professor John P. Burrows.
- Meinen Gutachtern Prof. Ulrich Platt und Prof. Konrad Mauersberger danke ich für die wertwollen Anregungen und die zahlreichen Korrekturen.
- Dem gesamten AMAXDOAS Team möchte ich für die gute Zusammenarbeit danken: Thomas Wanger und Irene Pundt, sowie „meinem Bremer Chef“ Andreas Richter danke ich für die gute Betreuung der Projekte.
  I thank Bing Chao Song for the tomographic inversion of the data and the fruitful cooperation.
  Ich danke in diesem Zusammenhang den Kollegen aus Bremen, Marco Bruns und Ping Wang, ohne die das AMAXDOAS Instrument nicht hätte realisiert werden können: „Auch die andere Hälfte kann nicht alleine fliegen“.
- Den Betreibern und Piloten der beiden Flugzeuge:
  Dem Flugbetrieb des DLR ein großes Dankeschön für die Hilfestellungen bei der Zulassung und Integration des Instrumentes (H. Brockstieger) und für die Vorbereitung und Koordination der SCIAVALUE-Messkampagnen (H. Finkenzeller). Vor allem aber für die gelungenen und sicheren Messflüge danke ich den Piloten.
  Der Firma AVIONIK Straubing ein ebenso grosses Dankeschön für die Hilfe bei der Integration des AMAXDOAS in die GITY (W. Knott). Georg Vogl, dem Piloten der GITY, danke ich für Unterstützung vor und während der FORMAT-Kampagnen und natürlich dafür, dass er uns immer wieder sicher auf den Erdboden zurückgebracht hat.
- Den Mitarbeitern der Werkstat, die „mein“ Instrument mitgeplant und anschließend gebaut haben, danke ich ebenfalls sehr.
- Danke an alle Mitglieder der Arbeitsgruppe Luftchemie für das freundliche Klima (besonderen Dank an Christina Peters). Vor allem danke ich natürlich meinen Kolleginnen und Kollegen aus der Tomographie- und der Satelliten-Gruppe: Claudia Hak, Kai Uwe Mettendorf, Andreas Hartl, Bing Chao Song und Denis Pöhler, sowie Barbara Dix, Walburga Wilms-Grabe, Suniti Sanghavi, Christian Frankenberg, Steffen Beirle, Jens Hollwedel, Sven Kühl, Muhammad Fahim Khokhar, Roman Sinreich und Thierry Marbach.
  Danke allen, die meine Arbeit ganz oder teilweise Korrektur gelesen haben.
- Einen besonderen Dank meinen Eltern, die mich während meiner Arbeit immer unterstützt haben und nie am Gelingen der Arbeit gezweifelt haben.
- Ganz herzlichen Dank an Katrin, die mich nicht nur mental unterstützt hat, sondern auch als Fachfremde die gesamte Arbeit Korrektur gelesen hat.